GROWTH OF LITHIUM TRIBORATE CRYSTALS

By

Christopher Luke Parfeniuk

B. A. Sc., The University of British Columbia, 1988

M. A. Sc., The University of British Columbia, 1991

A THESIS SUBMITTED IN PARTIAL FULFILLMENT OF

THE REQUIREMENTS FOR THE DEGREE OF

DOCTOR OF PHILOSOPHY

in

THE FACULTY OF GRADUATE STUDIES

METALS AND MATERIALS ENGINEERING

We accept this thesis as conforming

to the required standard

THE UNIVERSITY OF BRITISH COLUMBIA

May 1994

In presenting this thesis in partial fulfilment of the requirements for an advanced degree at the University of British Columbia, I agree that the Library shall make it freely available for reference and study. I further agree that permission for extensive copying of this thesis for scholarly purposes may be granted by the head of my department or by his or her representatives. It is understood that copying or publication of this thesis for financial gain shall not be allowed without my written permission.

Metals and Materials Engineering
The University of British Columbia
2075 Wesbrook Place
Vancouver, Canada
V6T 1W5

Date: April 20 1994

Abstract

Lithium Triborate (LiB_3O_5) is a nonlinear optical crystal used to produce short wavelength radiation from a longer wavelength source. Large lithium triborate crystals of good quality are difficult to grow. The present investigation was undertaken to examine the parameters influencing the growth process, and the growth process itself, for crystals pulled from an LiB_3O_5 melt containing the flux MoO_3.

The pseudo phase diagram of the LiB_3O_5 – MoO_3 system was established and the eutectic concentration shown to be 61.5 weight percent MoO_3. The viscosity of the LiB_3O_5 system was measured as a function of temperature and MoO_3 concentration. It was shown that the viscosity decreases with increasing MoO_3 content. As the crystal grows MoO_3 is rejected by the crystal at the interface. A major factor in growing larger crystals is the movement of the rejected flux away from the interface, which depends on the fluid flow in the melt. The fluid flow in turn is dependent on buoyancy forces due to temperature gradients, as well as crystal and crucible rotations.

Calculations were carried out using a mathematical model for heat and fluid flow in the melt to establish the temperature distribution, fluid flow velocity and flow direction in the melt as a function of crystal and crucible rotation. Temperature measurements were then made in the melt in a crystal grower with a simulated crystal over a range of crucible rotation rotation rates, and the results compared to the mathematical model predictions. The boundary conditions used in the model were determined from temperature measurements in the melt. Comparing the calculated radial and axial temperature gradients in the melt with the measured values showed good agreement between the calculated and measured temperatures.

The flow patterns in the melt predicted by the model were also compared to the observed flow in a physical, model using glycerine as the melt and ink as a tracer, for the same size crucible and crystal used in crystal growth. The observed flow pattern was consistent with the model predictions. The results of both the mathematical and physical models clearly showed that most of the mixing in the liquid is associated with the crucible rotation and very little from buoyancy forces. From these results it was concluded that maximum crucible rotation should be used during growth to move the concentrated MoO_3 away from the advancing interface as rapidly as possible. Maximum MoO_3 concentrations should also be used, consistent with other constraints, since the viscosity of the liquid decreases with increasing MoO_3 concentration. It was shown that increasing the size of the crucible increased the flow velocity in the melt. As a result larger crucibles were used in the crystal growth experiments.

The length of good quality crystal which can be grown, is limited by the formation of inclusions in the crystal at the interface. The inclusions are shown to be primarily MoO_3 and are considered to form when the concentration of the MoO_3 reaches the eutectic concentration of 61.5 wt% at the interface. Calculations of the diffusion of MoO_3 through the boundary layer away from the advancing interface, show that growth must be slow with strong liquid mixing below the interface, to produce a crystal 1 cm in length.

A series of crystals of LBO were grown in a commercial crystal grower selecting the MoO_3 concentration, crystal and crucible rotations, and the pulling rate from the optimum values of the growth parameters given by the model predictions. Using these growth parameters, larger and better quality crystals were produced. Facets were observed on the crystal surfaces for the [001] growth direction which resulted in stagnant areas on the interface and the earlier appearance of MoO_3 inclusions. It was also observed that the crystal cracked readily under thermal stresses during cooling. To prevent cracking, crystals have been cooled slowly after growth in a uniform thermal gradient.

Table of Contents

List of Figures

List of Tables

Acknowledgement

I would like to thank Dr Indira Samerasakera, Dr Fred Weinberg, Jeff Edel, Dr Kim Fjeldsted and Brian Lent for their interest, suggestions and help over the course of this project. The assistance of the professional and technical staff at Crystar and UBC in particular, Jeff Claydon, Mark Waddington, Tim Elwel, Don Freschi, Fran Steeds, Dave Webb, Ernie Minkowitz and Mary Mager is greatly appreciated.

I especially thank my parents, Walter and Ruth Parfeniuk, for their love, encouragement and understanding that they have given me over the years. I would also like to thank Tresca Batten for her friendship and for putting up with me and my work schedule during my thesis. The conversation and friendship of the ladies from the 6:30 and 9:00 fitness class is also much appreciated.

Thanks are also extended to my fellow graduate students, especially Bernardo Hernandez-Morales, Colin Edie, Dave Tripp, Ed Chong and Barry Wiskel for their help during this project. I would like to express my gratitude to the Natural Sciences and Engineering Research Council and the British Columbia Science Council for financial support and Johnson Matthey Electronics (Crystar Research) for material support during my studies.

Chapter 1

Introduction

Lithium triborate LiB_3O_5, refered to as LBO, is a recently developed nonlinear optical crystal [1]. The nonlinear optical behaviour of crystals is described by the electromagnetic equations, as they relate to optics. The most important characteristic in the present case is the ability of the nonlinear optical crystal to generate higher optical harmonics. If a monochromatic light beam, from a laser source, is passed through a nonlinear optical crystal, higher harmonic light is generated. Specificaly if infrared light from a Nd:YAG laser is used as a source, ultra violet light will be generated in the crystal. In many applications the shorter shorter wavelength of ultra violet light has important advantages over visible and infrared light. The specific advantages of LBO over other nonlinear optical crystals are [2, 3]: large transparency range (170 nm to 2.6 μm), the largest effective second harmonic generation conversion coefficient, high surface damage threshold (25 GW/cm^2 for a 0.1 nsec pulse at 1.064 μm), chemical stability and is non$-$hydroscopic. LBO crystals are used in medical and industrial Nd:YAG lasers, in high powered lasers for military applications, and in optical parametric amplifiers and oscillators. Other nonlinear optical crystals of the borate family include $\beta-BaB_2O_4$ and $KB_5O_6(OH)_4 \cdot 2H_2O$.

Lithium triborate crystals are difficult to grow due to properties that are intrinsic to the crystal and the growth process. One difficulty results from the high viscosity of LBO. The material contains 87.5 weight percent B_2O_3 which has a viscosity of 630 poise at 727°C [4]. The high viscosity sharply reduces fluid flow and mass transfer in the melt during crystal growth. A second difficulty is that LBO solidifies in an incongruent

manner. Unlike GaAs which solidifies congruently, LBO forms from a peritectic reaction ($Li_4B_{10}O_{17}$ + Liquid $\rightarrow$ LiB_3O_5 at 834°C). Although it is possible to produce LBO crystals by peritectic growth, the process is very slow and only small crystals can be grown. To overcome this difficulty additional quantities of B_2O_3 or the compound MoO_3 is added to the LBO which enables LBO to be grown directly from the liquid without a peritectic reaction. This is normally termed flux or solution growth. In this study MoO_3 was used as a flux.

Adding MoO_3 to LBO introduces new factors in the crystal growth process. The amount of MoO_3 added must be established. The viscosity of the melt decreases with increasing MoO_3 concentration which can result in increased fluid flow in the melt. This is a significant factor since the MoO_3 is rejected by the solid at the advancing solid/liquid interface and must move away from the interface for growth to continue. However, the higher the bulk concentration of MoO_3 in the melt the higher the concentration build up immediately ahead of the interface for a given rate of crystal growth. If the concentration of MoO_3 at the solid/liquid interface reaches the eutectic then eutectic growth will occur which results in the formation of MoO_3 rich phases in the solid. This reduces the optical quality of the crystal and will cause the crystal to crack as it cools since LBO has a different thermal expansion coefficient than the MoO_3 phase.

Crystal growth from solution, in other systems, has been examined previously. Most of the work has been experimental, giving empirical correlations between growth parameters and the quality of the grown crystal. LBO has been known to exist since 1926. Research into the solution growth of LBO was initiated in 1987 [5] following the discovery of its special nonlinear optical properties. Reports on the growth of LBO crystals to the present, do not include details of the growth process and do not relate the growth parameters to defects generated in the crystal during growth.

LBO crystals are normally grown using the Top Seeded Solution Growth (Modified

Czochralski) Process in which a rotating, oriented, seed crystal is dipped in a counter rotating bath at a temperature just above the LBO–MoO_3 liquidus. The furnace temperature is then slowly cooled to allow the crystal to grow in the radial and axial directions. When the crystal has grown to a sufficient diameter, it is slowly raised resulting in crystal growth in the axial direction. The control of thermal gradients in the system and the control of the mass transfer of the MoO_3 at the solid/liquid interface, is critical to the growth of high quality crystals. The mass transfer of MoO_3 is strongly dependent on the viscosity of the melt, the crystal and crucible rotations, and the diffusion rate of MoO_3 in the melt.

In the present investigation direct temperature measurements of the melt were made during simulated crystal growth. The viscosity and other physical parameters of the liquid were also measured as function of MoO_3 concentrations. A mathematical model of the system is developed, using the finite element method, to characterize both the thermal field and the fluid flow in the system during crystal growth. A simple mass transfer model is used, in conjunction with the fluid flow model, to examine the concentration of MoO_3 ahead of an advancing solid/liquid interface during growth. The models are employed to select the optimum MoO_3 concentration, crystal and crucible rotation rates, temperature fields and growth rates to produce large diameter LBO crystals having minimal defects. Crystals of LBO were grown using a range of growth parameters, and the size of crystal, and visible crystal defects, related to the model predictions.

Chapter 2

Literature Review

2.1 Growth of Borate Crystals

This review will consider the growth of Lithium Triborate (LBO) and Barium Metaborate (BBO) crystals. Barium Metaborate is reviewed to complement the very limited published information available for LBO. Both crystals are similar, having B_2O_3 as a major component, and both crystals are grown in the same manner.

2.1.1 LBO Crystal Growth

The Lithium Triborate phase was initially reported in 1926. The phase diagram of Li_2O/B_2O_3 system was reported in 1958 [7] and is shown in Figure 2.1. The LiB_3O_5, LBO, phase in this complex system is shown by the arrow at 87.5 wt% B_2O_3. On cooling the melt at this borate concentration, there is a peritectic transformation at $834 \pm 4°C$. There is a eutectoid transformation at $595 \pm 20°C$; however, LBO was found to be stable with no eutectoid transformation occurring on cooling below 595°C [5]. The successful growth of small crystals of LBO was reported in 1978 [8] and 1980 [9] using a solid state reaction process in which a B_2O_3 glass was covered with LiF powder and reacted at 750°C for 10 hours. The LBO crystal structure was analyzed and found to be orthorombic, symmetry class mm2 and having a space group of P_{na2_1}. The strong non−linear optical properties of LBO, reported in 1987, resulted in the development of the solution growth of these crystals.

Solution growth consists of adding fluxes to LBO which modifies the phase diagram and allows LBO to be grown directly as a solid from the liquid. Flux materials used are MoO_3[2], LiF [5] or B_2O_3 as a self fluxing agent. The flux must have a high solubility in the melt over a large temperature range and no solubility in the solid LBO. A derived phase diagram for the LBO – MoO_3 system is shown in Figure 2.2. It was constructed by extrapolating the Li_2O/B_2O_3 phase diagram from 87.5 wt% B_2O_3 towards 100% MoO_3. Crystals can be grown directly from the melt in the MoO_3 concentration range between C_1 and C_2. Reports of the successful growth of LBO crystals using various fluxes and starting materials are listed in Table 2.1. No details of the growth process are given, nor specifics concerning the quality of the crystals produced. The post growth cooling rate is important as the thermal stresses during cooling readily cause the crystal to fracture.

LBO crystals are grown by slow cooling and may be combined with pulling the crystals vertically from the melt. The melt is held in platinum crucibles, 50 mm in diameter and height [1, 2], platinum being required because of the corrosive nature of B_2O_3. The crucible is heated with nickel/chromium resistance heating elements in a vertical furnace system. The insulation consists of alumina based ceramics. The starting materials are made up of a combinations of LiOH, $Li_2B_4O_7$, $LiBO_2$, B_2O_3, H_3BO_3 or similar compounds which contain extra hydrogen, carbon or oxygen components, the final mixture containing 87.5 wt% B_2O_3. The amount of flux added can vary, near 55 wt% MoO_3, or enough to produce a bulk composition of at least 90.3 wt% for B_2O_3 [2]. The amount of LiF added as flux is not specified in the relevant reports.

The charge, including the LBO components and flux, is heated to 950°C to ensure that all the components melt, and held for 5 hours, to allow the melt to homogenize and H_2O and CO_2 vapour to form [1, 2, 5]. Following homogenization, the melt is cooled, and at a suitable melt temperature, a seed crystal is dipped into the melt. The crystal is grown by slowly cooling the furnace at a fixed rate. In some cases, the seed is slowly

pulled from the melt to allow for additional growth in the vertical direction. The seed orientation is generally [001] parallel to the growth direction. During growth the crystal is rotated as a constant rate. When growth is complete the crystal is lifted from the melt and slowly cooled in the furnace to room temperature. The crystals are sensitive to thermal strains and can fracture during cooling. Details of the growth procedure are dependent on the fluxing agent, as outlined below, for B_2O_3 self fluxing and MoO_3.

Crystal growth, with a B_2O_3 self fluxing system, is carried out near the liquidus temperature of 834°C for a 90 wt% B_2O_3 melt concentration. The procedure is to cool the melt to 848°C, dip the seed into the melt, hold for 30 minutes, then rapidly cool to 833°C. The melt is then slowly cooled between 0.5 to 2°C/day during which time the crystal slowly grows in the melt. The seed is not pulled vertically and the crystal is not rotated during growth [2]. Growth is terminated when the crystal has reached the specified dimensions. Since B_2O_3 has a high viscosity, the self fluxing process results in a melt having a high viscosity. This markedly reduces fluid flow in the melt due to bouyancy forces and reduces mass transfer in the melt adjacent to the growing crystal interface. This results in a high level of growth defects in the crystal [5].

With an MoO_3 flux, the homogenized melt is cooled to 673°C and held for 5 hours. The seed crystal is then dipped into the melt, held for 30 minutes, and the melt then cooled at 5°C/day as the crystal grows. During growth the seed is rotated at 30 rpm and pulled from the melt at a rate of 1 mm/day [5].

After crystal growth, the seed is separated from the melt and cooled to room temperature at rates between 40 to 100°C/hour. Stress in the crystal during cooling can cause the crystal to fracture, due to anisotropy of the expansion coefficients of the crystal and the solidified flux on the crystal surface [5].

It was found that LBO decomposes at high temperatures when exposed to water vapour in an ambient atmosphere [6]. The decomposed material is $Li_3B_7O_{12}$. A dry

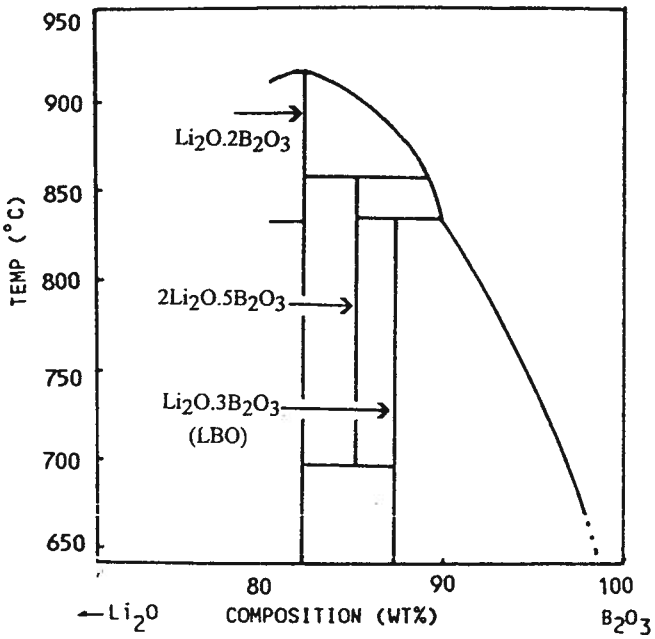

Figure 2.1: Phase Diagram of the Li_2O-B_2O_3 system [7].

nitrogen atmosphere was used to stop the decomposition. Figure 2.3 shows the difference in the weight loss of an LBO sample in a dry and wet nitrogen atmosphere.

Crystal sizes grown were reported to be as large as $35 \times 30 \times 15$ mm^3 using MoO_3 [5] and $30 \times 30 \times 15$ mm^3 using B_2O_3 [1]. The crystals were reported to be inclusion free, however no photographs of the LBO crystals were shown.

2.1.2 Barium Metaborate Crystal Growth

The successful growth of Barium Metaborate crystals (BBO), $\beta-BaB_2O_4$, was reported in 1985 [11] using Top Seeded Solution Growth (TSSG). The crystals were grown with B_2O_3 flux, the melt containing 43wt% B_2O_3. This is appreciably lower than the B_2O_3 content in LBO growth (87.5 wt%) which results in a much lower liquid viscosity in the BBO melt. Na_2O was examined as an alternative flux to B_2O_3 and was shown to produce better quality crystals [12]. Na_2O has a solubility range of 22 to 30 wt% in BBO in the temperature range of 755 to 925°C [13].

Year	Starting Materials	Flux	Growth Parameters	Crystal Size
1989 [1]	Li_2O, H_3BO_3,	? wt% B_2O_3	SOT = 833°C CR = 0.5°C/day PR = not given atm = not given CDR = 40°C/hour SROT = not given	$30 \times 30 \times 15$ mm^3
1989 [2]	Li_2CO_3, H_3BO_3,	90 wt% B_2O_3	SOT = 848°C CR = 0.5°C/day PR = not given atm = not given CDR = 40°C/hour SROT = 0 rpm	$18 \times 20 \times 6$ mm^3
1989 [2]	Li_2CO_3, H_3BO_3,	55 wt% MoO_3	SOT = 673°C CR = 5°C/day PR = not given atm = not given CDR = 100°C/hour SROT = 30 rpm	$20 \times 35 \times 9$ mm^3
1989 [10]	Li_2CO_3, H_3BO_3,	93 wt % B_2O_3,	SOT = 778°C CR = 1.3°C/day PR = not given atm = air CDR = not given SROT = not given	No values listed
1990 [5]	$LiCO_3$, Li_2O, LiOH, $Li_2B_4O_7$ $LiBO_2$, B_2O_3, H_3BO_3, etc	> 90 wt % B_2O_3, ? wt % LiF	SOT = 834°C CR = 0.2-2°C/day PR = 1mm/day CDR = not given	Size: $35 \times 30 \times 15$ mm^3

Table 2.1: Reports on LBO crystal growth. SOT = seed on temperature: CR = cooling rate; PR = pull rate; atm = atmosphere, CDR = post growth cooling rate, SROT = seed rotation rate.

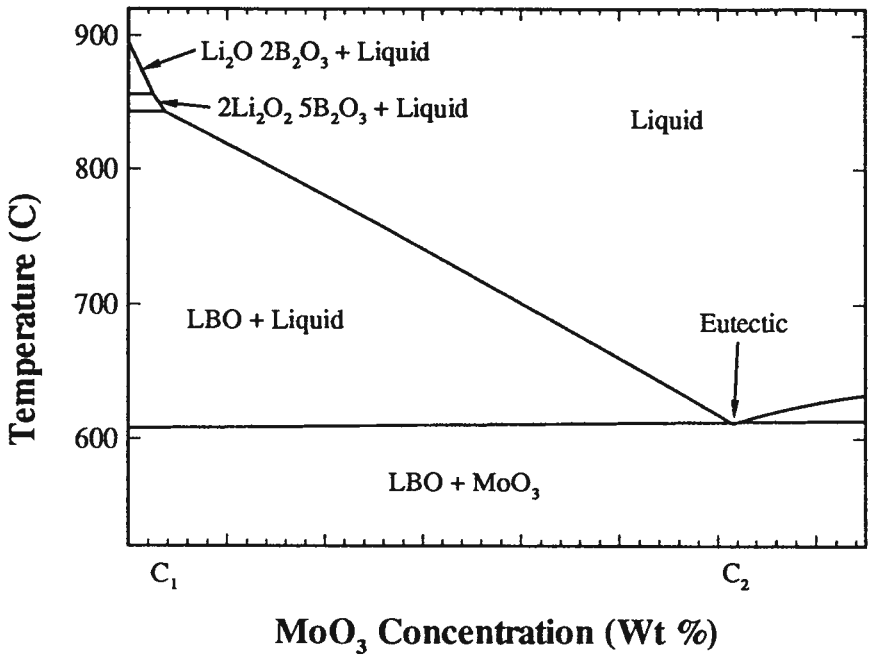

Figure 2.2: Derived phase diagram of the LBO - MoO_3 system. The composition between C_1 and C_2 is the region where the direct crystal growth of LBO is possible.

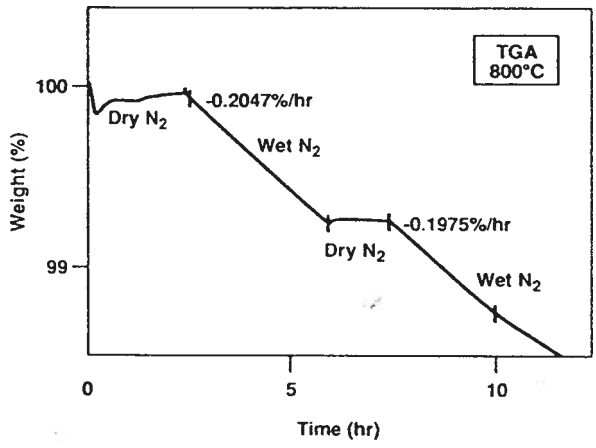

Figure 2.3: TGA analysis showing the effects of water vapour on the stability of LBO under dry and wet nitrogen [6].

The procedure for growing BBO crystals, and evaluation of their quality, is given by Feigelson et al. [13]. Two types of furnaces were used, a low gradient wire wound furnace and a high gradient SiC heated furnace. The platinum crucibles containing the melt were 55 mm in diameter and 55mm in height. The melt composition used was 80at% BBO−20at%Na_2O. The axial and radial gradients were approximately 50°C and 30°C for the high gradient furnace and 20°C and 10°C for the low gradient furnace. Temperature fluctuations due to thermal convection was measured to be ±8°C.

To grow a crystal, the charge was melted and then cooled to the temperature at which the seed crystal was dipped into the melt. The dipping temperature was established by immersing a platinum wire into the melt and cooling until a small amount of BBO solidified on the wire. The melt was maintained at this temperature for 12 hours. Next, the wire was removed and the melt temperature increased by several degrees after which the BBO seed was immersed into the liquid. During growth the seed was rotated at rates between 2 and 16 rpm. There was no crucible rotation. Fluid flow occurred in the melt, due to natural convection which could be detected by the presence of radial convective boundaries at the top surface, Figure 2.4.

Two seed crystal orientations were examined the **c** direction [001] and **b** direction [010] aligned parallel to the growth direction. The **c** orientation proved to be the better of the two, since the **b** direction crystals exhibited more cracking during cooling. The interface shape during growth was more concave towards the melt for the **c** orientation, because of the higher thermal conductivity of the crystal in this direction; one order of magnitude larger than in the **b** direction. Crystal quality improved at higher crystal rotation rates due to the increase in the fluid flow velocity at the interface. At the highest rotation rates the interface inverted from concave to the liquid to concave to the solid. During crystal growth, the cooling rate of the melt was maintained at 2°C/day and a pulling rate of 0.5 to 1.0 mm/day was used. After approximately 12 mm of crystal had

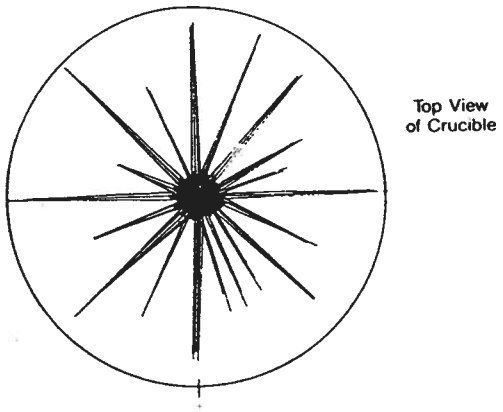

Figure 2.4: Top view of BBO–Na_2O melt showing radial convective cell boundaries and central cold spot [13].

grown the planar interface breaks down, resulting in flux inclusions being incorporated into the crystal.

Better crystal quality was obtained using the large gradient furnace. It was also found that crystal quality was best at the outside region of the crystal and worst at the centre. These correspond to high flow and stagnant regions in the melt below the growing interface [13].

2.2 Physical Properties of LBO

An extensive literature search was carried out to obtain the thermo-physical properties of the components of LBO and MoO_3, giving the values listed in Table 2.2 for LBO, Li_2O, B_2O_3, MoO_3 and Mo_2O_3. The specific heat and density for Li_2O, B_2O_3 and MoO_3 are well established [14, 15]. Experimental measurements of the viscosity of B_2O_3 [4] are available but no data was found for the other components of the LBO/flux mixtures. The viscosity of B_2O_3, Figure 2.5, is very high, 280 poise at 833°C and 692 poise at 727°C.

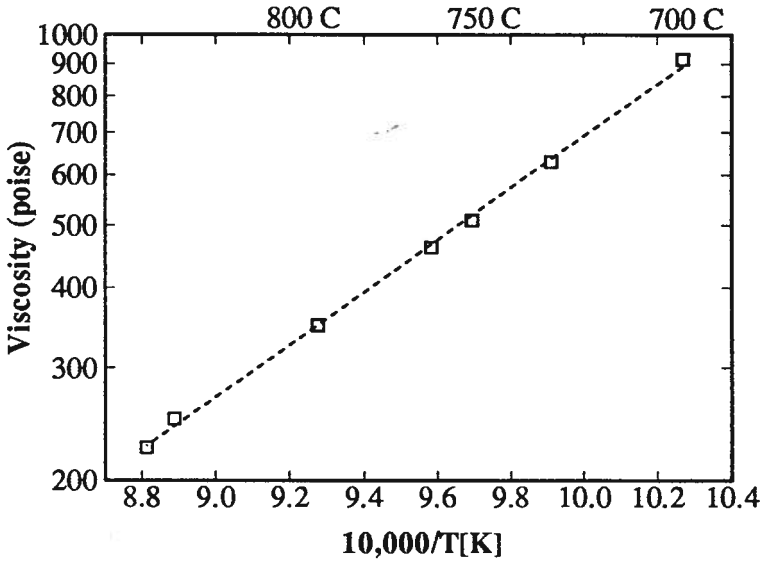

Figure 2.5: Viscosity versus 1/T for molten B_2O_3 [4]

The thermal conductivity of B_2O_3 [16] and LBO [17] are low as would be expected for oxide materials. The expansion coefficient of LBO [17] and Mo_2O_3 [16] are low when compared to metals such as liquid bismuth which has a expansion coefficient of 1.26 $\times 10^{-4}$ at 538°C. Since the LBO melt has a high viscosity and a small thermal expansion coefficient, bouyancy forces and thus fluid flow due to natural convection in the melt will be small. The LBO expansion coefficients are nonisotropic and the dimension change in the c direction will be opposite to that of the b and a directions [18]. This will increase the stress levels that are present in the crystal during cooling. Evaporation could be a problem during crystal growth due to the vapour pressure of MoO_3; 1 atmosphere at 1151°C.

The crystal structure of LBO is orthorombic of class mm2 and has a space group of P_{na2_1}. The cell dimensions for LBO are **a** = 7.379, **b** = 8.447 and **c** = 5.140 Å. Growth directions are generally parallel to the primary axes of a crystal which in this case could be **a** [100], **b** [010] or **c** [001]. We note, following the mm2 class designation, the

Property (units)	Material	Temperature	Polynomial
Specific Heat (J/g)	Li_2O	298K < T < 500K	$69.58 + 17.857 \times 10^{-3}T$ $-19.041 \times 10^{5}T^{-2}$
	B_2O_3	723K < T < 1400K	$245.814 - 145.511 \times 10^{-3}T$ $-171.167 \times 10^{5}T^{-2} + 48.166 \times 10^{-6}T^{2}$
	MoO_3	298K < T < 1068K	$75.186 + 32.635 \times 10^{-3}T$ $-8.786 \times 10^{5}T^{-2}$
density (g/cm^3)	Li_2O	-	2.013
	B_2O_3	-	1.812
	LBO	solid	2.474
	MoO_3	-	4.692
viscosity (poise)	Li_2O	-	-
	B_2O_3	-	see figure 2.5
	MoO_3	-	-
conductivity (W/cm K)	Li_2O	-	-
	B_2O_3	800 K	0.01
	LBO (a) †	298 K	0.039
	LBO (b) †	298 K	0.031
	MoO_3	-	-
Expansion Coefficient (K^{-1})	Li_2O	-	-
	B_2O_3	-	-
	LBO (c) †	50°C - 400°C	11.6×10^{-6}
	LBO (d) †[001]	30°C	-88.0×10^{-6}
	LBO (e) †[010]	30°C	108.2×10^{-6}
	LBO (f) †[100]	30°C	33.6×10^{-6}
	MoO_3	-	-
	Mo_2O_3	395°C	5.35×10^{-6}
Vapour Pressure (atm)	Li_2O	-	-
	B_2O_3	-	-
	MoO_3	1151°C	1

Table 2.2: Physical properties of Li_2O, B_2O_3, MoO_3 and Mo_2O_3.

†
LBO (a) = perpendicular to the c direction
LBO (b) = parallel to the c direction.
LBO (c) = LBO glass.
LBO (d) = LBO crystalline material, [001] direction.
LBO (e) = LBO crystalline material, [010] direction.
LBO (f) = LBO crystalline material, [100] direction.

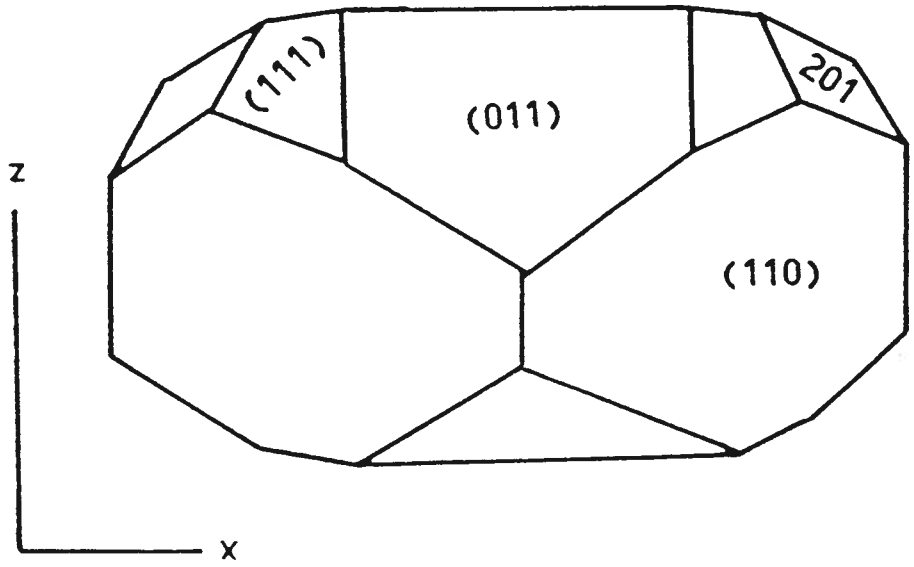

Figure 2.6: Habit shape of grown LBO crystal [5]

(001) and (00$\bar{1}$) faces on a growing crystal will have different faceted surfaces. The other principle axes **a** and **b** will have the same facets on the opposing faces of the cell. A faceted LBO crystal is shown in Figure 2.6 [5]. In orienting a seed crystal parallel to the growth direction care must be taken to determine whether the (001) or (00$\bar{1}$) is at the growing interface since the growing behaviour could be different.

2.3 Growth Defects

Growth defects found in single crystals include segregation, dislocations, flux entrapment, inclusions, cracks, and voids. In the case of LBO crystals the segregation coefficient of the flux is zero, therefore no solid solution forms. While dislocation density is important in semiconductor crystal growth it is not critical in optical crystals. However, defects which reduce the optical quality of a crystal, such as voids, cracks, flux entrapment and inclusions are a matter of great importance. The amount of published information on defects in LBO is small [1, 2, 3, 5]. In the literature, similarities between LBO crystals

and other oxide crystals are examined. This is particularly relevant when the oxide crystals are of materials with high viscosities similar to B_2O_3 [20].

2.3.1 Flux Inclusions/Interface Breakdown

Flux inclusions in BBO crystals are commonly found at the centre of the crystal [13, 23]. Figure 2.7 shows an increase in inclusion density at the centre of a BBO crystal. These core inclusions correspond to the region were fluid flow due to crystal rotation is minimal [13]. Core inclusions have been found in other oxide crystals such as $Bi_4Ge_3O_{12}$ [21, 22]. It was concluded that the core inclusions formed as a result of rapid changes in the growth rate. The fast solidification produces a sudden increase in concentration of segregated material ahead of the interface. Inclusions will be generated when the flux concentration ahead of the interface increases more rapidly than the rate at which material diffuses away from the interface. Flux inclusions have also been found at the outer region of BBO crystals [23]. The inclusions at this area are attributed to the large temperature gradients and temperature fluctuations that occur in these regions.

Interface breakdown can occur during BBO crystal growth, as shown in Figure 2.8, after the crystal has grown 12 mm [13]. The interface breakdown begins at the centre of the growth interface and spreads to the edges as growth proceeds. This was correlated with the fluid flow under the crystal [13]. The interface breakdown initiates at stagnant regions, such as the region below the centre of the crystal.

Flux solidified on the outside of the crystal is responsible for cracking in BBO crystals [13]. Similarly, inclusions or solidified flux at a surface of an LBO crystal may cause cracking due to the strong anisotropy of the flux and LBO crystals [5].

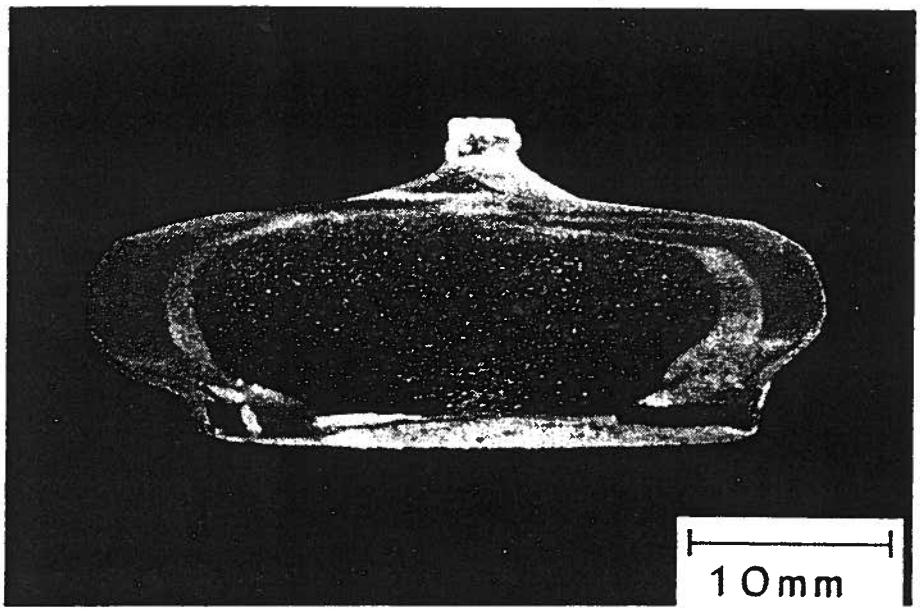

Figure 2.7: Transverse dark field view through a BBO crystal grown at a very high growth rate, orientation [001] parallel to growth direction. Many scattering centres are observed throughout, and concentrated in the core region beneath the seed [13].

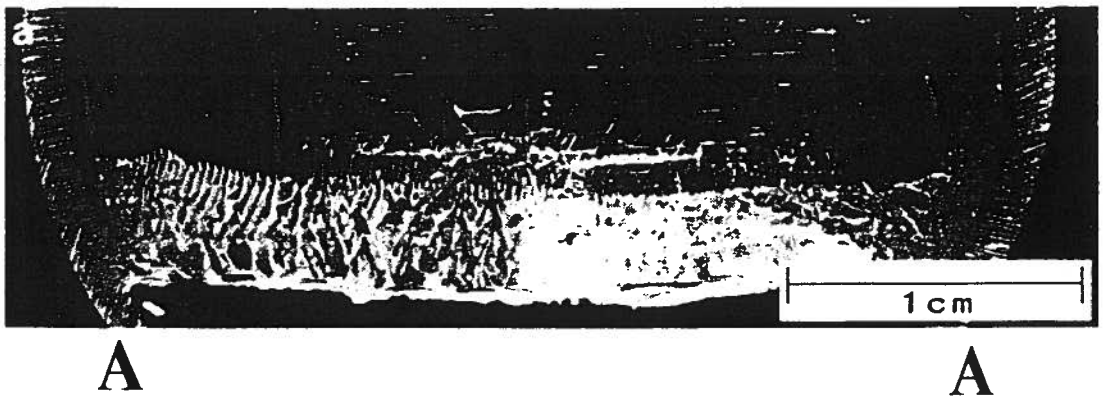

Figure 2.8: BBO crystal. Breakdown of growing interface breakdown at A-A [13].

2.3.2 Voids

Void formation in crystals may be due to the entrapment of gas from the melt during solidification [28, 25, 23]. The gas may be from byproducts of the charge material, such as CO_2, that are dissolved in the melt. The solubility of dissolved gases in the liquid is higher than the solid. Thus, as the material solidifies, dissolved gas will be rejected by the solid at the interface. Bubbles will nucleate when, at a given pressure, the dissolved gas volume reaches a critical value. The bubbles trapped in the momentum boundary layer ahead of the interface will likely be incorporated in the crystal. The dissolved gas boundary layer will be thicker at the centre of the crystal, which contains a stagnant liquid region, and thinner at the edges of the crystal. Figure 2.9 illustrates a possible mechanism for the entrapment of gas bubbles in the crystal.

The rotation of the crystal will cause two events to occur in the liquid. First, mixing will increase in the liquid and reduce the thickness of the dissolved gas boundary layer below the crystal. Second, the pressure below the rotating crystal will increase proportionally with the centrifugal acceleration [25]. The increase in pressure at the growing interface will delay or reduce bubble formation in the crystal. A correlation between rotation rate, crystal diameter and void formation during crystal growth has been reported [25, 36]. Figure 2.10 shows the extent of the incorporation of gas bubbles in $Pb_5Ge_3O_{11}$ as a function of crystal rotation rate and crystal diameter. At a fixed crystal diameter a void free crystal could be grown at high rotation rates. At low crystal rotation rates natural convection dominates fluid flow. Increasing the crystal rotation rate results in forced convection dominating the fluid flow and the interface inverting from concave to the liquid to concave to the solid [25, 13].

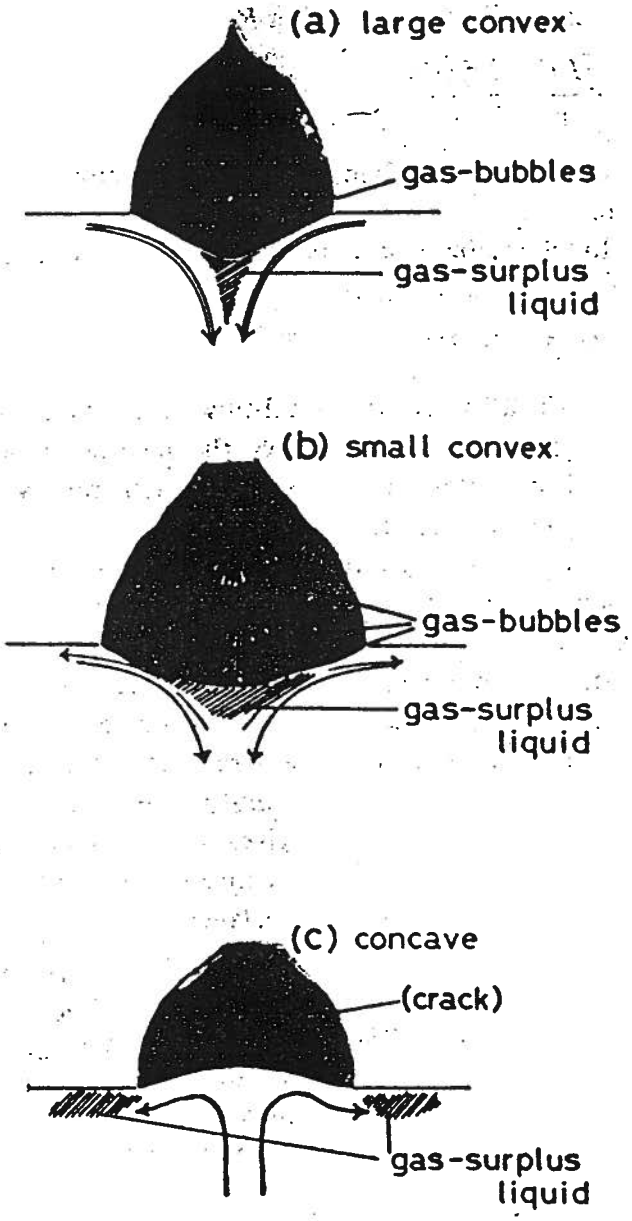

Figure 2.9: An entrapment mechanism of gas–bubbles in crystals taking account of fluid flow modes associated with crystal rotation [25].

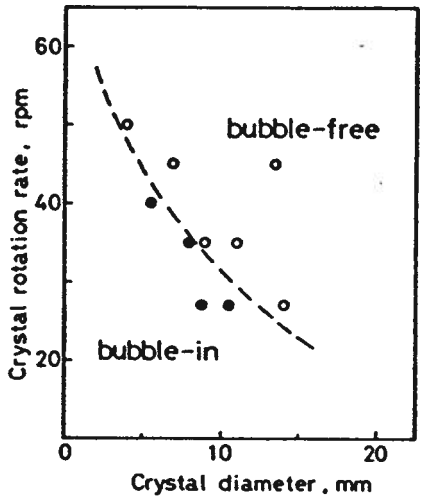

Figure 2.10: Incorporation of gas–bubbles in $Pb_5Ge_3O_{11}$ as a function of crystal rotation and rate and crystal diameter [25].

2.4 Fluid Flow

Fluid flow in top seeded solution crystal growth is complex due to the rotation of both the crystal and the crucible. Numerous fluid flow models have been developed to characterize Czochralski (Cz) fluid flow [28, 29, 30, 31, 32, 33, 35, 38, 39].

2.4.1 General Concepts

Fluid flow in a crystal growth system in which the crucible is rotated in one direction, and the crystal in the opposite direction was initially examined by Taylor and Proudman [28]. The solid body of rotating fluid is two dimensional with respect to coordinate axis rotating with the liquid. The crystal and crucible rotating in opposite directions creates a number of individual rotating fluid regions each separated from the other by a detached shear layer. A shear layer is where the fluid velocity changes from one solid body rotation to another. There is no mixing, with the exception of molecular diffusion, across a shear

layer. The detached shear layers are shown in Figure 2.11 and 2.12 [28, 27].

The crucible rotates at an angular velocity Ω_2 and the crystal rotates at an angular velocity of Ω_1 The fluid adjacent to the crucible walls has solid body rotation with an angular velocity equal to crucible rotation rate. Directly below the crystal two individual cells, known as Taylor–Proudman cells, develop. The lower cell has fluid that rotates in the same direction as the crucible but slower (Ω_5). The upper cell rotates in the same direction as the crystal but again at a lower angular velocity (Ω_4).

Figure 2.12 shows the axial and radial fluid motion that occur. The fluid at the crystal surface boundary layer and the crucible bottom boundary layer are forced outward due to the centrifugal force from the rotation. The upper cell has upward fluid flow to replace the fluid that is moved due to the centrifugal force from the crystal and the lower cell has some downward fluid flow to replace the fluid that is moving outward due to the centrifugal force of the crucible. In turn this fluid is replenished by the middle shear layer, the direction of its fluid motion is inward and up/down into the two cells.

Natural convection due to buoyancy forces are also present during Cz crystal growth. The fluid flow for natural convection is shown in half the crucible in Figure 2.13 The temperature in the liquid is highest at the bottom and lowest at the top. The lower density liquid at the bottom rises up the wall and cools, while the higher density liquid at the top moves down the centre of the crucible.

2.4.2 Standard Growth Practices

Fluid flow during crystal growth results from both natural convection and the forced rotation predicted by the Taylor–Proudman analysis. Since the forced convection condition is what was described with the Taylor–Proudman theorem we will begin with these results shown in Figure 2.14. Two cells form as theoretically predicted. The outside solid body rotation is almost nonexistent with the lower Taylor-Proudman cell and its

detached shear layer going to the crucible wall. The strong upward motion of the upper Taylor-Proudman cell cause the temperature isotherms to flatten below the crystal. The crystal interface will become concave to the solid as the amount of forced convection becomes higher [32].

If the crystal rotation rate is small, natural convection and/or crucible rotation dominates (Figure 2.15) and the upper cell disappears. The resulting shape of the isotherms indicate that there is more radial heat flow and the shape of the interface changes to concave to the liquid. The driving force of many of the modeling papers has been to predict interface changes from concave to convex [32, 33, 34, 36, 37].

2.4.3 Accelerated Crucible Rotation

As an alternative to crystal and crucible counter rotation during growth, the crucible (and crystal) can be accelerated and decelerated alternately in clockwise and counter clockwise directions. The accelerated crucible rotation technique (ACRT) reduces the thickness of the stagnant boundary layer, thus allowing faster stable growth rates [42]. When a crucible is accelerated from rest, the liquid around the crucible wall will follow the change in crucible motion, whereas the liquid in the centre will remain at rest due to inertia. Thus shear rings in the liquid are produced by the difference in the outer and centre fluid velocities. The number of shear rings which develop increase with increasing acceleration. A top view of the shear rings produced is given in Figure 2.16. The increase in surface area due to the shear rings results in an increase in diffusion. The resulting fluid flow in the radial and axial direction are shown in Figure 2.17. The rapid flow close to the crucible bottom is referred to as Ekman-layer flow [43]. The rapid suction of fluid close to the bottom is due to the pressure difference between the outside and inside of the crucible not being balanced by the centrifugal forces. High Ekman flow rates occur not only at the crucible bottom but also on the crystal growth face that is

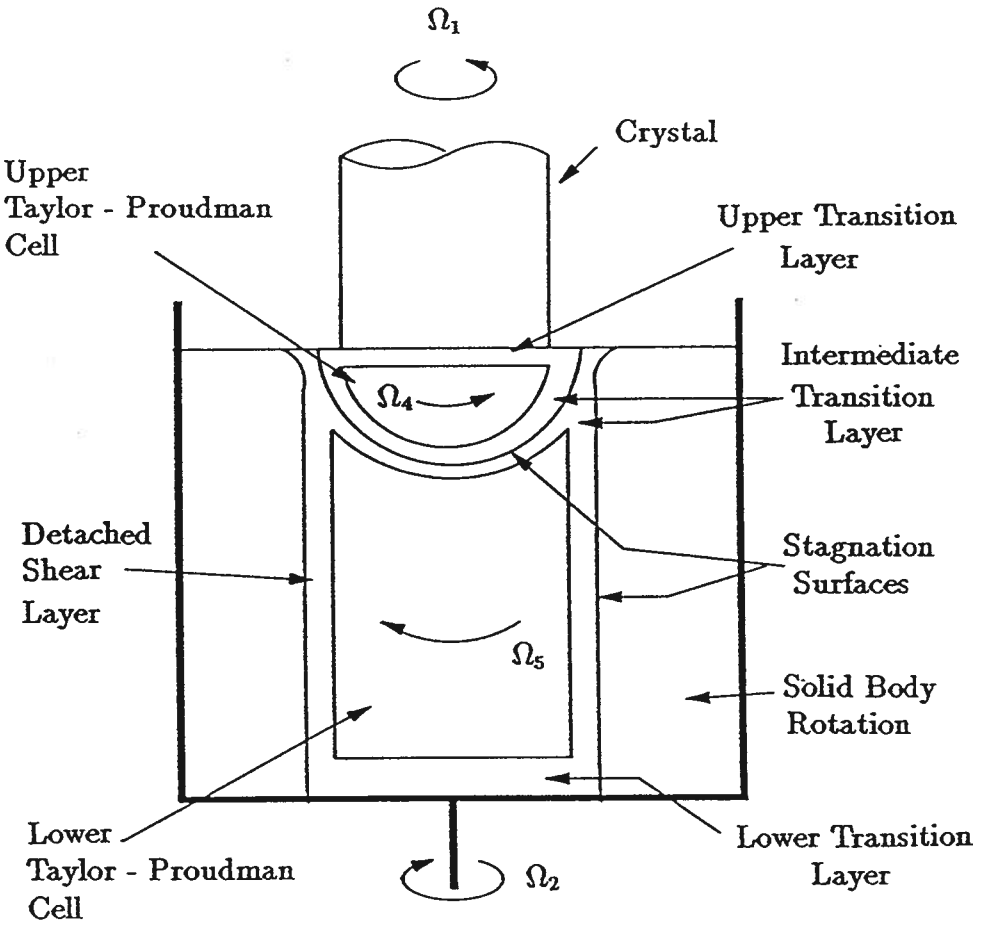

Figure 2.11: Theoretical Taylor-Proudman cell shapes for counter rotation [28].

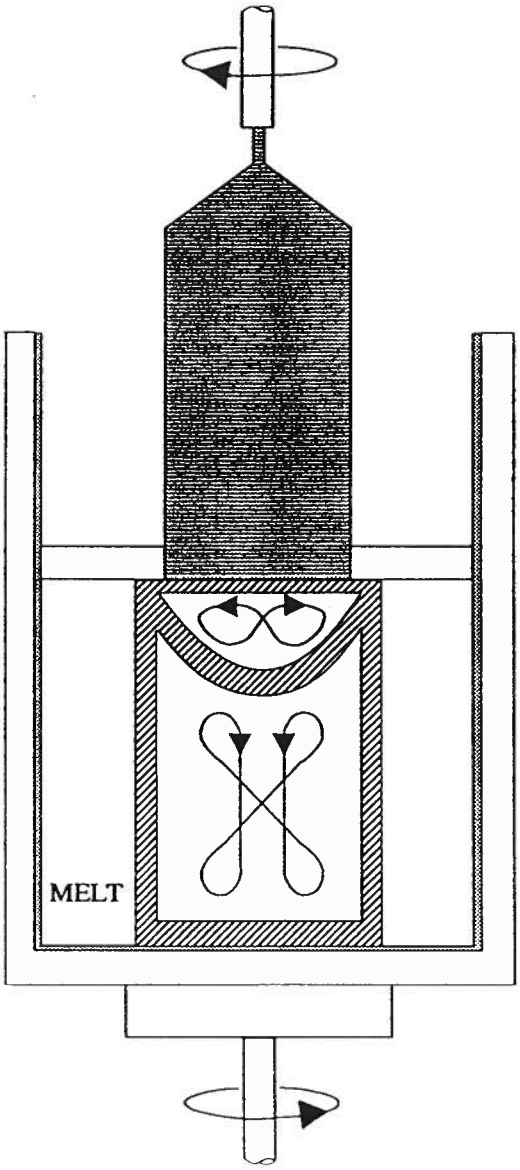

Figure 2.12: The direction of fluid motion predicted in the Taylor–Proudman cells [28].

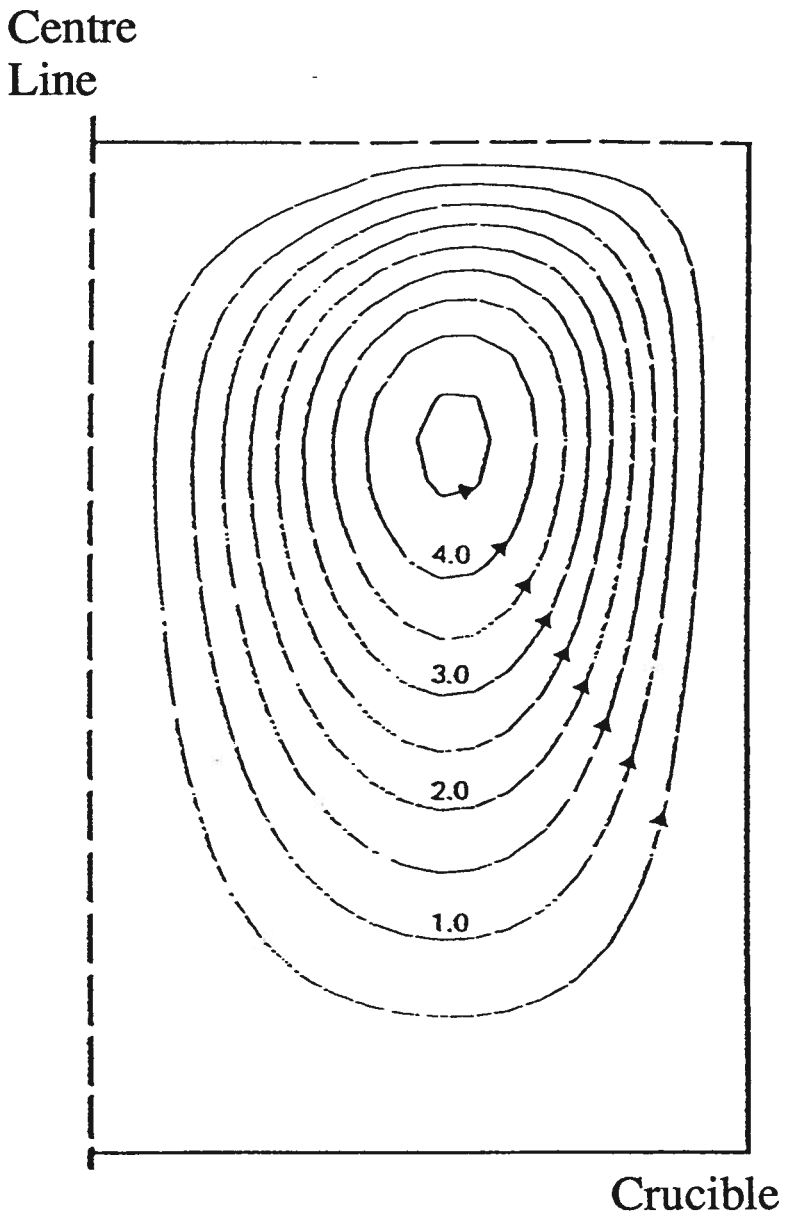

Figure 2.13: Fluid motion due to natural convection [29].

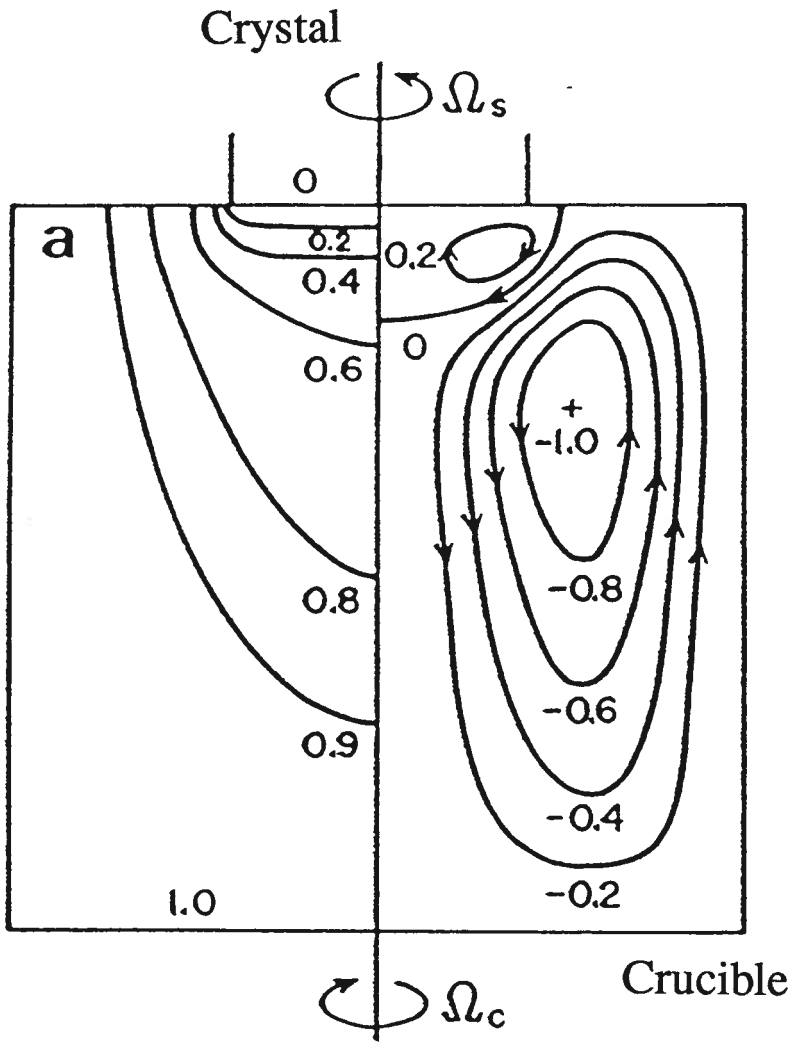

Figure 2.14: Predicted flow with counter rotation large enough that forced convection dominates [32]. Flow shown on right half and temperature shown on left half.

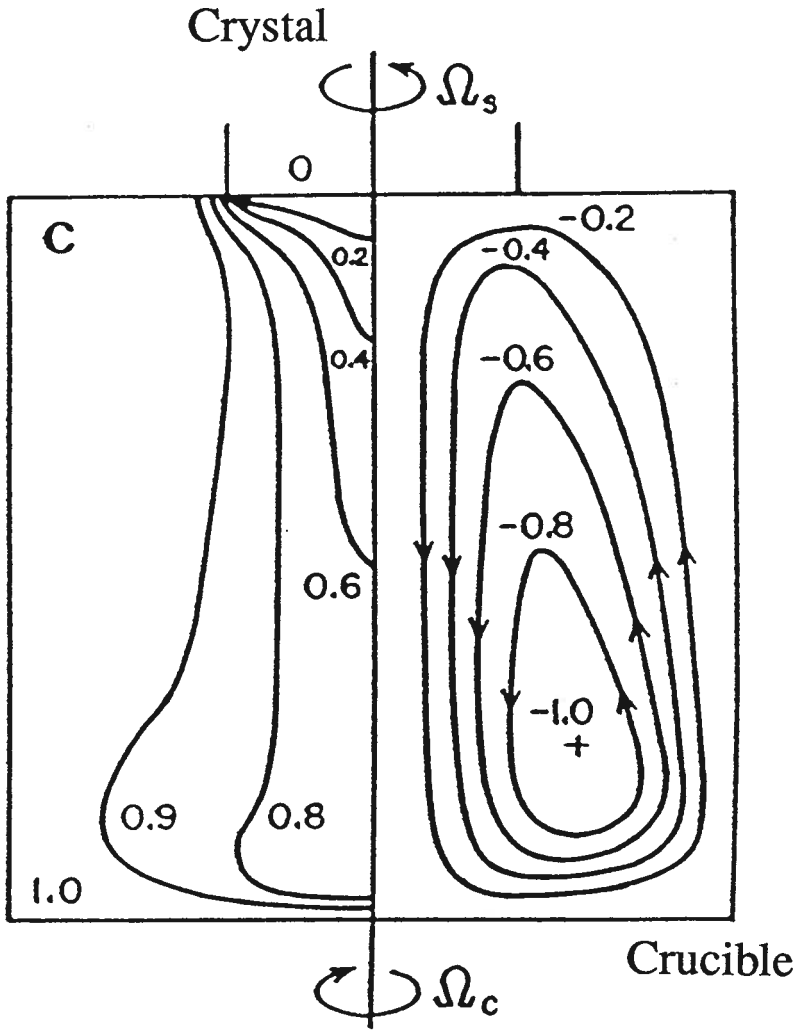

Figure 2.15: Predicted flow with counter rotation small enough that natural convection dominates [32]. Flow shown on right half and temperature shown on left half.

perpendicular to the rotation axis. Ekman-layer flow ceases as soon as uniform rotation is reached. A mathematical model has been used to examine the fluid flow that results from combined forced and free convection of accelerated crucible rotation Cz growth of metals and semiconductors [40, 41]. The best mixing of the fluid is reported to occur when the crystal and crucible are rotated/accelerated in the same direction. The upper Taylor-Proudman cell is only present during the acceleration of the crucible (Figure 2.18). Thus the model predicts that the bulk fluid will mix best under these conditions. The variation of a solute boundary layer was not examined. The fluid properties of the model are not close to those of LBO. This is especially noticeable with the kinematic viscosity of 0.005 cm^2/s. Using the density of LBO, 2.474 g/cm^3, the model viscosity is calculated as 0.0123 poise. The viscosity of an LBO solution for growth is nearly three orders of magnitude higher. It is difficult to predict if the same type of mixing would occur in a higher viscosity liquid.

2.5 Mass Transfer

The most important aspect of mixing in the melt is that which occurs in the boundary layer under the crystal. In the past the difficulty of conducting comprehensive numerical integration of the Navier-Stokes equations and diffusion equations to determine the flow, the temperature, and solute distribution, has led to the development of boundary layer theory to provide simple models of key regions of the flow in Cz growth [44]. There has also been no real attempt to verify the boundary layer models or numerical models with measured solute distributions ahead of the crystal interface. Burton, Prim and Slichter [45] considered changes in the momentum boundary layer thickness and the resultant transport of solute, on the effective segregation of solute for steady state crystal growth in germanium. The domain was assumed to be an infinite rotating disc on

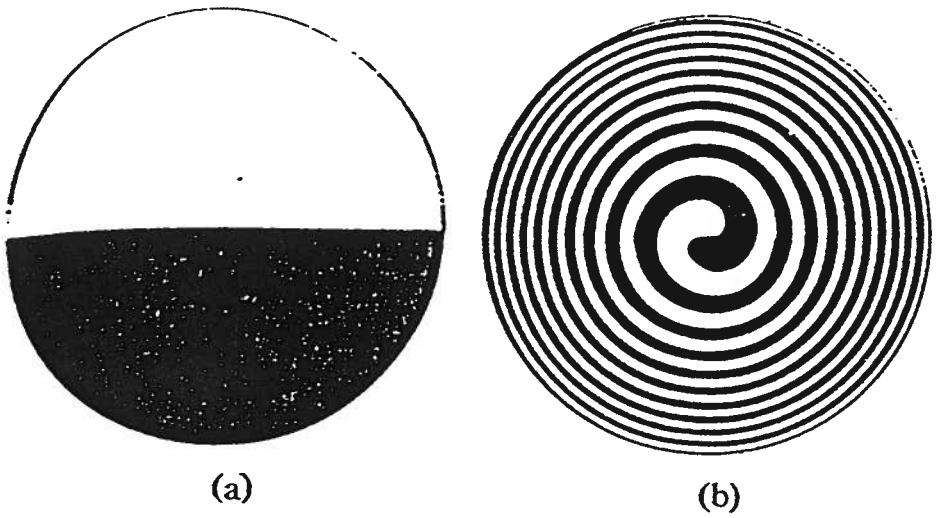

Figure 2.16: General rotational fluid flow (shearing) due to ACRT [43]. (a) Top view of circular tube filled with two distinguishable fluids. Tube and contents are in uniform rotation. (b) Final shape of fluid after tube and contents have come to rest. Spiral shearing distortion is evident.

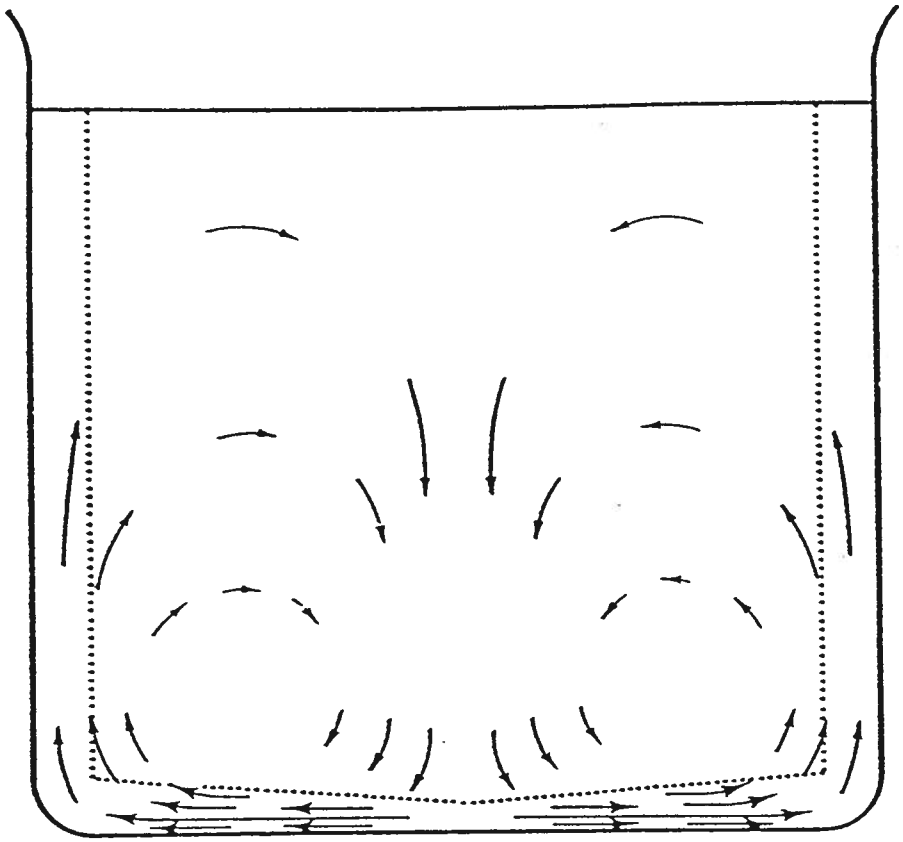

Figure 2.17: General fluid flow in the axial and radial direction due to ACRT [43].

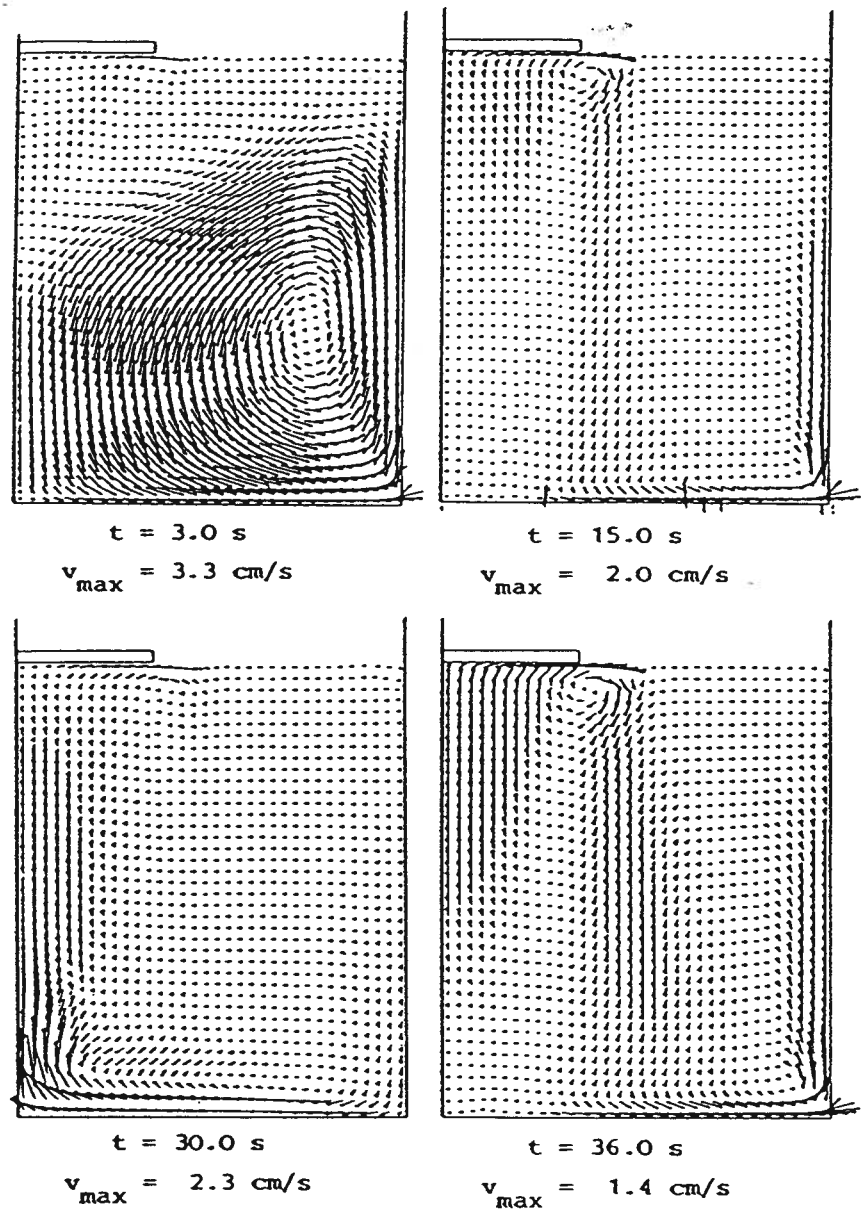

Figure 2.18: Model prediction of fluid flow due to ACRT [41]. Crucible rotation 10 to 30 rpm. Crystal rotation 40 to 80 rpm. Time period of acceleration 15 seconds.

the surface of a semi-infinite fluid. The boundary conditions used in the mass transfer calculations are shown in Figure 2.19. It is assumed that the bulk concentration of the fluid is at the edge of the diffusion boundary layer. The diffusion boundary layer thickness is assumed to be constant over the radius of the rotating disk. This is very relevant when laminar flow and a thin diffusion layer are present [49]. The only velocity present in the solute boundary layer is from the growing interface. The calculation of solute diffusion reverts to a simple steady state one dimensional diffusion calculation with a term to account for the advancing interface.

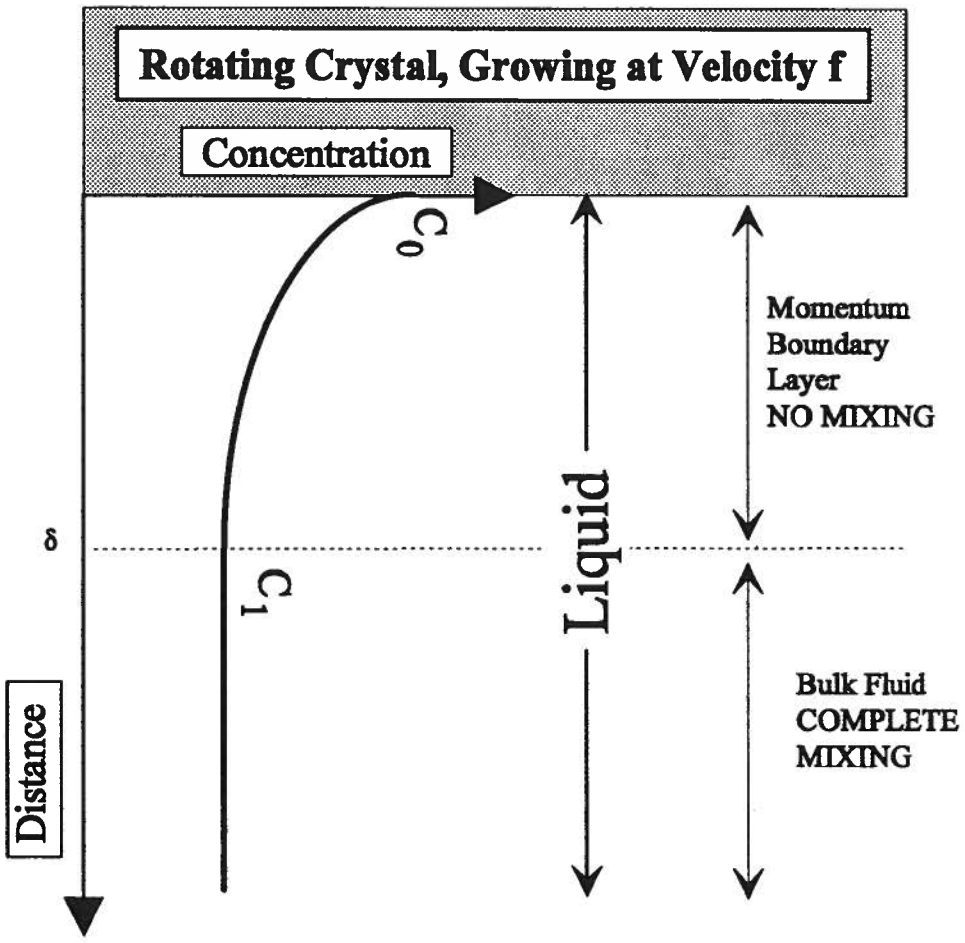

Figure 2.19: Assumptions used in Burton, Prim and Slichter [45] calculation of the concentration in the momentum boundary layer.

Chapter 3

Objectives

The objective of this investigation was to examine the crystal growth process using mathematical modeling, experimental measurements and crystal growth experiments in order to establish procedures for growing larger and higher quality LBO crystals. The mathematical modeling quantitatively describes the parameter interactions in the complex growth system. Experimental measurements were conducted to establish the required physical parameters of the system and the boundary conditions required for the model. A physical model of the flow due to crucible rotation was used to visualize the flow patterns in the melt. The crystal growth experiments were carried out to verify the model predictions. These experiments also demonstrated that better crystals can be produced by modifying the growth parameters in conformity with the model predictions. The principal tasks undertaken to accomplish the objectives were as follows:

1. The development of a mathematical model of heat transfer and fluid flow in the LBO crystal growth system.

2. Application of the Burton, Prim, and Slichter analysis to examine the mass transfer of MoO_3 away from the solid/liquid interface.

3. Use of a physical model to visualize the type of flow that occurs due to crucible rotation.

4. Measurement of the temperature distribution in the melt and a comparison with model predictions.

5. Temperature distributions for the mathematical models' boundary conditions.

6. Prediction of the effect of crucible rotation rate on the temperature distribution in the melt.

7. The phase diagram of the LBO/MoO_3 system, as determined by differential thermal analysis.

8. The dependence of viscosity of the melt as a function of temperature and MoO_3 content.

9. The type, size and distribution of defects in the grown crystals.

Chapter 4

Experimental

4.1 Growth Process

4.1.1 Growth Furnace

The system utilized in this investigation to grow LBO crystals is the modified NRC crystal puller shown in Figure 4.20. The crystals are grown in the chamber marked A, using the power and control system B. The upper chamber, C, is not significant for LBO growth. The growth chamber A is 26.3 cm in diameter and 44.5 cm high. A schematic diagram of the interior of the growth chamber is shown in Figure 4.21. The LBO/MoO_3 charge is contained in a crucible which sits on a rotating pedestal, thermally insulated by a block of ceramic. The resistance heaters have Iron-chrome-aluminum elements. The insulation shown in Figure 4.21, consists of alumina. A 6.35 cm diameter hole is located at the top of the chamber.

The crucible is made of platinum. Two crucible sizes were used, a small crucible 66 mm in diameter and height, and a larger crucible 88 mm in diameter and height. The expansion coefficient of LBO/MoO_3 is much larger than that of platinum causing severe crucible distortion upon cooling. To ensure that the crucible remains firmly attached to the insulation block during rotation, a cylinder of insulating material 5 mm in height is attached to the crucible and 3 pegs are attached to the cylinder which sit in holes in the insulating block that is attached to the rotating pedestal. The pegs keep the crucible from moving with respect to the block. The cylinder is attached to the crucible with

Cotronics Ultra–Temp 360 insulating tape and Cotronics 904 Ceramic Adhesive. The insulating tape at the side of the crucible must be the same for each consecutive crystal growth run. If not, the liquid temperature will change.

The crystal growth furnace temperature is controlled with a Eurotherm 818 controller. This instrument is very accurate and is capable of maintaining ramp rates as low as 0.01 degrees per hour. The type K control thermocouple is located adjacent to the furnace wall. The crucible rotation, seed rotation and seed lift were all modified from the original NRC equipment. The crucible rotation, Figure 4.22, consists of a Bodine motor and a pulley unit attached to the original rotation unit. A thermocouple goes up the center of the rotation shaft for measuring the temperature at the base of the crucible. The gearing of the pulleys allows for crucible rotations between 0 and 74 rpm. The seed is rotated using a Maxi-Pile gear motor and planetary reduction gears to obtain a rotation of 5 rpm, Figure 4.23.

A stepper motor and indexer/driver package, was used for slow pulling of the seed. The seed lift velocity is 1.66 mm/day to 1.49 cm/min. A platinum mixing paddle, shown in Figure 4.24 is used to homogenize the liquid, after the charge has been melted. The seed rod is made of hastelloy. The bottom of the seed rod is attached to either the paddle or to the platinum seed holder.

4.1.2 LBO Seed

LBO seeds were oriented such that the growth direction was parallel to the [001] direction. The orientation was determined by using the back reflection Laue method on the cleaved surface of the crystal, Figure 4.25. The unoriented LBO crystals was attached to a goniometer, Figure 4.26, using wax. Samples were positioned such that the surface was 3cm from film holder and were irradiated from a Cu target for 20 minutes at 30 kV and 20 mA. After irradiation, the X-Ray film was developed and the orientation of the crystal

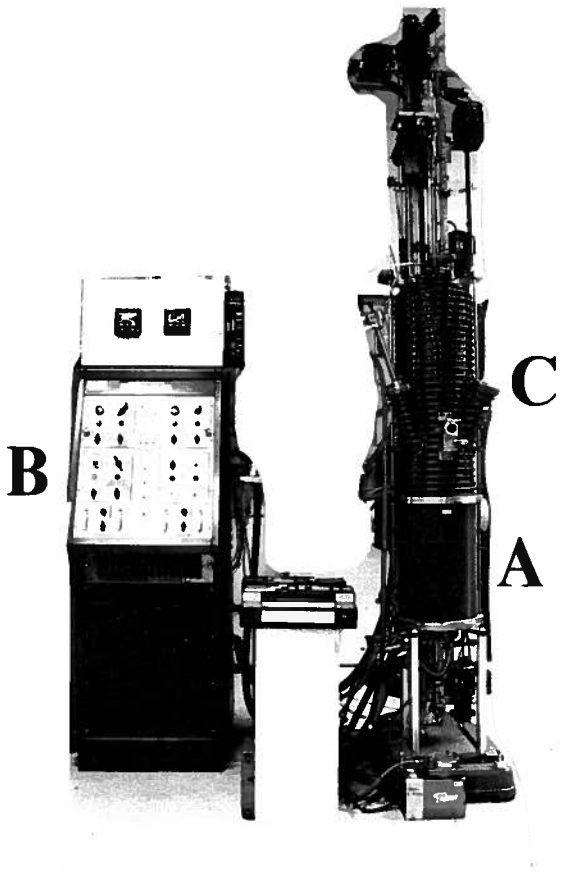

Figure 4.20: LBO crystal growth furnace, A and C are the crystal puller, and B is the power and control box.

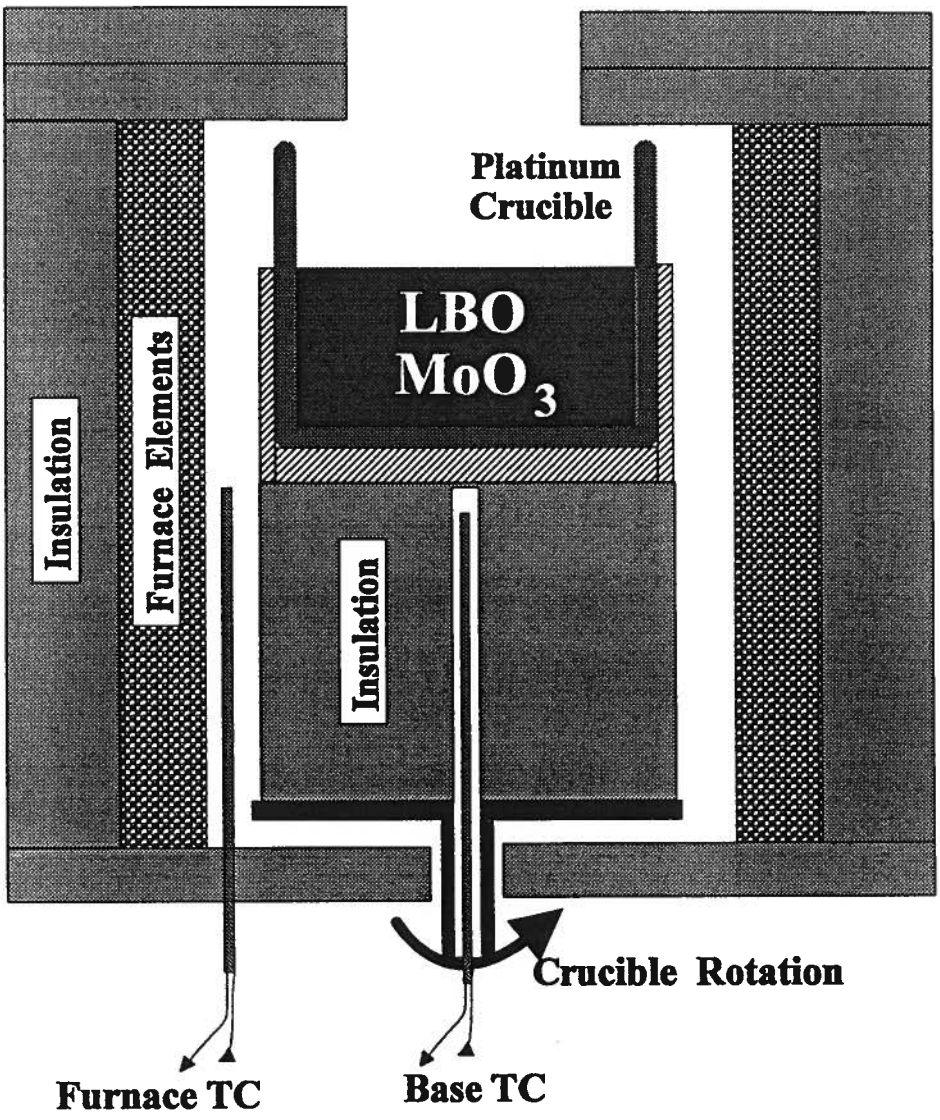

Figure 4.21: Schematic of LBO growth chamber

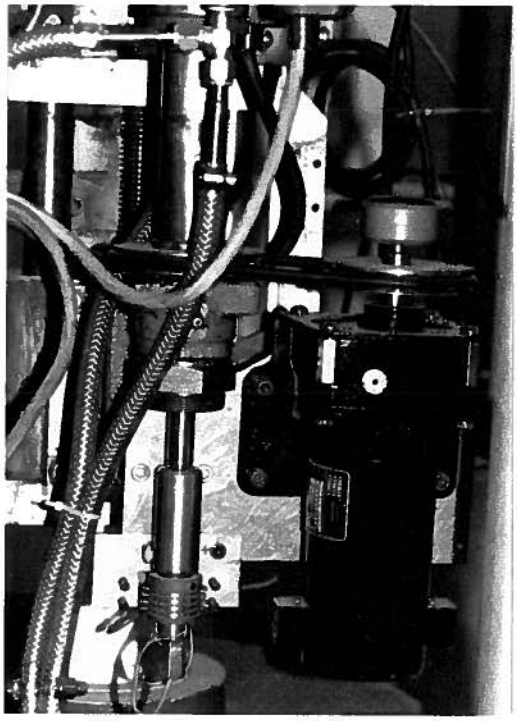

Figure 4.22: Crucible rotation device.

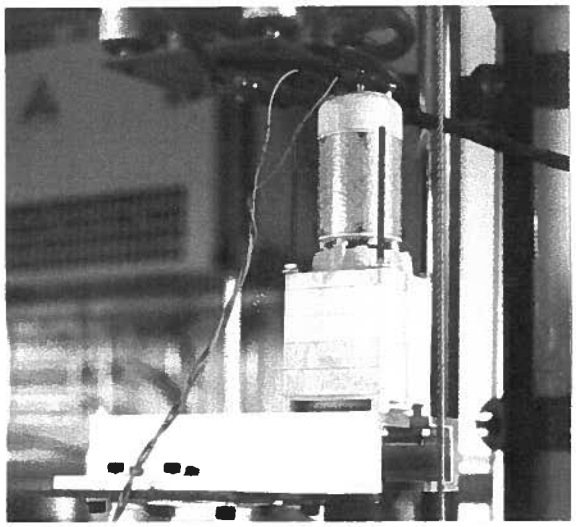

Figure 4.23: Seed rotation device.

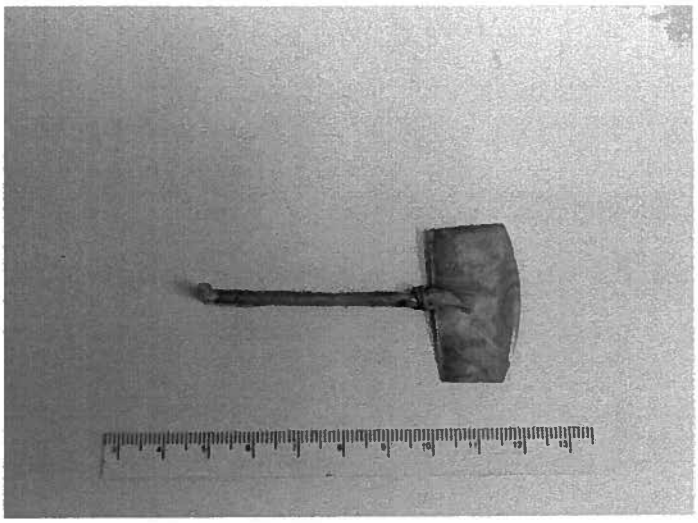

Figure 4.24: Platinum paddle for mixing the melt.

was determined using a Greninger chart and Wulff net as described in reference [19]. On the basis of the established crystal orientation with respect to the X-Ray beam, the goniometer was adjusted such that the **c** axis was parallel to the X-Ray beam. This procedure was repeated until the **c** axis of the sample was parallel to the X-Ray beam within 0.2 degrees.

Once the **c** axis was determined the (001) face was ground flat using a PM2A Logitech lapping and polisher machine with SiC grit as the lapping media. The goniometer was attached to the polishing instrument to ensure that the ground face was identical to the measured orientation.

The LBO crystal was repositioned on the goniometer by heating the wax. It was reattached to the goniometer such that the **c** axis was perpendicular to the X-Ray beam direction. The above procedure was then repeated to determine the **b** axis. After this axis was determined and polished the procedure was repeated for the **a** axis.

Once the sample was oriented and the principle faces polished the LBO crystal was

Figure 4.25: Cleavage plane of an LBO Crystal

cut into smaller pieces using a Buehler Isomet low speed saw. The seed size is $5 \times 2 \times 10$ mm with the **c** axis being the longest dimension. Special notches are cut in the seed for attaching it to the platinum seed holder. The notches are 1 mm in depth. The final seed shape is shown in Figure 4.27. The seed is attached to its holder by running a platinum wire though the notches in the seed and holder. The wire is wound tightly on the platinum holder to ensure that the seed is held in place. Figure 4.28 shown the seed and holder.

4.1.3 Growth Procedure

The LBO growth solution consist of lithium tetraborate ($Li_2B_4O_7$), extra borate (B_2O_3) to obtain the correct stoichiometric amount of LBO and molybdenum triborate (MoO_3).

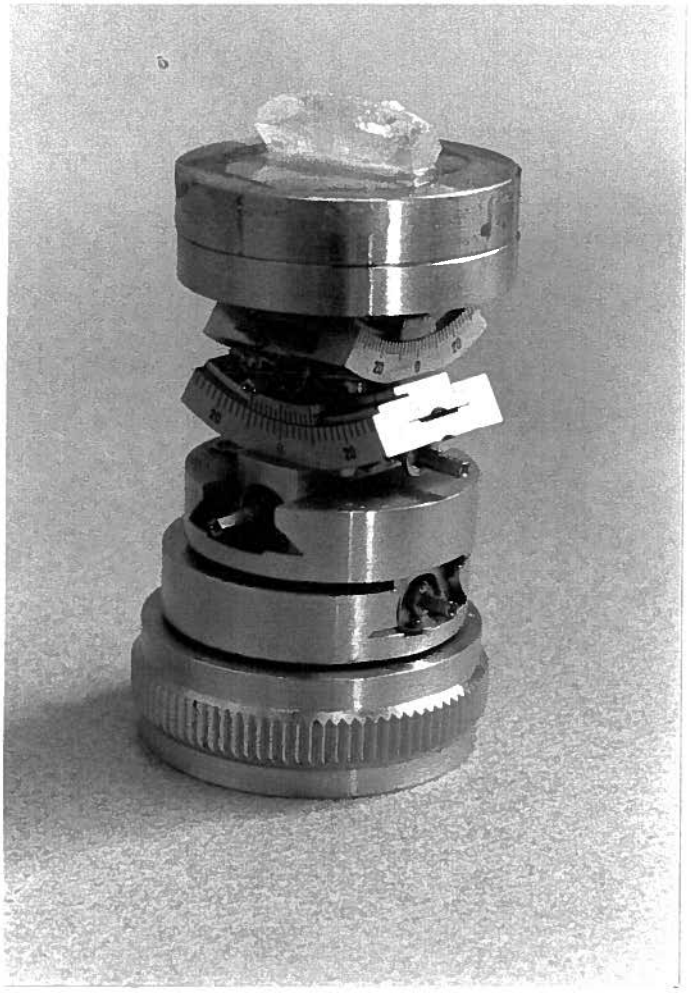

Figure 4.26: Goniometer used for orienting LBO crystals

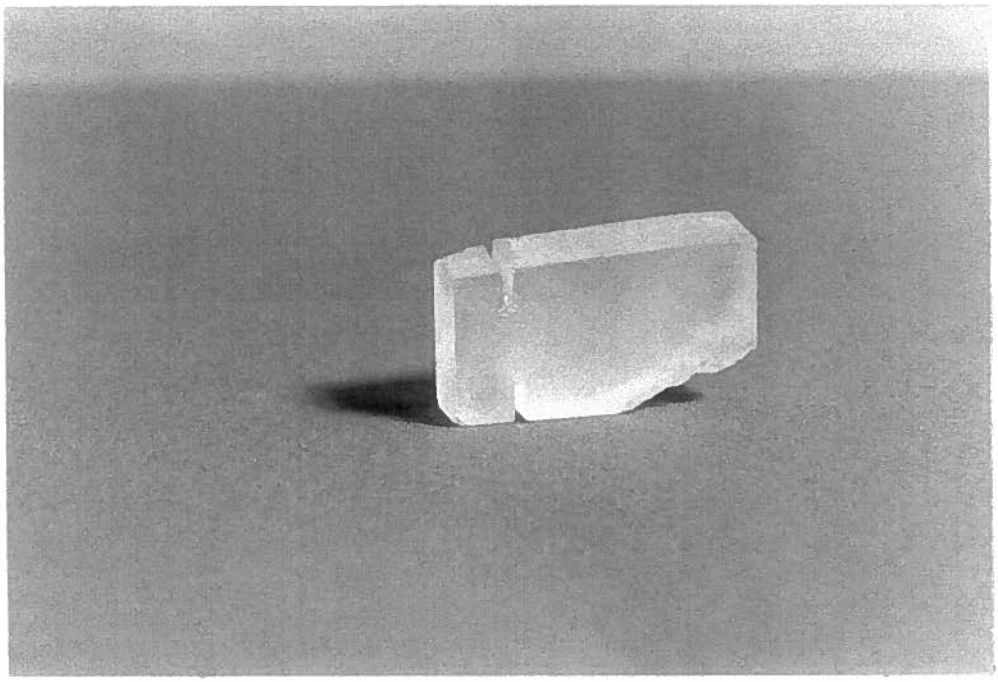

Figure 4.27: LBO Seed

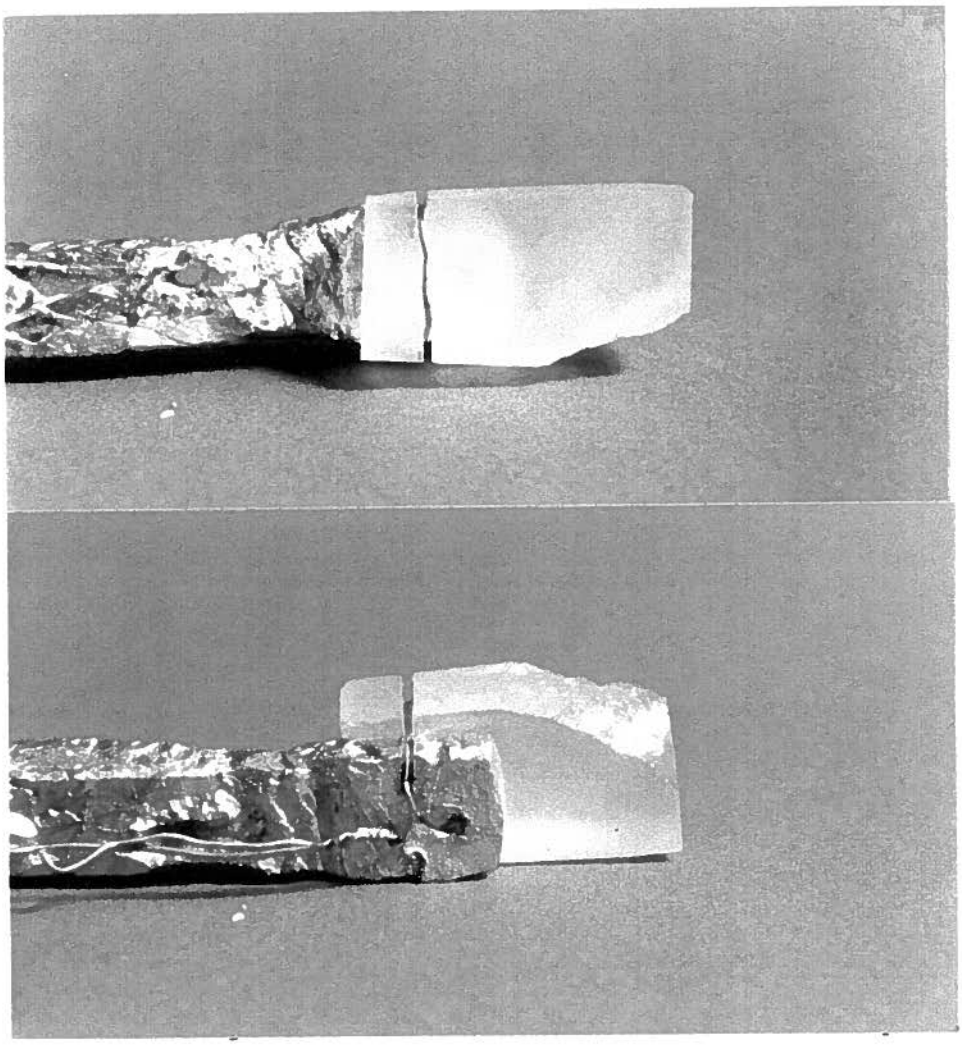

Figure 4.28: LBO Seed attached to platinum seed holder

The melting point of lithium tetrabotate is 930°C of borate is 450°C, and molybdenum trioxide is 795°C. All compounds were obtained from Johnson Matthey and were 99.999% pure. The charge composition selected was 45 wt% MoO_3 (40 mol%). The compounds were packed into a crucible with B_2O_3 at the bottom followed by the lithium tetraborate and the top layer was MoO_3. Dry nitrogen was introduced to the furnace at 12 cubic feet per hour. This flow rate was used during the entire crystal growth run. The charged crucible is heated to 1050°C to allow the lithium tetraborate to completely melt at this temperature for 48 hours. The liquid at this temperature has an opaque amber colour. The mixing paddle is lowered into the liquid until it is completely submerged. The crucible is then rotated at 30 rpm for 48 hours to ensure the liquid is completely mixed. After mixing is completed the liquid is a clear amber color. The stirring paddle is then removed from the furnace and replaced with the seed crystal which is attached to the seed rod and lowered to within 2.5 cm of the melt surface.

The furnace temperature is then slowly cooled at 20°C/hr to the dip temperature of approximately 930°C. The crucible rotation is increased to that used for growth while the furnace is cooling. The LBO seed is dipped by slowly lowering it into the liquid until the meniscus of the fluid is broken. The appearance of the fluid after the seed has been dipped is shown in Figure 4.29.

If the insulation on the side of the crucible changes between crystal growth runs so will the furnace setting for the seed dip temperature. When this occurs the liquid temperature is either below or above the liquidus temperature. If the seed is dipped and the liquid is above the liquidus temperature there will be a longer time before the crystal grows out in size. The seed will not be melted away since the LBO melting temperature is approximately 150°C above the liquidus temperature. If the seed is dipped and the liquid temperature is below the liquidus temperature spurious crystal will grow on the seed. The furnace temperature was increased 5°C every two hours until the spurious

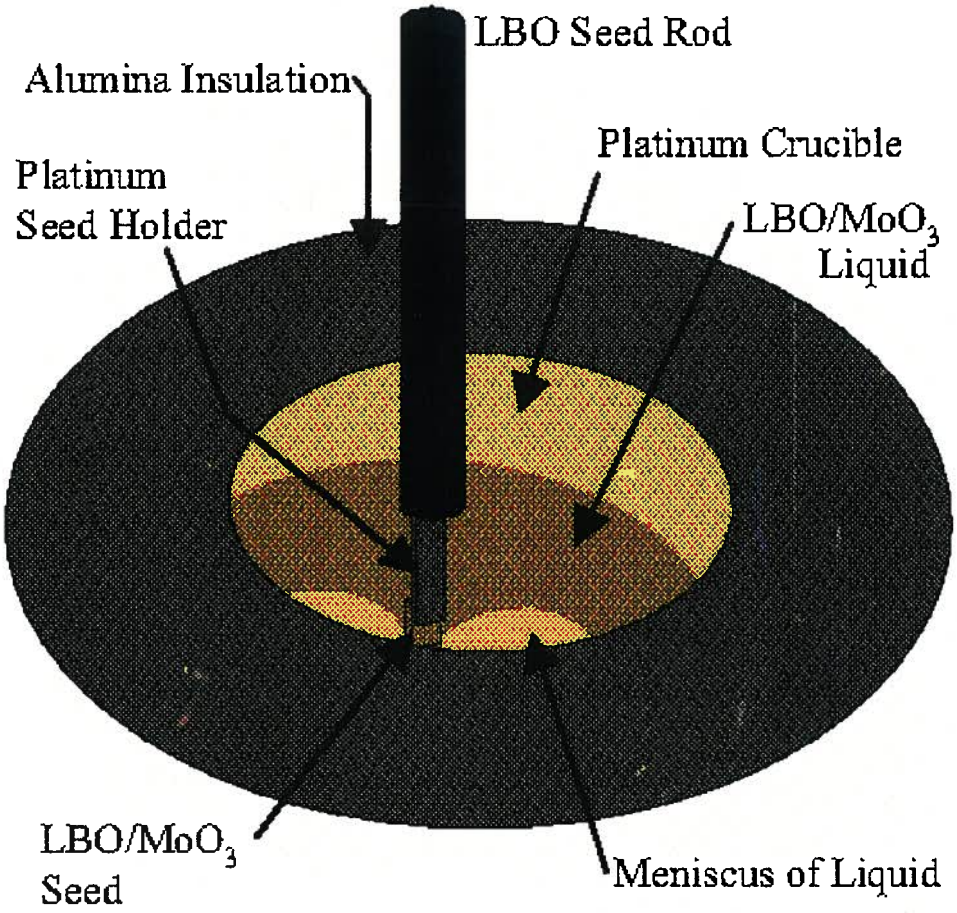

Figure 4.29: Appearance of LBO melt surface after the seed has been dipped

growth melted back to the seed. Growth is continued as per normal from that point.

The furnace is cooled at 0.1°C/hour after the seed had been dipped. Crystal growth is not apparent for up to 1 week after the start of the cooling. Once the crystal diameter has reached 2/3 of the crucible diameter it is pulled at 1.66 mm/day and continued for 5 days. Crystal growth is terminated by rapidly withdrawing the crystal from the melt at a rate of 2.1×10^{-3} cm/s. Once separated from the melt the crystal is slow cooled to room temperature at 10°C/hour.

The crucible is cleaned by heating it to 1000°C and decanting the liquid. Any residual material is removed by soaking the inside of the crucible with reagent grade HCL. The HCL fluid is mixed and heated for one day using a combination hot plate/magnetic stirrer.

4.2 Temperature Measurements in the Melt

Temperature measurements in the melt are required to establish the temperature boundary conditions in the mathematical model, investigate the effect of crucible rotation on the thermal field, and for comparison with results from the mathematical model. The temperature measurements were accomplished in three separate trials. The first set of temperature measurements were undertaken to measure the temperature boundary conditions of the melt for use in a mathematical model that examines the crystal growth operating parameters. A 6.6 cm diameter crucible with no rotation was used to contain the melt for these measurements. The second and third set of temperature measurements were conducted for determining the model boundary conditions to validate the model by examining the effect of crucible rotation on the thermal field in the melt. A 6.6 cm diameter crucible was used to contain the melt for second set of temperature measurements and an 8.8 cm diameter crucible contained the melt for the third set of measurements.

4.2.1 Initial Temperature Measurements with No Crucible Rotation

Temperature measurements were carried out with a chromel/alumel thermocouple in a quartz sheathed tube connected to the seed rod. The thermocouple could be placed at three different radial positions; at the center of the crucible, at the mid−radius of the crucible and at the wall of the crucible. The axial temperature profile was determined by recording the thermocouple output as it was slowly pulled out of the liquid. The furnace temperature was set at 145°C above that normally used for the start of crystal growth to ensure that no nucleation occurs in the melt. The charge concentration used was 50Wt% MoO_3. A sample of the melt was not sent for chemical analysis. A 6.6 cm diameter crucible with no rotation was used to contain the LBO−MoO_3 melt. No insulation was on the outside wall of the crucible.

4.3 Temperature Measurements With and Without Crucible with Rotation

Two sets of temperature measurements were carried out, one in a 6.6 cm diameter crucible and the other in a 8.8 cm diameter crucible. Both crucibles had insulation on the outside. Samples of the melt were sent for chemical analysis to an external lab. Two platinum sheathed chromel/alumel thermocouples were used for the temperature measurements. The position of the thermocouples were adjusted using a positioning device. A platinum sheet formed to simulate the crystal shape, as shown in Figure 4.31, was positioned to replace the crystal. The fluid flow conditions below the simulated crystal and its thermophysical properties, are believed to be close to the actual conditions during LBO crystal growth. As a result, the temperature measurements conducted with the simulated crystal could be applied to the actual growth system for model verification.

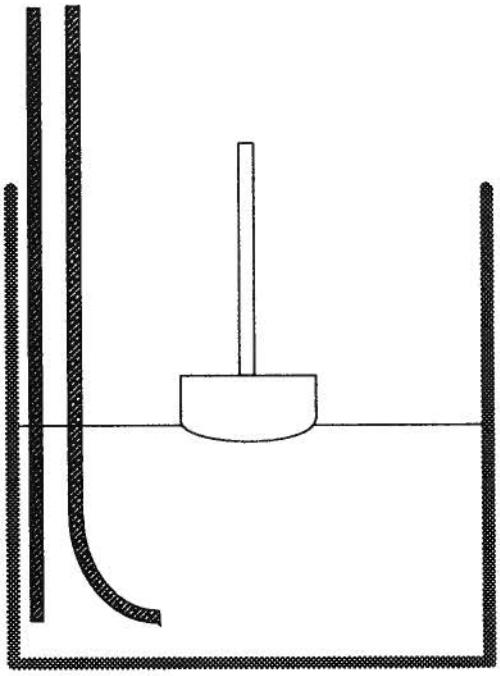

Figure 4.30: Positions of thermocouples and simulated crystal for melt temperature measurements.

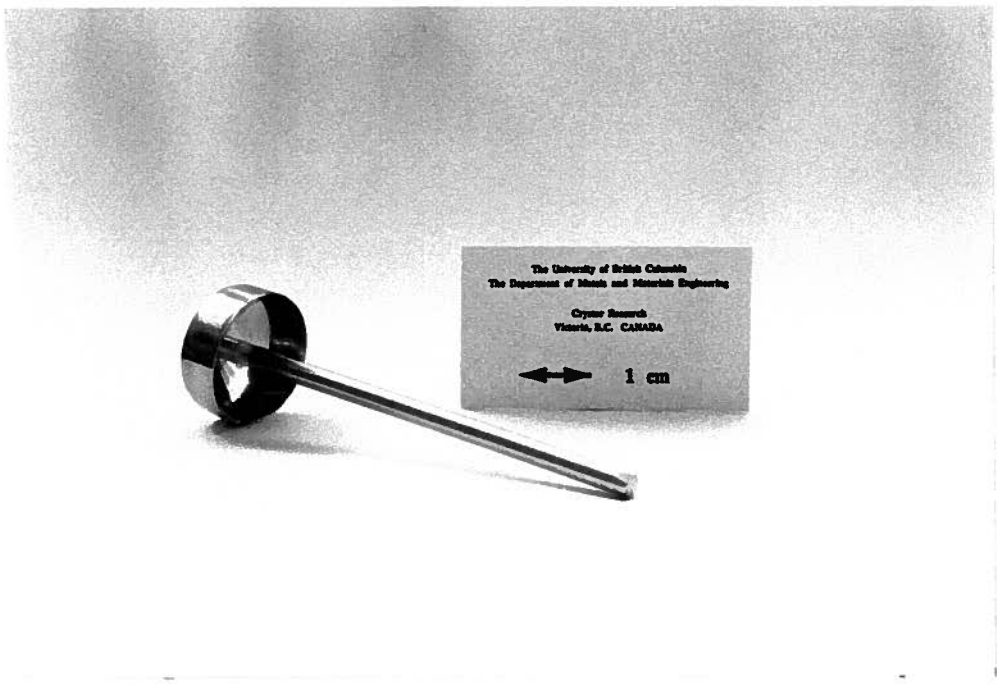

Figure 4.31: Platinum cap used to simulate the crystal.

Apparatus

The thermocouple positioning was accurate and repeatable to within 1 mm, using the apparatus shown in Figure 4.32; note that the thermocouples are inside the furnace and the positioning mechanism is outside the furnace. The apparatus consists of four key parts which are a horizontal guide track for radial movement, a rack and pinion gear for axial movement, a thermocouple holder and a micrometer/calibrated dial for spatial positioning. The apparatus was positioned on the crystal puller as shown in Figure 4.33. The thermocouple positioned closest to the wall is vertical and the inside thermocouple is curved at the bottom to allow it to measure temperatures under the simulated crystal. Figure 4.30 shows the thermocouple shapes and positions with respect to the simulated crystal. Electronic cold junction compensation was used for the measurements and a chart recorder or computer based data acquisition system was used to record the temperatures.

General Procedure

The chromel/alumel thermocouples used in the measurements were calibrated at the freezing point of tin (231.9681°C). The temperature measurements were made in an LBO/MoO_3 bath similar to that used for crystal growth. The furnace temperature was set at 100°C above that normally used for the start of crystal growth to ensure that no nucleation occurs in the melt or on the simulated crystal surface. The thermocouple positioning system was set by determining the micrometer and dial settings with the thermocouples touching the top of the melt, and the inside wall of the crucible. In the small crucible temperatures were measured at axial and radial intervals of 0.5 cm. The melt temperature in the large crucible were measured at axial intervals of 0.36 cm and radial intervals of 0.5 cm.

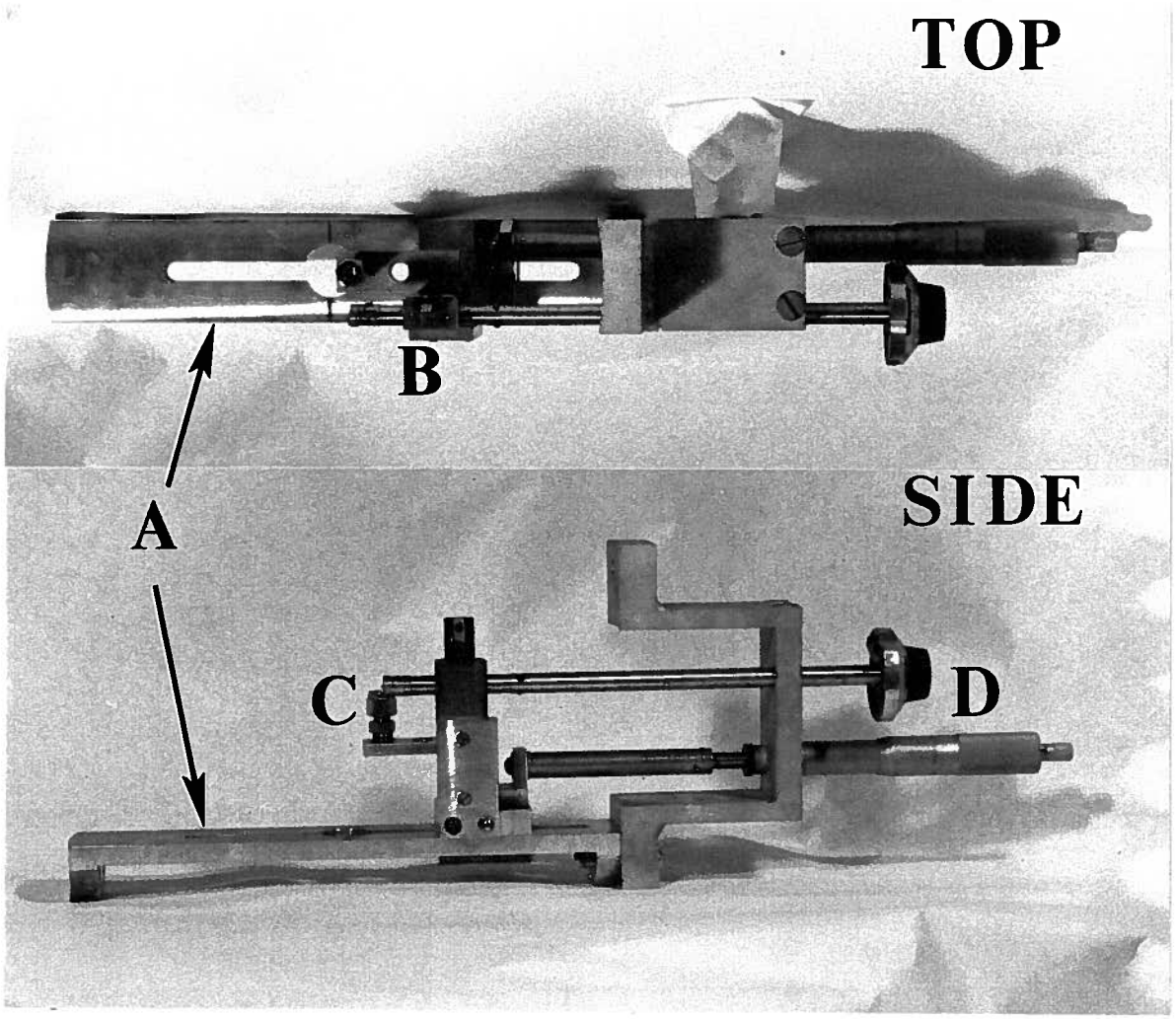

Figure 4.32: Thermocouple probe holder. A - guide track for radial movement of TC probe. B - rack and pinion gear for axial movement. C - thermocouple holder. D - micrometer and dial for positioning of the thermocouples.

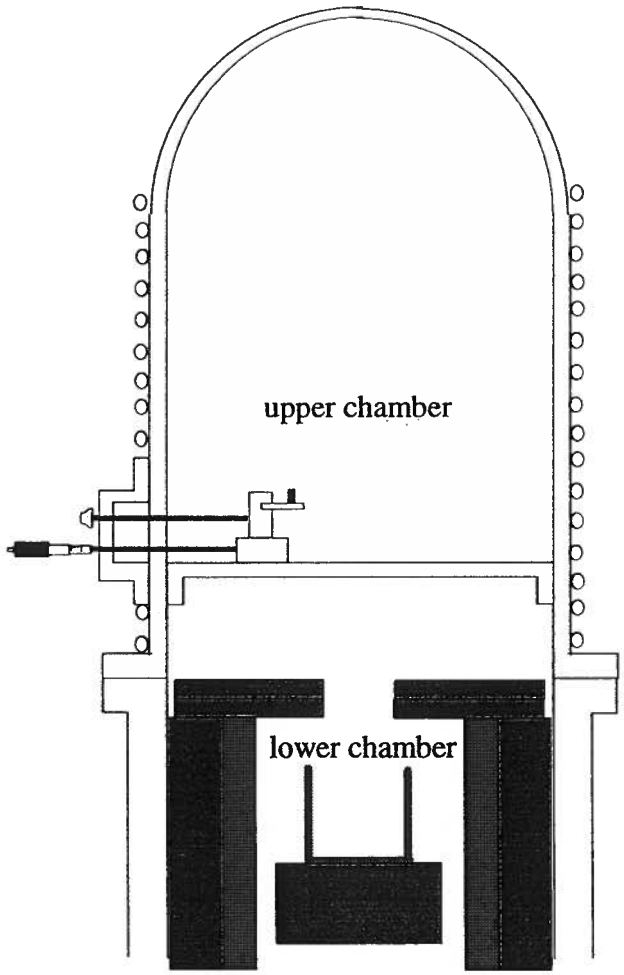

Figure 4.33: Apparatus for moving thermocouples attached to the crystal puller.

Procedure for Temperature Measurements in the Small Crucible

Initial temperature measurements were made for one flux concentration with no crucible rotation, without the simulated crystal. The measurements were repeated with the simulated crystal added to the system, and finally with the simulated crystal and crucible rotations of 15, 20, 25 and 30 rpm. For the measurements, thermocouple A was initially positioned 0.2 cm from the wall and 0.47 cm from the bottom surface. Thermocouple B, being offset 1.6 cm vertically from thermocouple A, was 1.8 cm from the wall and 0.47 from the bottom surface. The thermocouples were then moved vertically 0.18 cm then at intervals of 0.45 cm until they reached the maximum height of the fluid at 2.45 cm. The vertical temperature measurements were repeated at horizontal spacings of 0.5 cm until thermocouple B was at the center of the crucible. The model crystal interfered with the thermocouples limiting the horizontal movement to 1.55 cm above the bottom of the crucible and thermocouple B to be at 1.0 cm from the center of the crucible. The radial location that the temperatures were measured at in the small crucible were 1.0, 1.5, 2.6 and 3.1 cm.

Procedure for Temperature Measurements in the Large Crucible

Temperature measurements were made for one flux concentration with no crucible rotation, without the simulated crystal. The measurements were repeated with the simulated crystal added to the system, and finally with the simulated crystal and crucible rotations of 10, 15, and 30 rpm. For the measurements, thermocouple A was initially positioned 0.2 cm from the wall and 0.36 cm from the bottom surface. Thermocouple B, being offset 2.9 cm vertically from thermocouple A, was 2.9 cm from the wall and 0.36 from the bottom surface. The thermocouples were moved vertically at intervals of 0.36 cm

until they reached the maximum height of the fluid at 3.24 cm. The vertical temperature measurements were repeated at horizontal spacings of 0.5 cm until thermocouple B was close to the center of the crucible. The radial location that the temperatures were measured at in the large crucible were 0.4, 0.9, 2.8, 3.3 and 3.8 cm.

4.4 Physical Model of The Crystal Growth Process

A physical model was employed to visualize the general flow patterns that occur during crystal growth. The model consists of an 8.8 cm diameter plexiglass crucible, an 5.6 cm diameter plexiglass crystal and a rotation device. The crystal had 0.2 cm diameter holes at 1/2 and 3/4 of the crystal diameter for the injection of a tracer fluid. Glycerine was used to simulate the LBO/MoO_3 melt. Blue dye mixed with glycerin is used as a tracer to examine the flow patterns. Figure 4.34 shows the plexiglass crucible and crystal.

4.5 Physical Properties

4.5.1 Chemical Analysis

Chemical analysis for Mo and Li was conducted using atomic absorption at an external lab. Samples from the phase diagram determination and the viscosity measurements were analyzed for two different reasons. The phase diagram samples were used to determine the accuracy of the external lab's results. The theoretical and actual composition of these samples will be very close since the samples that are sent for analysis spend no time at an elevated temperature. The viscosity samples must be analyzed since the composition changes with extended time at temperature due to the vapour pressure of MoO_3.

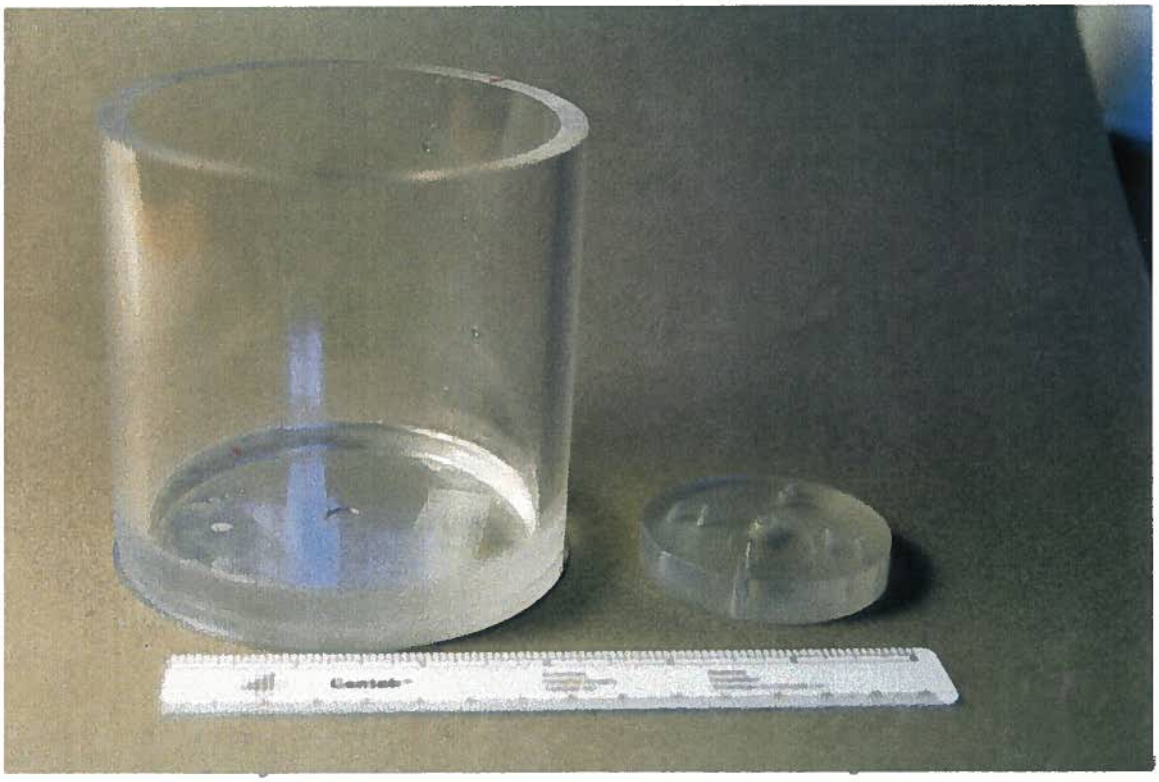

Figure 4.34: Plexiglass crucible and crystal used for the physical model.

4.5.2 LBO/MoO_3 Phase Diagram

A phase diagram is necessary in crystal growth for selecting the liquid temperature at which the seed is dipped. It is also important in mass transfer studies of the growing crystal. Of particular importance is the eutectic concentration, at which interface breakdown occurs. The LBO/MoO_3 phase diagram was determined using differential thermal analysis (DTA). This process consist of measuring the temperatures, of an alumina sample, and an LBO/MoO_3 sample simultaneously as they are heated. The alumina is used as a standard since it does not undergo a phase change in the temperature range examined. The temperatures are plotted as the temperature difference between the two samples (ΔT) as a function of the furnace temperature. When the LBO/MoO_3 sample undergoes a phase change, the heat released or absorbed will be indicated by a positive or negative deviation from the temperature of the alumina sample. The peaks and valleys on the ΔT - furnace temperature curve thus correspond to phase changes in the LBO/MoO_3 sample.

The equipment used consisted of a Dupont 1090 Thermal Analyzer and a Dupont 910 differential scanning calorimeter fitted with a 1200°C DTA furnace. Special platinum crucibles were used for containing the LBO/MoO_3 samples. The initial sample was 55.4 wt% LBO and 44.6 wt% MoO_3. Samples were prepared by combining lithium tetraborate, borate and molybdenum trioxide. The lithium tetraborate and molybdenum trioxide were in powder form and were easily mixed. The borate came in large blocks and was broken and ground to powder before it was mixed with the other constituents. Further mixing was done using a shaker with alumina balls as the grinding media. The samples were placed in a plastic bottle with alcohol and alumina balls which were then placed in the shaker and mixed for two 20 minutes periods. The samples were then placed in a drying furnace to evaporate the alcohol. The dried sample was remixed

using a mortar and pestle. A portion of the sample was kept to be sent for chemical analysis. Another portion of the sample was used for the DTA analysis. The remainder of the sample was mixed with more MoO_3 and used for the next DTA experiment. The theoretical LBO/MoO_3 wt% composition ranges examined were 55.5/44.5, 50.3/49.7, 40.4/59.6, 35.6/64.4 30.9/69.1 and 26.2/73.8. The powdered samples ranged in color from light green to blue as the MoO_3 concentration increased.

A sample was placed in the platinum crucible and placed in the DTA furnace. The furnace was rapidly heated to 150°C then slowly heated at 10°C/min to a final temperature of 750°C. The differential temperature was recorded between 500°C and 730°C. At the same time the sample was examined for a change in color associated with the phase change.

4.5.3 Viscosity

The viscosity of LBO containing MoO_3 was measured, as a function of the MoO_3 concentration, with a Brookfield Model RVTDV II viscometer, using a modified procedure of the ASTM standard C936-81. This procedure is used for measuring the viscosity of glass above its softening point. The LBO/MoO_3 sample, in a platinum crucible, was heated in an electric furnace. The crucible dimensions are 66 mm diameter and height. A platinum paddle, shown in Figure 4.35 was fabricated for these measurements following ASTM specifications. The system, including the paddle, was calibrated by measuring the viscosity of a solution of glycerine and corn syrup which had a specified viscosity.

Samples for the viscosity measurements were prepared using the same procedure as was used for crystal growth. Depending on the test, either an air or dry argon atmospheres were used, the later was to unsure that no Li was lost from the melt due to water vapour. Once the LBO/MoO_3 melt was homogenized, a sample was removed for quantitative chemical analysis of the molybdenum and lithium content. This was done

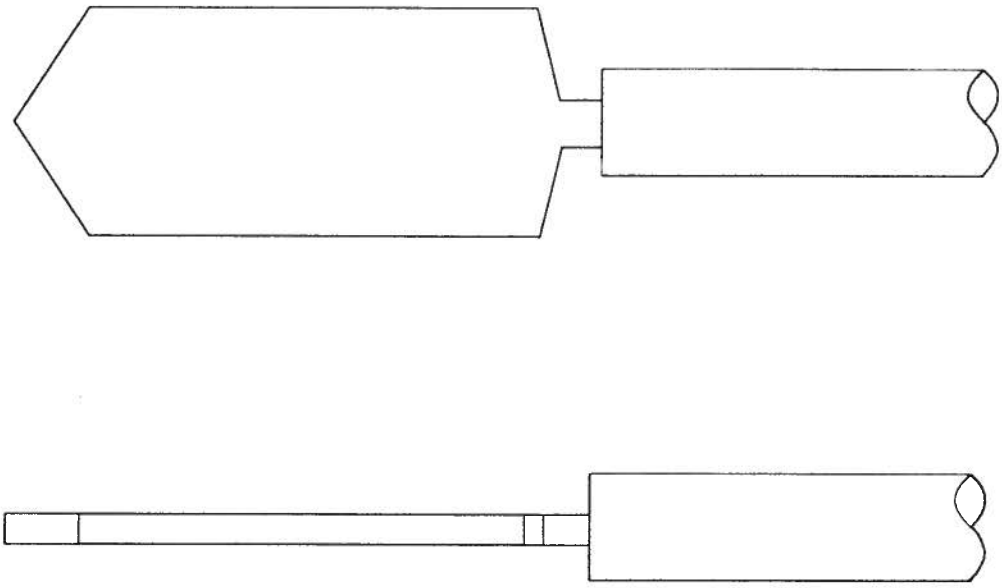

Figure 4.35: Platinum paddle for measuring viscosity of LBO/MoO_3.

with a quartz tube into which a sample from the high temperature melt was drawn. The paddle used for the viscosity measurements was then immersed in the melt together with a platinum sheathed chromel/alumel thermocouple. The viscometer was then turned on, the temperature stabilized at the specified test value and the thermocouple removed. The viscosity of the melt as indicated by the viscometer was then recorded. The procedure was then repeated at a lower set melt temperature, allowing approximately 10 minutes for the melt to equilibrate at the new temperature. The viscosity measurements were continued until the viscosity of the solution was in excess of 100 poise.

4.6 Crystal Quality

The crystal quality of LBO was examined for MoO_3 inclusions, cracking and bubbles using optical microscopy and scanning electron microscopy (SEM). Quantitative chemical analysis for molybdenum was performed using wavelength dispersive spectroscopy (WDX). Samples were prepared by polishing the surface with a 1μ diamond suspension on a Buehler Ecomet IV. Polishing was continued until the surface of the sample was flat and had no visible scratches. Optical examination was conducted using an Zeiss Stereomicroscope SV8. The samples for SEM/WDX analysis were sputter coated with a layer of amorphous carbon. SEM/WDS analysis was done using a Hitachi S-570 SEM with Microspec WDX attachment. Measurement of the nonlinear optical properties were considered beyond the scope of this project and not carried out. The variation in visible/electron image inclusion density was assumed to be a sufficient indication of crystal quality.

Chapter 5

Experimental Results

5.1 Phase Diagram for the LBO/MoO_3 System

The concentration of the DTA samples examined are listed in Table 5.3. The charge concentrations listed were determined from the mass of the constituents used. The concentrations were measured by a commercial laboratory using atomic absorption. The measured values are given in weight percent Mo and Li. Equivalent MoO_3 and LBO concentrations were calculated from the measured data assuming that these were the only species present in the melt.

$$MoO_3(\text{equivalent}) = Mo(\text{measured}) \times \frac{\text{molecular weight of } MoO_3}{\text{molecular weight of Mo}}$$

$$LBO(\text{equivalent}) = Li(\text{measured}) \times \frac{\text{molecular weight of LBO}}{\text{molecular weight of Li}}$$

Comparing the equivalent concentration of MoO_3 and LBO to the charge concentrations, the former is observed to be approximately 5% below the later in all cases. The equivalent MoO_3 concentration was normalized.

$$MoO_3(\text{normalized}) = \frac{MoO_3(\text{equivalent})}{MoO_3(\text{equivalent}) + LBO(\text{equivalent})}$$

The normalized MoO_3 concentration were close to the values of the charge concentration. These values were taken as the actual melt concentrations.

The DTA results for 45 Wt% MoO_3 (sample 1), are shown in Figure 5.36. The curve has four points of interest, the negative temperature difference at A (555°C) and

Sample	Weight Percent						
	Charge Concentration		Measured		Equivalent		Normalized
	MoO_3	LBO	Mo	Li	MoO_3	LBO	MoO_3
1	44.56	55.54	26.50	2.86	39.76	49.19	**44.76**
2	49.66	50.34	30.00	2.64	45.01	45.40	**49.78**
3	59.58	40.42	–	–	–	–	**60**
4	64.40	35.60	41.00	1.89	61.51	61.51	**65.42**
5	69.13	30.87	46.50	1.63	69.76	69.76	**71.34**
6	73.77	26.22	47.30	1.38	70.96	70.96	**74.94**

Table 5.3: MoO_3 and LBO concentrations used in determining the phase diagram.

D (575°C), the positive temperature difference at B (682°C) and the change of slope at C (610°C). During heating the sample appearence was noted. The sample was initially a uniform light green colour until 555°C (point A) was reached where a reaction occurred and the sample turned brown. The surface texture also changed from being uniform to having evenly distibuted shiny regions on a dull surface. Between 575°C (point B) and 610°C (point C) the sample turned to a transparent white colour and the surface texture changed to being shiny in appearance. Between 610°C and 682°C the sample colour slowly changed to an amber colour. At 682°C (point D) the sample melted.

The liquidus of the sample was taken as the point where the temperature difference started to increase at point D and the slope between point C and D as the solid–liquid phase region. The gradual change in slope around point C makes it difficult to accurately determine the solidus.

The temperatures at which the phase transformations occured are listed in Table 5.4 and plotted in Figure 5.37. The liquidus changes from 682°C at 44.76 Wt% MoO_3 to 619°C at 60 Wt% MoO_3 just before the eutectic concentration, 61.5 Wt% MoO_3. The DTA analysis indicates that two other phases occur above the eutectic composition at temperature in excess of 610°C. The structure of these phases were not investigated.

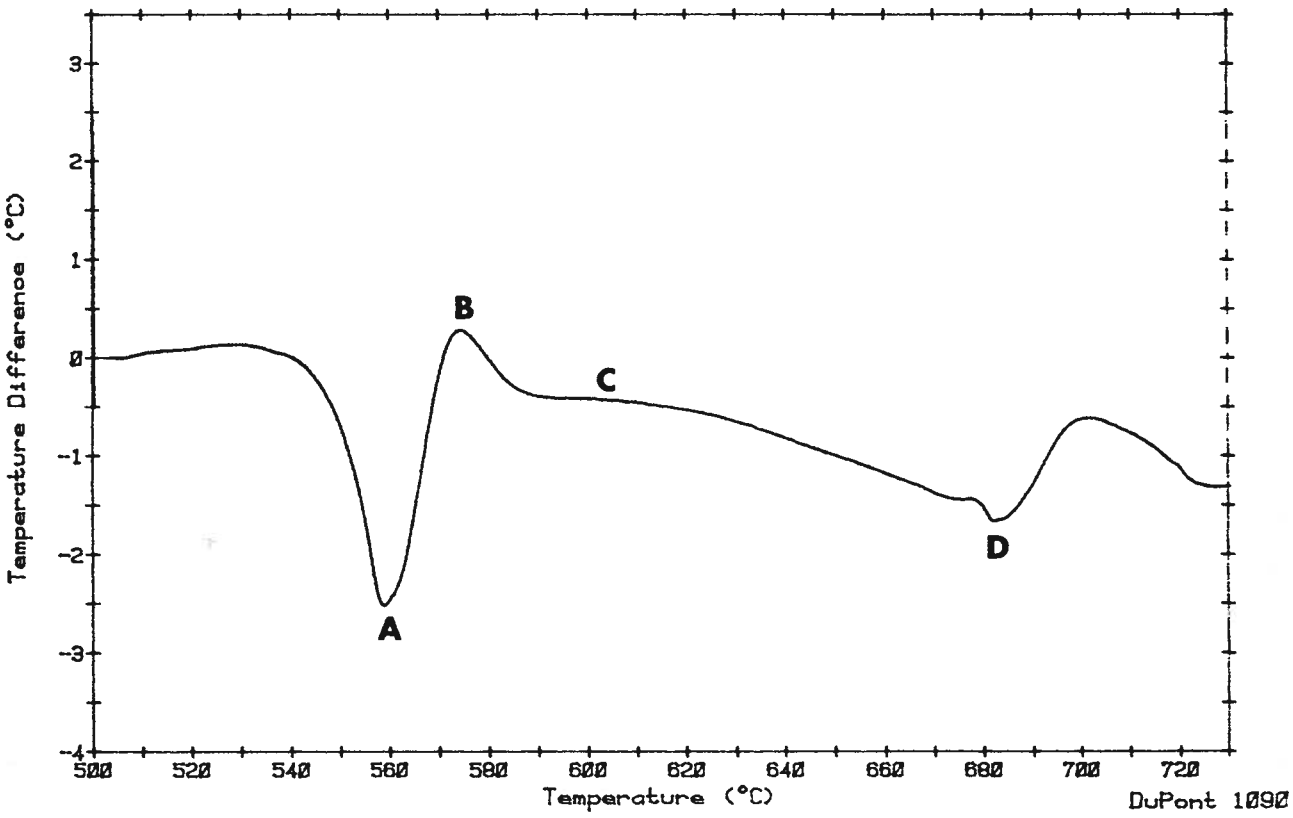

Figure 5.36: Temperature difference versus temperature for 45 Wt% MoO_3 (sample 1) determined by DTA.

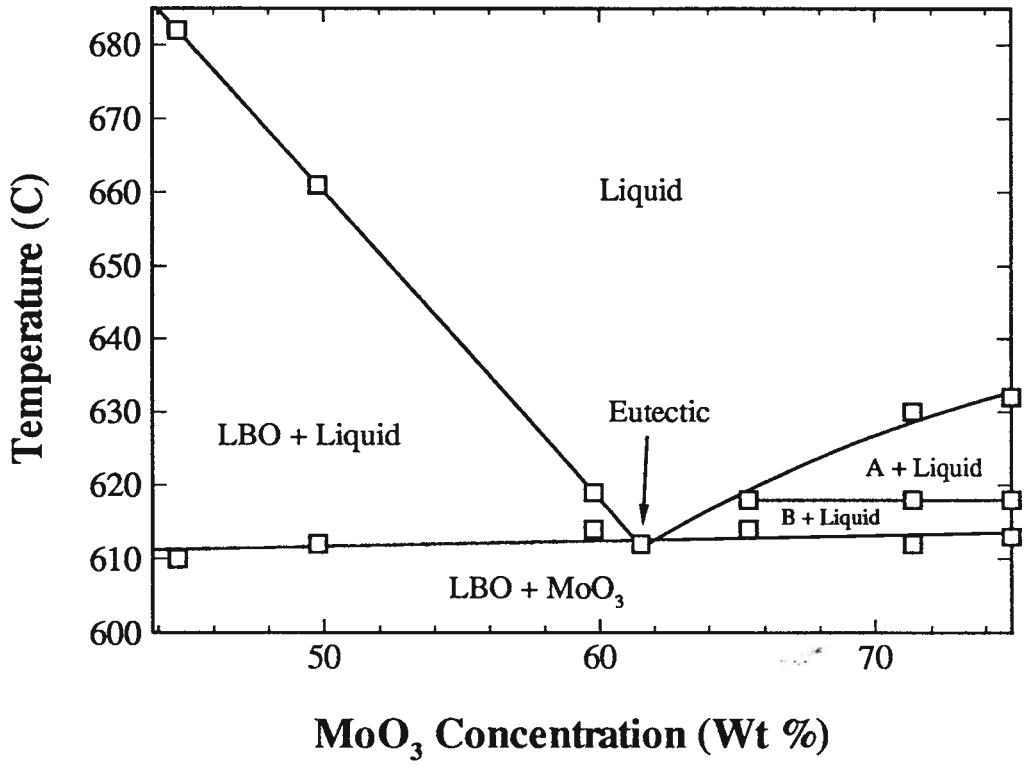

Figure 5.37: Phase Diagram of the LBO – MoO_3 system.

Sample	Wt% MoO_3	Solidus(s)	Liquidus
1	44.76	610°C	682°C
2	49.78	612°C	661°C
3	60	614°C	619°C
4	65.42	614°C	618°C
5	71.34	612°C, 618°C	630°C
6	74.94	613°C, 618°C	632°C

Table 5.4: The solidus and liquidus temperatures of the MoO_3 – LBO samples

5.2 Viscosity

The viscosity of five samples (7-11) were measured as a function of temperature. The composition of the samples are listed in Table 5.5. The viscosities are listed in Table 5.6 and 5.7. The temperatures listed are the average temperatures in the melt. The temperature difference across the sample was measured to be 10°C. Two atmospheres were used, air and dry argon. The later was used to ensure that no Li was lost from the melt due to the presence of water vapour in the atmosphere.

The viscosity is plotted on a logarithmic scale against the reciprocal of the test temperature, in Figure 5.38. In general, the viscosity is high, ranging from 4 poise to greater than 70 poise between 863°C and 661°C. The viscosity decreases with increasing temperature and increasing MoO_3 concentration. The viscosity measurements are in good agreement with each other above 702°C ($10000/T[K] < 10.25$). Sample 11 (37.06 Wt% MoO_3) deviates from sample 10 (38.67 Wt% MoO_3) below 702°C ($10000/T[K] > 10.25$). The best fit lines for samples 7, 8 and 9 are plotted on the graph.

29.66Wt% MoO_3: $$\nu(\text{poise}) = exp\left(72.26 - 0.155 \times T[C] + 8.51 \times 10^{-5} \times (T[C])^2\right)$$

36.18Wt% MoO_3: $$\nu(\text{poise}) = exp\left(45.59 - 0.0946 \times T[C] + 5.04 \times 10^{-5} \times (T[C])^2\right)$$

40.89Wt% MoO_3: $$\nu(\text{poise}) = exp\left(37.31 - 0.0784 \times T[C] + 4.21 \times 10^{-5} \times (T[C])^2\right)$$

Sample	Weight Percent						
	Charge Concentration		Measured		Equivalent		Normalized
	MoO_3	LBO	Mo	Li	MoO_3	LBO	MoO_3
7	34.8	65.2	17.30	3.58	25.96	61.56	**29.66**
8	36.8	63.2	21.90	3.37	32.86	57.96	**36.18**
9	39.3	60.7	26.40	3.33	39.61	57.96	**40.89**
10	43.0	57.0	20.60	2.85	30.91	49.01	**38.67**
11	50.0	50.0	21.20	3.14	31.81	54.00	**37.06**

Table 5.5: MoO_3 and LBO concentration of the samples used in the viscosity measurements.

The viscosity variation with temperature for sample 10 (38.67 Wt% MoO_3) and the fitted value for sample 8 (36.18 Wt% MoO_3) are similar below 702°C ($10000/T[K] > 10.25$). Thus it is assumed that the low temperature viscosity measurements, $T < 702$°C ($10000/T[K] > 10.25$), for sample 11 are erroneous. The variation of viscosity with concentration is plotted in figure 5.39. The viscosity decreased with increasing MoO_3 at a constant temperature.

The viscosity of sample 7, 8 and 9 at their respective liquidus's were determined. The liquidus temperatures were estimated by extrapolating the LBO/MoO_3 liquidus line on Figure 5.37 to the composition of the samples. The liquidus temperatures were used with the best fit viscosity equations for their respective compositions. The variation in viscosity and liquidus temperature is given in Figure 5.40. The viscosities at the liquidus decrease linearly with increasing MoO_3 content.

5.3 Preliminary LBO Crystal Growth Runs

This section examines the crystal growth parameters used and the resulting crystal growth quality in runs conducted prior to the start of this investigation. Most of the preliminary crystal growth runs used crystal rotation rates of approximately 15 rpm, no

Sample	Atmosphere	Temperature	10,000/T[k]	Viscosity (poise)
7	Air	765°C	9.64	26.8
	Air	785°C	9.46	18.2
	Air	807°C	9.26	12.9
	Air	824°C	9.12	9.5
	Air	847°C	8.93	7.1
	Air	862°C	8.81	5.8
8	Air	736°C	9.91	25.3
	Air	754°C	9.74	18.2
	Air	779°C	9.51	12.1
	Air	800°C	9.32	8.4
	Air	817°C	9.17	6.6
	Air	847°C	8.85	4.7
	Air	863°C	8.80	4.2
	Air	914°C	8.43	3.7
9	Air	730°C	9.97	13.4
	Air	749°C	9.79	9.47
	Air	766°C	9.63	7.1
	Air	788°C	9.43	5.5
	Air	808°C	9.25	4.47
	Air	833°C	9.04	3.69
	Air	847°C	8.93	3.42
	Air	869°C	8.76	2.63
10	Dry Argon	691°C	10.37	124.27
	Dry Argon	702.5°C	10.25	59.97
	Dry Argon	720°C	10.07	41.95
	Dry Argon	741°C	9.86	27.09
	Dry Argon	767°C	9.62	16.31
	Dry Argon	769°C	9.60	16.7
	Dry Argon	784°C	9.46	12.89
	Dry Argon	788°C	9.43	11.97
	Dry Argon	817°C	9.17	8.16

Table 5.6: Viscosity versus temperature for samples 7 to 10.

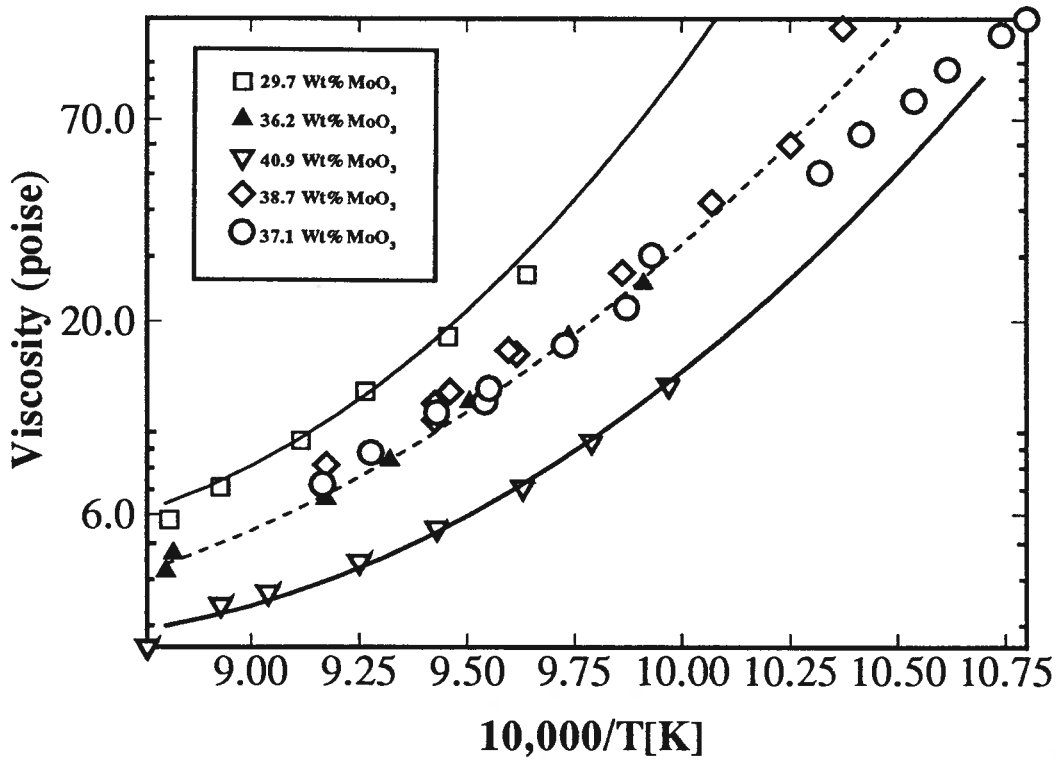

Figure 5.38: Dependence of viscosity on temperature and MoO_3 concentration.

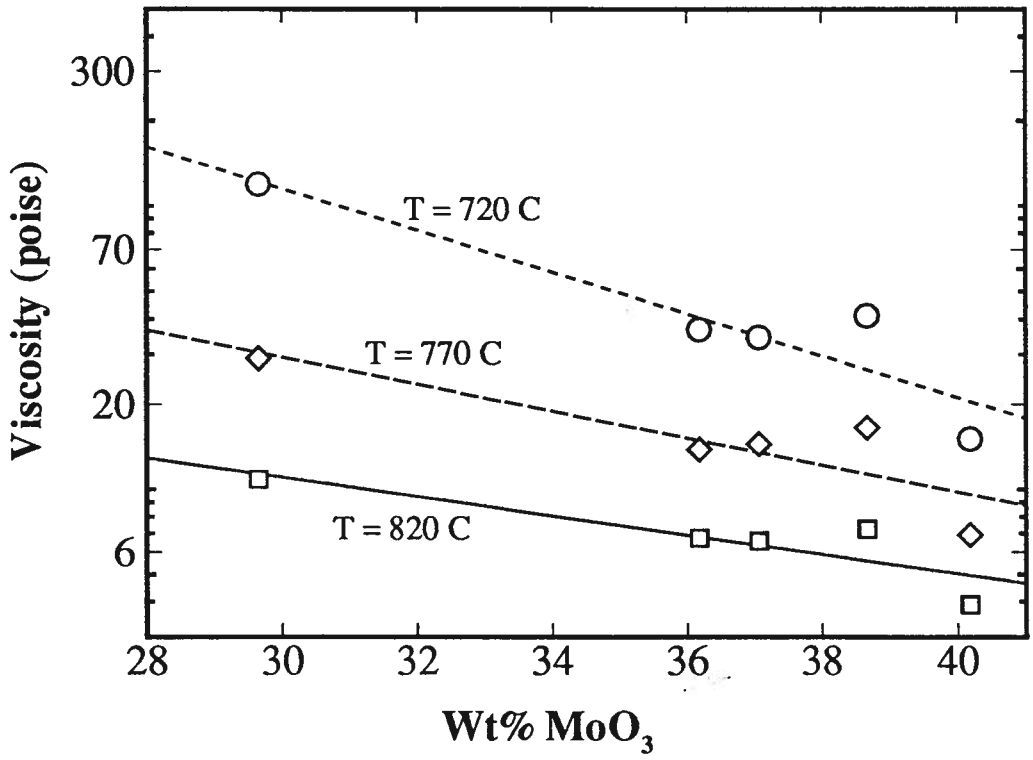

Figure 5.39: Variation of viscosity with MoO_3 at the temperatures indicated.

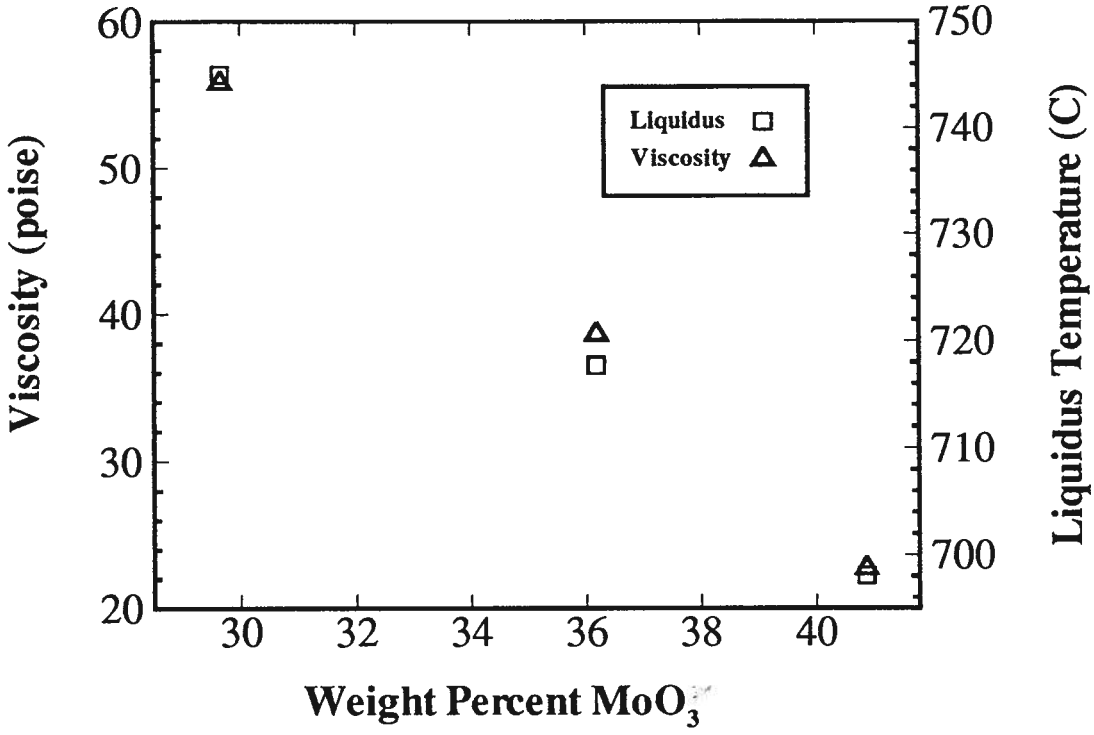

Figure 5.40: Liquidus temperature and viscosity as a function of MoO_3.

Sample	Atmosphere	Temperature	10,000/T[k]	Viscosity (poise)
11	Dry Argon	653°C	10.80	132.03
	Dry Argon	658°C	10.74	119.14
	Dry Argon	669°C	10.62	96.13
	Dry Argon	676°C	10.54	78.90
	Dry Argon	687°C	10.42	64.18
	Dry Argon	696°C	10.32	50.50
	Dry Argon	734°C	9.93	30.25
	Dry Argon	740°C	9.87	21.83
	Dry Argon	755°C	9.73	17.23
	Dry Argon	774°C	9.55	13.15
	Dry Argon	775°C	9.54	12.10
	Dry Argon	787.5°C	9.42	11.31
	Dry Argon	805°C	9.28	8.81
	Dry Argon	818°C	9.17	7.24

Table 5.7: Viscosity versus temperature for sample 11.

crucible rotation and a cooling rate of 3°C/day. The initial charge concentration of MoO_3 in the melt was 34 Wt%.

All the crystals cracked during the post growth cooling to room temperature. The average size of the uncracked portions of the crystal were $7 \times 3 \times 3$ mm^3. Opaque white/green colored inclusions were in the crystals having an average size of $3 \times 3 \times 3$ mm^3. Samples of the grown crystals were examined using a scanning electron microscope (SEM) equipped with a wavelength dispersive spectrometer (WDS). Figure 5.41 show the backscatter images of the cross section of an LBO crystal. WDS analysis was used to examine the crystal defects as well as the defect free crystal matrix. There was no molybdenum present in the defect free portions of the crystal.

The molybdenum inclusions on this sample formed as two types; line inclusions and normal inclusions. Line inclusions run for distances that are greater than half the specimen size and the width is much smaller than the length. Normal inclusions have lengths

that are comparable to their widths. Backscatter images and the corresponding dot maps for a normal inclusion are shown in Figure 5.42. The inclusion shape corresponds directly to the molybdenum dot map. A backscatter image and its corresponding molybdenum line scan of a line inclusion is shown in Figure 5.43. The dot map and line scan of the molybdenum region corresponds to the inclusions in the backscatter photos. The line inclusions are parallel and perpendicular to the crystal growth axis.

Flux inclusions in ceramic materials are more significant than for other materials. An inclusion with an expansion coefficient different from the matrix is the most likely cause of the crystal fracturing during cooling to room temperature. The expansion coefficient of LBO in the [001] direction and Mo_2O_3 are $-88.0 \times 10^{-6}/°C$ and $5.35 \times 10^{-6}/°C$ respectively (see Table 2.2).

From these initial findings it was evident that the main crystal defects (inclusions and cracking) are due to the MoO_3 flux. It was clear that the build up of MoO_3, due to the high viscosity of the melt, has a large influence on the crystal quality. Mathematical and physical modeling of the crystal growth process has been employed to improve the mixing in the melt thus reducing the MoO_3 ahead of the growing interface.

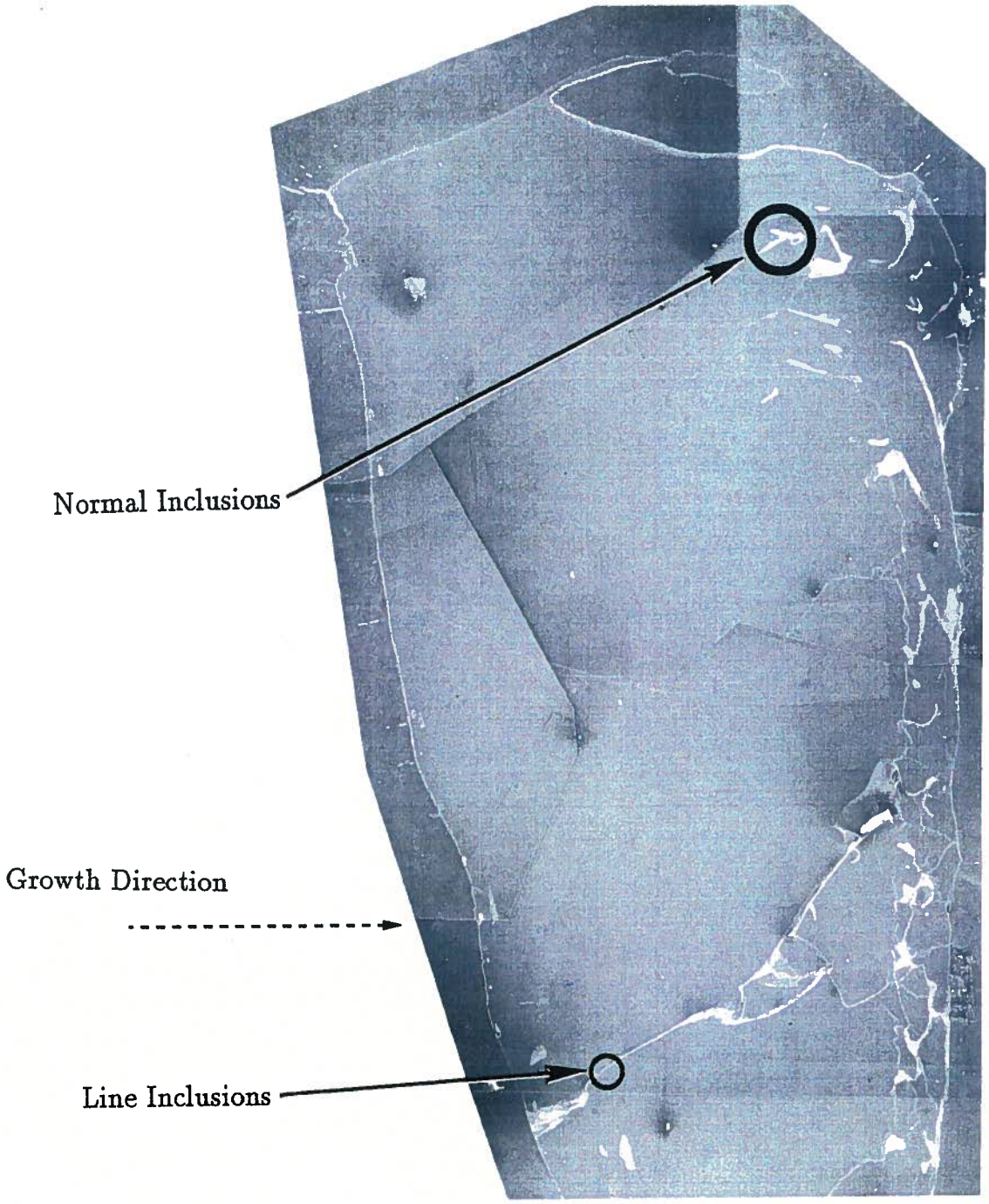

Figure 5.41: Surface of an LBO crystal with inclusions. Magnified 30 times

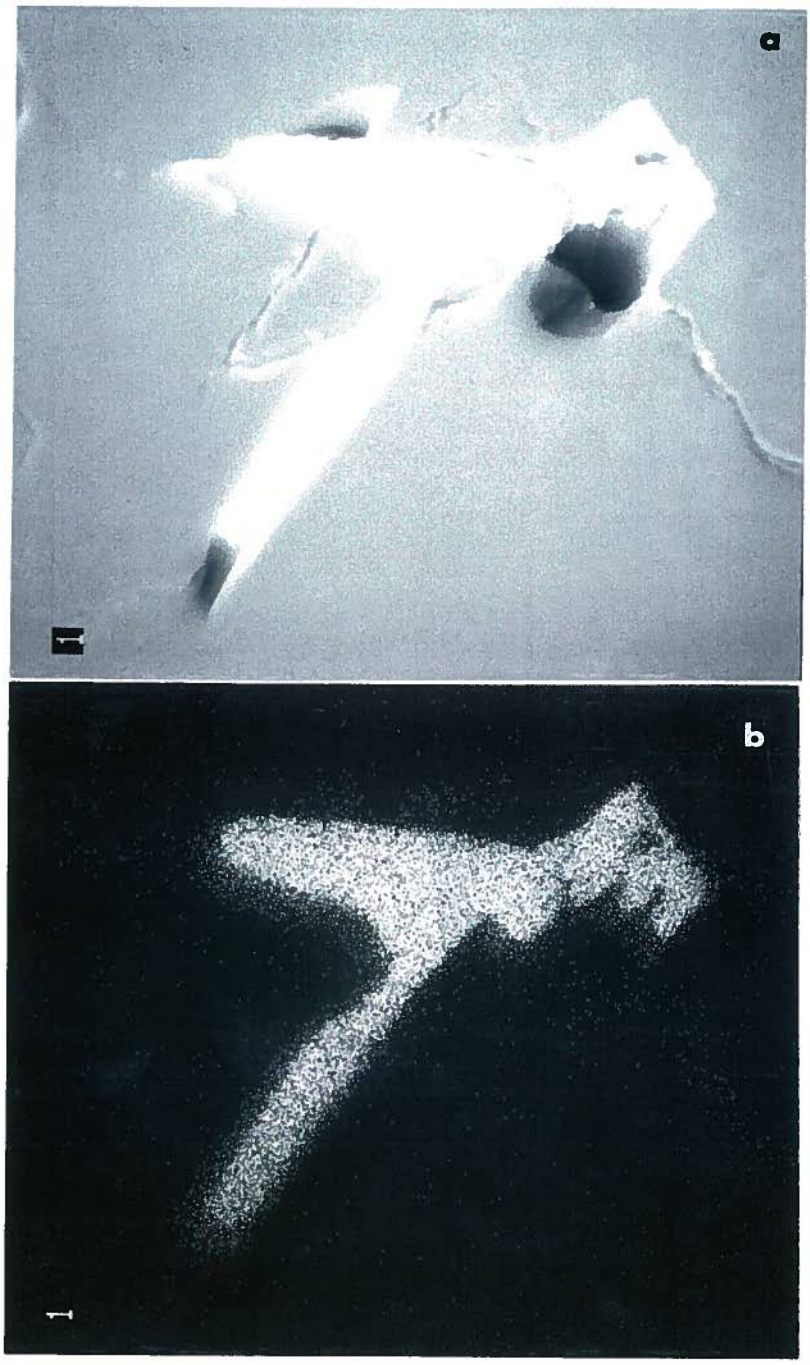

Figure 5.42: Normal molybdenum inclusion in an LBO crystal magnified 400 times. (a) Backscatter image. (b) WDS molybdenum dot map

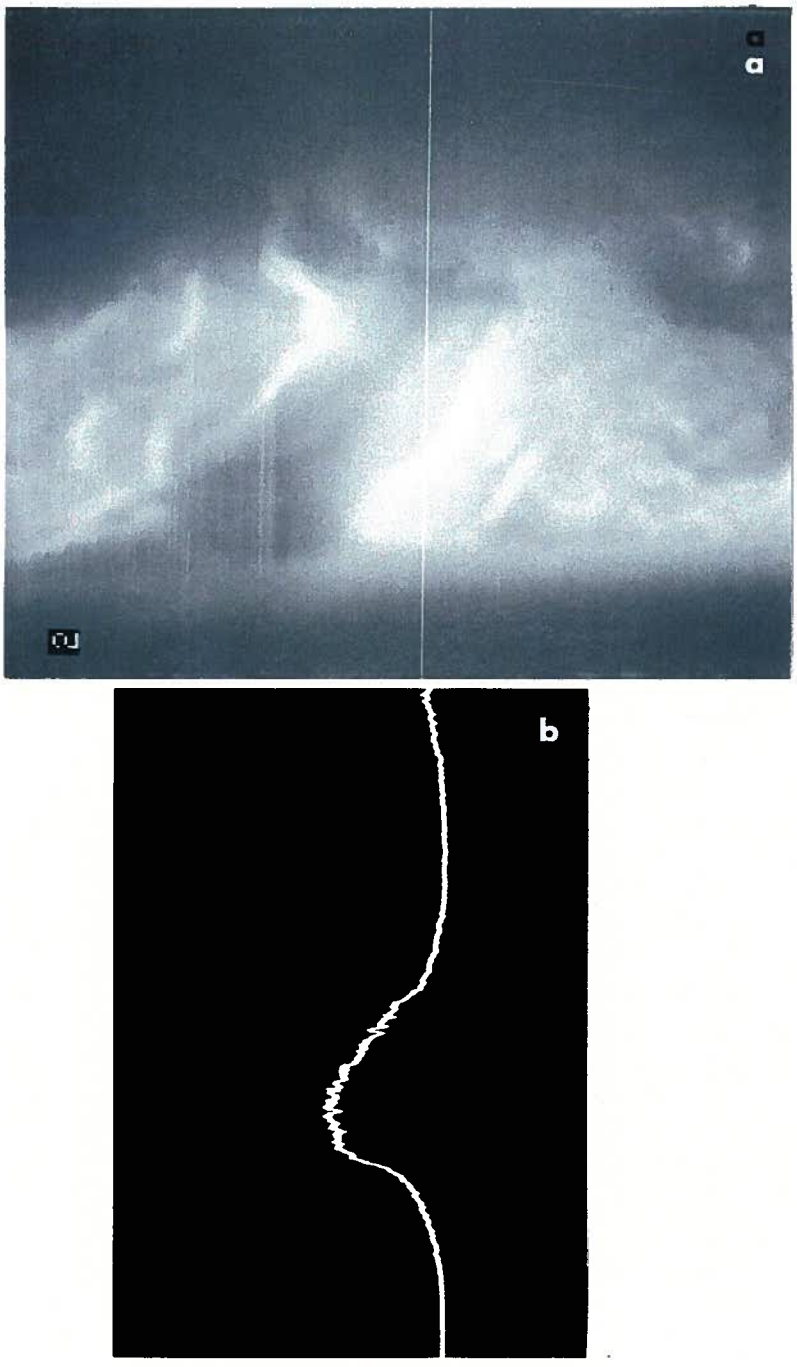

Figure 5.43: Molybdenum line inclusion in LBO crystal magnified 2,200 times. (a) Backscatter image. (b) WDS molybdenum line scan

Chapter 6

Physical Model of the LBO Crystal Growth Process

The flow of liquid under a growing crystal was investigated by observing the flow directly in a physical model of the growth system using a transparent liquid as the melt. The physical model gives a better visualization of the flow patterns while a mathematical model will give semi–quantitative fluid velocity results that will be superior to the physical model results. This type of flow has been previously examined in detail for a rotating crystal in an infinite fluid [46]. Thus the physical model will only examine the flow fields due to a rotating crucible with a stationary crystal.

The physical model consisted of a plexiglass crucible 8.8 cm in diameter and a plexiglass crystal 5.6 cm in diameter. The melt level in the crucible was 2.5 cm in height. The fluid consisted of a glycerine solution having a viscosity of 7 poise. This corresponds to an 41.6 Wt% MoO_3 melt at 820°C, which is 130°C above the liquidus temperature. The plexiglass model of the crystal was positioned such that the bottom surface of the crystal was in contact with the melt. Blue dye was injected in a hole in the crystal at 0.5 of the crystal radius and red dye in a hole at 0.75 of the crystals radius. The blue and red dye consisted of chart recorder ink mixed with glycerine in order to give it the same buoyancy as the fluid. The crystal was stationary for all of the experiments and the crucible was rotated at either 45 or 78 rpm in a clockwise direction. The flow is discussed in terms of the fluids radial (v_r), axial (v_z) and theta (swirl,v_θ) velocity components.

6.1 Observed Fluid Flow Patterns

Figure 6.44a shows the initial dye pattern from the top of the crystal for a crucible rotation of 45 rpm. The injection holes for the red and blue dye are shown in figure as A and B respectively. Similar injection holes at the same radial location but rotated by one quarter of a circumferential arc are shown as A′ and B′. The dye traces are moving in a semicircular arc and also have a radial flow component that moves them towards the centre of the crystal. This is shown by the red dye trace. It is injected at a 0.75 of the crystal radius (Point A) and its position is at 0.5 of the crystal radius (Point B′) after it travels one quarter of a circumferential arc. The view of the dye from the side of the crucible is shown in Figure 6.44b. The dyes remain very close to the model crystal after they have been injected. It is noted that each picture in Figure 6.44 corresponds to different experimental runs. Differences in the position of the red and blue dye with respect to each other are due to different injection start times. Thus initially the dyes have a large swirl velocity a smaller radial velocity and a non existent axial velocity.

The dye tracers patterns between the injection locations and near the centre of the crystal are shown in Figure 6.45. The view from the top of the crystal, Figure 6.45a, show that the dyes reach the centre of the crystal after they travel 0.75 of a circumferential arc. The view for the side of the crucible, Figure 6.45b, shows that the dye tracers start moving toward the bottom of the crucible near point A. Point A is 0.75 of a circumferential arc from the location where the dyes are injected. It is evident that the axial velocity downward increases as the dye traces get near the center line of the melt.

The flow of the dyes at the centre line of the crucible are shown in Figure 6.46. The flow near the crucible, point A, and at 0.5 of the fluid height, point B, are examined. The swirl in the θ direction is larger at point A and small at point B also the vertical travel distance is large between both points. This shows that the axial fluid velocity is

dominant at the centre of the crucible near the mid height of the fluid.

The flow patterns of the dye tracers near the bottom of the crucible, Figure 6.47, are different at the mid height of the fluid, point A, the centre bottom of the crucible, point B, and the outside bottom of the crucible, points C and D. The dye traces start moving in the radial directions and get a larger swirl as they approach the bottom of the crucible, points A to B. Once the dye traces have reached the bottom of the crucible their axial travel distance decreases to near zero and there radial and swirl component increased as they move outward along the bottom of the crucible. When the dye reaches the side of the crucible, point C and D, it is no longer a separate phase from the pure glycerine. This indicates that there is significant mixing occurring at the bottom of the crucible. Figure 6.48a shows the flow patterns after approximately 3 minutes. The initial dye has mixed to make the fluid a uniform red color except directly below the crystal were new dye is being injected into the liquid.

The location of the maximum of the radial and axial flow components for steady state crucible rotation are at the following location. Maximum radial fluid flow occurs directly below the crystal and above the bottom of the crucible. Axial fluid flow is largest at the centre of the crucible half way between the crystal and bottom of the crucible. This is similar to what has been previously been predicted [28, 32].

The change in flow patterns at different crucible rotation rates are examined. Figure 6.48 shows the change in flow pattern between 45 and 78 rpm. The sequence of photos with respect to the crucible rotation rates are, figure 6.48a is the flow pattern at 45 rpm, figure 6.48b is the transient flow pattern and figure 6.48c is the flow pattern at 78 rpm. Point A, located at the mid height of the fluid, will be the location of the fluid that is examined. The location of the swirl at point A with a crucible rotation rate of 45 rpm, Figure 6.48a, is large. The size of the swirl gets smaller as the flow adjusts to the higher crucible rotation rate of 78 rpm, Point A Figure 6.48b. The steady state

flow pattern at 78 rpm, Figure 6.48c, results in reducing the swirl of the dye tracer at point A to near zero. The dye tracer follow a straight vertical line below the centre of the crystal. This shows that the axial velocity at the centre line of the melt gets larger with increasing crucible rotation rates.

The change in flow patterns directly below the crystal for crucible rotation rates of 45 and 78 rpm are shown in Figure 6.49. The dyes in the 45 rpm case reach the centre of the crystal in 0.75 of a circumferential arc. A crucible rotation rate of 78 rpm causes the dyes to reach the centre of the crystal in 0.5 of a circumferential arc. This shows that the radial velocity of the fluid increases with increasing crucible rotation rates. Both Figures 6.48 and 6.49 clearly show that axial and radial fluid velocities increase with increasing crucible rotation rates.

6.2 Physical Explanation of Fluid Flow Patterns

This type of flow has been previously examined in detail for a rotating crystal and stationary crucible [46]. These results will be referred to in considering the forces acting on the fluid, and the resulting fluid motion, for the case of crucible rotation with and without a stationary crystal in contact with the top of the melt.

When a crucible starts to rotate from rest without a crystal present, liquid near the bottom of the crucible starts to move in the θ direction due to viscous drag. As the fluid rotates it gets a centripetal acceleration ($-\omega^2 r$). The presence of the centripetal acceleration with no radial pressure gradient causes the fluid to move outward in the radial direction. When the fluid reaches the crucible wall it is forced to move upward. Fluid at the center of the crucible fluid moves downward to balance the outward flow in the radial direction. As the flow progresses the surface of the fluid rises at the outside, and falls at the centre as shown in Figure 6.50. The variation in fluid height with radius

creates a radial pressure gradient which balance the centripetal acceleration and stops the radial flow at the bottom of the crucible. When the radial flow stops the fluid moves as a solid body with the rotating crucible. Consider the radial forces that act on a control volume of fluid. In terms of Newtons law of motion the balance of forces in the radial direction is:

$$F_r = ma_r$$

Where F_r is the force acting in the radial direction, m is the mass and a_r is the acceleration in the radial direction. The previous equation in terms of pressure is

$$\frac{\partial P}{\partial r} = -\rho a_r$$

were P is pressure and ρ is density. With crucible rotation and no radial pressure gradient the forces acting on the fluid at the bottom of the crucible is only due to the centripetal acceleration. Thus there is a net force in the radial direction

$$-\rho\left(-\omega^2 r\right)$$

A radial pressure gradient is created with the change in fluid height, which balances with the centripetal acceleration giving:

$$\frac{\partial P}{\partial r} = -\rho\left(-\omega^2 r\right)$$

For a stationary crystal present it will be assumed that the crystal is inserted into the melt after the fluid has become a solid body in the rotating crucible. It is also assumed that the bottom of the crystal is the same shape as the surface of the fluid. The stationary boundary condition, $v_\theta = 0$, at the fluid surface with the crystal present is shown in Figure 6.51.

The crucible is rotating and the fluid has solid body rotation. Constraining a portion of the fluid surface causes the fluid directly below it to have a lower θ velocity than it had

during solid body rotation. Thus the centripetal acceleration is lower. Since, in this case, the radial pressure gradient is the same there is a net force in the inward radial direction. Thus, fluid below the constrained surface will move in the inward radial direction until it reaches the centre were it will move downward. The fluid moving downward will reach the bottom of the crucible, then it will move radially outward to the crucible wall, upward along the crucible side, and finally inward once it reaches the surface of the fluid. This flow will continue since the centripetal acceleration will not be balanced by the radial pressure gradient below the crystal. The flow patterns as explained using fluid mechanics are the same as has observed in the physical model.

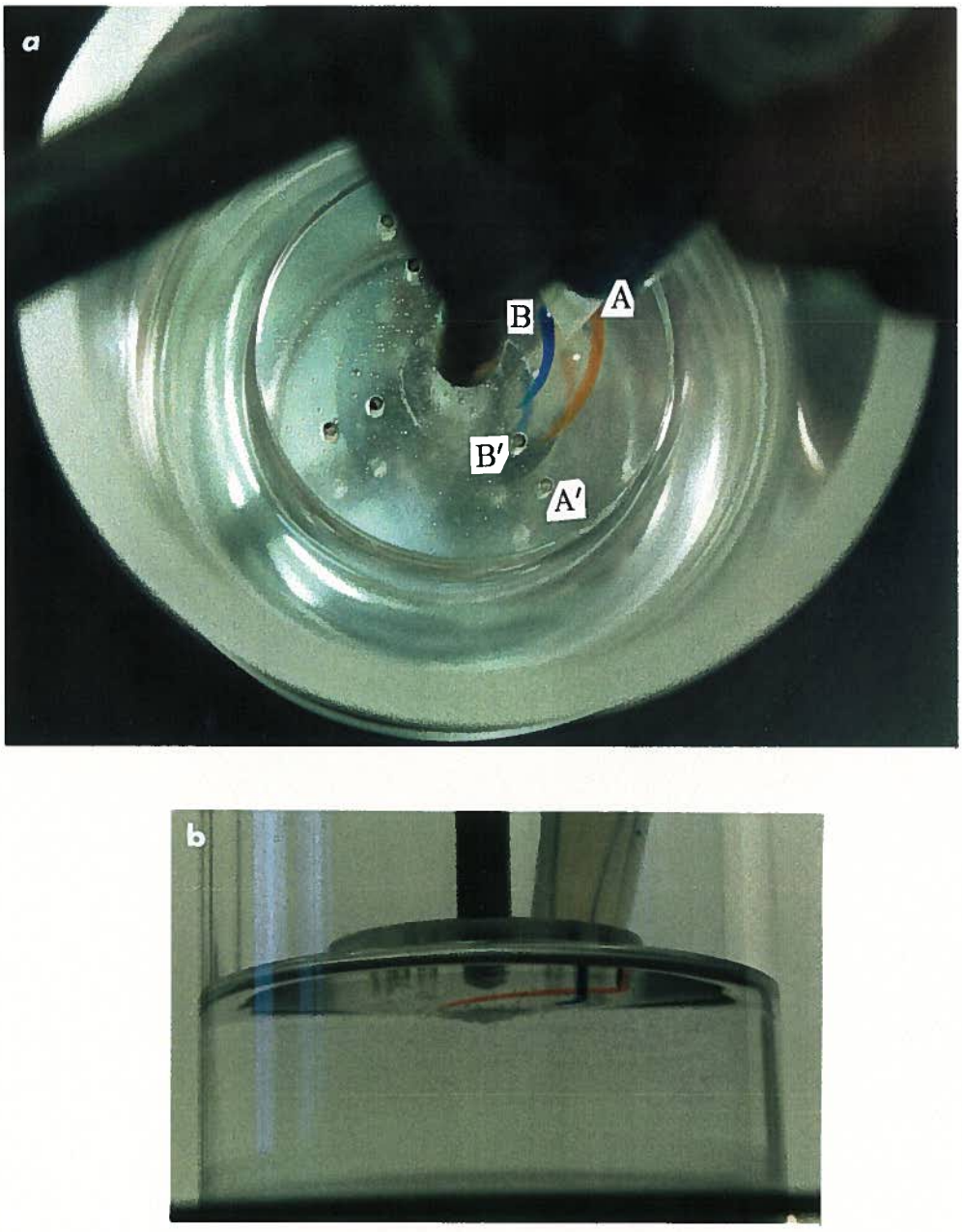

Figure 6.44: Initial dye tracer pattern in the glycerine. a) Top view. b) Side view. Crucible rotated at 45 rpm.

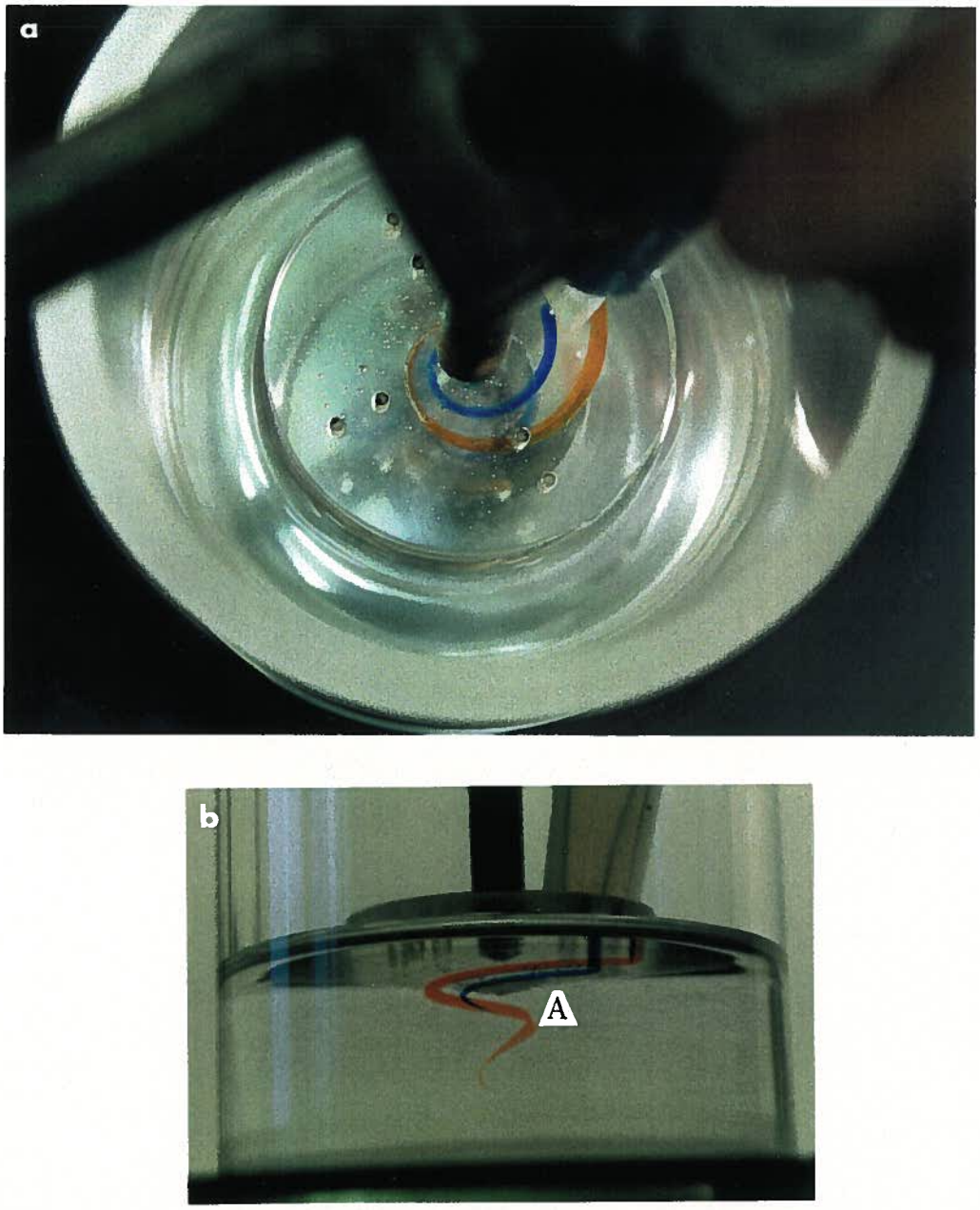

Figure 6.45: Dye tracer pattern in the glycerine when the blue and red tracers reach the centre of the fluid. a) Top view. b) Side view. Crucible rotated at 45 rpm.

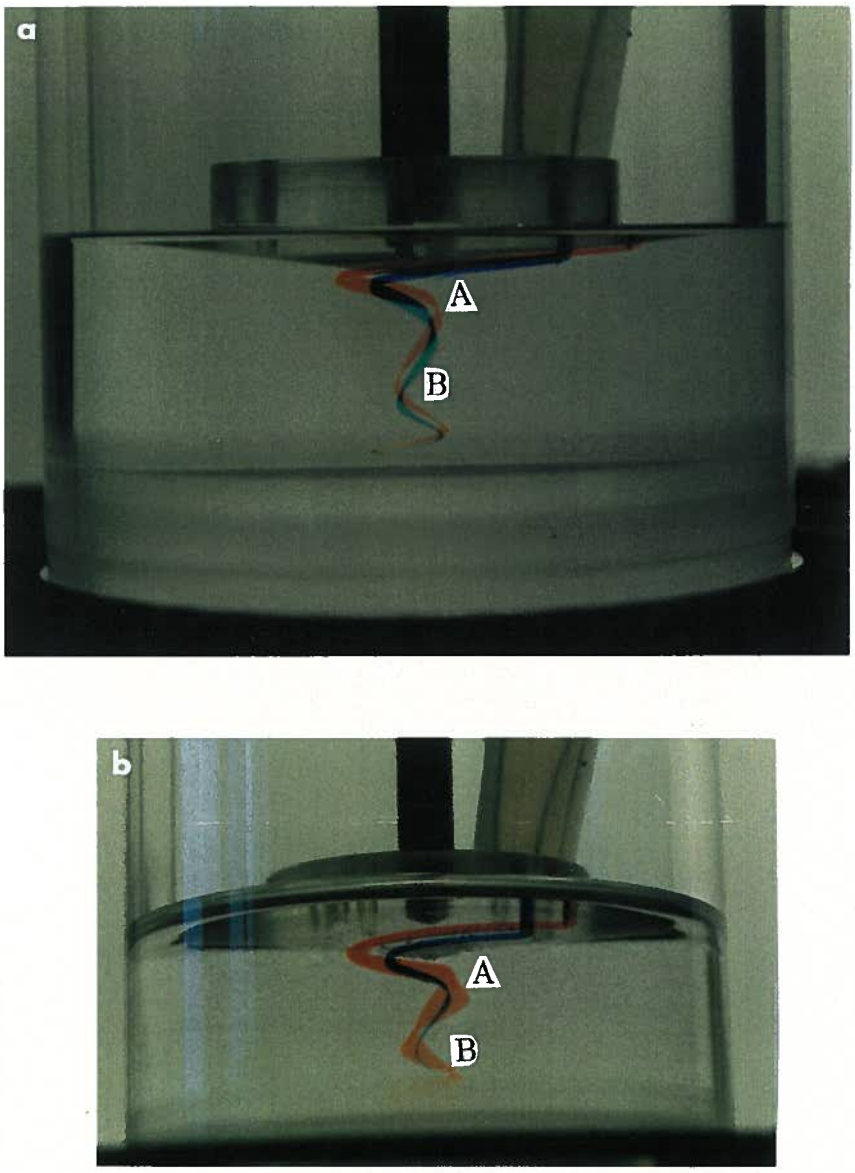

Figure 6.46: Dye tracer pattern in the glycerine when the dye reaches the bottom of the crucible. a) Side view b) View under the crystal. Crucible rotated at 45 rpm.

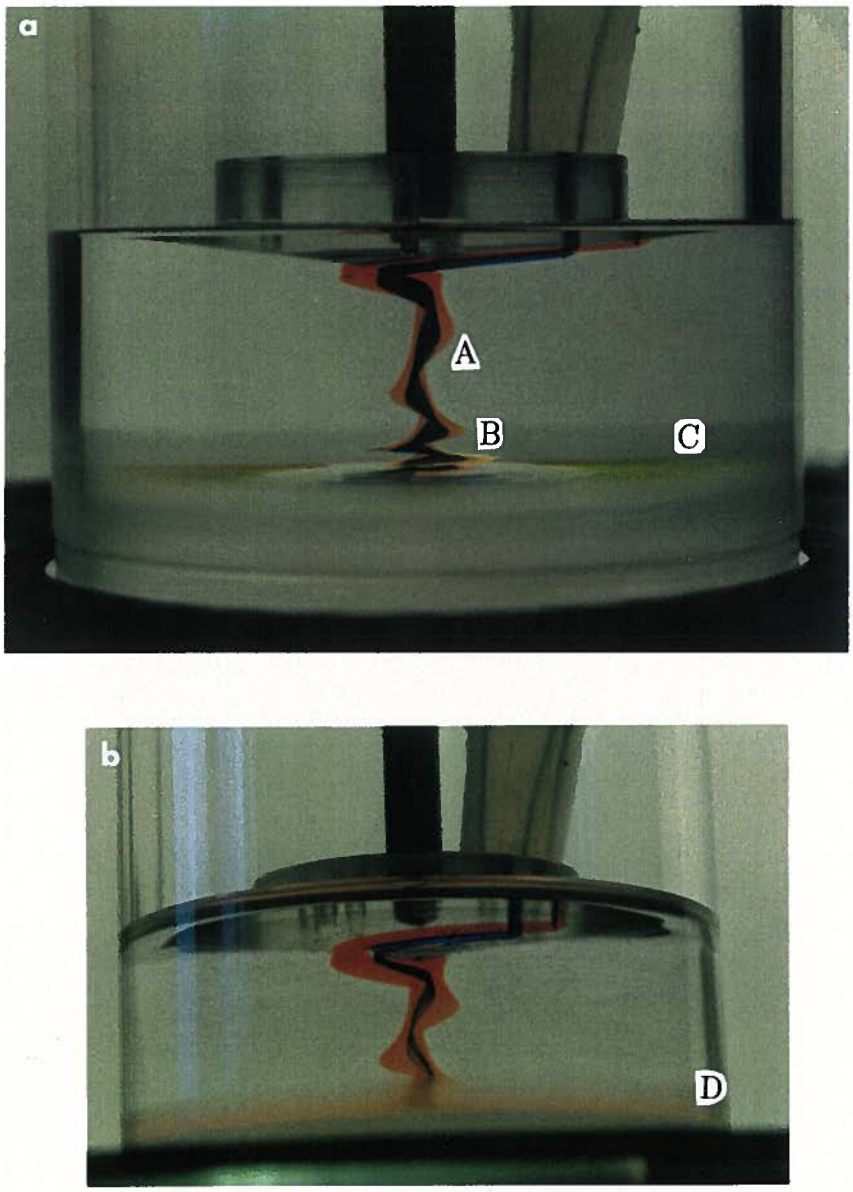

Figure 6.47: Dye tracer pattern near the bottom of the crucible. a) Side view. b) View under the crystal showing the red and blue die moving up the side walls of the crucible. Crucible rotated at 45 rpm.

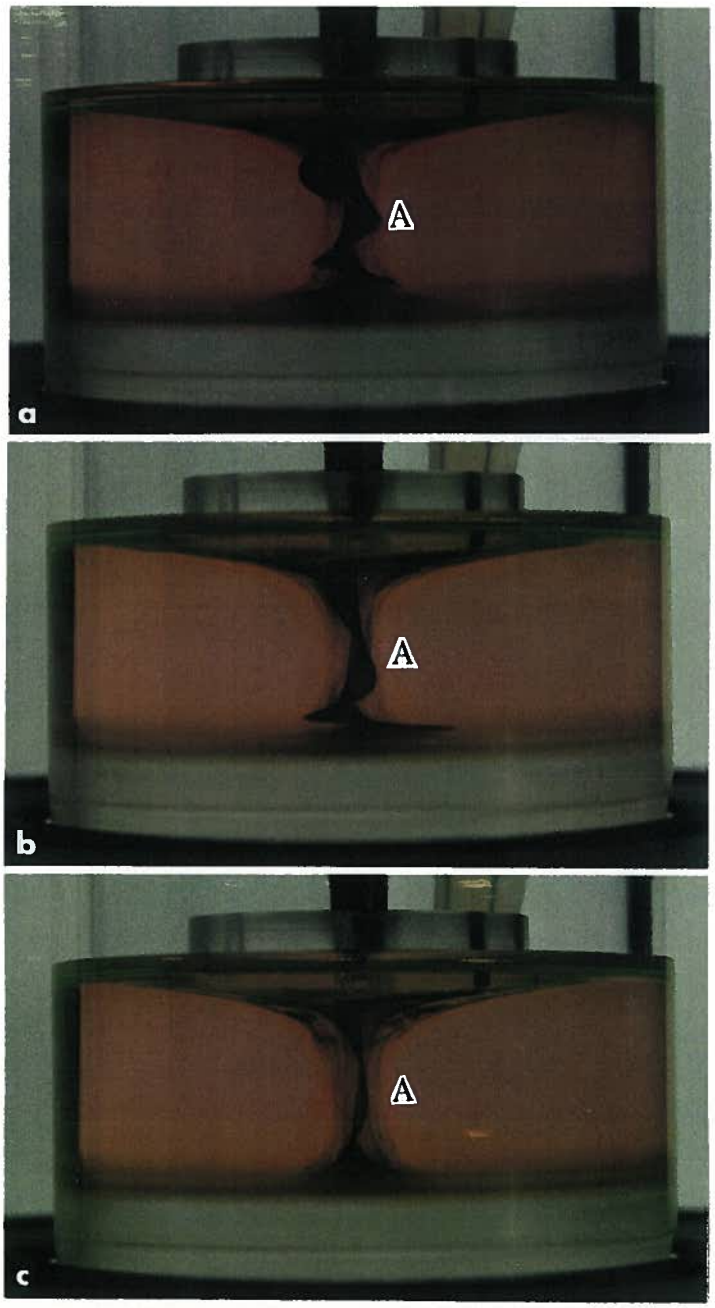

Figure 6.48: Dye tracer pattern at different crucible rotation rates. a) Crucible rotation rate of 45 rpm. b) Transition flow for a crucible rotation rate between 45 and 78 rpm. c) Crucible rotation rate of 78 rpm.

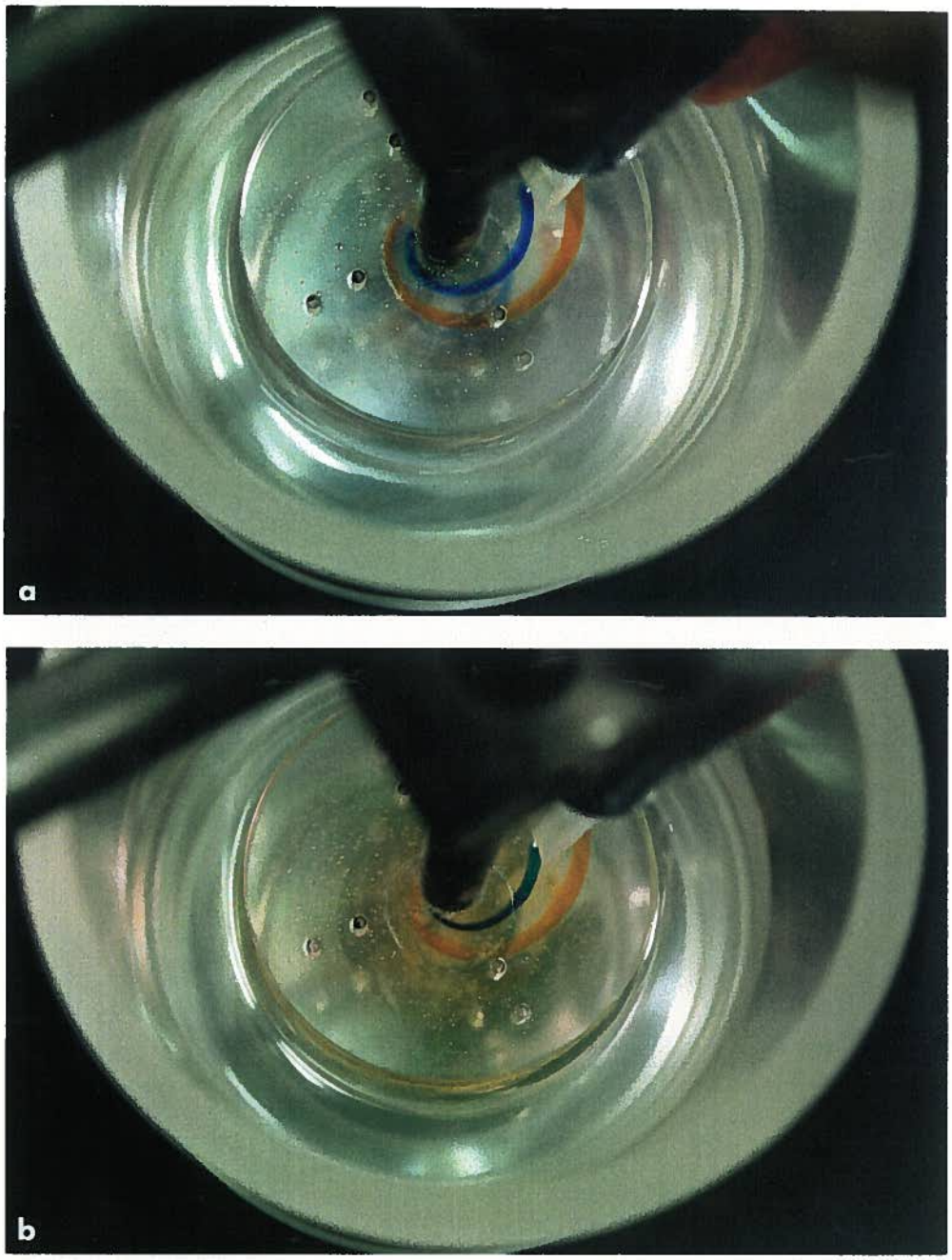

Figure 6.49: Top view of the dye tracer patterns at different crucible rotation rates. a) Crucible rotation rate of 45 rpm. b) Crucible rotation rate of 78 rpm.

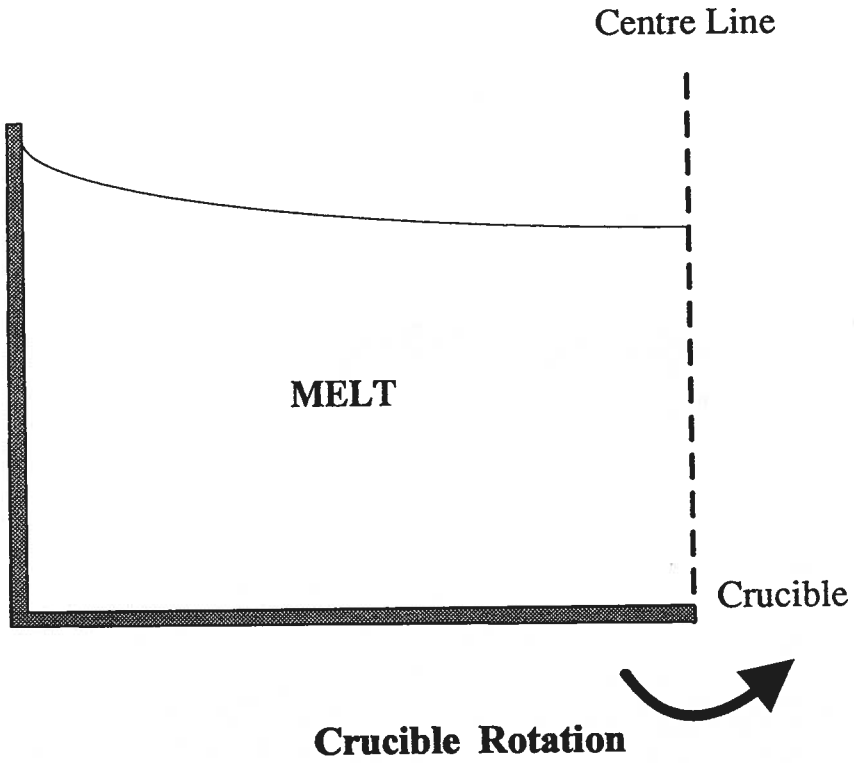

Figure 6.50: Interface curvature due to solid body rotation.

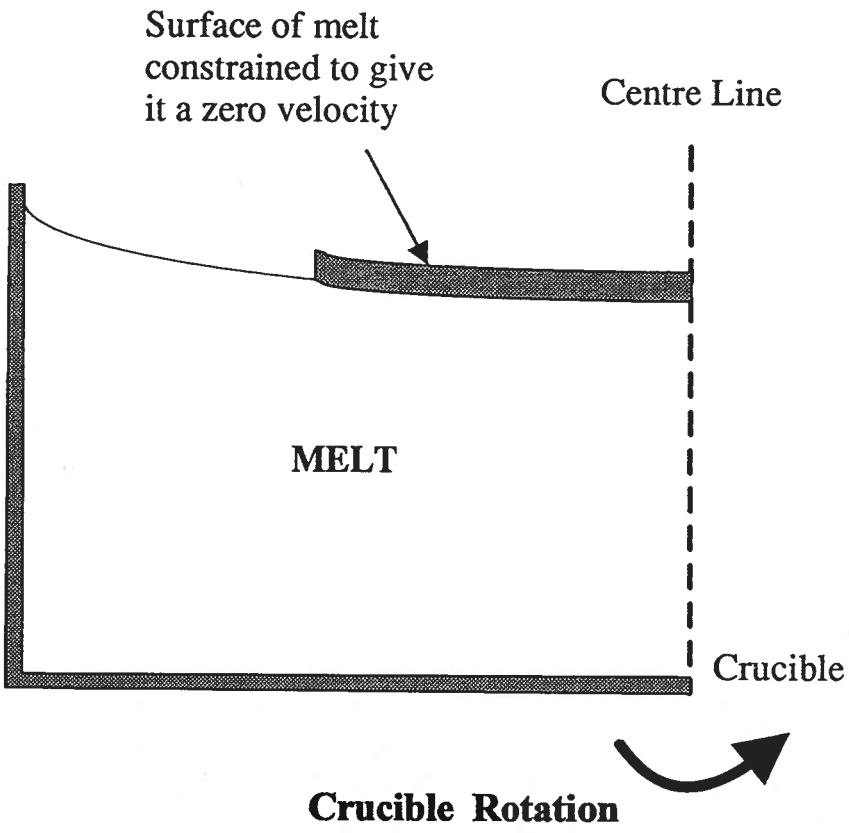

Figure 6.51: Crucible with portion of the upper surface constrained to zero.

Chapter 7

Temperature Measurements

Temperature measurements were conducted to establish the boundary conditions in the model, to investigate the effect of crucible rotation on the thermal fields, to compare the temperature fields measured with those predicted by the model and to examine the thermal gradients in the crystal as it is cools to room temperature.

7.1 Initial Temperature Measurements with No Crucible Rotation

The melt was a clear amber color. No convective cells were observed at the liquid surface. Temperature as a function of axial position at three radial locations; the center (r = 0 cm), the mid position (r = 1.6 cm) and near the wall (r = 3.2 cm) of the crucible are shown in Figure 7.52

The temperature oscillations at r = 1.6 and 3.2 cm result from the furnace heaters turning on and off and are not significant. The oscillations were suppressed by employing electrical shielding on the thermocouples. The melt temperatures were assumed to be the lowest temperature recorded in the oscillations. The melt temperatures range from 760°C at the top of the melt to 868°C at the bottom.

The temperature measurements were conducted with the furnace set approximately 145°C (Δ T) higher than the conventional setting for crystal growth. It is assumed that the values of the measured temperatures change proportionally with the furnace setting. Thus the boundary conditions for the mathematical model were obtained by decreasing

the measured temperatures by the appropriate ΔT.

$$\text{T(boundary condition)} = \text{T(measured)} - \Delta\text{T}$$

The temperatures used as boundary conditions are assumed to be the temperature of the inside walls of the platinum crucible which do not change. The temperature boundary conditions used in the sensitivity analysis are given in Figure 7.53.

7.2 Temperature Measurements With and Without Crucible Rotation

Temperature measurements were conducted to examine the influence of crucible rotation on the thermal fields for crucible diameters of 6.6 and 8.8 cm. Rotation rates of 0, 15, 20, 25 and 30 rpm were used in the 6.6 cm diameter crucible. Measurements were conducted at crucible rotation rates of 0, 10, 20 and 30 rpm in the 8.8 cm diameter crucible. Table 7.8 gives the concentration of the melts that were investigated. In all cases the outside of the crucible was thermally insulated. The bottom of the small crucible was deformed due to the expansion coefficient of LBO/MoO_3 being much larger than that of platinum. The bottom of the crucible was no longer flat, the center was 0.5 cm lower than the side. Thermal boundary conditions were determined from the 0 rpm crucible rotation data. The measured thermal fields for different rotation rates were compared to the model predictions.

7.2.1 Boundary Temperature Results

Small Crucible (6.6 cm diameter)

Temperature measurements 0.2 cm from the vertical crucible wall, in a melt containing 45.5 Wt% MoO_3, are shown in Figure 7.54. The dashed curve are the measurements without a simulated crystal present, and shows that the temperature decreases from 818°C.

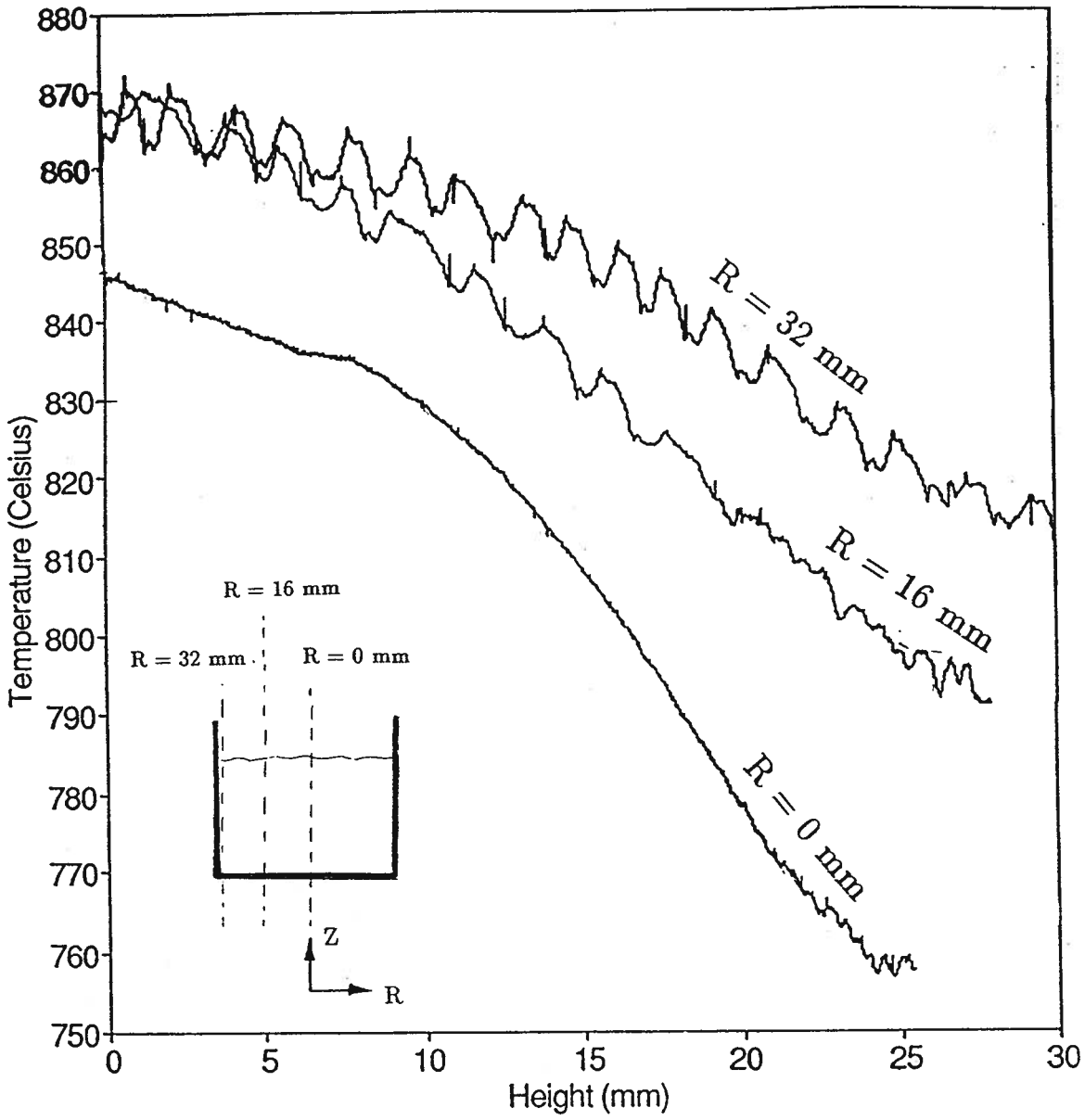

Figure 7.52: Temperature variation with axial position in a 55 Wt% MoO_3 solution. The three radial locations are r = 0 mm, r = 16 mm, and r = 32 mm. There is no crucible rotation during the temperature measurements. Crucible diameter is 6.6 cm.

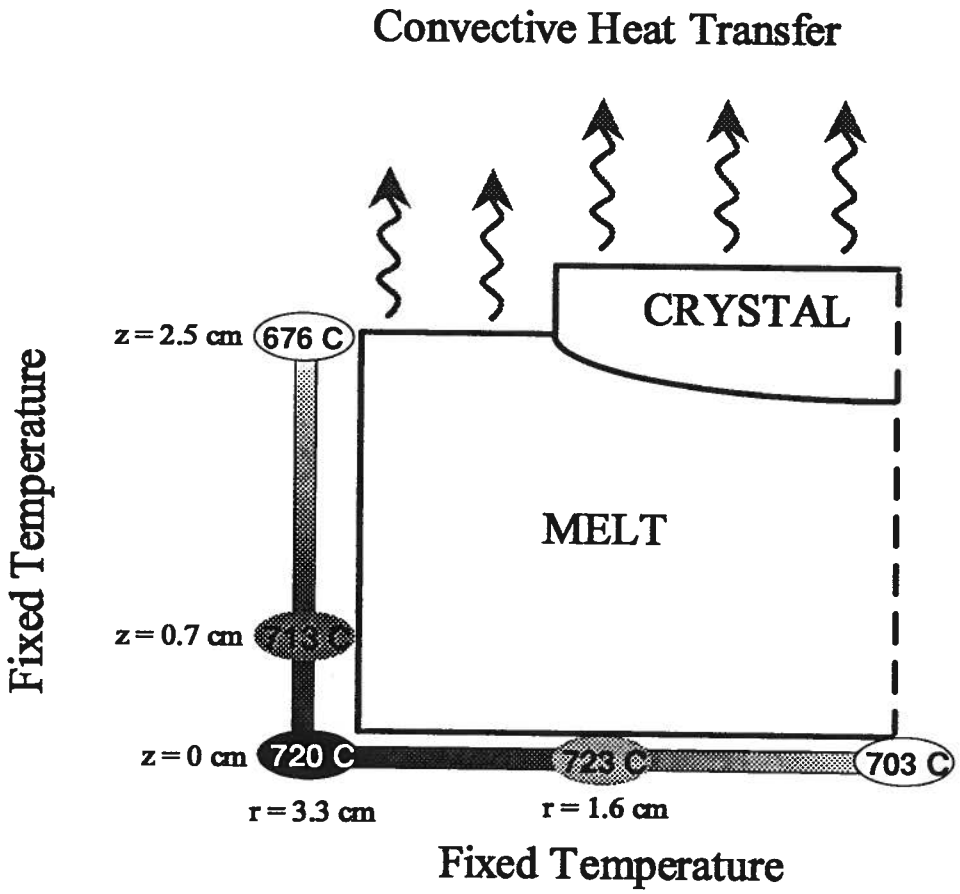

Figure 7.53: Temperature boundary conditions used in the fluid flow model for the sensitivity analysis and the examination of the operating parameters. Crucible diameter is 6.6 cm.

Crucible Diameter	Weight Percent						
	Charge Concentration		Measured		Equivalent		Normalized
	MoO_3	LBO	Mo	Li	MoO_3	LBO	MoO_3
6.6 cm	50.05	49.95	29.00	3.03	43.51	52.11	**45.50**
8.8 cm	44.56	55.44	33.30	3.13	48.46	53.83	**47.38**

Table 7.8: MoO_3 and LBO concentrations in the melt that were used for the temperature measurements with and without crucible rotation.

0.47 cm from the bottom, to 805°C at 2.45 cm. With a simulated crystal positioned in the melt the melt temperature increased at the wall by approximately 12°C. The radial temperature distribution in the melt 0.47 cm from the bottom of the crucible, is shown in Figure 7.55. The temperature remains essentially constant at 807°C for 1 cm from the centre then increases progressively to 818°C at 0.2 cm from the crucible wall.

In obtaining the temperature measurements shown in Figure 7.55 two thermocouples were used, one for r < 1.6 cm and the second for r > 1.6 cm. The small increase in temperature at A may be associated with a slight difference in behavior of the two thermocouples. The repeatability of the temperature measurements were determined by making multiple measurements at points B and C. The difference in temperature was less than 1°C. Adding the simulated crystal increases the melt temperature, but does not significantly change the temperature gradient. Following this observation, the boundary temperatures were determined from the data without a crystal by adding 12°C to account for the temperature rise when a crystal is added, and extrapolating the measurements to the outside surface of the platinum crucible. The resultant temperature boundary conditions are given in Figure 7.56. Using these boundary conditions, temperature profiles in the melt were calculated, using the mathematical model, and compared to the experimental measurements with no crucible rotation and with a simulated crystal. The

boundary conditions were then adjusted, and the calculations repeated until the calculated temperatures fitted the experimental values. The boundary conditions determined in this manner were then used to calculate the thermal field with crystal rotation and the results were compared to the corresponding measurements.

Large Crucible (8.8 cm diameter)

The melt temperature 0.2 cm from the wall of the crucible is shown in Figure 7.57. The melt temperature, without the crystal, is essentially constant at 824.5°C between at 0.36 and 2 cm from the bottom of the crucible. Above 2 cm the temperature progressively decreases reaching 807.3°C at 3.15 cm. Introducing the simulated crystal increases the melt temperature by approximately 5°C. The radial temperature distribution 0.36 cm from the bottom of the crucible is shown in Figure 7.58. The temperature varies from 806°C at 0.17 cm from the center of the crucible to 824°C at 0.2 cm from the wall of the crucible. The gradient does not appear to dramatically change with the insertion of the simulated crystal. The temperature boundary conditions used in the mathematical model are determined using the procedure described in the previous section. Figure 7.59 shows the temperature boundary conditions used in the model calculations.

7.2.2 Melt Temperature Results

Small Crucible (6.6 cm diameter)

Melt temperatures at crucible rotation rates in the range 0 and 30 rpm, with the simulated crystal present, were determined. The axial temperature profile 1 cm from the centre of the crucible is given in Figure 7.60. With 0 rpm crucible rotation, the temperature decreases with distance from the bottom, the curve being concave upward. With 15 rpm crucible rotation, the temperature at 0.4 cm from the bottom decreases and above

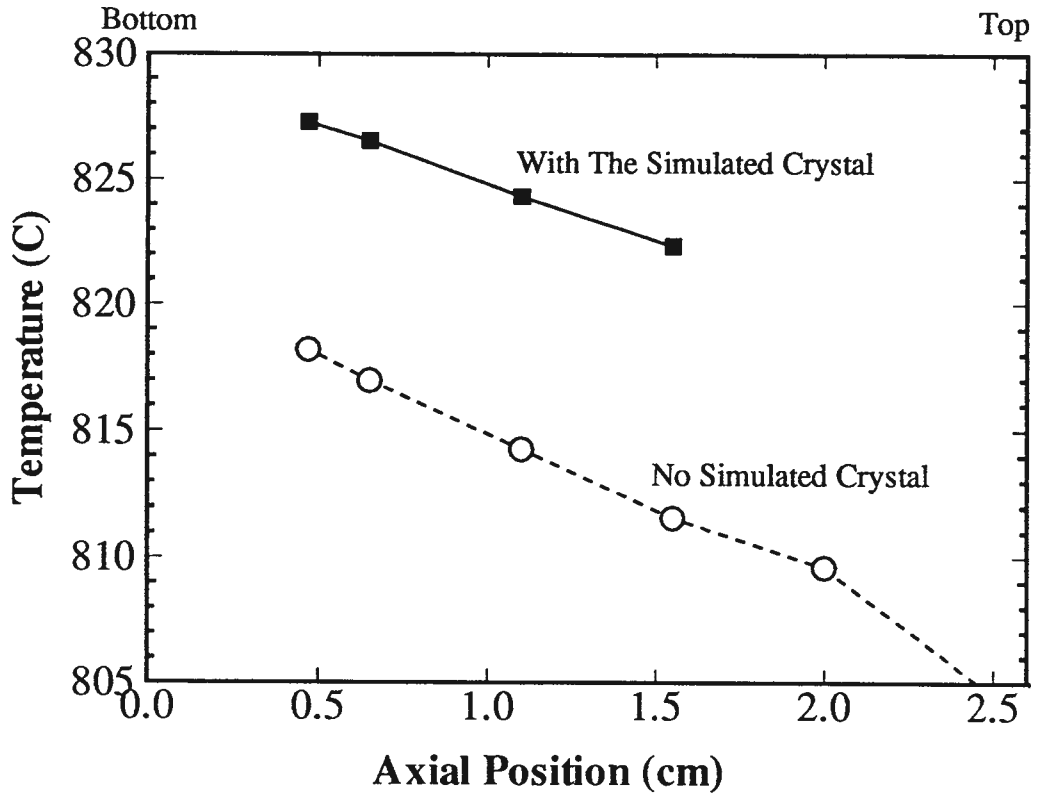

Figure 7.54: Melt temperature 0.2 cm from the crucible wall with and without the simulated crystal. Crucible diameter is 6.6 cm.

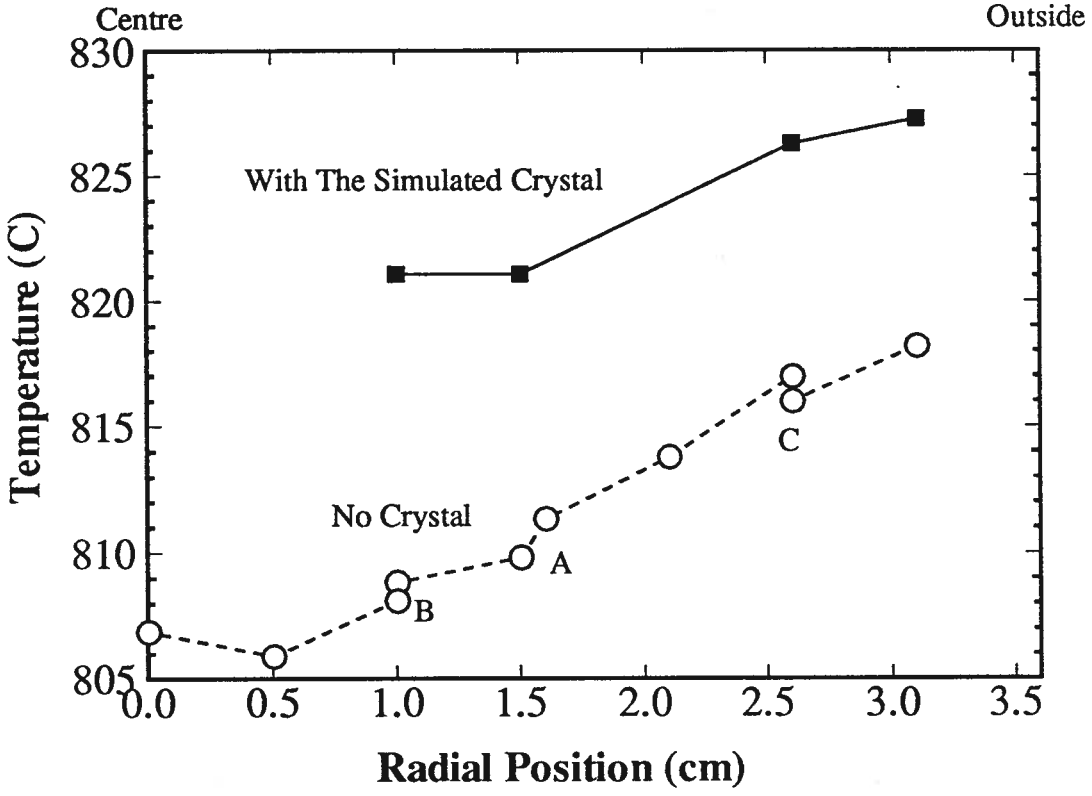

Figure 7.55: Melt temperature 0.47 from the crucible bottom with and without the simulated crystal. Crucible diameter is 6.6 cm.

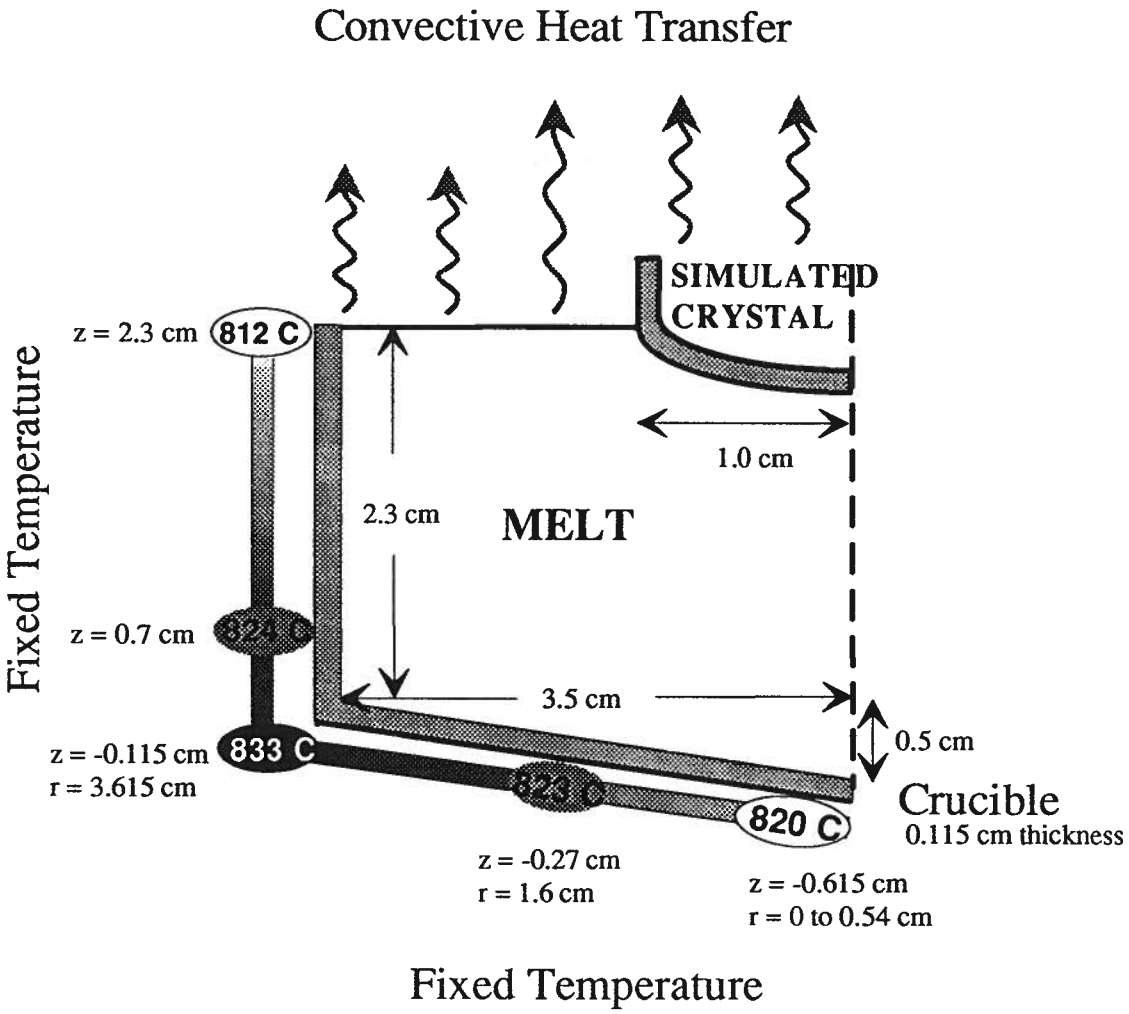

Figure 7.56: Temperature boundary conditions used in the mathematical model of melt with the simulated crystal. Crucible diameter is 6.6 cm.

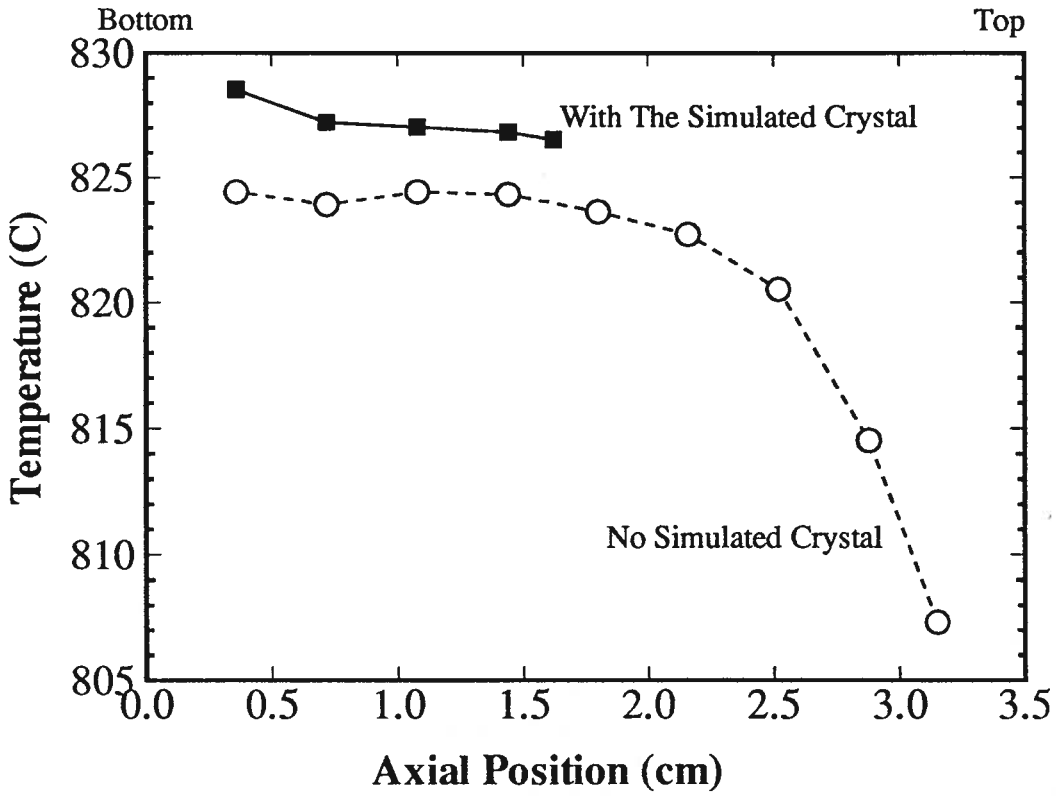

Figure 7.57: Melt temperature 0.2 cm from the crucible wall with and without the simulated crystal. Crucible diameter is 8.8 cm.

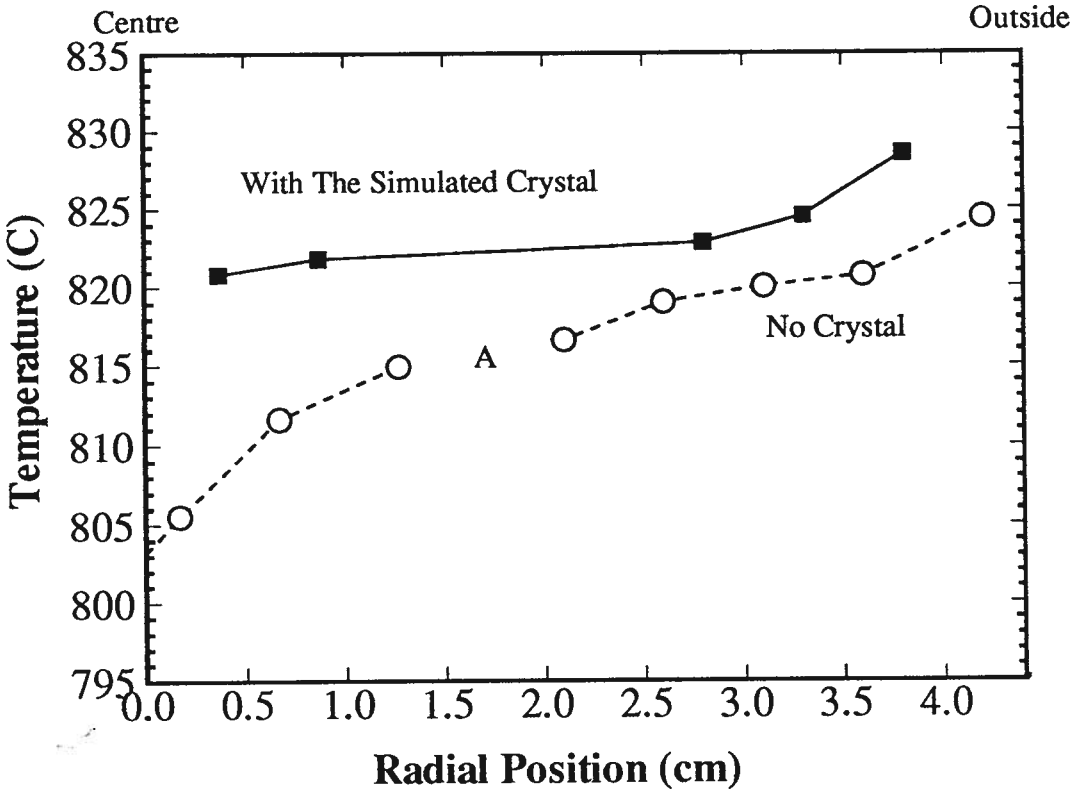

Figure 7.58: Melt temperature 0.36 from the crucible bottom with and without the simulated crystal. Crucible diameter is 8.8 cm.

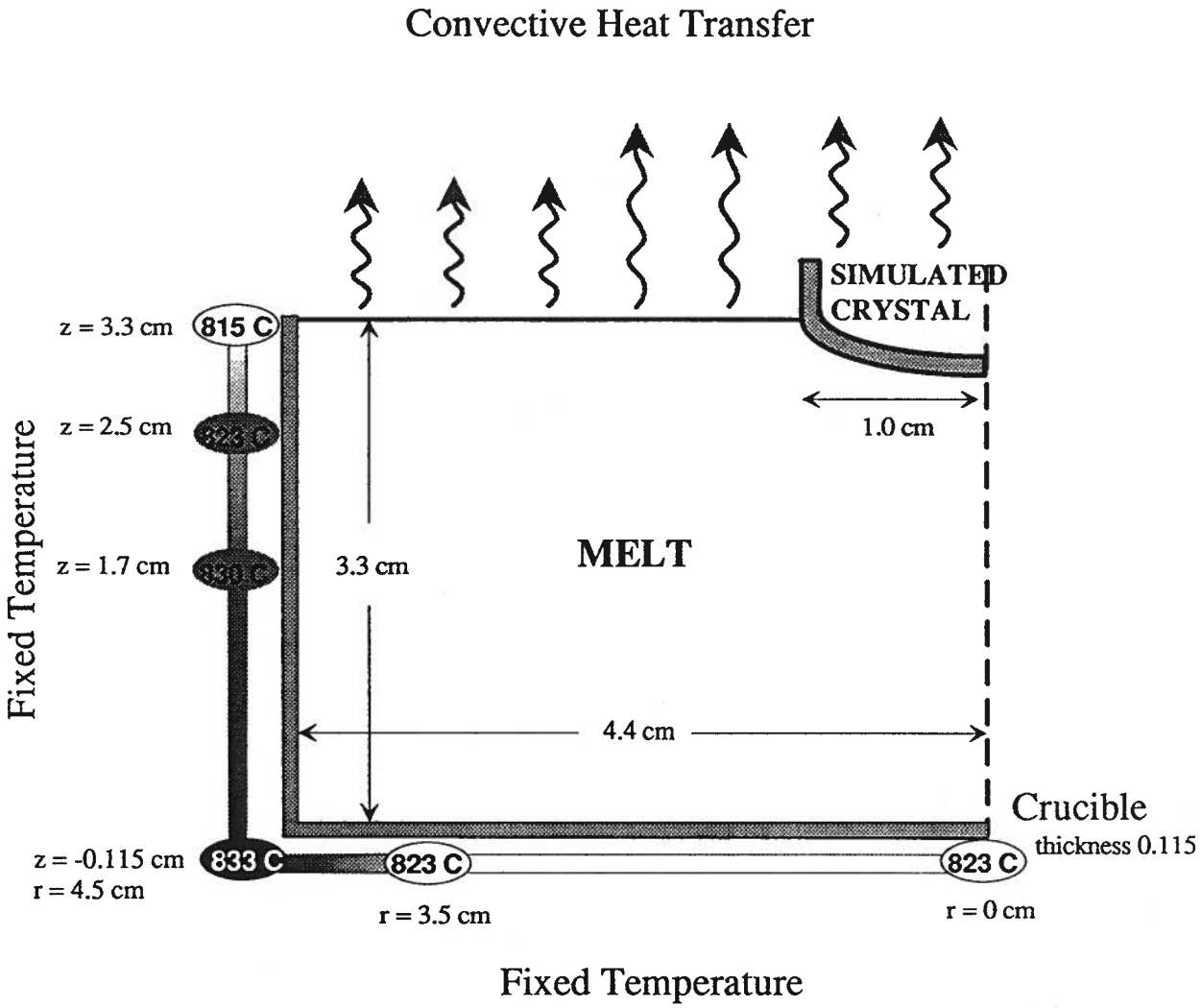

Figure 7.59: Temperature boundary conditions used in the mathematical model of melt with the simulated crystal. Crucible diameter is 8.8 cm.

0.5 cm increases. The shape of the curve changes to concave downward. Increasing the crucible rotation above 15 rpm progressively raises the melt temperature with the axial temperature distribution essentially remaining the same. The largest temperature increase occurs in the 25 to 30 rpm interval.

The corresponding axial temperature distribution at a radial distance of 1.5 cm are given in Figure 7.61. In this case at 0 rpm the temperature is observed to decrease linearly with distance from the bottom. With crucible rotation, the temperature of the melt progressively increases, and the temperature distribution curve is concave downward, as before. The axial temperature distribution at radial distances of 2.6 cm and 3.1 cm from the centre are given in Figure 7.62 and 7.63. At both distances at 0 rpm, the temperatures are higher than at r = 1.5 cm, and decrease linearly with distance from the bottom of the crucible. With rotation rates between 15 and 25 the temperature distribution becomes concave upward. The axial temperature profile becomes flat at a rotation rate of 30 rpm.

The movement of the fluid due to crucible rotation has been qualitatively shown and described in Chapter 6. Crucible rotation results in the movement of hot fluid up at the crucible wall and cold fluid down under the crystal. The movement of hot and cold fluid causes the liquid isotherms to become more concave. The change in the liquid isotherm shape with the fluid motion is shown schematically in Figure 7.64. The axial temperature profiles become flat at high crucible rotation rates The experimental results shown in Figures 7.60 through 7.63 are in agreement with the physical model (qualitative) analysis.

Large Crucible (8.8 cm diameter)

Melt temperatures at crucible rotation rates between 0 and 30 rpm, with the simulated crystal present, were determined. The axial temperature profile at 0.4 cm from the

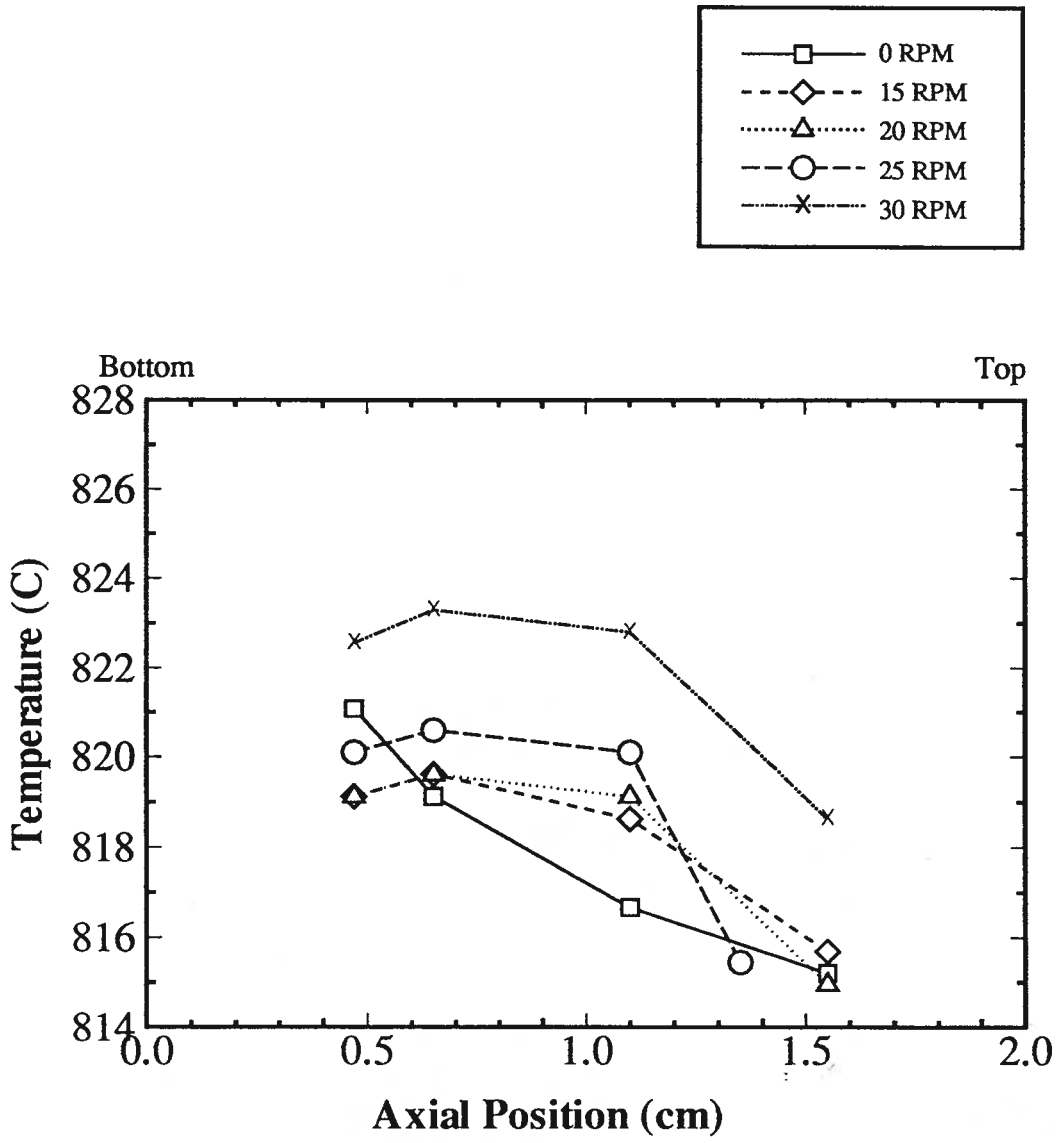

Figure 7.60: Temperature distribution at r = 1.0 cm for crucible rotations of 0, 15, 20, 25 and 30 rpm. Crucible diameter is 6.6 cm. Simulated crystal present.

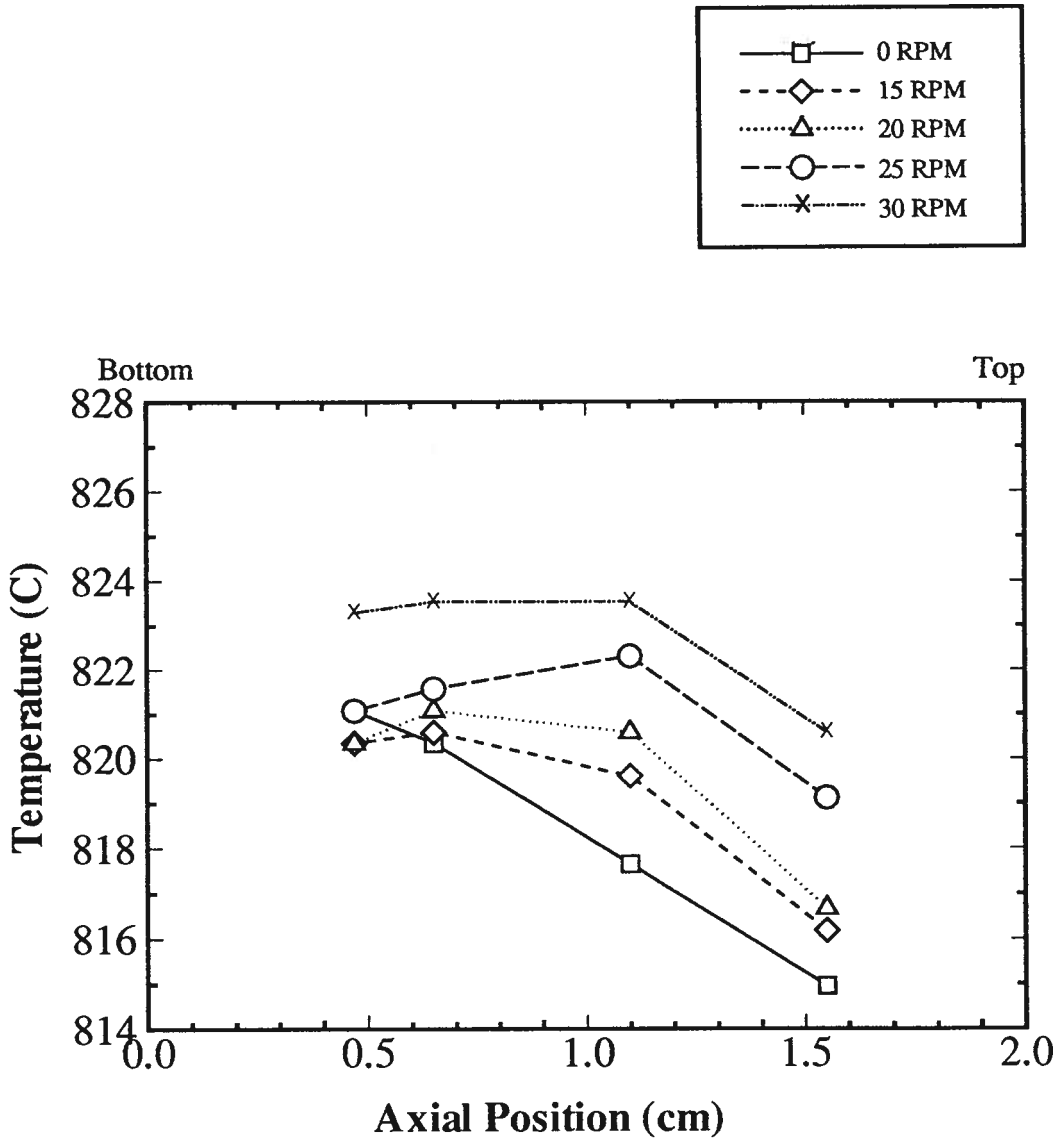

Figure 7.61: Temperature distribution at r = 1.5 cm for crucible rotations of 0, 15, 20, 25 and 30 rpm. Crucible diameter is 6.6 cm. Simulated crystal present.

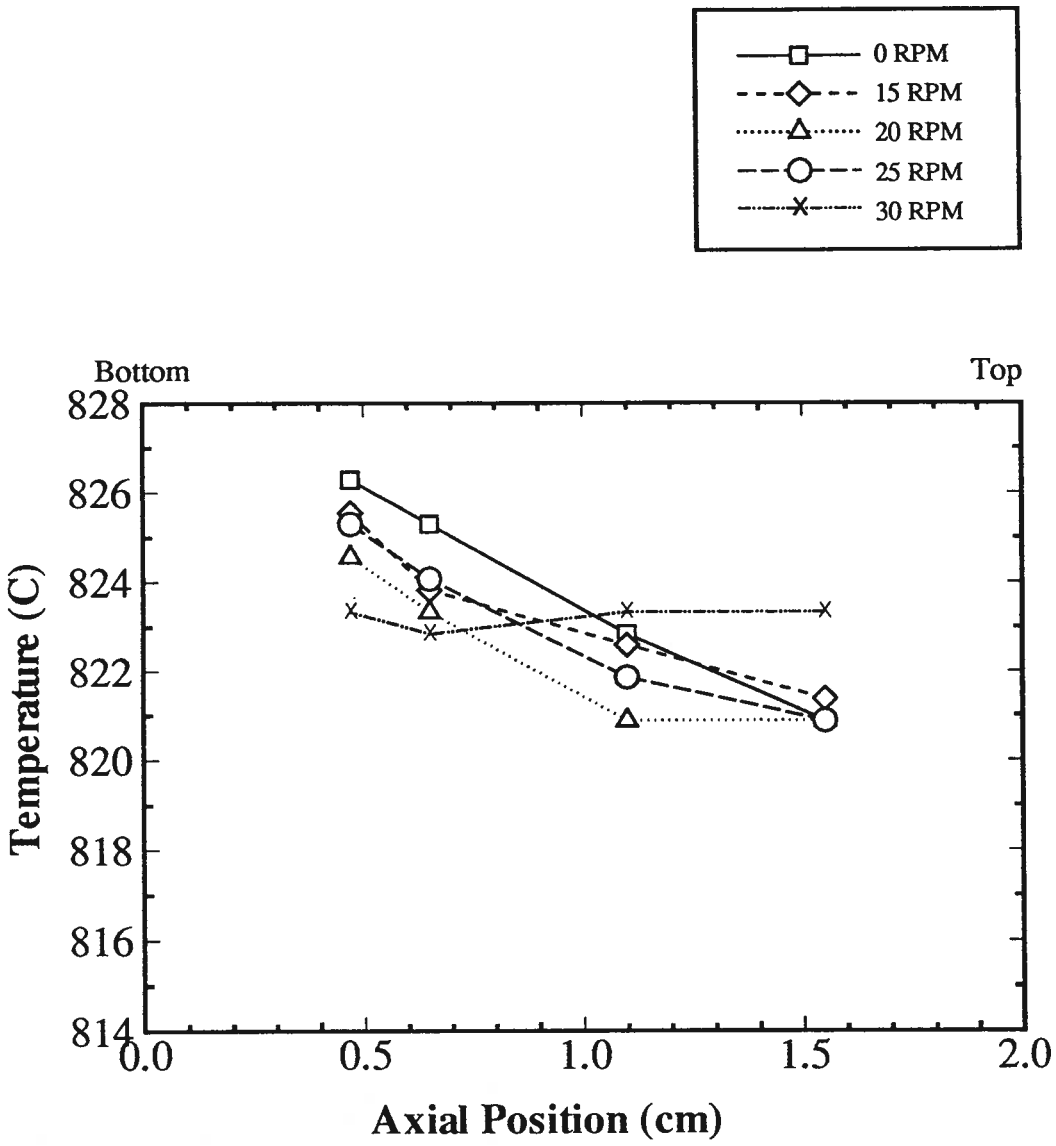

Figure 7.62: Temperature distribution at r = 2.6 cm for crucible rotations of 0, 15, 20, 25 and 30 rpm. Crucible diameter is 6.6 cm. Simulated crystal present.

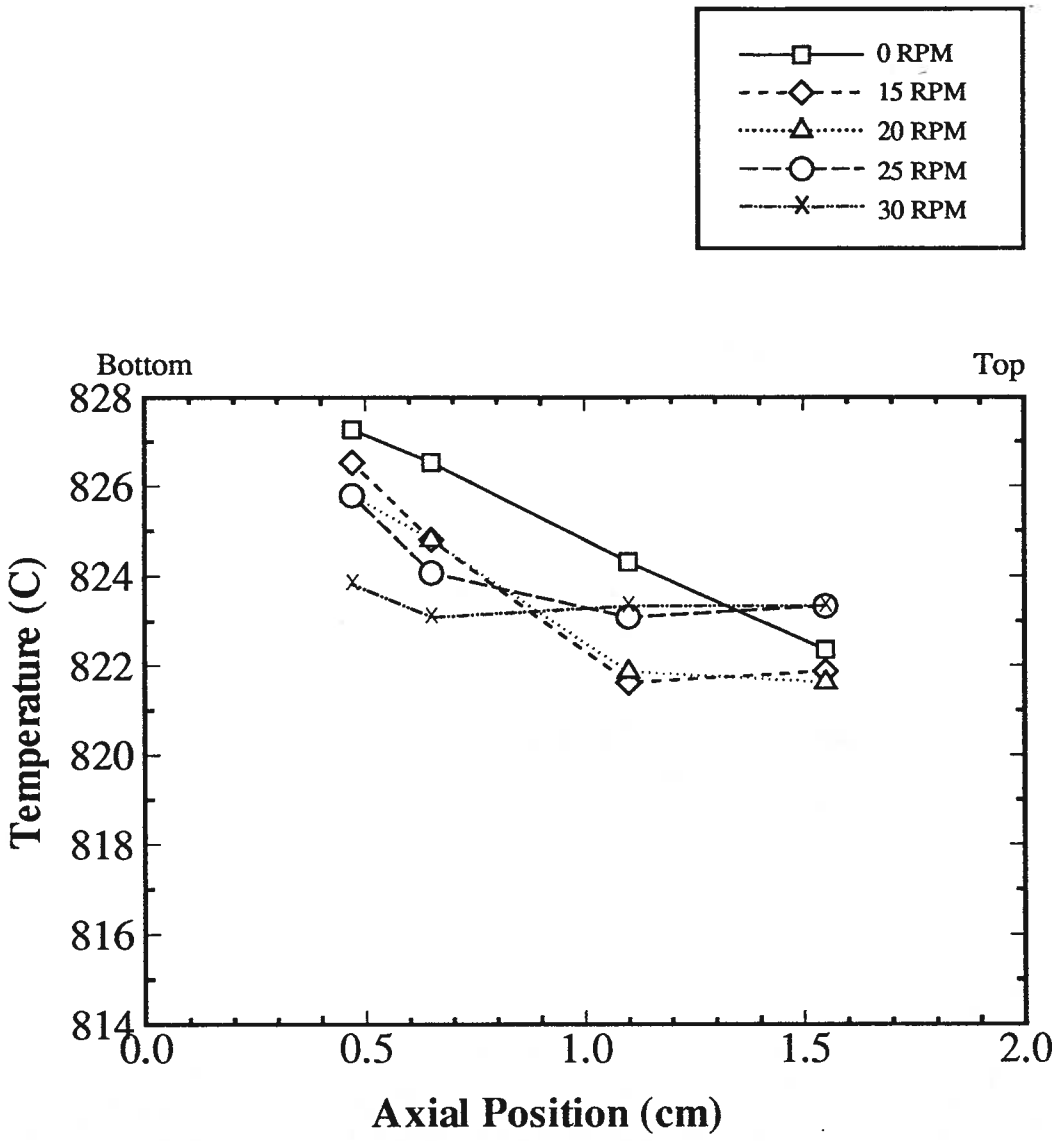

Figure 7.63: Temperature distribution at r = 3.1 cm for crucible rotations of 0, 15, 20, 25 and 30 rpm. Crucible diameter is 6.6 cm. Simulated crystal present.

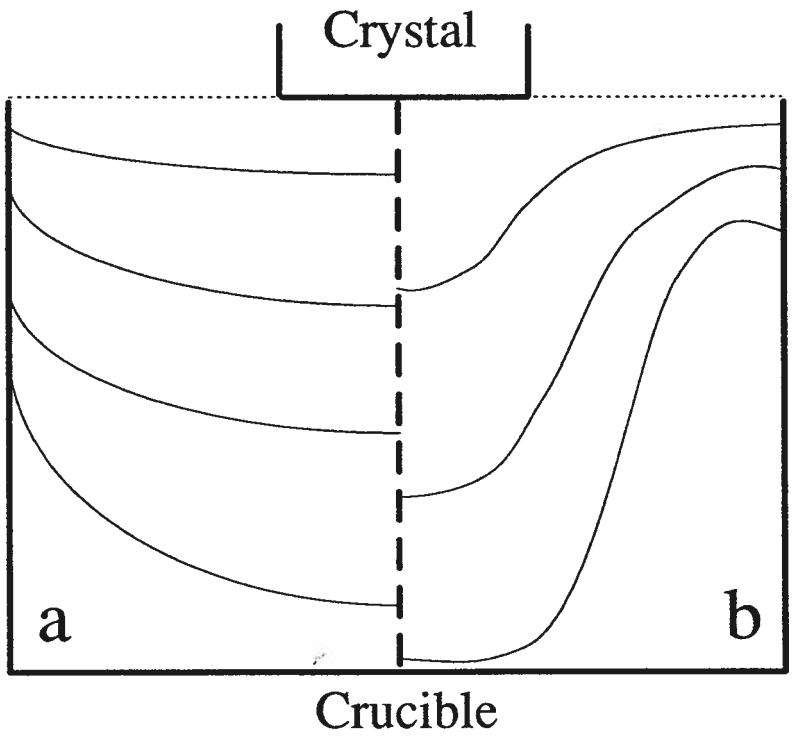

Figure 7.64: Change in liquid isotherms with crucible rotation. (a) No crucible rotation. (b) Large crucible rotation.

centre of the crucible is given in Figure 7.65. The melt temperature profile with no crucible rotation is concave downward. With rotation, the concavity remains the same and the average melt temperature increases. The change in average melt temperature with crucible rotation is large between 0 and 20 rpm and small between 20 and 30 rpm.

The axial temperature profile at r = 0.9 cm with no crucible rotation, Figure 7.66, is slightly concave downward. A rotation rate of 10 rpm causes the melt temperature to increase but the axial temperature profile remains concave upward. Higher rotation rates, 20 and 30 rpm, make the axial temperature profile flat. The axial temperature distribution at radial distances of 2.8 cm and 3.3cm from the centre are given in Figure 7.67 and 7.68. At both distance the temperature profile at 0 rpm is flat. The interface becomes concave downward at a crucible rotation rate of 10 rpm. Between 20 and 30 rpm the axial temperature profiles becomes approximately flat. For all of the previous temperature profiles the largest change in melt temperature with crucible rotation rate occurs between 0 and 20 rpm. Figure 7.69 shows the axial temperature profile at 3.8 cm. The axial temperature profile is flat with no crucible rotation. Rotation rates of 0 to 30 rpm do not change the shape of the temperature profile. The melt temperature changes linearly with crucible rotation speed.

Fluid motion due to crucible rotation has been qualitatively examined in Chapter 6. Crucible rotation causes the movement of hot fluid up at the crucible wall and cold fluid down under the crystal. This type of fluid motion causes the liquid isotherms to become more concave (Figure 7.64). The axial temperature profiles become flat at high crucible rotation rates (Figure 7.64(b)) as shown experimentally in Figures 7.65 and 7.66.

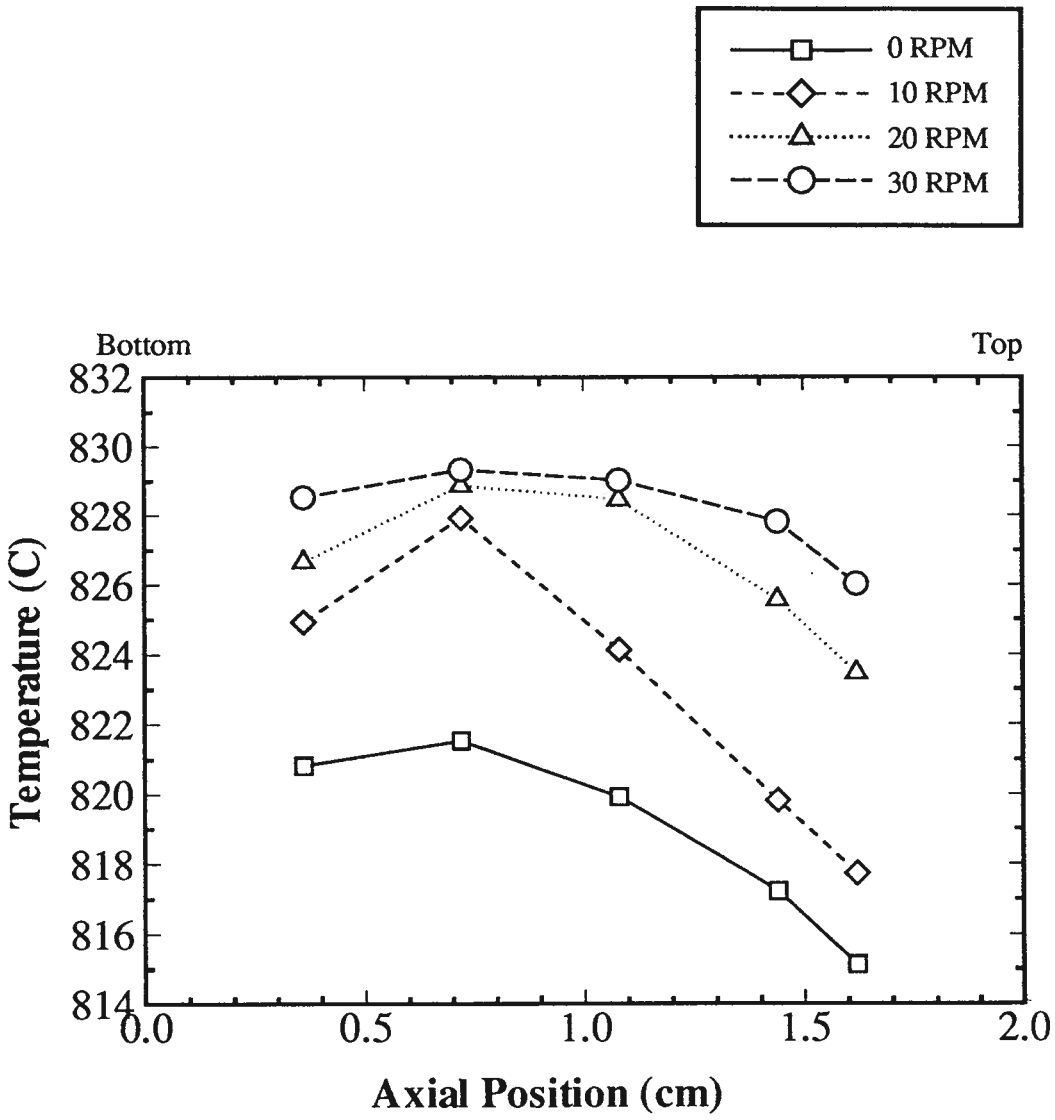

Figure 7.65: Temperature distribution at r = 0.4 cm for crucible rotations of 0, 10, 20 and 30 rpm. Crucible diameter is 8.8 cm. Simulated crystal present.

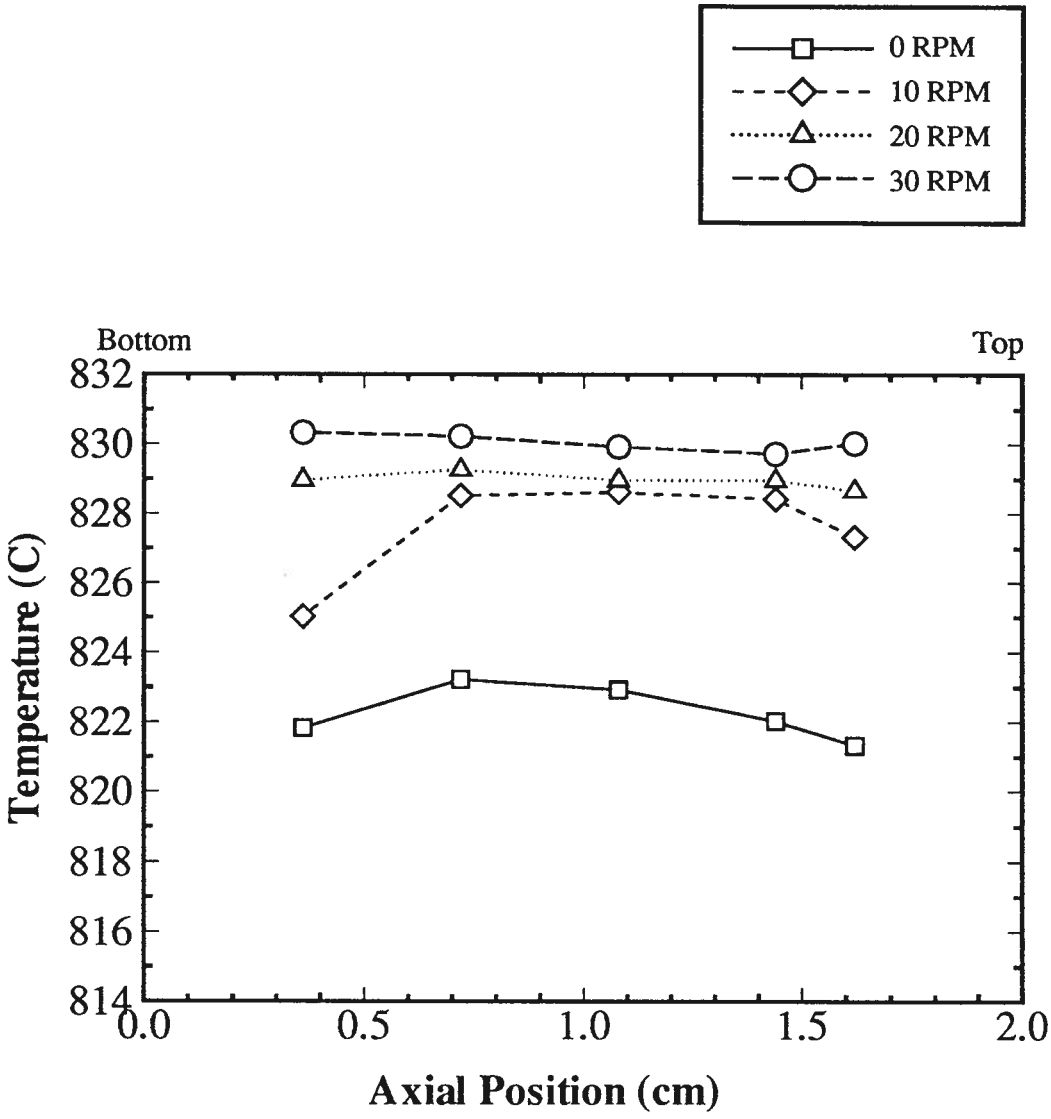

Figure 7.66: Temperature distribution at r = 0.9 cm for crucible rotations of 0, 10, 20 and 30 rpm. Crucible diameter is 8.8 cm. Simulated crystal present.

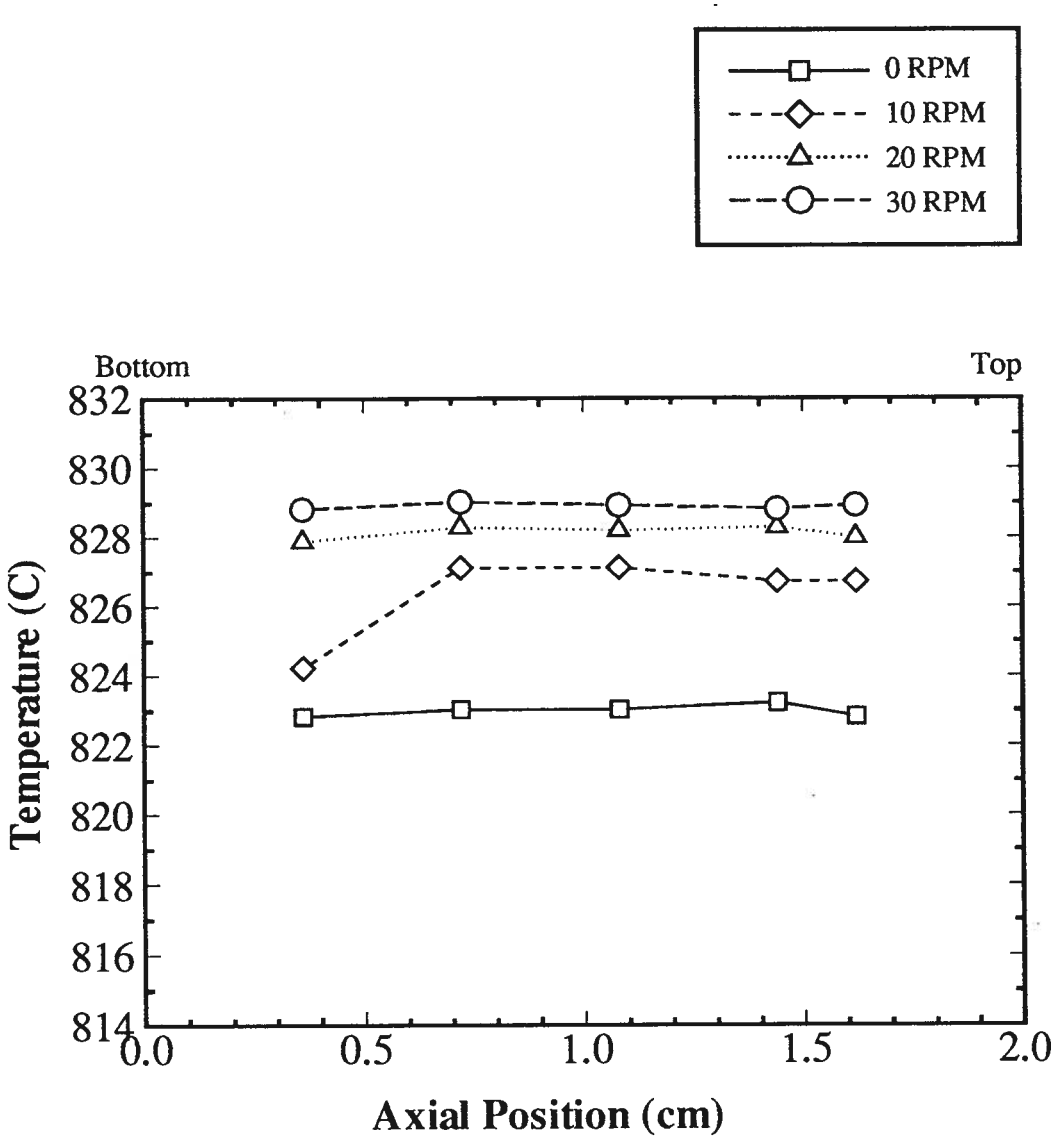

Figure 7.67: Temperature distribution at r = 2.8 cm for crucible rotations of 0, 10, 20 and 30 rpm. Crucible diameter is 8.8 cm. Simulated crystal present.

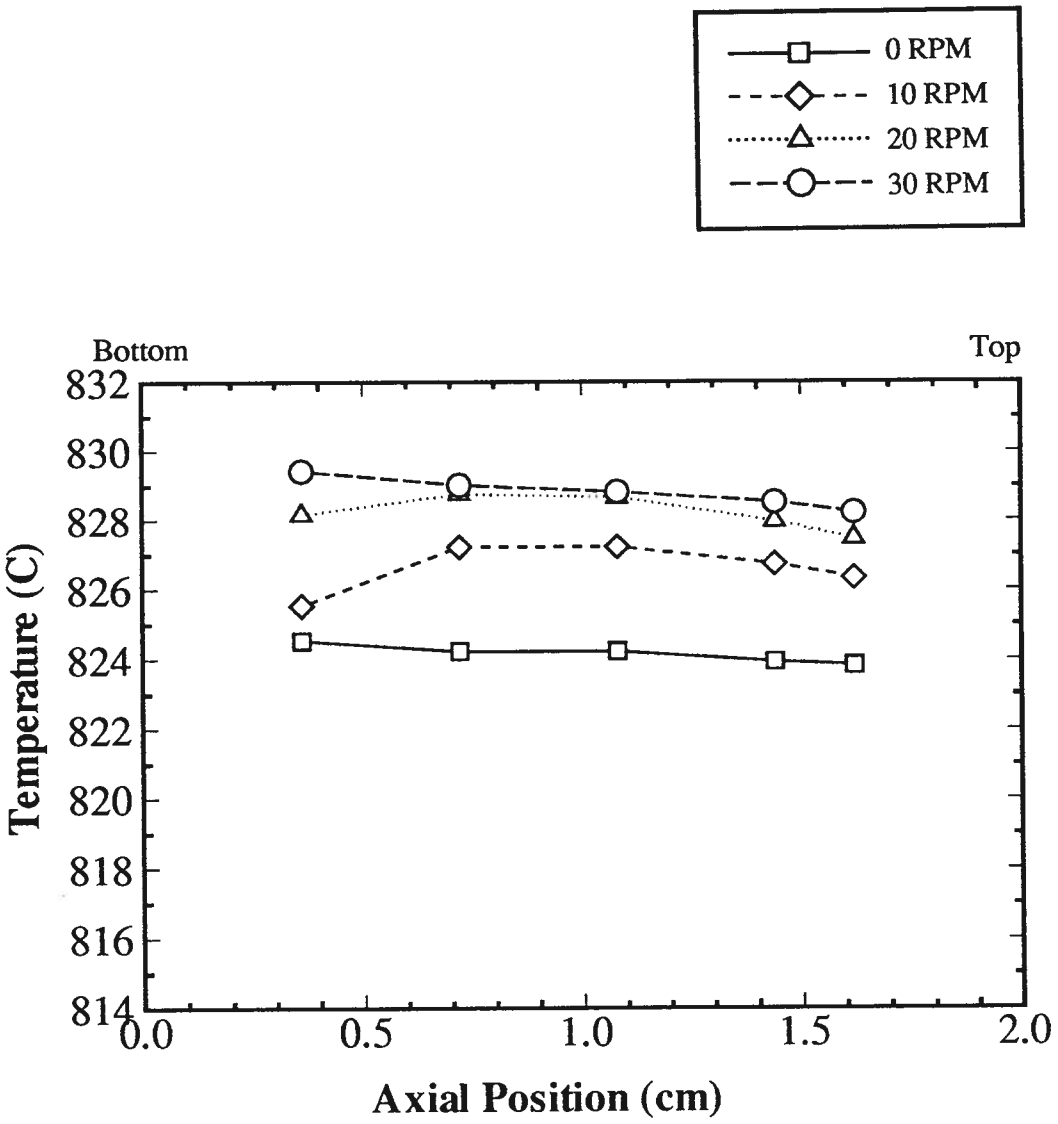

Figure 7.68: Temperature distribution at r = 3.3 cm for crucible rotations of 0, 10, 20 and 30 rpm. Crucible diameter is 8.8 cm. Simulated crystal present.

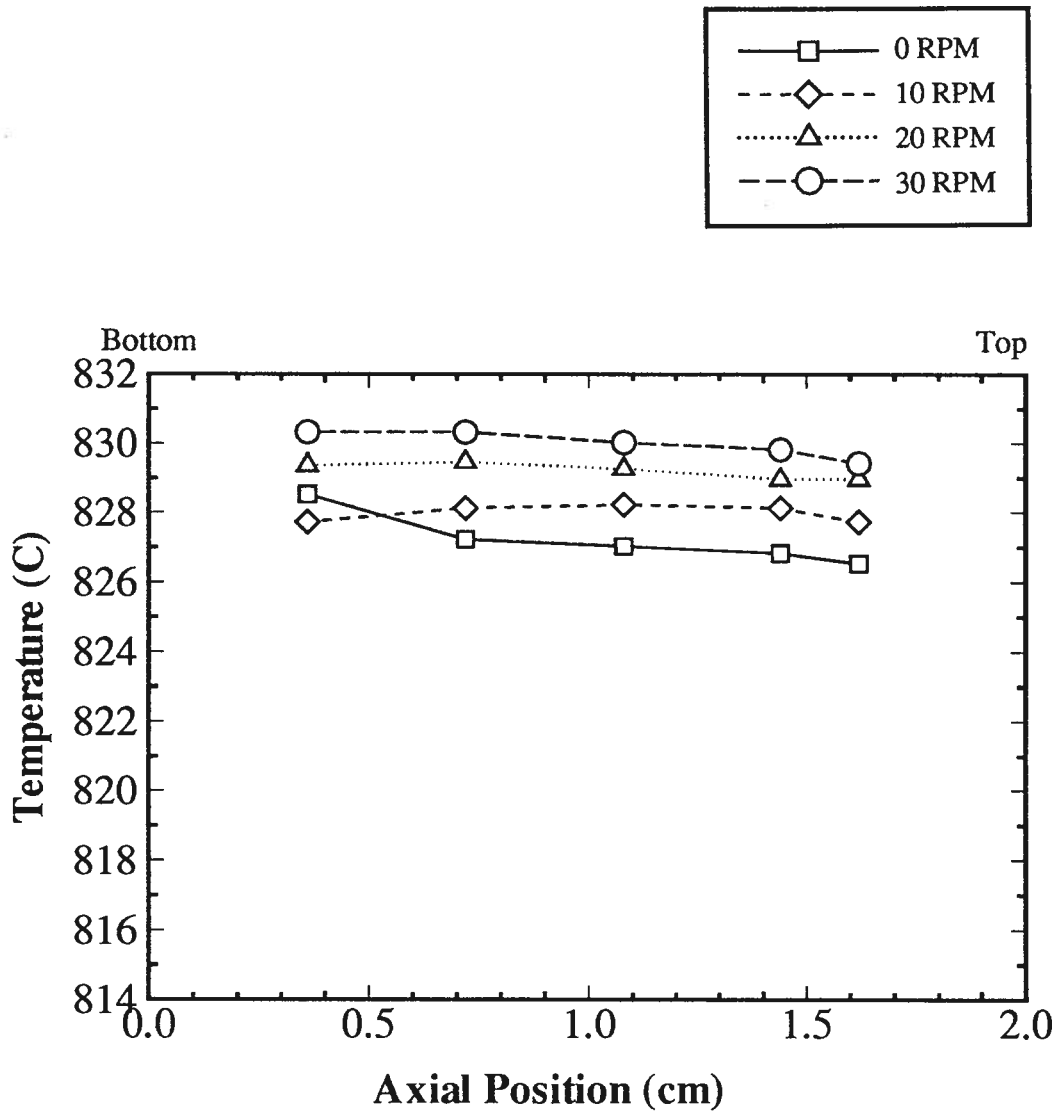

Figure 7.69: Temperature distribution at r = 3.8 cm for crucible rotations of 0, 10, 20 and 30 rpm. Crucible diameter is 8.8 cm. Simulated crystal present.

7.3 Thermal Gradients in the Crystal During Cooling

High thermal stresses which lead to cracking are due to large temperature gradients in the crystal [51]. Thus, it is important to know the thermal gradients that occur in the crystal during cooling for different furnace configurations. It is not practical to measure the thermal gradients in the crystals with imbedded thermocouples. As an alternative a simulated crystal made of alumina aggregate was used, having the configuration shown in Figure 7.70. Four thermocouples were imbedded in the alumina in the positions indicated in the figure. The thermal conductivity of the ceramic alumina aggregate is comparable to that of LBO which makes it a suitable model material.

Temperature measurements in the simulated crystal were made under equilibrium conditions with the furnace set at 400°C and after an interval of five hours to allow the furnace to reach equilibrium. Measurements were made at two vertical locations in the furnace, position A and B in Figure 7.71, corresponding to the normal cooling positions of crystals grown in the large and small crucibles respectively. Note that the bottom of the large crucible is positioned 1.1 cm above the bottom of the small crucible. Temperature gradients were determined with no crucible present, with a small crucible in the furnace and with a large crucible in the furnace with and without an insulating block at the top of the furnace as shown in Figure 7.71.

The crucible and simulated crystal positions in the furnace for which temperature measurements were made are shown in Figure 7.72. The values of the temperature gradients are listed in Table 7.9 with the corresponding measured temperature gradients across the pairs of thermocouples indicated.

With no crucible in the furnace the gradients are larger for the simulated crystal in the upper position A as compared to B. The radial gradients are close for both A and B and lower than the axial gradients with the axial gradient at A being appreciably larger

than the others.

Adding the small crucible to the furnace changes the temperature gradients in the simulated crystals. The radial gradient between thermocouples 1 and 2 is increased when the crucible is added and the the simulated crystal is above of the crucible. All of the other radial and axial gradients are lower with the crucible at positions A and B. In particular there is a large decrease in the axial gradients with the addition of the crucible. The decrease in gradients for position B can be attributed to the presence of the crucible surrounding the crystal in this position. The high conductivity of the platinum crucible, and its close proximity to the crystal reduces the gas temperature gradient adjacent to the crystal which leads to lower gradients in the crystal. The higher radial gradients at position at position A follow, since position A is above the top of the crucible.

The radial gradient in the crystal with the large crucible in the furnace is essentially the same as that observed with the crystal in the smaller crucible. (position B). The axial gradients however are effectively twice that of the smaller crucible, and compared to the condition of no crucible in the furnace. In effect the large crucible walls are sufficiently far away from crystal that they have little effect on the gradients in the crystal. Adding an insulating brick over the top of the seed hole significantly reduces the radial gradients and to a lesser extend the axial gradients.

Independent of crucible size, the thermal gradients in the crystal are most sensitive to the addition of insulation over the seed hole in the furnace and the vertical position of the crystal. Moving the simulated crystal towards the centre of the furnace reduces the axial gradients and the insulated top reduces the radial gradients. Using a small crucible for crystal growth reduces both the axial and radial gradients provided that the crystal is surrounded by the walls of the crucible during the post growth cooling stage.

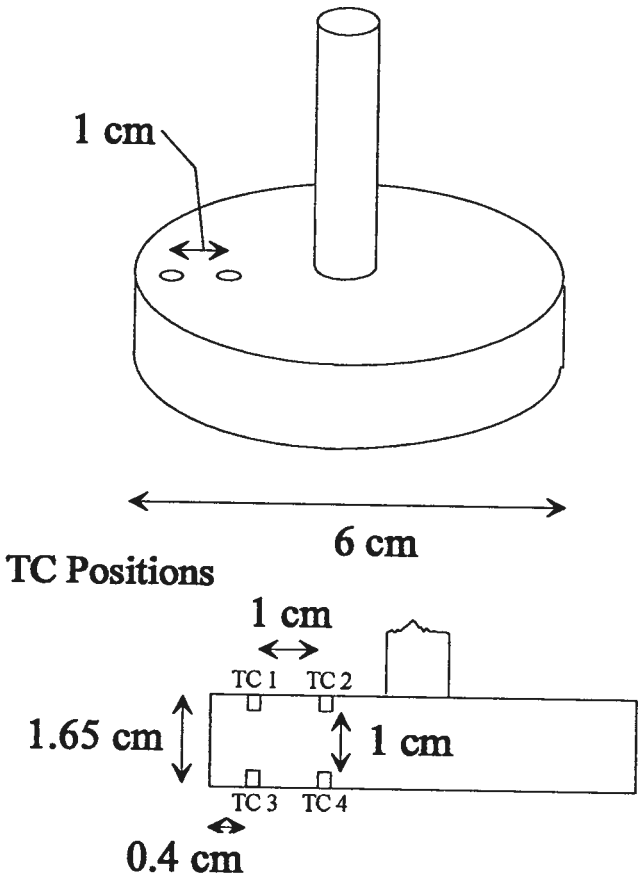

Figure 7.70: Alumina aggregate used for determining the thermal gradients in the furnace.

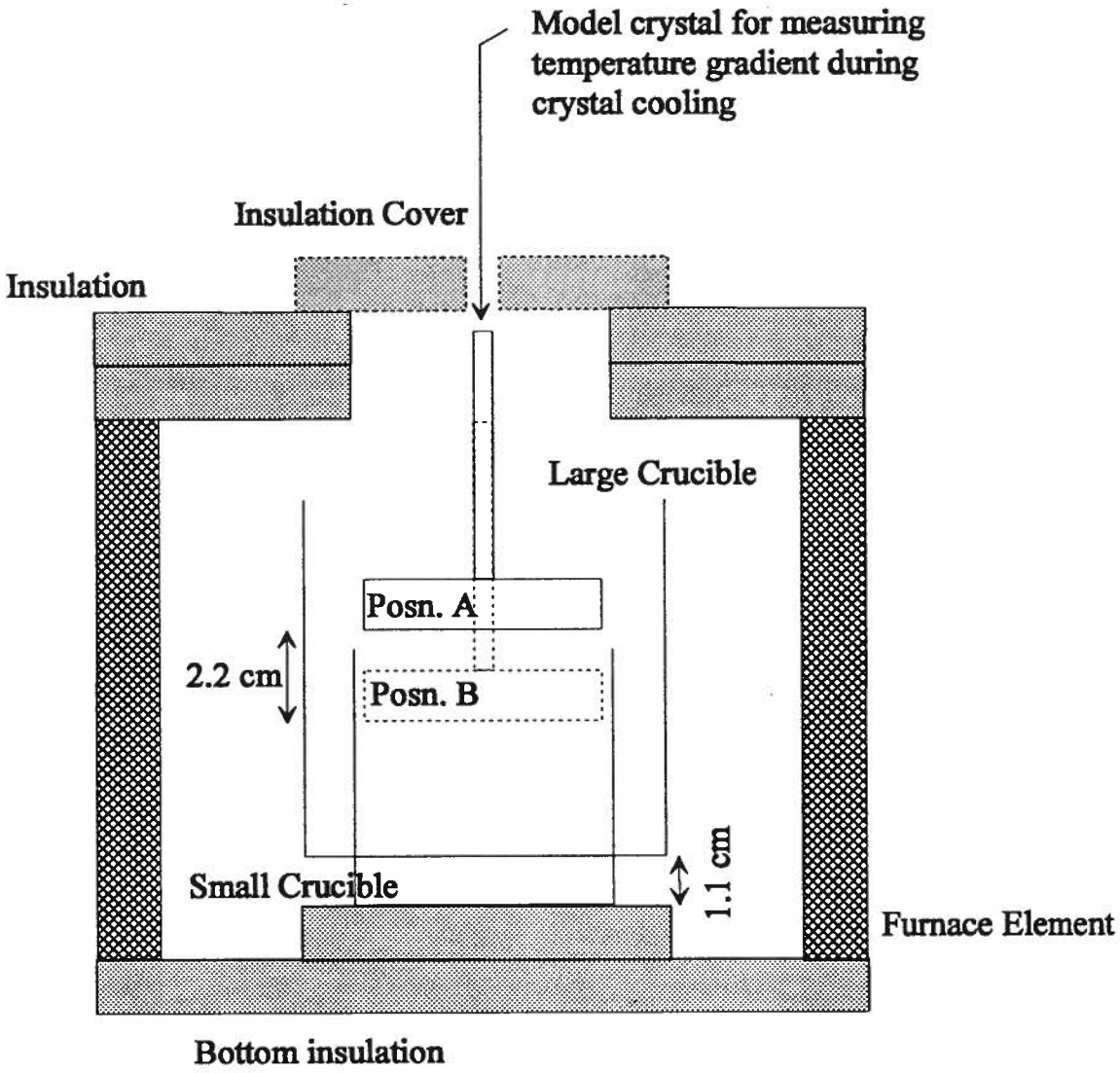

Figure 7.71: The axial positions of the alumina model crystal used when measuring the thermal gradients.

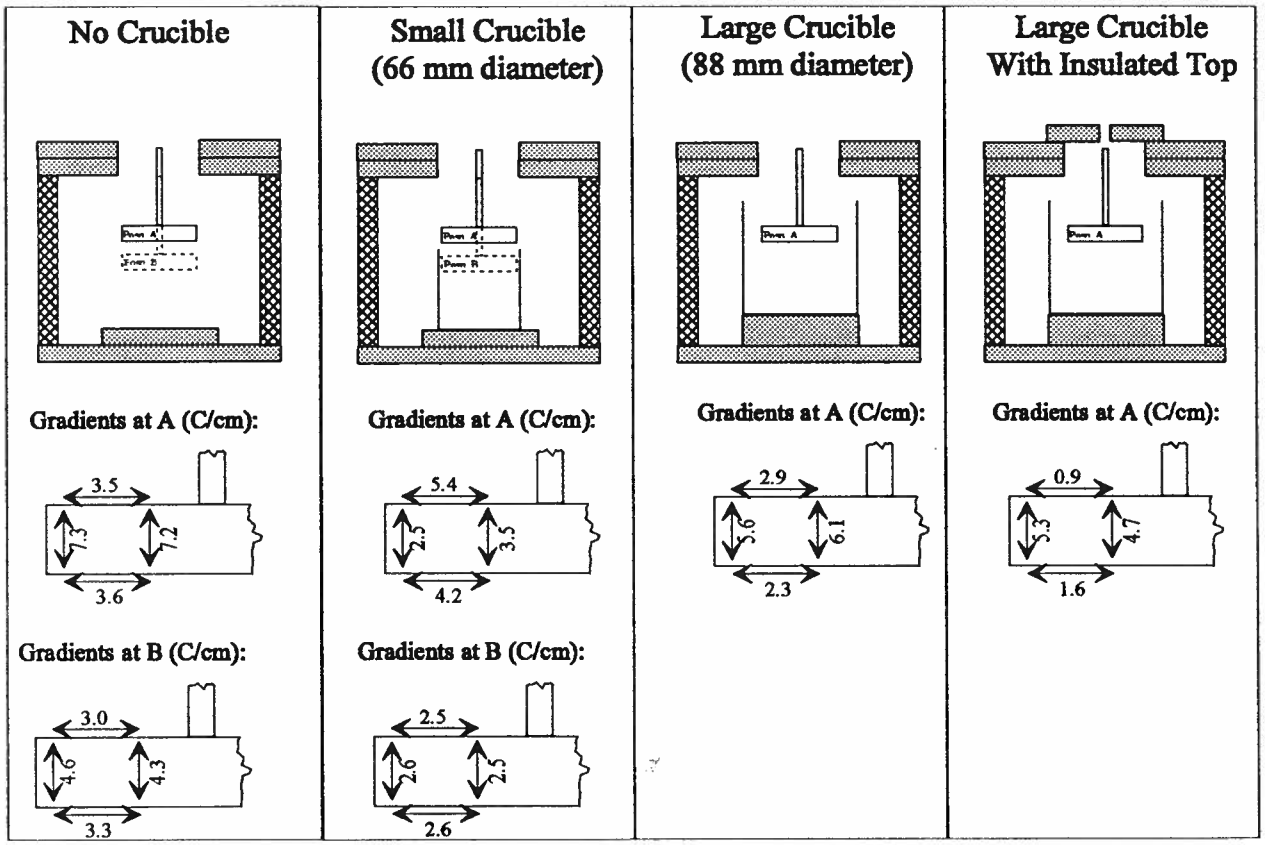

Figure 7.72: Temperature gradients measured for the different furnace configurations as indicated.

Condition	Temperature Gradient °C/cm			
	Radial		Axial	
	TC1–TC2	TC3–TC4	TC1–TC3	TC2–TC4
1. No Crucible				
(a) crystal in upper position (A)	3.5	3.6	7.3	7.2
(b) crystal in lower position (B)	3.0	3.3	4.6	4.3
2. Small Crucible				
(a) crystal in upper position (A)	5.4	4.2	2.5	3.5
(b) crystal in lower position (B)	2.5	2.6	2.6	2.5
3. Large Crucible				
crystal in upper position (A)	2.9	2.3	5.6	6.1
4. Large Crucible				
crystal in upper position (A)				
and seed hole insulated.	0.9	1.6	5.3	4.7

Table 7.9: Temperature gradients measured for the different furnace configurations as indicated.

Chapter 8

Mathematical Model For LBO Crystal Growth

8.1 Scope of Model and Assumptions

The objective of the model is to quantitatively determine the temperature and velocity distributions in the melt during solidification as a function of the growth variables. This requires establishing the thermal conditions related to the furnace, calculating the thermal field, and fluid flow velocities, with and without crystal and crucible rotations.

A fluid flow model, which incorporates heat transfer, has been developed by Fluid Dynamics International (FIDAP) [52]. The FIDAP package can be used to determine the velocities and temperatures in the melt during crystal growth. In growing a crystal, the melt temperature is adjusted to just above the liquidus temperature, a small seed crystal is dipped into the melt, and the temperature further lowered to allow the seed to grow. Crystal and crucible rotation is employed to enhance fluid flow in the melt. The crystal is slowly pulled away from the melt, effectively under steady state conditions, once the required crystal diameter is reached by the seed. The model is used to predict the fluid flow and temperature distribution in the melt at steady state.

A number of assumptions were used in the model, to simplify the calculations. These are listed in Table 8.10, along with a rating of the validity of each assumption and comments on the validity rating. The assumption of an axisymmetric temperature field is necessary to simplify the calculations. The crystal growth furnace is designed to have an axisymmetric temperature field, and crystal and crucible rotation will tend to

level out any local temperature variations in the melt. The assumption that the crystal growth system is at steady state is essential to the model, and is considered valid on the basis of the very slow cooling rate of 5°C/day or withdrawal rate of 1.6 mm/day for LBO. In comparison the withdrawal rate of Ge is much faster at 100 mm/hr. The assumption of laminar fluid flow is necessary for the model calculations. The assumption is reasonable for LBO since the melt has a high viscosity (10 to 100 poise). For flow past a smooth plate, laminar flow breaks down to turbulent flow when the Reynolds (Re) number exceeds 5×10^5.

$$Re = \frac{V\ L\ \rho}{\mu}$$

where V = flow velocity (cm/s), L is the characteristic length (cm), ρ = melt density (g/cm^3) and μ = melt viscosity (poise). For a limiting case situation, assume V = 1000 cm/s, L = 3.2 cm, μ = 12.3 poise (40.9% MoO_3 at 730°C) and ρ = 3.26 g/cm^3. Using these values gives Re = 848, which is very much lower than 5×10^5, indicating that the flow is laminar.

The air/melt interface is assumed to be flat, consistent with the high viscosity and low fluid velocities in the melt. Heat transfer at the air/melt and air/crystal interface is assumed to be by convective heat transfer only, which is consistent with the low surface melt temperature (below 700°C). The model assumes that the melt is homogeneous during crystal growth. As the crystal grows, MoO_3 is rejected at the interface resulting in an increase in the concentration of MoO_3 in the melt ahead of the crystal.

The LBO/MoO_3 thermophysical properties and the dimensionless groups of interest are listed in Table 8.11 and Table 8.12 respectively. Thermophysical values which are not available in the literature are estimated.

The Grashof, Prandtl and Schmidt numbers calculated for a LBO/MoO_3 liquid and for liquid gallium are given in Table 8.12. The values for Gallium are typical for a liquid

Assumptions Used In Model	Validity	Comment
System is axisymmetric	Excellent	Normal practice
System is in steady state	Excellent	Very slow growth rates
Fluid flow is laminar	Excellent	Fluid has high viscosity
MoO_3 build up ahead of the interface is neglected	Good-Poor	Viscosity is dependent on MoO_3 concentration
The air-melt surface is flat	Excellent	Fluid has high viscosity
Radiative heat transfer at the air-melt interface is neglected	Good	Air-melt surface is below 700°C

Table 8.10: Assumptions used in fluid flow model

Name	Value
LBO/MoO_3 Viscosity	12.3 poise
ΔT	200°C
Fluid Velocity	1000 cm/s
Length 'L'	3.2 cm
Diffusivity [57]	1×10^{-7} cm^2/s

Table 8.11: Values used in the nondimensional analysis of the LBO/MoO_3 system

Group	Definition	Gallium	LBO + MoO_3 (24.6 % Mo)
Grashof Number (Gr)	$\frac{g\,\beta\,\Delta T\,L^3}{\nu^2}$	2.4×10^6	0.0827
Prandtl Number (Pr)	$\frac{C_p\,\mu}{k}$	0.024	172
Schmidt Number (Sc)	$\frac{\nu}{D_{AB}}$	2.4×10^2	4×10^7

Table 8.12: Non Dimensional Numbers for Gallium and LBO.

metal system. The small Grashof number for the LBO/MoO_3 liquid indicates buoyancy forces are smaller than viscous forces which implies that natural convection will be much smaller than forced convection. Gallium, in comparison, will have strong natural convection. A small Prandtl number (≤ 1) which is the ratio of thermal mass diffusivity, as present with gallium, indicates that the energy diffusion rate is much larger than the momentum diffusion rate. The large Prandtl number for LBO/MoO_3 (172) indicates that the momentum diffusion rate is much larger than the energy diffusion rate. Thus for a given boundary layer, the thermal boundary layer thickness is much smaller than the velocity boundary layer ($\delta_t \ll \delta$). The Schmidt number is the ratio of momentum and mass diffusivities. For convective mass transfer in laminar flow the Schmidt number is proportional to the velocity and concentration boundary layers ($Sc \approx \delta/\delta_c$) The LBO/$MoO_3$ Schmidt number is large at 4×10^7 indicating that any concentration boundary layer will be much thinner than the velocity boundary layer. In contrast liquid metals. as shown by gallium, have nondimensional parameters that are very different to that of LBO/MoO_3.

8.2 Idealized Domain and Description of Calculations

The crystal growth domain adopted for the mathematical model is shown in Figure 8.73. Note that the model assumptions make the domain a simplified version of actual growth conditions. For example, the crucible walls are assumed to be smooth. The bottom

of the crucible is assumed to be flat for all calculations except when the temperature measurements are compared to the model calculations for the the small crucible. The rotation of the crucible and crystal are assumed not to be eccentric.

Cylindrical polar coordinates are used in the model. Thus there exists a radial, rotational (θ) and axial component for all variables. In the case of the velocity vector, it consists of a radial velocity, theta velocity and an axial velocity component (v_r, v_θ, v_z). It is noted that the rotational component is treated differently from the axial and radial components due to the assumption of axial symmetry. The θ component of the velocity and temperature variables are real, but they are constant and the spatial derivative is zero $\left(\frac{\partial v_\theta}{\partial \theta} = 0\right)$.

The model is applied to small and large crucibles, 66 mm in diameter and height and 88 mm in diameter and height respectively. The sensitivity analysis, determination of the dominant parameters and model validation were conducted using the small crucible. The comparison of the model predictions with the experimental temperature measurements for different crucible rotations were conducted on the small and large crucibles. A simulated crystal, formed from a platinum sheet, Figure 4.31, was used for these measurements.

8.3 Steady State Axisymmetric Fluid Flow Model

8.3.1 Equations of Fluid Flow - Lagrangian Coordinates

The conservation of mass, momentum and energy govern the flow of a viscous fluid. In order to present them in their simplest form the equations are formulated in Lagrangian coordinates. In this case the reference frame is moving with the fluid and the equations are applied to a moving control volume of fluid. The conservation of mass in the control volume states that the mass in the control volume is constant with time, $\frac{dm}{dt} = 0$.

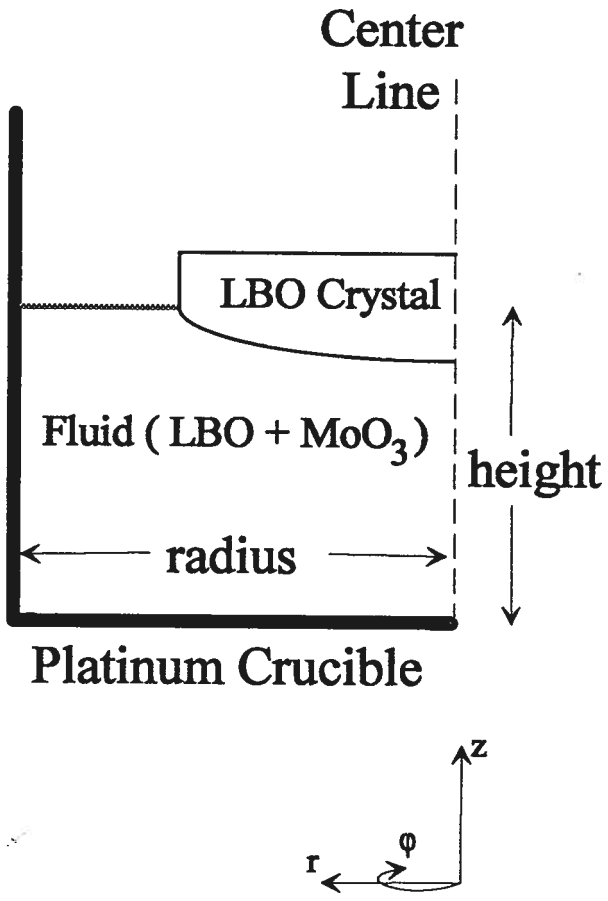

Figure 8.73: Schematic representation of domain examined with the model.

Expressing this equation in terms of the density of the fluid gives.

$$\frac{d(\rho \cdot volume)}{dt} = 0 \tag{8.1}$$

The conservation of momentum follows from Newtons second law being applied to the control volume, $\bar{F} = m\bar{a}$. Dividing by the volume gives the force per unit volume, changing the mass term to a density term.

$$\bar{f} = \rho\bar{a} \tag{8.2}$$

The energy equation describes the change in internal energy of the control volume (dE_t). It is equal to the sum of the change in heat added (dQ) and the work done (dW).

$$dE_t = dQ + dW \tag{8.3}$$

8.3.2 Equations of Fluid Flow - Euler Coordinates

Converting the equations of fluid flow from Lagrangian coordinates to fixed (Euler) coordinates gives equations that are easily applied to real situations. The following section will give an overview of the final forms of the equations. Converting to Euler coordinates requires that the Material Derivative ($\frac{D}{Dt}$) be used on any property that changes with time.

$$\frac{d}{dt} = \frac{D}{Dt} = \frac{\partial}{\partial t} + \left(\bar{v} \cdot \nabla\right)$$

where the div term (∇) in cylindrical coordinates is

$$\left(\frac{\partial}{\partial r}, \frac{1}{r}\frac{\partial}{\partial \theta}, \frac{\partial}{\partial z}\right)$$

The fluid being examined is incompressible, that is ρ is constant, which is used to simplify the equations. Using the material derivative on the conservation of mass equation (Equation8.1) yields the following in Euler coordinates.

$$\rho\nabla\bar{v} = 0 \tag{8.4}$$

Likewise, the conservation momentum equation in Euler coordinates becomes:

$$\rho \frac{D\vec{v}}{Dt} = \vec{f}_{body} + \vec{f}_{surface}$$

The force term has been divided into a body and surface force. The only body forces acting on the fluid are due to gravity. The body force is $\rho\vec{g}$. The Boussinesq approximation is used to account for a density change with temperature. This is done by varying the density in the body force term using $\rho_o(1 - \beta\Delta T)$, where β is the expansion coefficient of the liquid, and ΔT is the temperature change. The surface forces consists of the external stresses acting on the sides of the control volume. A length derivation of the stresses acting on the control volume gives the surface forces as $\vec{f}_{surface} = \nabla\tau_{ij}$, where τ_{ij} is the stress tensor. Manipulated, the equation further gives:

$$\vec{f}_{surface} = -\nabla p + \nabla^2\left(\mu\vec{v}\right)$$

where p is pressure and μ is viscosity. Substituting these into the conservation of momentum equation gives final form of the momentum equation:

$$\rho_o \frac{D\vec{v}}{Dt} = \rho_o(1 - \beta\Delta T)\,\vec{g} - \nabla p + \nabla^2\left(\mu\vec{v}\right) \tag{8.5}$$

The energy equation in Euler coordinates is

$$\frac{DE_t}{Dt} = \frac{DQ}{Dt} + \frac{DW}{Dt}$$

The incompressible form of the energy equation is

$$\rho C_p \frac{D\vec{T}}{Dt} \approx \nabla\left(k\nabla\vec{T}\right) \tag{8.6}$$

The equations are further simplified by using the penalty function approach for the pressure variable. For this method the conservation of mass equations is discarded and the pressure is eliminated from the momentum equation using $p = -\frac{1}{\epsilon}\nabla v$. ϵ is the

penalty parameter. The problem is solved for steady state; thus all time derivatives are zero. The resulting equations that are solved by FIDAP are:

$$\rho_o \left(\vec{v} \cdot \nabla\right) \vec{v} = \rho_o \left(1 - \beta \Delta T\right) \vec{g} - \nabla \left(\frac{1}{\epsilon} \nabla \vec{v}\right) + \nabla^2 \left(\mu \vec{v}\right) \tag{8.7}$$

$$\rho C_p \left(\vec{v} \cdot \nabla\right) \vec{T} = \nabla \left(k \nabla \vec{T}\right) \tag{8.8}$$

The type of flow solved for this problem is described as STRONGLY coupled. This term is used when the full set of equations are solved simultaneously. Nine noded quadratic elements are used in the model. Velocity and temperature degrees of freedom are present at each node.

8.3.3 Temperature Boundary Conditions

The temperature boundary conditions used in the model were experimentally measured as discussed in Chapter 4. The location of the boundary conditions are different for each set of model calculations. The temperature distribution along the wall and bottom of the platinum crucible were considered as fixed temperature boundaries, assumed to be linear between points, and independent of time. The top of the fluid and crystal were modeled as a convective temperature boundary condition. The ambient temperature was approximated using the experimental measurements. The convective heat transfer coefficient was taken as 0.006 W/cm^2, which is an average value for a natural convection heat transfer surface. The values of the temperature boundary conditions used for each set of calculations will be given prior to the presentation of the results.

Sensitivity analysis and Parameter Examination

These calculations focus on the fluid flow in the melt. As a result the model only considers the melt and the inside surface of the platinum crucible, which simplifies the calculations.

The temperature measurements were conducted at a furnace setting higher than that used for crystal growth. The temperatures used in the model are the measured values less the temperature difference between the furnace setting at which the measurements were made and the crystal growth furnace setting which gives the thermal field for a crystal that is approximately 2/3 of the crucible diameter.

Comparison with Experimental Data

These calculations examine the change in thermal field with crucible rotation, with the simulated crystal in the melt. The boundary conditions are taken from the experimental measurements that have no crucible rotation with the simulated crystal in the melt. The melt temperatures are extrapolated to give the boundary condition temperatures which are located at the outside of the crucible. Minor adjustments are done to the boundary temperatures by fitting the model predictions to the experimental melt temperatures.

8.3.4 Velocity Boundary Conditions

For the velocity boundary conditions it is assumed that no slip occurs at the crucible and crystal surfaces in contact with the melt, and that free slip occurs at the air-melt surface. The azimuthal velocities are dependent on the crystal and crucible rotation rate, Ω_x and Ω_c respectively. The velocity boundary conditions are as follows:

Bottom of Crucible

$$
\begin{aligned}
v_z &= 0 \\
v_r &= 0 \\
v_\theta &= \Omega_c\,(\text{rps}) \times 2\pi \times r\,(\text{cm})
\end{aligned}
$$

Side of Crucible

$$\begin{aligned} v_z &= 0 \\ v_r &= 0 \\ v_\theta &= \Omega_c\,(\text{rps}) \times 2\pi \times r\,(\text{cm}) \end{aligned}$$

Fluid/Air Interface

$$\begin{aligned} v_z &= 0 \\ v_r &= \text{No Constraint} \\ v_\theta &= \text{No Constraint} \end{aligned}$$

Crystal/Fluid Interface

$$\begin{aligned} v_z &= 0 \\ v_r &= 0 \\ v_\theta &= \Omega_x\,(\text{rps}) \times 2\pi \times r\,(\text{cm}) \end{aligned}$$

Fluid Center Line

$$\begin{aligned} v_z &= \text{No Constraint} \\ v_r &= 0 \\ v_\theta &= 0 \end{aligned}$$

8.3.5 Solution Procedure

Sensitivity analysis and Parameter Examination

The calculations were carried out in sets of iterations. The initial shape of the crystal/melt interface was taken as flat since the thermal field is unknown prior to the first calculation. With the solid-liquid interface position and the boundary conditions defined, the model predicts the fluid velocities and temperature field using the successive substitutions iterative method. The new interface position, predicted by the model, is compared to the position from the preceding model calculation. If they differ by more than 0.08 mm the interface location is adjusted and the fluid velocities and temperature field are recalculated. The adjustment of the interface and model calculations continues until the defined crystal/melt boundary location is within 0.08 mm of the calculated value.

Comparison with Experimental Data

The calculations with the simulated crystal were carried out in two steps. First, the boundary conditions were adjusted until the model accurately predicted the thermal field of the melt for the case of no crucible rotation. These boundary conditions were then used in the model which determines the thermal field as for different crucible rotations.

Chapter 9

Sensitivity Analysis of the Fluid Flow Model

A sensitivity analysis was conducted to examining the flow due to natural and forced convection, and to establish how variations in the mesh density, viscosity and conductivity values used in the model affect the calculations. The values of the mesh densities, conductivities and viscosities considered in the sensitivity analysis are given in Table 9.14.

The mathematical model analysis was conducted for the small, 6.6 cm diameter, crucible with a fluid height of 2.5 cm. The temperature boundary conditions employed in the sensitivity analysis are shown in Figure 9.74. These values were obtained by measurements, Figure 7.53, which were higher than usually employed for LBO crystal growth. The ambient gas temperatures, determined in Appendix A, were also approximately 145°C higher. A correction of −145°C was applied to these measurements to bring them into the correct range. The established values of the thermophysical properties are given in Table 9.13. The determination of the thermal conductivity used in the calculations is given in Appendix A. The MoO_3 concentration for all of the calculations is 40.9 Wt.% MoO_3 with the exception of the viscosity analysis where all three MoO_3 concentrations are considered. It is noted that the liquidus is assumed to be 650°C for all sensitivity analysis calculations.

9.1 Natural Convection

The vector plot of the flow that occurs due to natural convection is shown in Figure 9.75. The average magnitude of the flow velocity is low at approximately 10^{-4} cm/s. This is

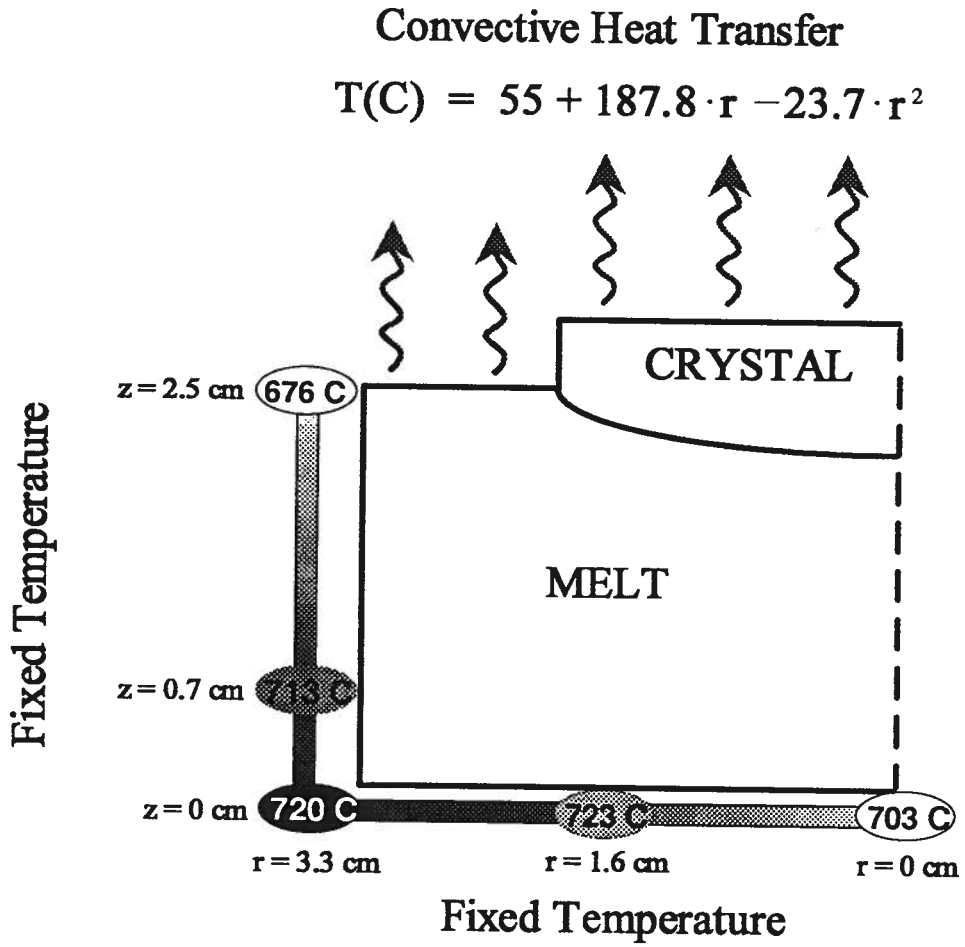

Figure 9.74: Temperature boundary conditions used in the sensitivity analysis.

Property	Units	Values
Specific Heat	J/g K	0.63
density	g/cm^3	3.26
Viscosity for 40.9 Wt% MoO_3	poise	$exp\,(37.31 - 0.0784 \times T[C] + 4.21 \times 10^{-5} \times (T[C])^2)$
Conductivity	W/cm K	0.05
Liquidus	Celsius	650
β	K^{-1}	6×10^{-6}

Table 9.13: Standard thermophysical properties used in the sensitivity analysis.

Parameter	Units	Values
Mesh Density	nodes	585, 1795
Viscosity	poise	
(29.7 Wt% MoO_3)	($\approx$ 86 at 730°C)	$exp\,(72.26 - 0.155 \times T[C] + 8.51 \times 10^{-5} \times (T[C])^2)$
(36.2 Wt% MoO_3)	($\approx$ 30 at 730°C)	$exp\,(45.59 - 0.0946 \times T[C] + 5.04 \times 10^{-5} \times (T[C])^2)$
(40.9 Wt% MoO_3)	($\approx$ 12 at 730°C)	$exp\,(37.31 - 0.0784 \times T[C] + 4.21 \times 10^{-5} \times (T[C])^2)$
Conductivity	W/cm K	0.04, 0.05, 0.06

Table 9.14: Parameters examined for sensitivity analysis.

due to the high viscosity and low thermal expansion coefficient (β) of the LBO/MoO_3 melt. The flow pattern is counter clockwise moving up the wall and down below the crystal. There is a stagnant region, marked "S" in Figure 9.75, that the fluid rotates around. The flow regime shown in Figure 9.75 results from the density gradient in the fluid, which is directly related to the temperature distribution. The density variation is proportional to the temperature difference the melt is above the liquidus, given by $\rho = \rho_o(1 - \beta\Delta T)$. The temperature contours in the melt are shown in Figure 9.76.

The hottest region of the fluid corresponds to the area were the melts density is a minimum. In the LBO/MoO_3 melt the hottest region is located near the outside bottom of the crucible. This low density fluid rises upwards and displaces the other fluid as it advances. The displaced fluid near the outside surface of the melt moves under the crystal were it drops to the bottom of the crucible, then moves horizontally towards the hottest region to replace the less dense fluid that is moving upward.

The fluid velocities are examined at various locations in the melt. The axial velocities along radial lines at 0.25, 0.5, and 0.75 of the height of the fluid are shown in Figure 9.77. The flow is upward near the crucible wall and downwards under the crystal at velocities near 3×10^{-4} and 3.2×10^{-4} cm/s respectively. The vertical flow is a maximum at 0.5 of the fluid height, and is a minimum, approaching zero, both below the centre of the crystal, and at approximately the 2.2 cm radial position.

The radial velocity along vertical lines positioned at 0.25, 0.5 and 0.75 of the crucible radius are shown in Figure 9.78. The radial flow is negative below the crystal and positive near the bottom of the crucible with velocities near -2.4×10^{-4} cm/s and 2.5×10^{-4} cm/s respectively. The largest radial velocity occurs at 0.5 of the crucible radius.

The velocity tangential to the crystal surface at 0.25, 0.5, and 0.75 of the radius of the crystal is shown in Figure 9.79. The largest fluid velocity below the crystal occurs at 0.75 of the crystal radius. The smallest tangential velocity occurs near the centre of the

crystal. The variation on tangential fluid velocity is proportional to the amount of mass transfer that occurs ahead of the crystal. This is important since inclusion formation or interface breakdown occurs when the mass transfer of MoO_3 away from interface is lower than the rate of MoO_3 being rejected at the growing crystal surface. Thus, inclusion or interface breakdown is less likely to occur at outer regions of the crystal where the magnitude of the tangential velocity is a maximum.

9.2 Forced Convection

9.2.1 Crystal Rotation

The velocity and temperature fields are calculated for a crystal rotation rate of 12 rpm and no crucible rotation. The velocity vectors are shown in Figure 9.80. The magnitude of the flow that occurs in the axial and radial directions is approximately 5×10^{-3} cm/s, which is an order of magnitude higher than the flow that occurs due to natural convection. There is also a rotational component of the fluid velocity, Figure 9.81, which is large being 2.6 cm/s near the edge of the crystal. Thus the flow that moves upward below the crystal and downward at the side of the crucible will also swirl in the θ direction as it moves under the crystal.

This type of flow has been previously explained in Chapter 6. The viscous drag of the rotating crystal surface creates an upward swirling flow. The rotation of the crystal causes the fluid near it to move in the θ direction. The imbalance between the fluids centripetal acceleration ($-\omega^2 r$) and pressure cause it to move outward in the radial direction. Fluid moves upward below the crystal to balance the outward flow in the radial direction. The fluid moving in the radial direction reaches the crucible walls and them drops to the bottom of the crucible to take the place of the fluid that moves upward below the crystal. There is a stagnant region, marked "S" in Figure 9.80, that the fluid rotates around.

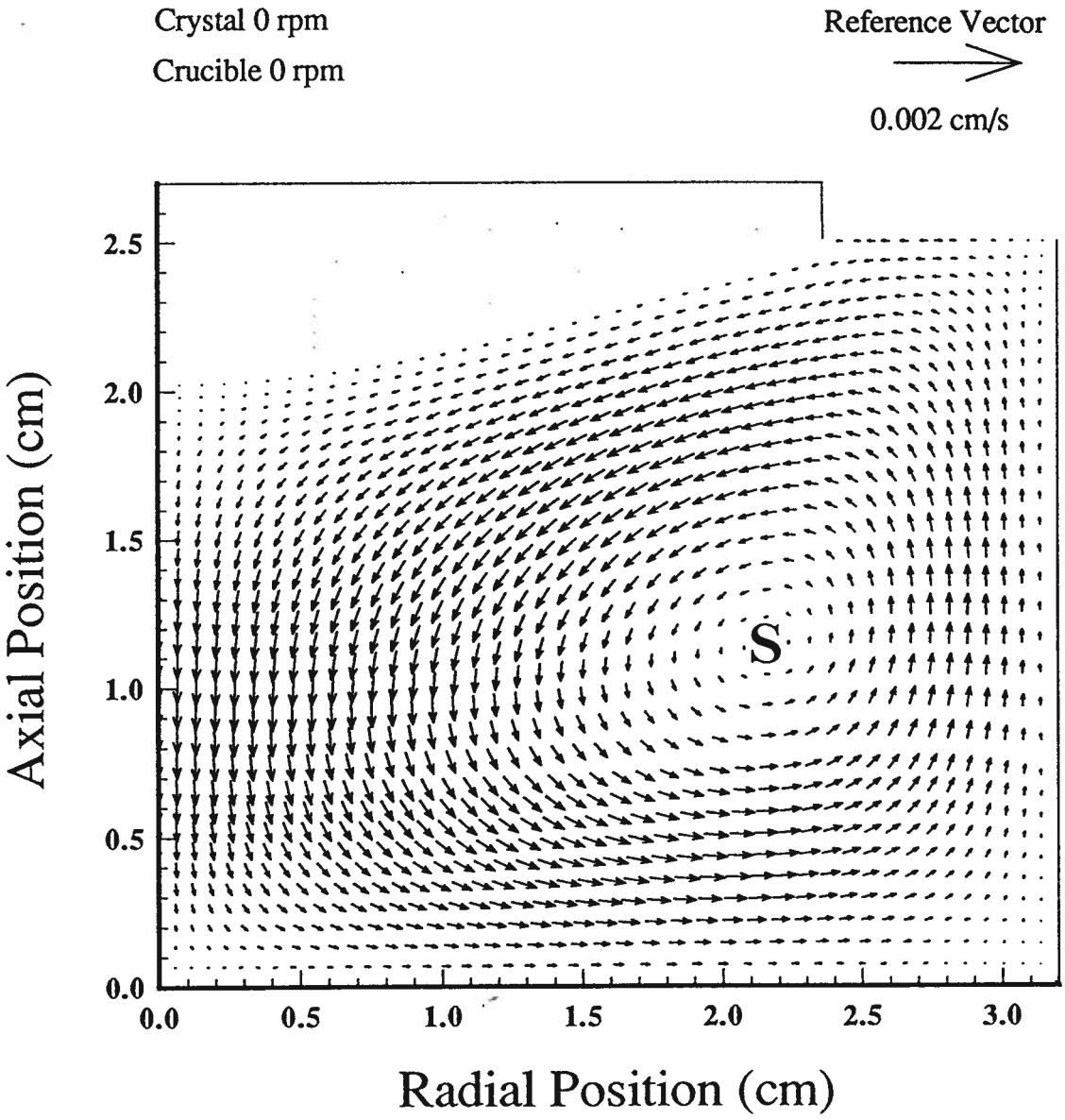

Figure 9.75: Vector plot of fluid velocity due to natural convection.

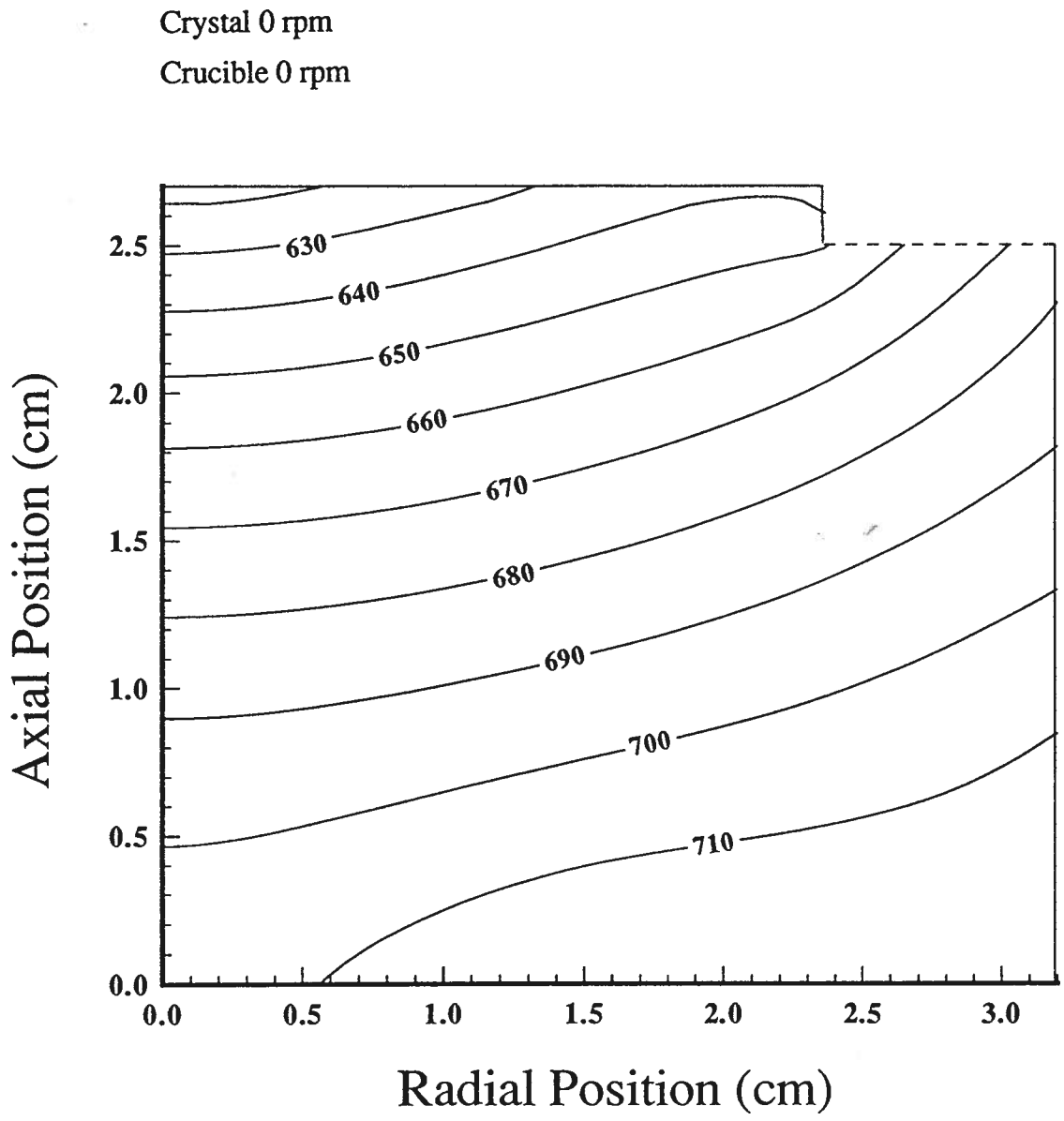

Figure 9.76: Temperature contours that occur in the LBO/MoO_3 melt.

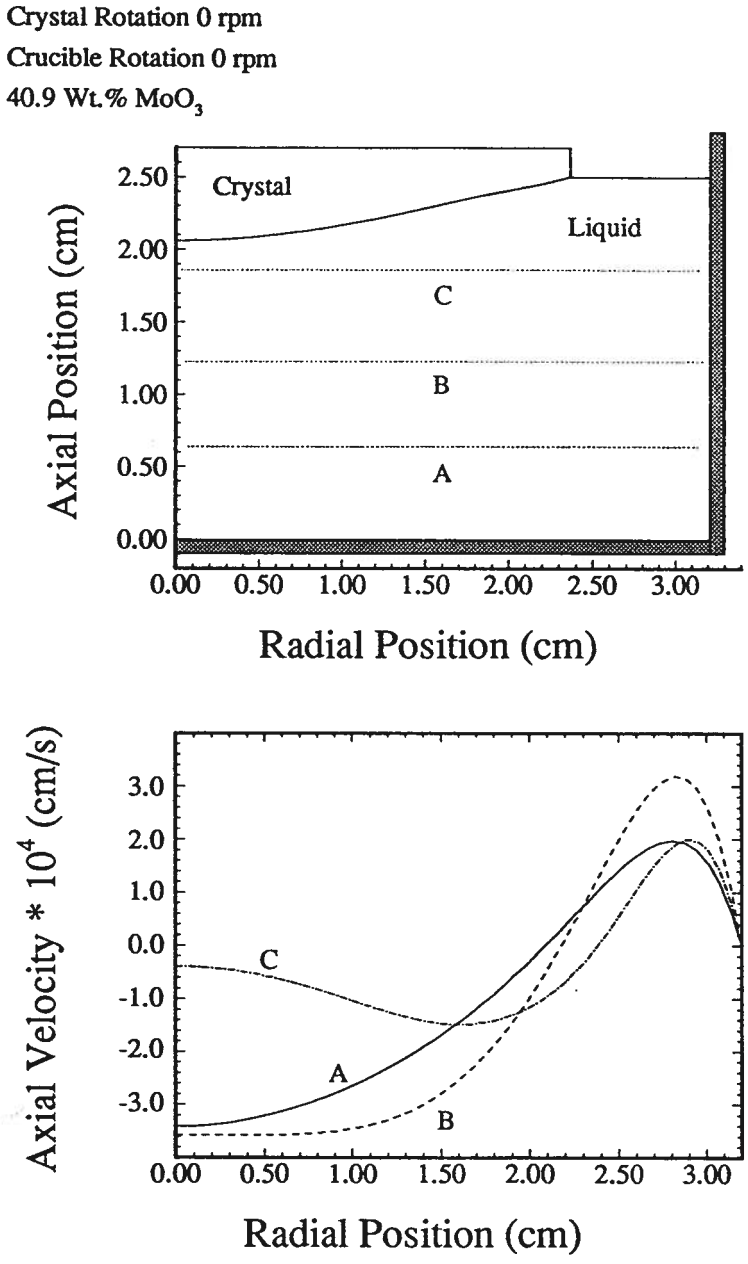

Figure 9.77: Axial velocity due to natural convection.

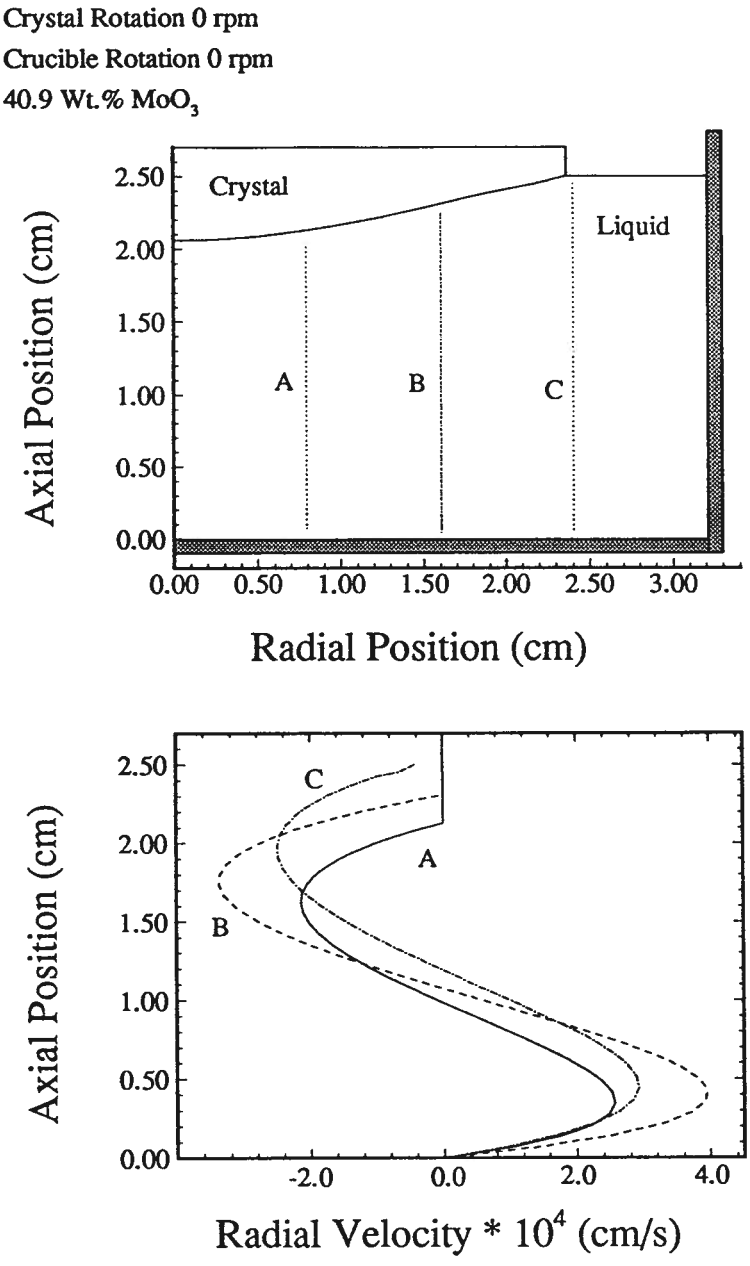

Figure 9.78: Radial velocity due to natural convection.

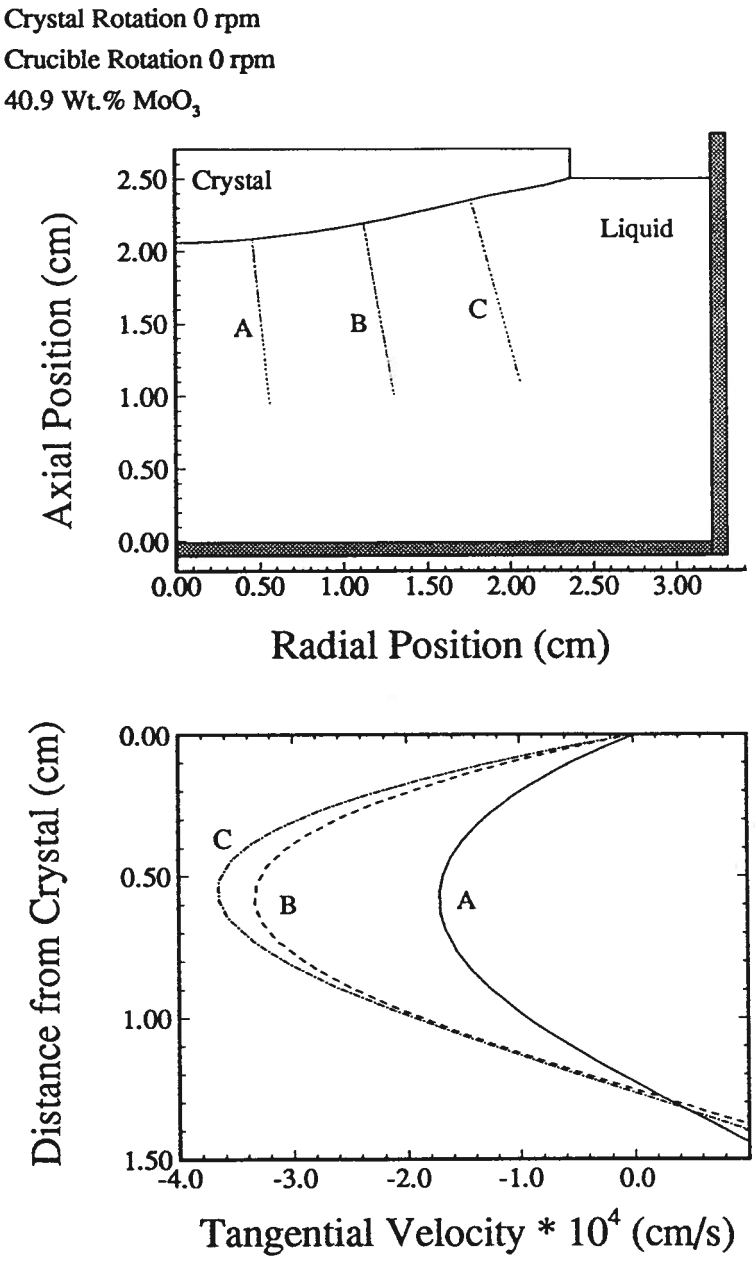

Figure 9.79: Tangential crystal surface velocity due to natural convection.

The temperature contours, Figure 9.82, are similar to the natural convection temperature contours. The flow velocities are not large enough to affect the shape of the contours. The flow velocities in the axial directions at liquid heights of 0.25, 0.5, and 0.75 of the height of the fluid are shown in Figure 9.83. The liquid flows upwards at a velocity of approximately 6×10^{-3}cm/s below the crystal and downward at -3×10^{-3} cm/s near the crucible wall. As with natural convection, the largest axial flow occurs at 0.5 of the fluid height and approaches zero both directly below the crystal and near the 2.0 cm radial position.

The flow velocity in the radial direction at positions 0.25, 0.5 and 0.74 of the crucible radius are shown in Figure 9.84. The radial velocity is positive at approximately 4×10^{-3} cm/s, below the crystal and negative, -4×10^{-3} cm/s, near the bottom of the crucible. The largest radial velocity occurs at 0.5 of the crucible radius.

The velocity tangential to the crystal surface at 0.25, 0.5 and 0.75 the radius of the crystal is shown if Figure 9.85. The fluid velocities coincide along the tangential lines at 0.5 and 0.75 of the crystal radius reaching 6×10^{-3} cm/s. The fluid velocity is lower towards the center of the crystal, reaching a maximum of 3×10^{-3} cm/s. The variation in the magnitude of the tangential velocity with radius is similar to that obtained for the natural convective flow.

9.2.2 Crucible Rotation

The flow is calculated for a crucible rotation rate of 45 rpm and no crystal rotation. The vector plot of the flow that occurs is shown in Figure 9.86. The magnitude of the axial and radial flow is approximately 6×10^{-2} cm/s, which is two orders of magnitude higher that the flow that occurs during natural convection. The rotational component of the flow is shown in Figure 9.87, with maximum flow near the crucible wall at 14 cm/s and minimum flow, approaching zero below the centre of the crystal. The flow resulting

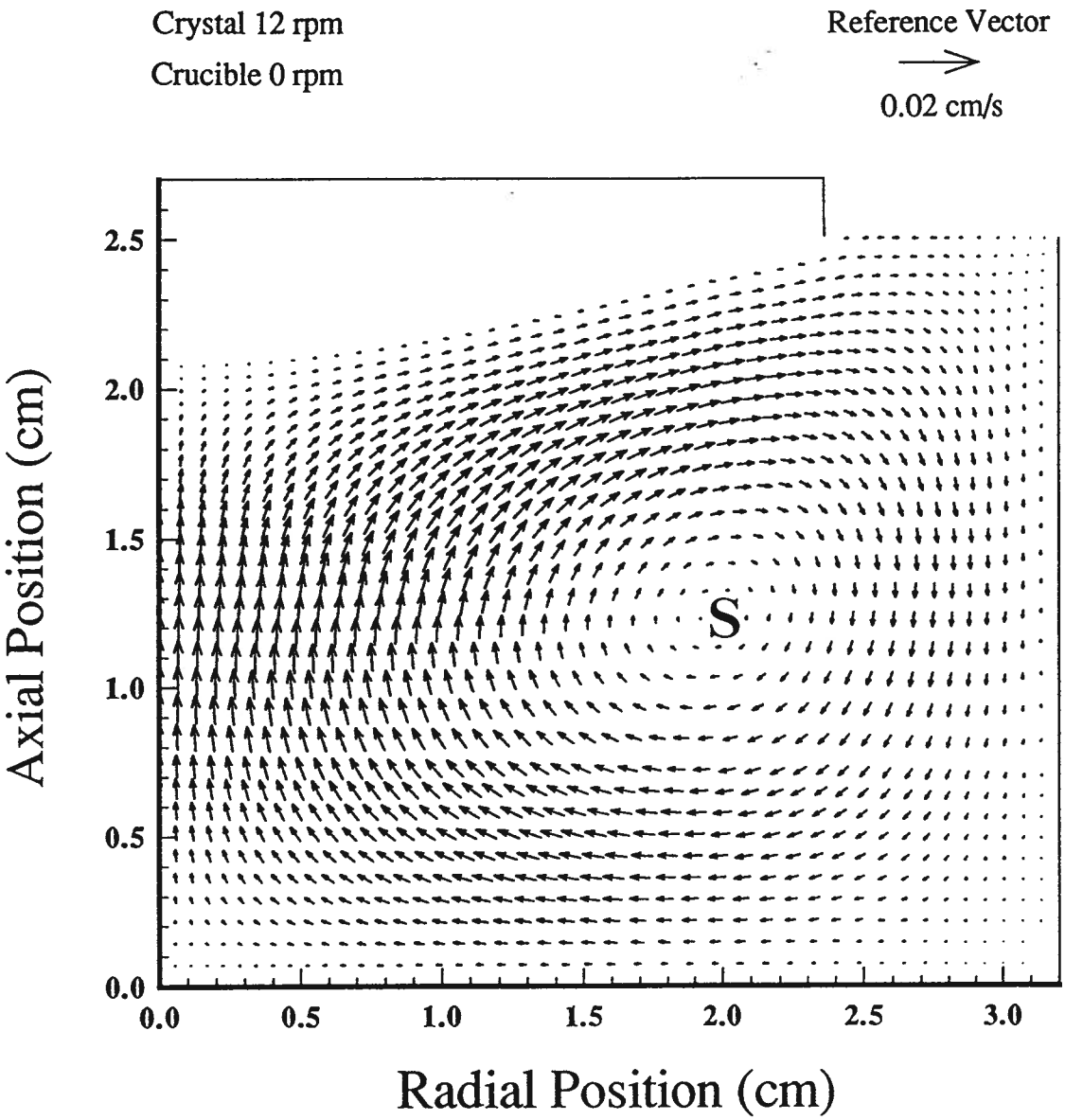

Figure 9.80: Vector plot of fluid velocity due to crystal rotation.

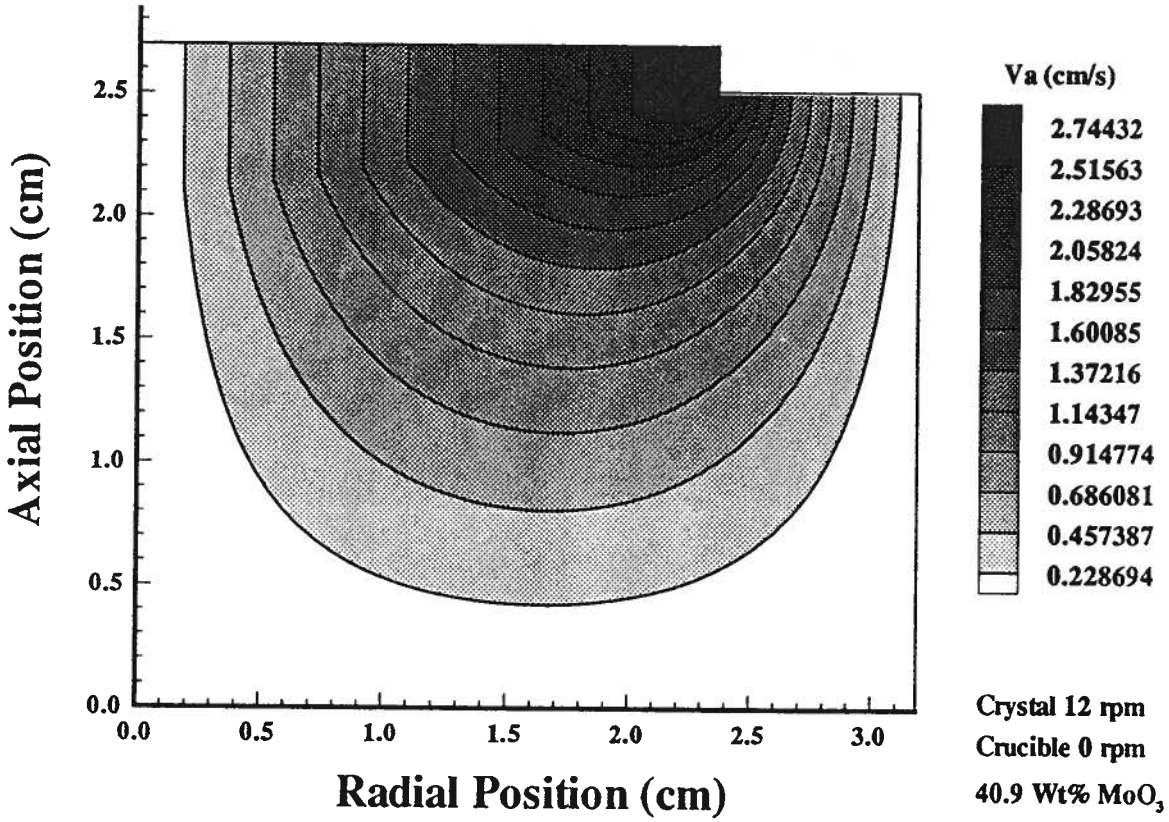

Figure 9.81: Rotational velocity plot of the LBO/MoO_3 melt with crystal rotation.

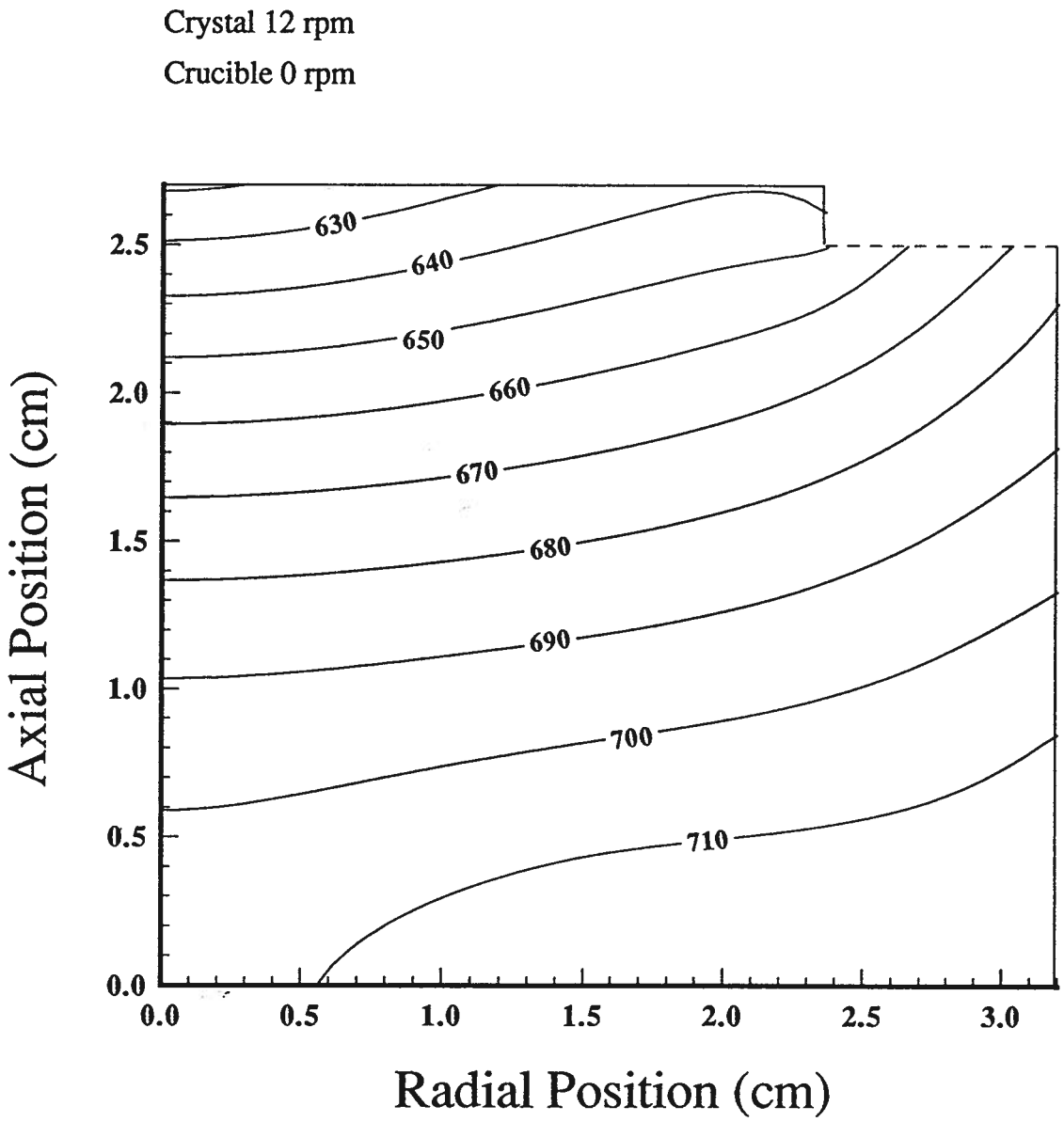

Figure 9.82: Temperature contours that occur in the LBO/MoO_3 melt with crystal rotation.

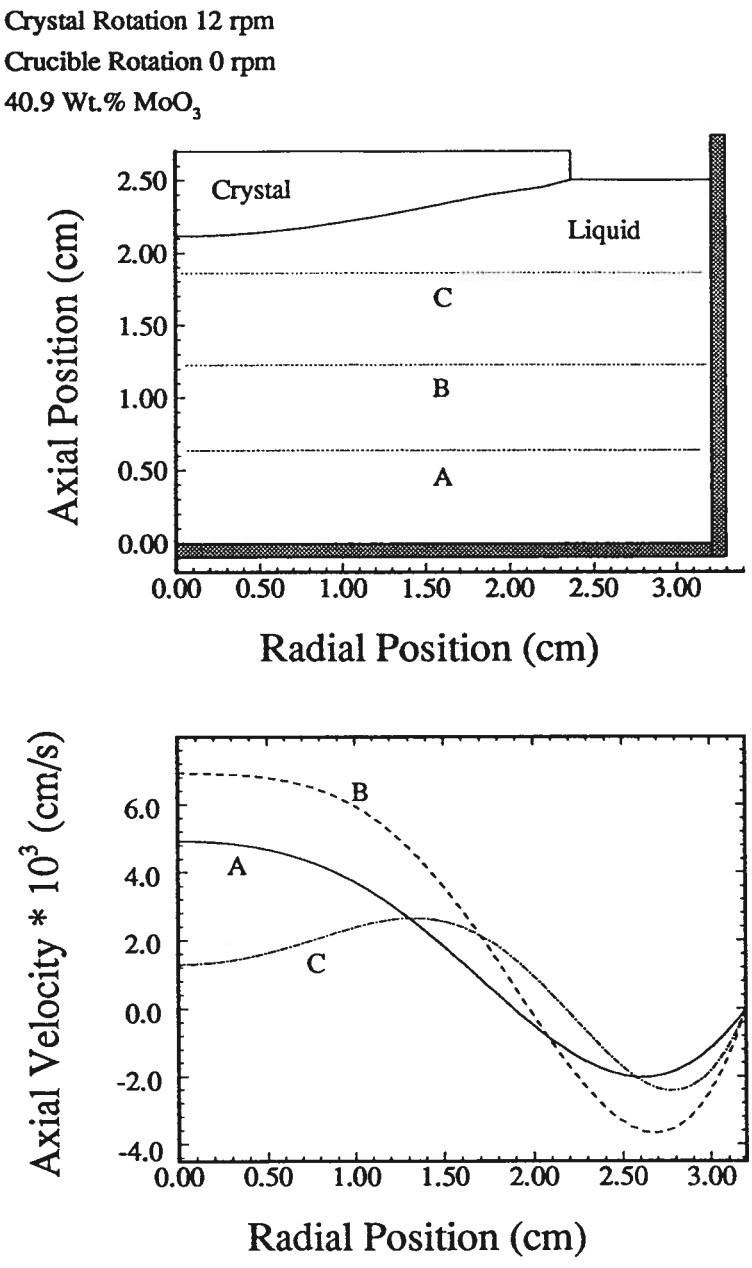

Figure 9.83: Axial velocity due to crystal rotation.

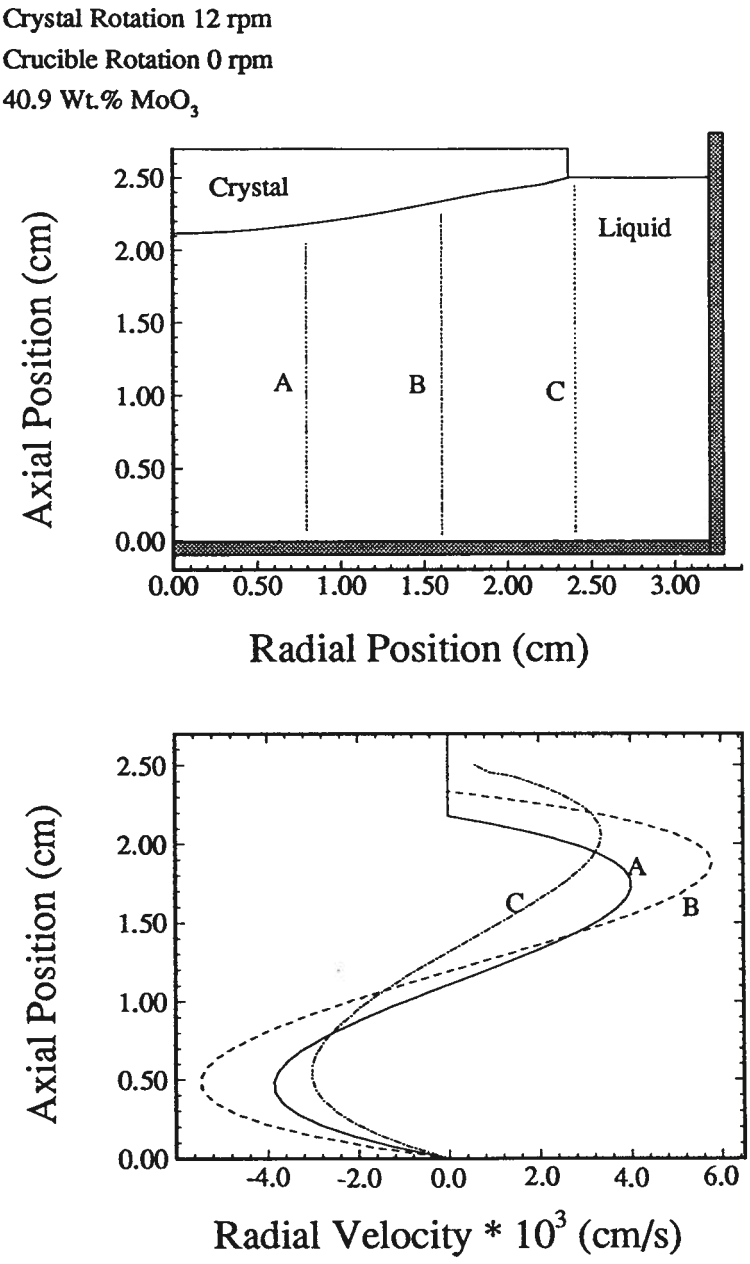

Figure 9.84: Radial velocity due to crystal rotation.

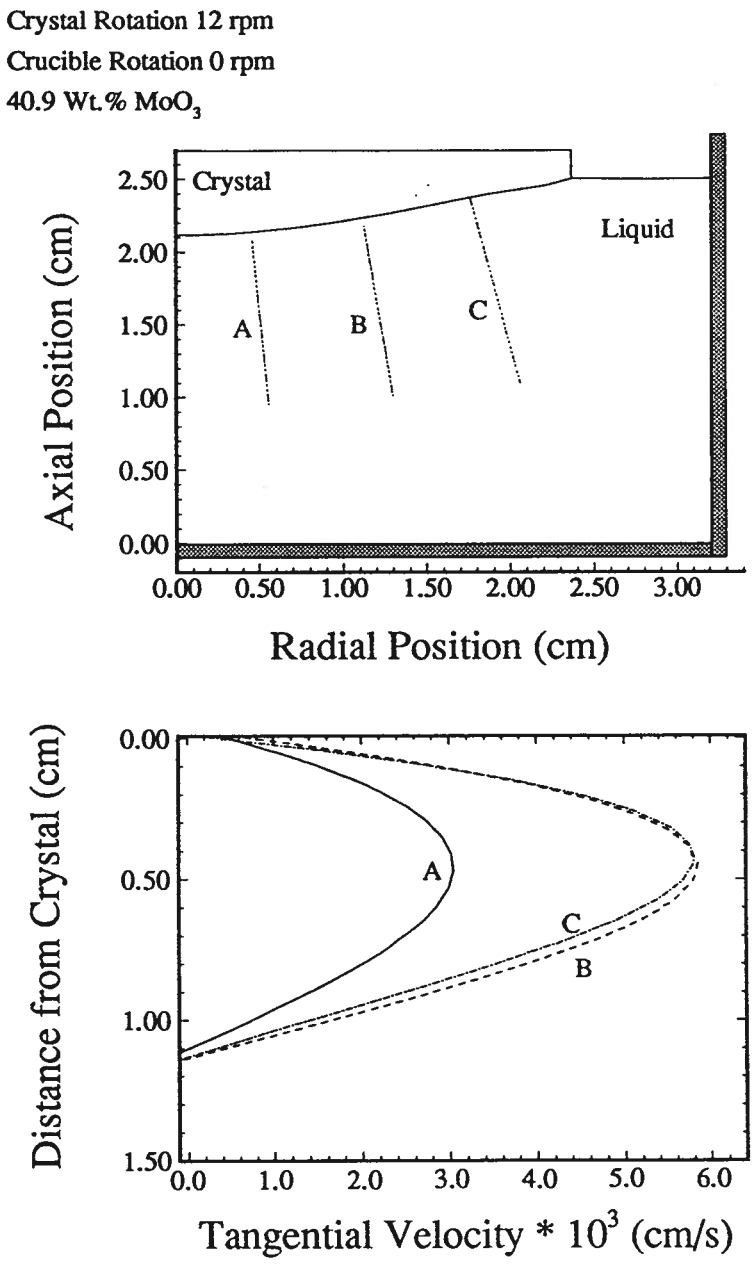

Figure 9.85: Tangential crystal surface velocity due to crystal rotation.

from the crucible rotation is similar to that of crystal rotation. except for the viscous drag at the rotating crucible surface which results in an downward swirling flow. There is a stagnant region, marked "S" in Figure 9.86, around which the fluid rotates. The rotational or theta component of the velocity causes the fluid to swirl as it moves in the radial and axial directions, which is important. The flow predicted by the mathematical model is similar to what was shown by the physical model. The rotational and swirl of the fluid as determined using the physical model are shown in Figures 6.44 through 6.47 in Chapter 6.

The high fluid flow velocities resulting from crucible rotation markedly affect the temperature isotherms in the melt. The calculated isotherms with crucible rotation are shown in Figures 9.88. These can be compared with the corresponding isotherms for natural convection shown in Figure 9.76, which are markedly different. With large crucible rotation, hot liquid moves upward adjacent to the crucible wall resulting in the upward movement of the isotherms in this region. The corresponding downward flow of the cold liquid under the crystal moves the isotherm downward.

The flow velocities in the axial direction at liquid heights of 0.25, 0.5 and 0.75 of the height of the fluid are shown in Figure 9.89. The liquid flows upward at a velocity of 6×10^{-2}cm/s near the edge of the crucible and downward at at -6×10^{-3} cm/s under the centre of the crystal. As with all the previous cases the largest axial flow occurs at 0.5 the fluid height. The axial flow approaches zero near the crystal as shown by the 0.75 fluid height velocity trace (line C on Figure 9.89) which goes to zero as the line intersects the crystal.

The radial velocity at positions 0.25, 0.5 and 0.75 of the crucible radius are shown in Figure 9.90. The liquid flow directly below the crystal is inwards at a value of -6×10^{-2} cm/s. The flow near the bottom of the crucible is outward and has a maximum value of 6×10^{-2} cm/s. The largest radial velocity occurs at 0.5 of the crucible radius.

The velocity tangential to the crystal surface at 0.25, 0.5, and 0.75 of the radius of the crystal is shown if Figure 9.91. The fluid velocity decreases with decreasing radius, and changes from -7.6×10^{-2} cm/s at 0.75 of the crystal radius to -2×10^{-2} cm/s at 0.25 of the crystal radius.

9.3 Mesh Size

In order to determine the influence of mesh size on the accuracy of the calculations the temperature and velocity fields were calculated using two node densities, 585 and 1795, shown in Figure 9.92. The calculations were conducted for a crystal rotation of 6 rpm and a crucible rotation of -48 rpm. The axial, radial and tangential velocities are examined at 0.5 of the fluid height, 0.5 of the crucible radius and 0.5 of the crystal radius respectively. The axial velocity fields for the two selected mesh sizes are shown in Figure 9.93 and the corresponding radial velocities in Figure 9.94. In both cases it is evident that the velocities are the same for both mesh sizes. The calculated fluid velocity tangential to the crystal surface, Figure 9.95, shows a small difference, less than 5×10^{-3} cm/s, between the two mesh sizes. The results indicate that a mesh density of 585 or 1795 nodes can be used in the calculations without introducing errors.

9.4 Fluid Viscosity

The effect of varying the viscosity in the calculations of the temperature and velocity fields was examined for melt concentrations of 29.7, 36.2 and 40.9 Wt% MoO_3. The corresponding viscosity of the melts is 86, 30 and 12 poise at 730°C. For these calculations the crystal and crucible rotations were zero. The axial velocities for the three melts at 0.5 of the fluid height are shown in Figure 9.96. The axial liquid velocity of the melt with the lowest viscosity, (40.9 Wt% MoO_3) is small, approaching 3×10^{-4} cm/s under

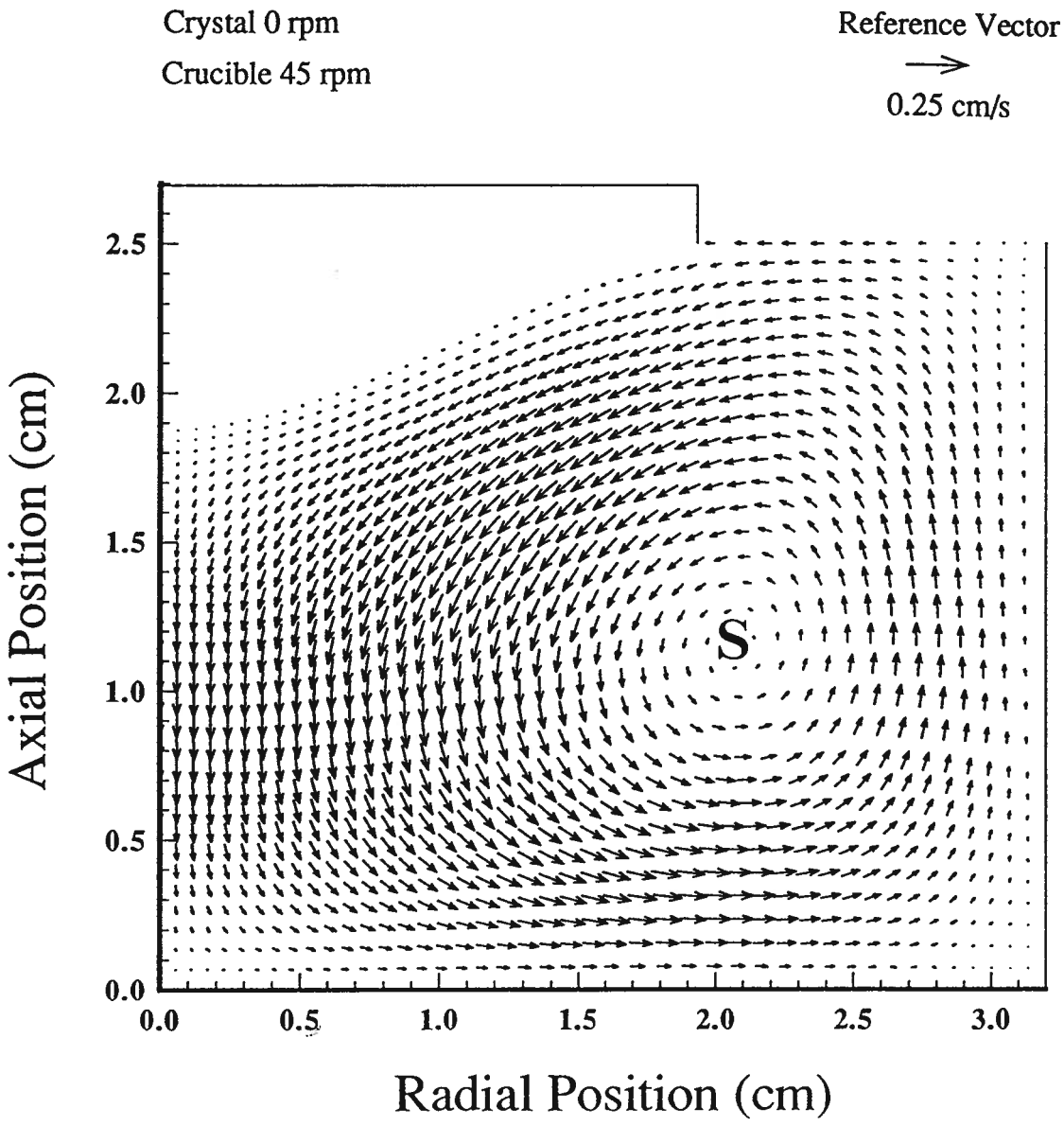

Figure 9.86: Vector plot of fluid velocity due to crucible rotation.

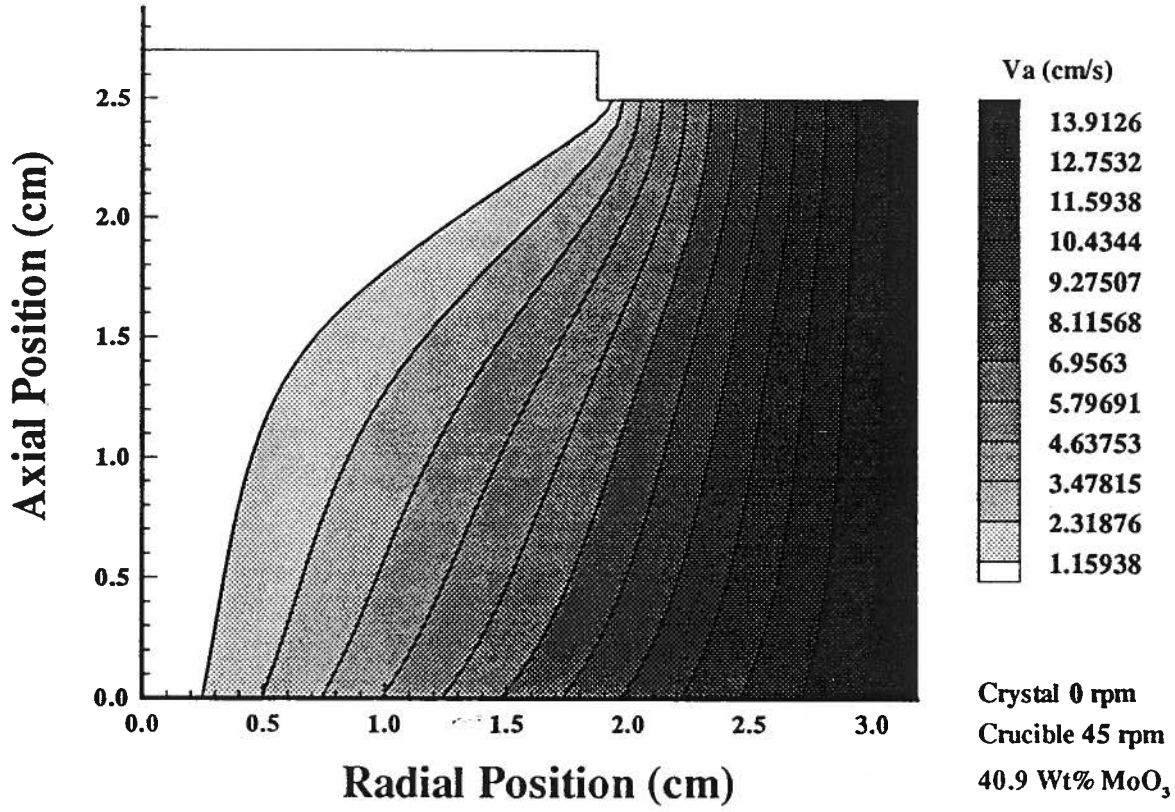

Figure 9.87: Rotational velocity plot of the LBO/MoO_3 melt with crucible rotation.

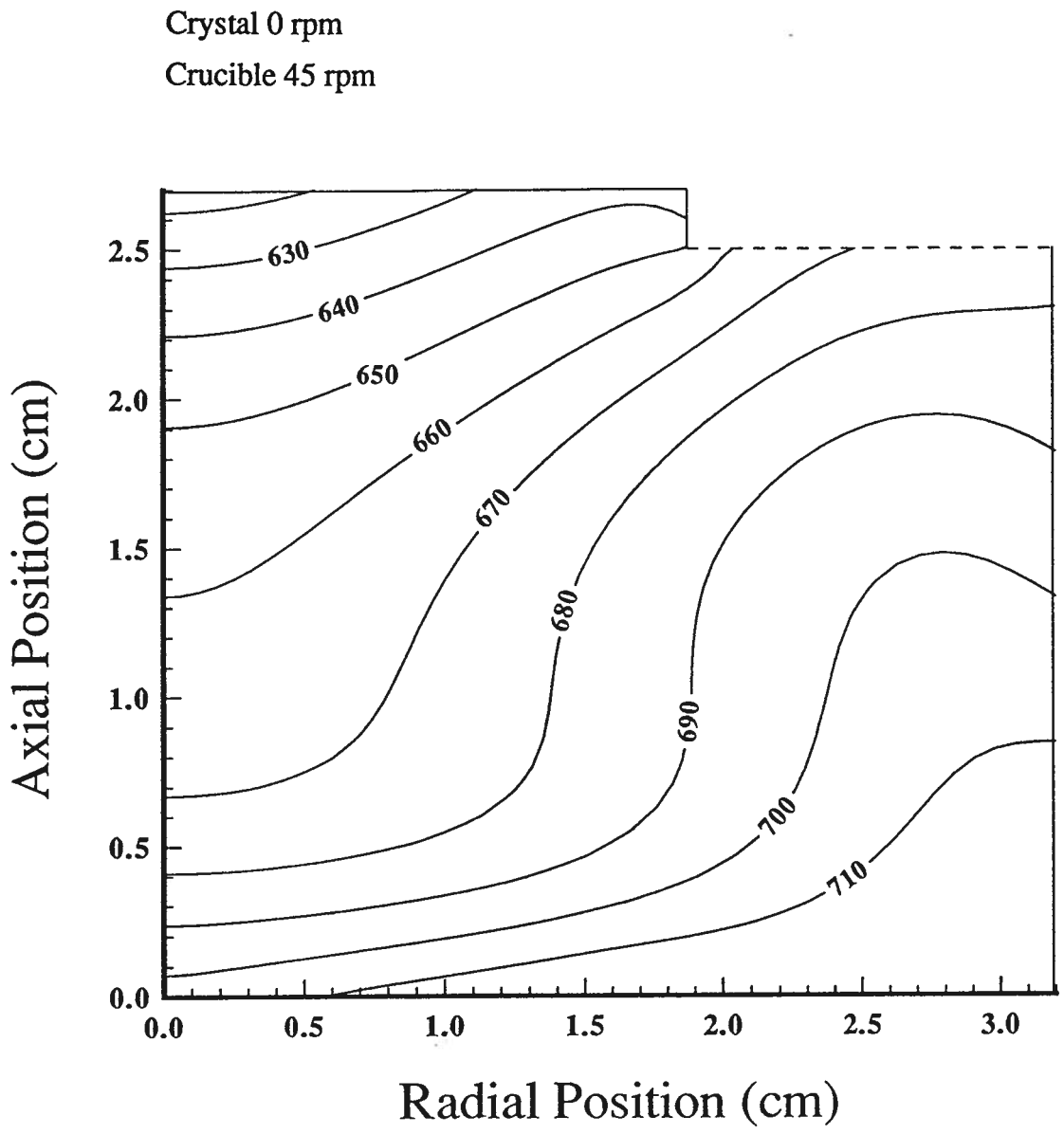

Figure 9.88: Temperature contours that occur in the LBO/MoO_3 melt with crucible rotation.

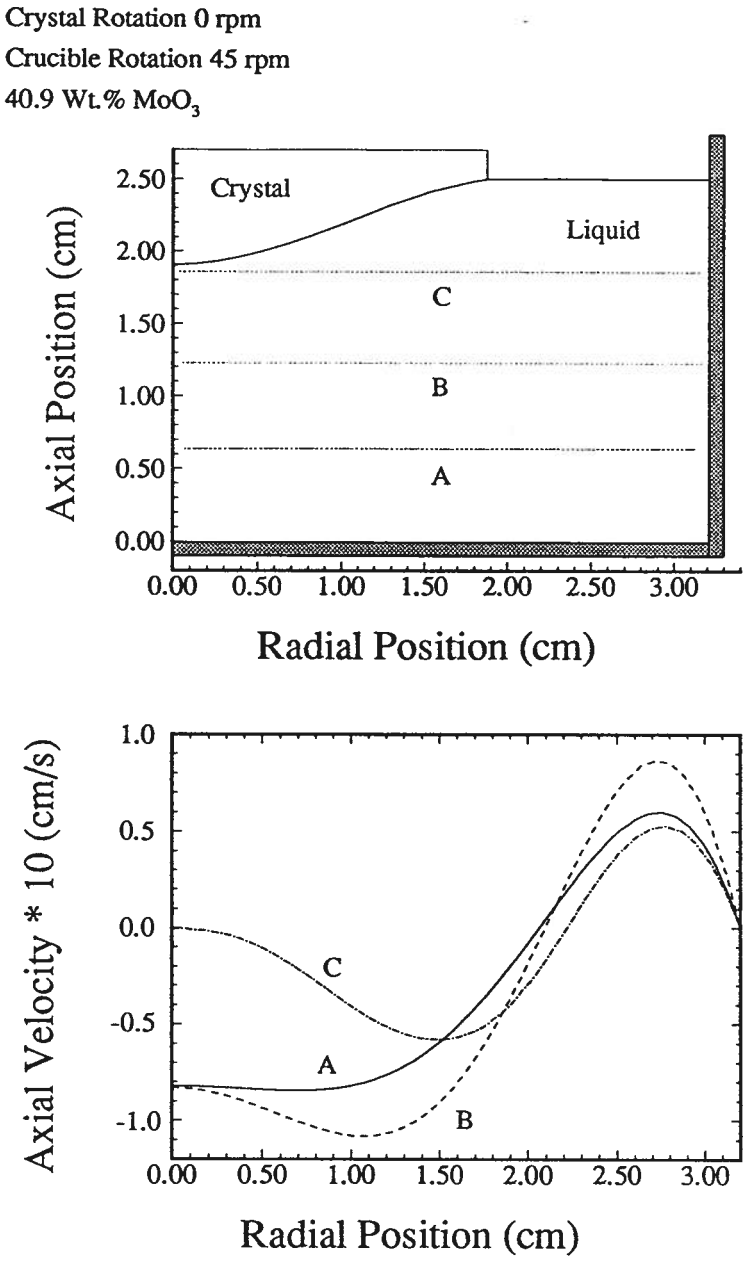

Figure 9.89: Axial velocity due to crucible rotation.

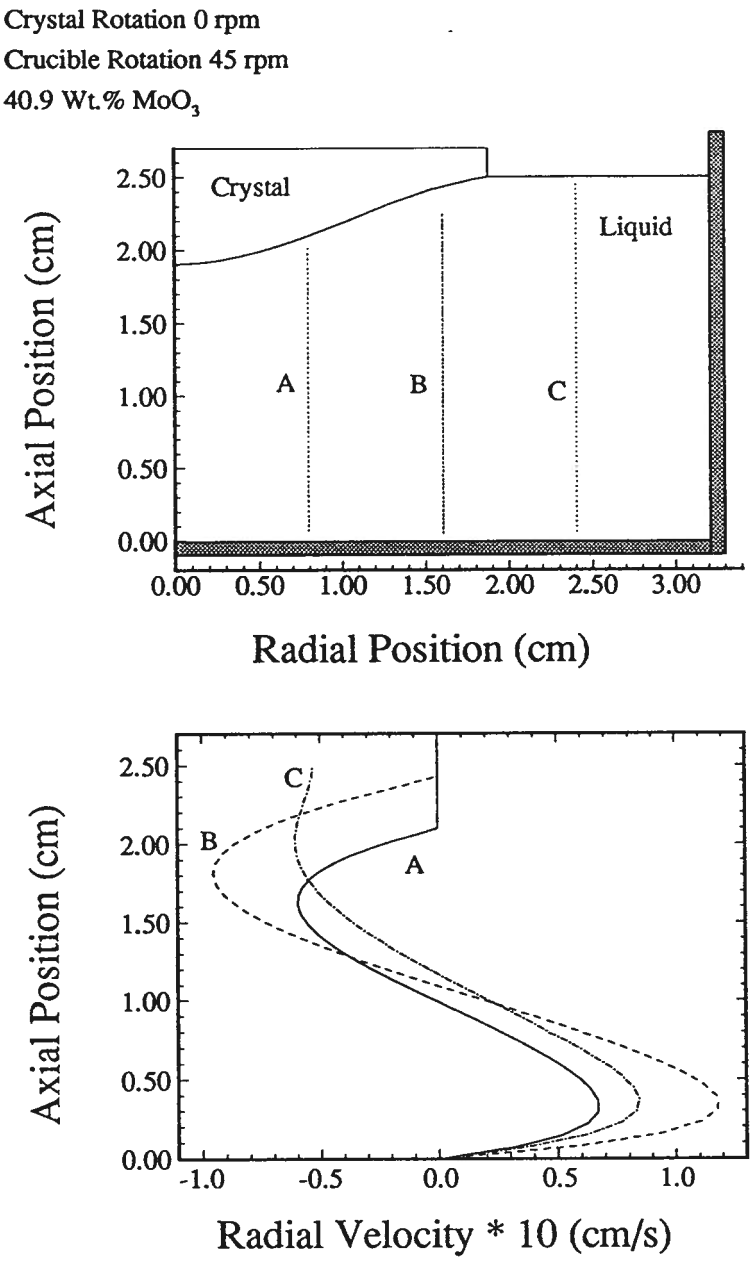

Figure 9.90: Radial velocity due to crucible rotation.

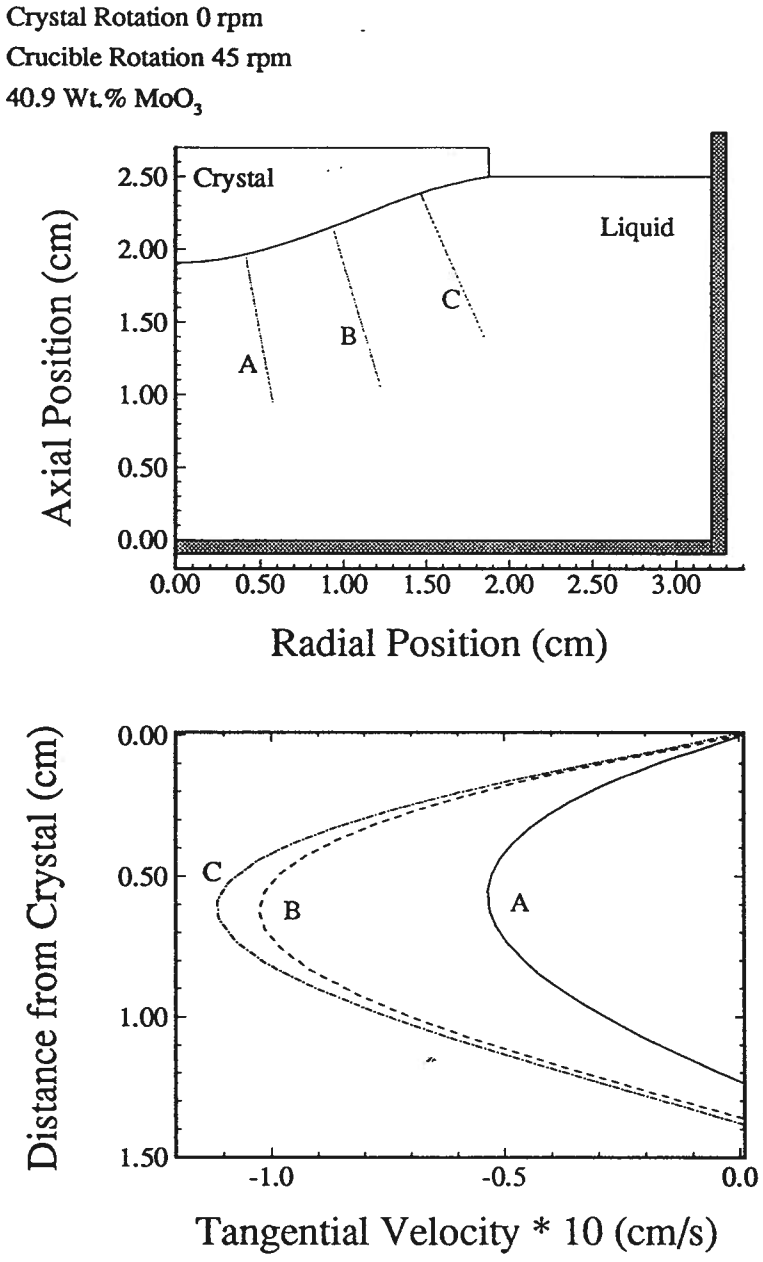

Figure 9.91: Tangential crystal surface velocity due to crucible rotation.

(a)

(b)

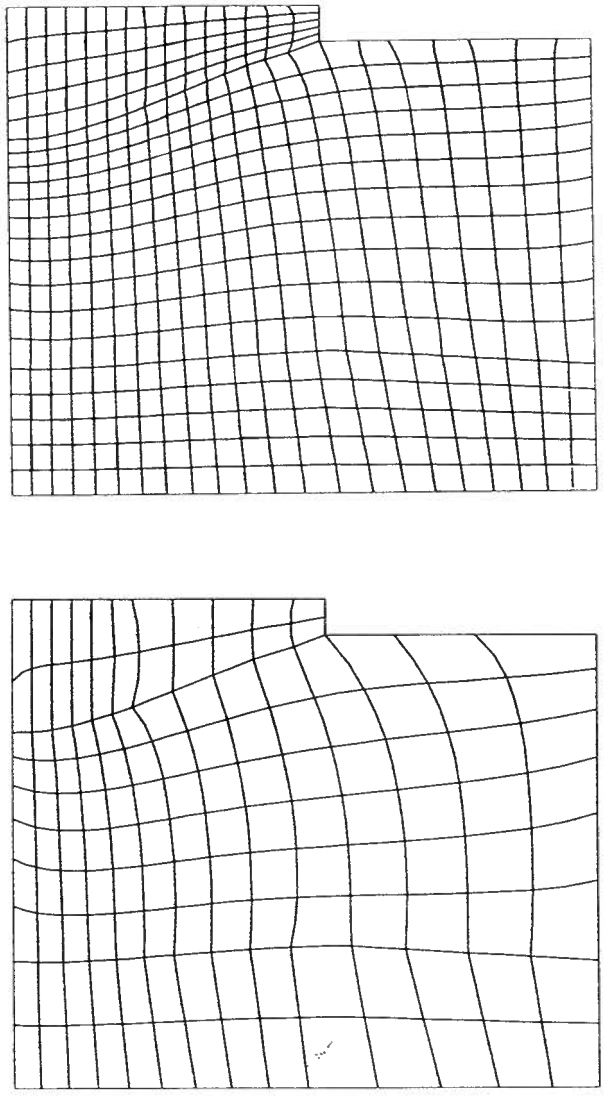

Figure 9.92: Two mesh densities used to examine the models sensitivity. (a) Regular mesh density, approximately 1795 nodes. (b) Coarse mesh density, approximately 585 nodes

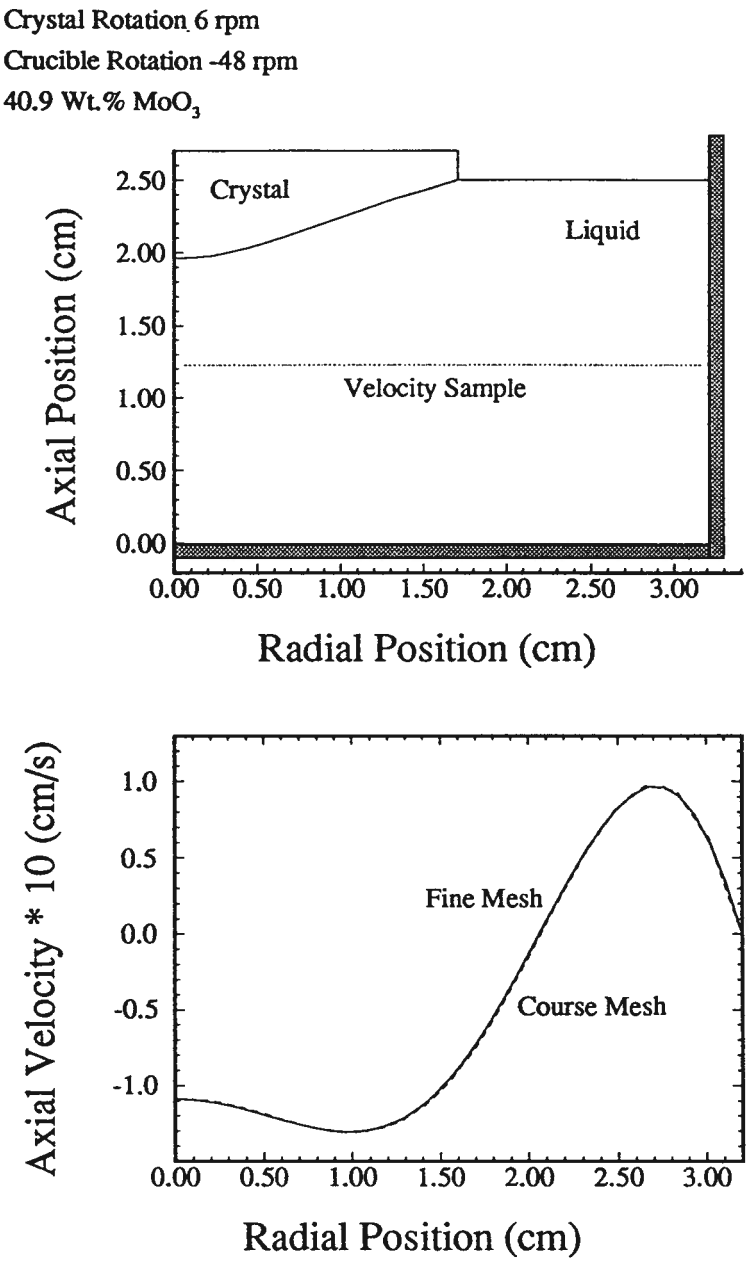

Figure 9.93: Axial velocity for different mesh densities.

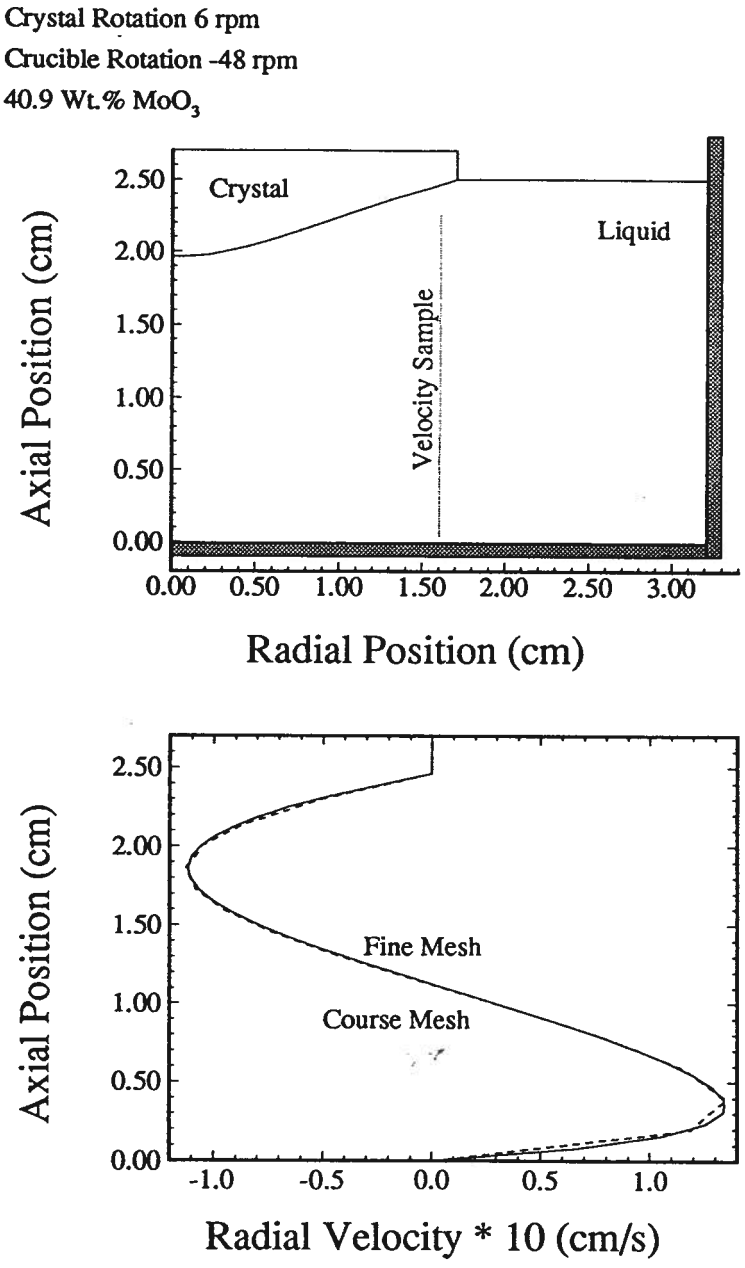

Figure 9.94: Radial velocity for different mesh densities.

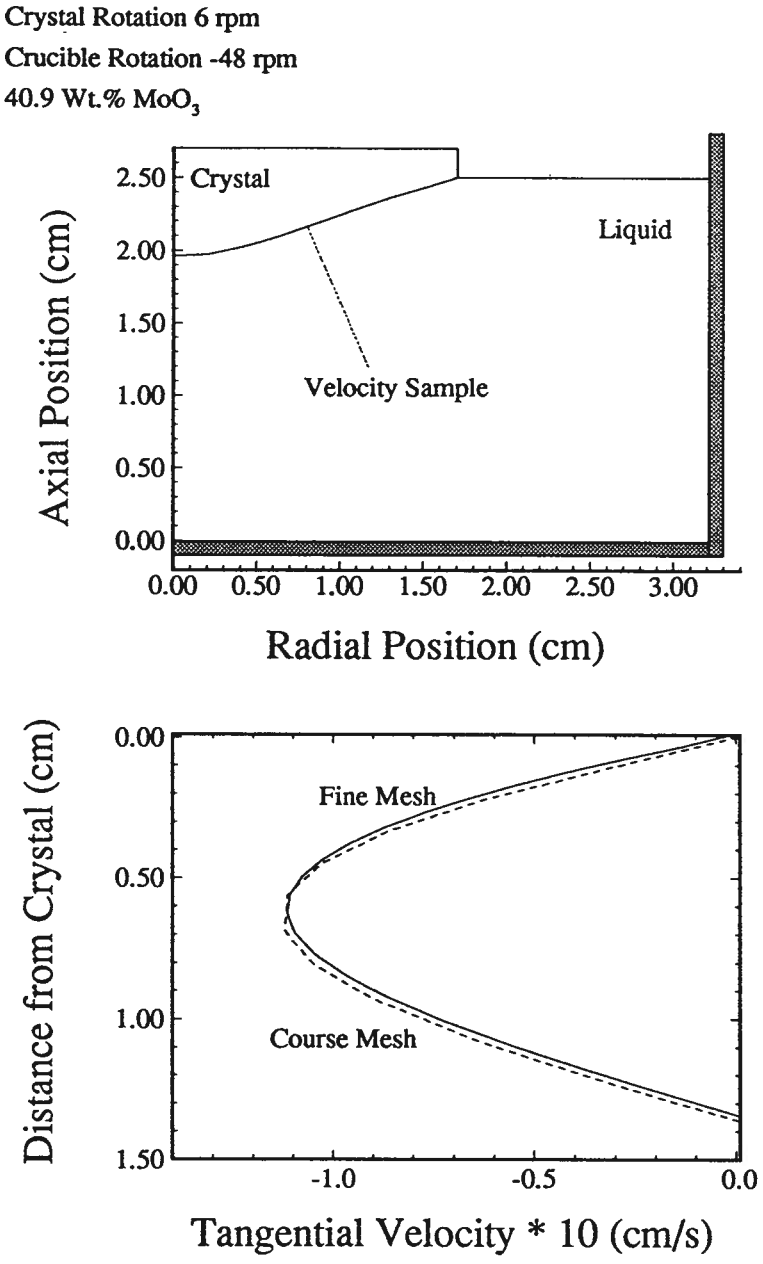

Figure 9.95: Tangential crystal surface velocity for different mesh densities.

the crystal. Increasing the viscosity of the melt from 12 poise (40.9 Wt% MoO_3) to 30 poise (36.2 Wt% MoO_3) decreases the magnitude of the axial velocity by a factor of 4. Increasing the viscosity to 86 poise (29.7 Wt% MoO_3) effectively reduces the velocity to zero. The corresponding radial and tangential calculated flow velocities for the viscosities considered are shown in Figure 9.97 and 9.98. For both the radial and tangential velocities the velocities are shown to be strongly reduced as the melt viscosity is increased. Clearly, the melt viscosity/MoO_3 concentration is a significant factor in calculating fluid flow in an LBO/MoO_3 melt.

9.5 Conductivity

The effect of thermal conductivity on the melt temperatures and velocities was examined. Three melt thermal conductivities were considered, 0.04, 0.05 and 0.06 W/cm K. The conductivities of the crystal and the melt was assumed to be the same. Calculations were carried out for a crystal rotation of 6 rpm and crucible rotation of -12 rpm. The resulting calculated temperature profiles at 0.5 of the crucible radius are shown in Figure 9.99. The axial temperature gradient is observed to decrease progressively with increasing conductivity. The interface position changes by 2 mm with a 20% change in conductivity. Changing the conductivity does not change the temperature at the bottom of the crucible, since it is a fixed temperature boundary condition.

The corresponding axial, radial and tangential melt velocities are shown in Figures 9.100, 9.101, and 9.102 respectively. The axial velocity (Figure 9.100) is observed to increase significantly with increasing conductivity. The change in axial velocity is due to the change in crystal size. The crystal size increases in the axial direction with decreasing conductivity, moving the zero velocity boundary condition at the crystal/fluid interface closer to the axial velocity sample location. The sample velocity will decrease the closer

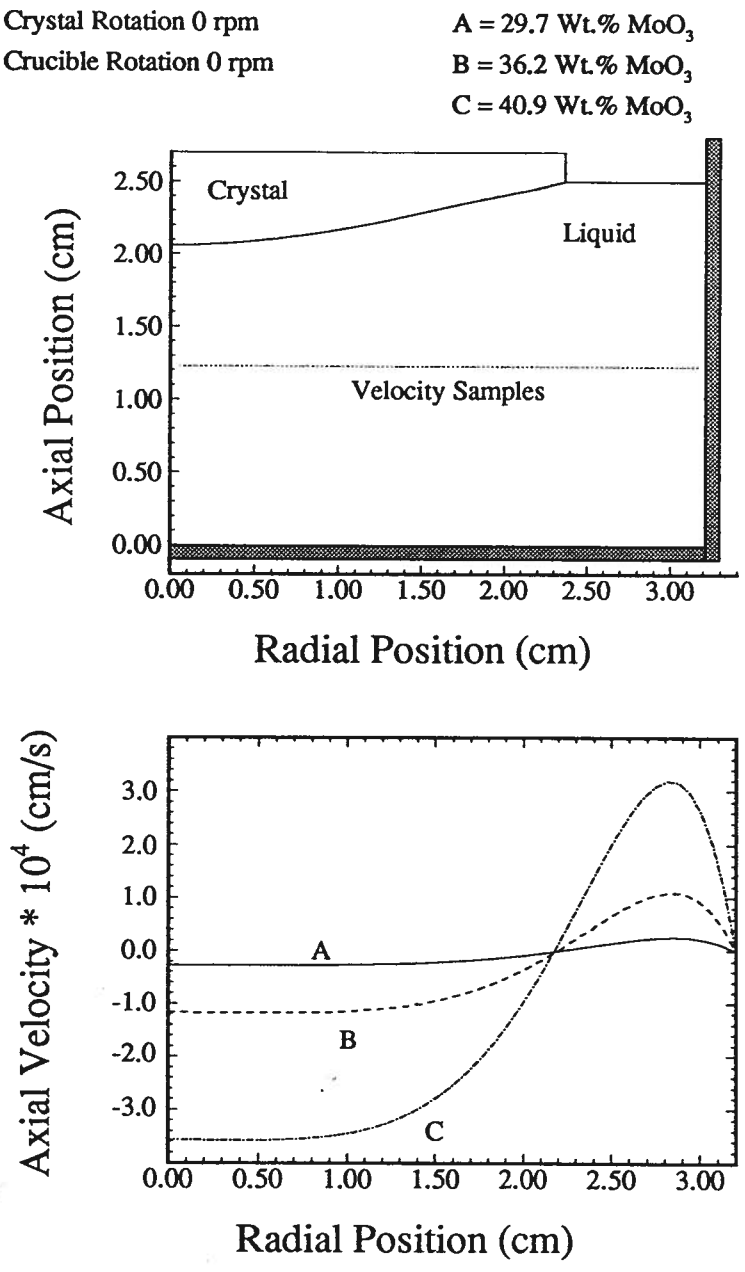

Figure 9.96: Axial velocity for different viscosities.

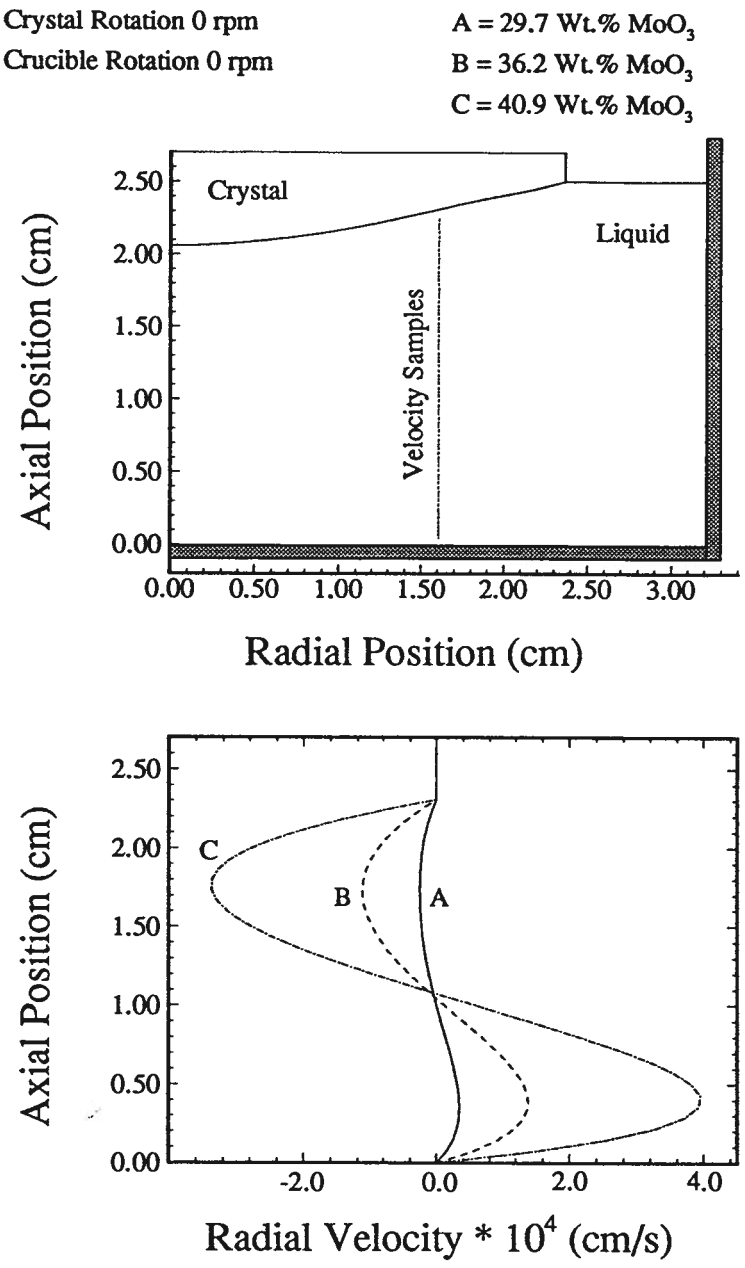

Figure 9.97: Radial velocity for different viscosities.

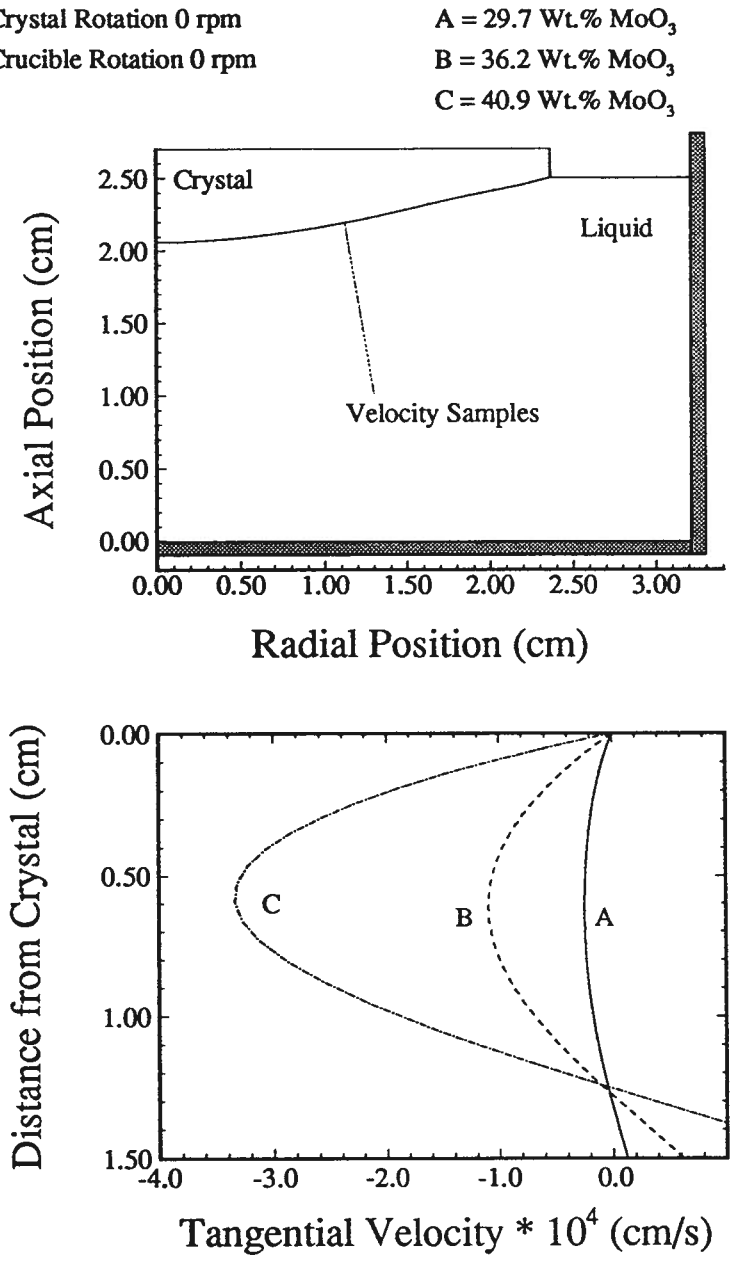

Figure 9.98: Tangential crystal surface velocity for different viscosities.

the zero velocity boundary condition gets to the sample location.

The radial velocity, Figure 9.101, and tangential velocity, Figure 9.102, are also observed to increase with increasing conductivity. However, the change in velocity at these locations is smaller than the change in the axial velocity. The decrease in the radial and tangential velocity is believed, again, to be due to the increase in crystal radius.

The value of the conductivity has a significant affect on the thermal fields in the melt and less of an effect in the liquid velocity fields.

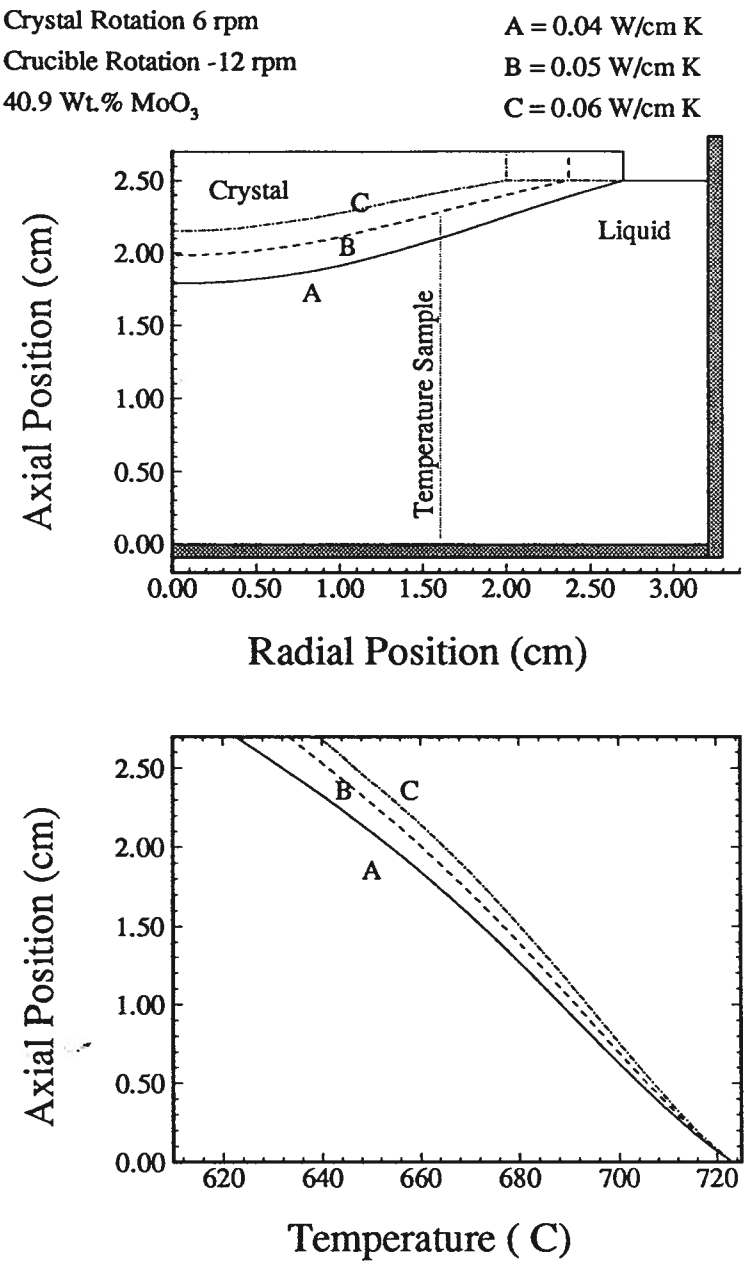

Figure 9.99: Axial temperature profiles for different conductivities.

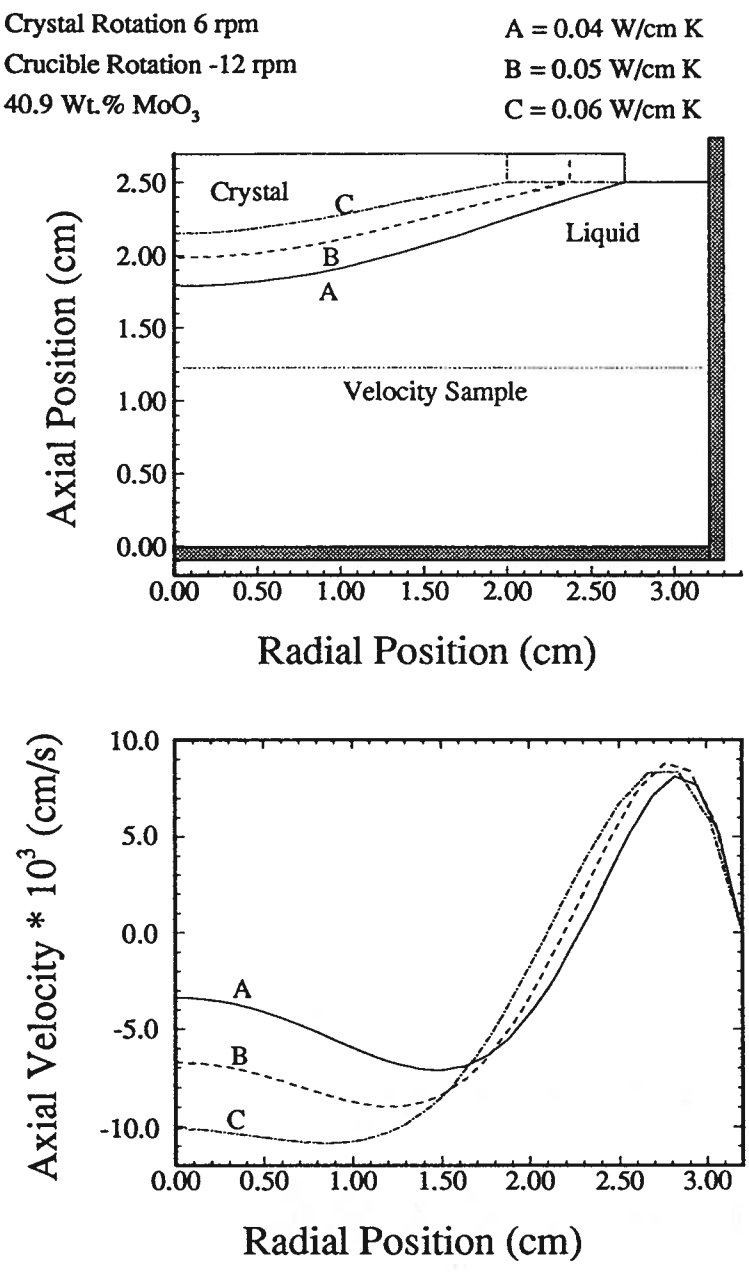

Figure 9.100: Axial velocity for different conductivities.

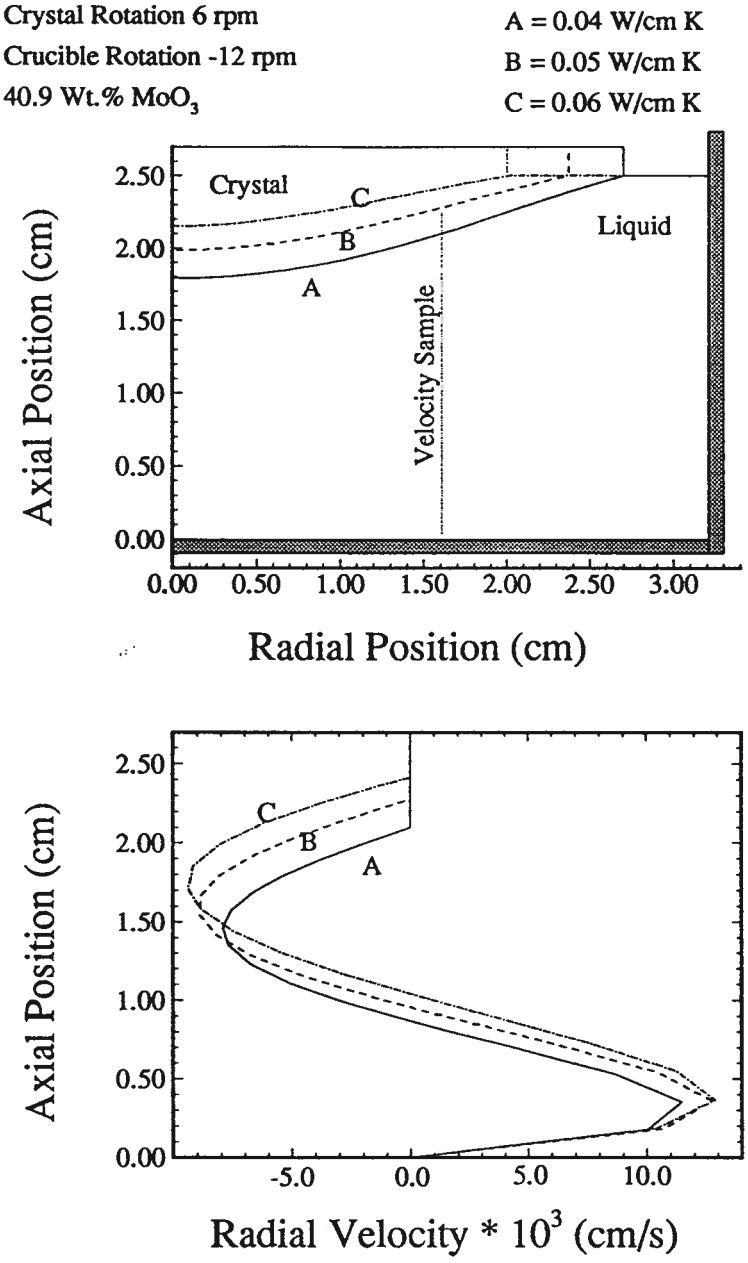

Figure 9.101: Radial velocity for different conductivities.

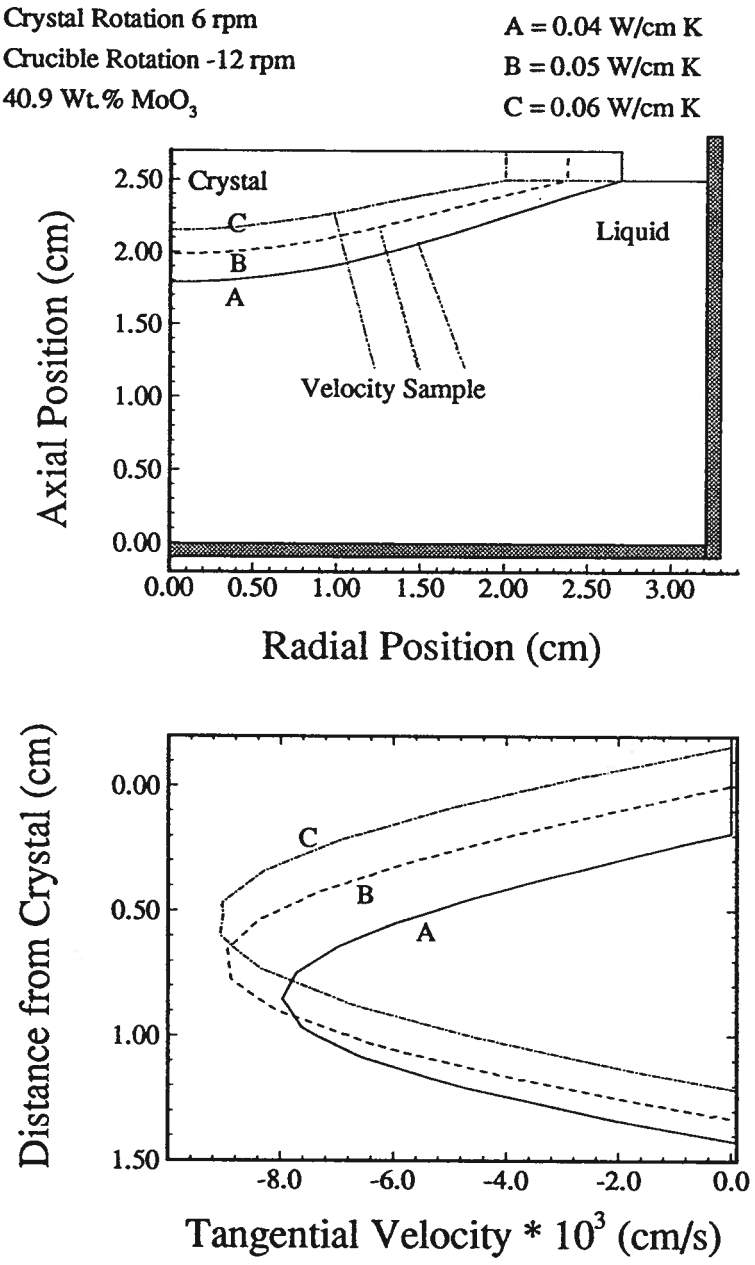

Figure 9.102: Tangential crystal surface velocity for different conductivities.

Chapter 10

Modeling Results

The mathematical model was used to examine the effect of crystal and crucible rotation rates and crucible size on the interface shape and fluid velocity fields. The analysis in Chapter 9 indicates that the fluid velocity decreases rapidly with increasing melt viscosity. To obtain reasonable flow rates from the calculations, the minimum melt viscosity was selected by using a MoO_3 concentration of 40.9 wt% in the melt, based on the composition at 698°C in Figure 5.40. The values of the thermophysical properties used are given in Table 10.15, the same values used in the sensitivity analysis. A small crucible (6.6 cm diameter) was used for all but one calculation. The large crucible dimensions were used in comparing the flow fields in a large and small crucible with the same crucible rotation rates. The temperature boundary conditions are the same as those used in the sensitivity analysis and are given in Figure 10.103. The boundary conditions used with the large crucible are given in Figure 10.104. The crucible and crystal rotation rates examined are given in Table 10.16.

Crystal rotation influences the shape of the solid/liquid interface. The calculations with only crystal rotation were directed towards determining the rotation rate which results in the interface becoming concave to the liquid, due to the upward flow of hot liquid under the crystal. Crucible rotation also influences the shape of the solid/liquid interface. Crucible rotation causes the cold liquid under the crystal to move downward. This will result in the solid/liquid interface becoming convex to the liquid. The calculations with only crucible rotation were to determine maximum rotation rate before the crystal

Property	Units	Values
Specific Heat	J/g K	0.63
Density	g/cm^3	3.26
Viscosity for 40.9 Wt% MoO_3	poise	$exp\,(37.31 - 0.0784 \times T[C] + 4.21 \times 10^{-5} \times (T[C])^2)$
Conductivity	W/cm K	0.05
Liquidus	Celsius	698
Expansion Coefficient (β)	K^{-1}	6×10^{-6}

Table 10.15: Thermophysical properties used in the results analysis.

becomes extremely concave to the melt. Modeling a large rotating crucible (8.8 cm diameter) with a stationary crystal was to determine the affect that the crucible size has on the flow due to crucible rotation. Combined crystal and crucible rotation will create different flow fields than what occurs with only crucible or crystal rotation. Thus, combined crystal and crucible rotation rates were examined to determine the resulting flow fields that occurred. Both isorotation and counter rotation of the crucible and crystal are examined to determine their affect on the flow fields in the melt.

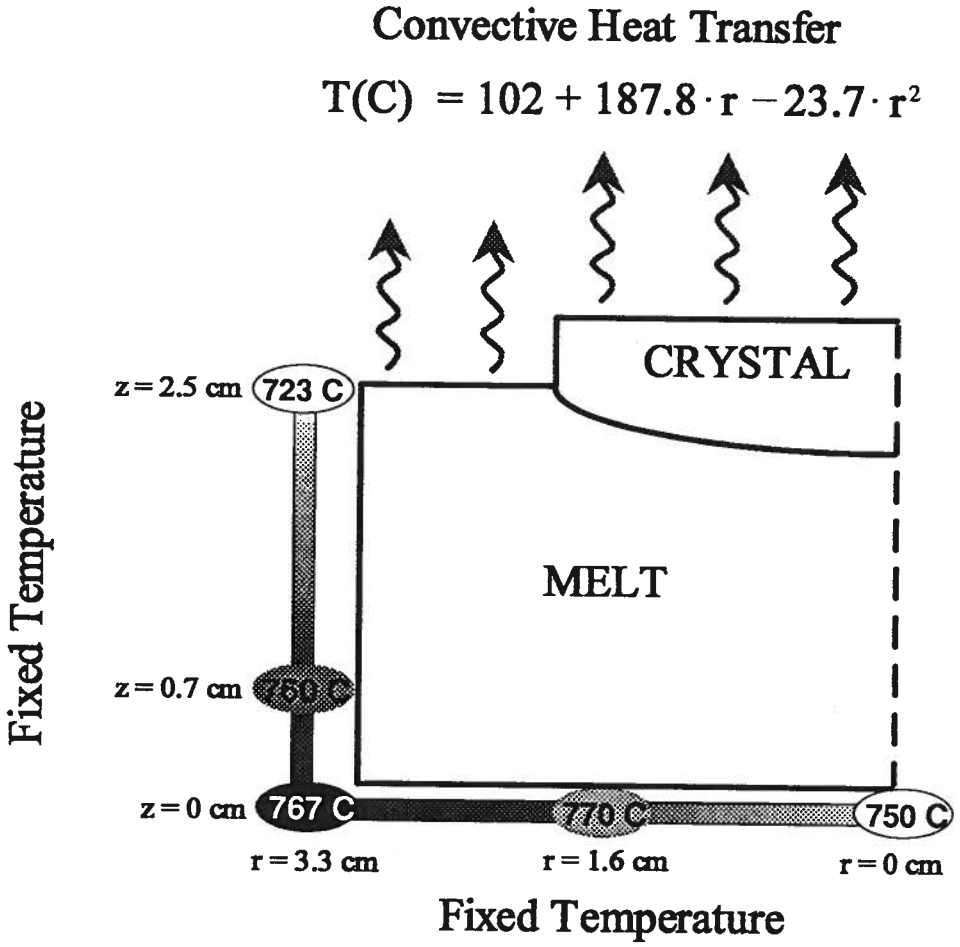

Figure 10.103: Small crucible temperature boundary conditions used in the results analysis.

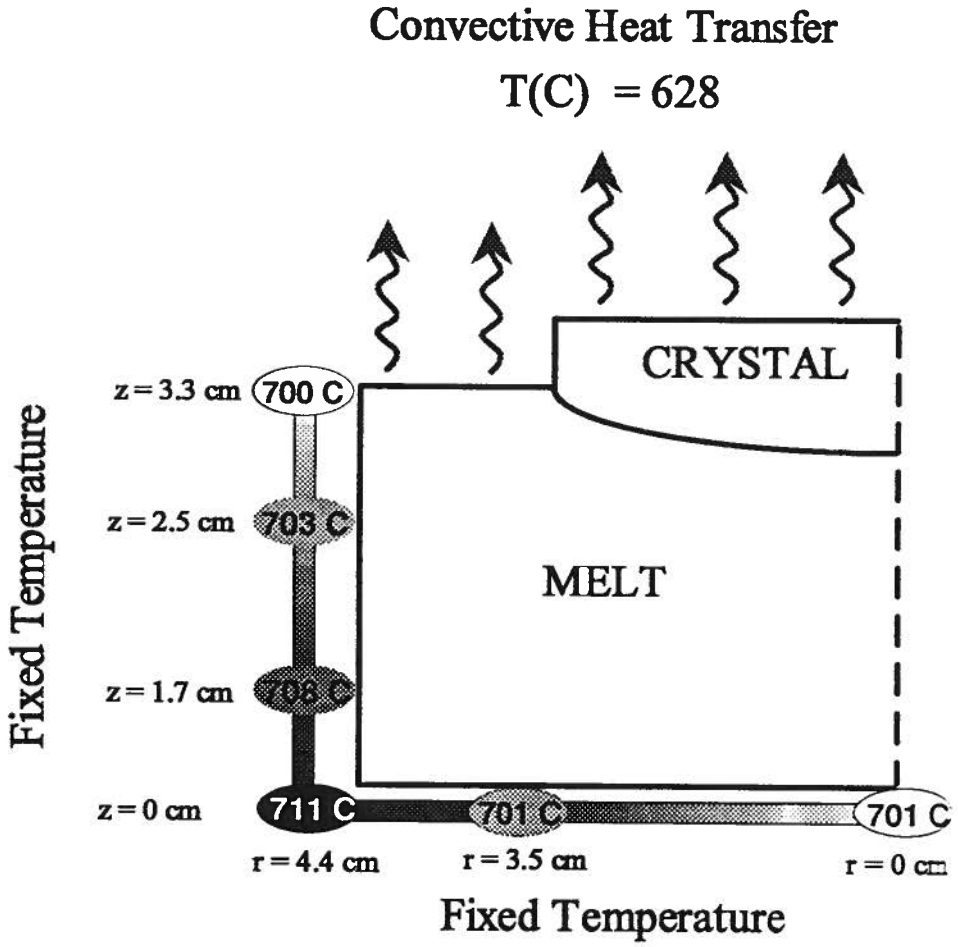

Figure 10.104: Large crucible temperature boundary conditions used in the results analysis.

Mixing Conditions	Crucible Size	Units	Values
Crystal Rotation and no Crucible Rotation			
Crystal Rotation	small	rpm	0, 10, 20
Crucible Rotation		rpm	0
Crucible Rotation and no Crystal Rotation			
Crystal Rotation	small	rpm	0
Crucible Rotation		rpm	0, 20, 40, 60
Crystal Rotation	large	rpm	0
Crucible Rotation		rpm	60
Isorotation of Crystal and Crucible			
Crystal Rotation	small	rpm	10
Crucible Rotation		rpm	30
Counter Rotation of Crystal and Crucible			
Crystal Rotation	small	rpm	10
Crucible Rotation		rpm	−30

Table 10.16: Parameters examined for the mathematical model analysis.

10.1 Crystal Rotation

The effect of varying the crystal rotation rate on the temperature and velocity fields was examined. For these calculations the crystal rotation rates were 0, 10 and 20 rpm and the crucible rotations were zero. The solid/liquid interface and the axial velocities for the three rotation rates at 0.5 of the fluid height are shown in Figure 10.105(b). The axial liquid velocity of the melt at zero crystal rotation is negative at -3×10^{-4} cm/s under the crystal. Increasing the crystal rotation rates causes the flow direction to change and move upward under the crystal and down at the side of the crucible. At 10 rpm the fluid velocity is 1.0×10^{-2} cm/s below the crystal and -4.0×10^{-3} cm/s near the crucible wall. At 20 rpm the fluid velocity is 6.8×10^{-2} cm/s under the crystal and -2.4×10^{-2} cm/s near the crucible wall. The solid/liquid interface, shown in Figure 10.105(a), moves upward and becomes flat with increasing crystal rotation, due to the increase in hot fluid moving upward below the crystal at higher rotation rates. The model predicts that the

solid/liquid interface becomes concave to the melt at rotation rates larger than 20 rpm.

The flow velocities in the radial direction at 0.5 of the the crucible radius are shown in Figure 10.106(b). The radial velocities below the crystal are -3×10^{-4} cm/s, 8×10^{-2} cm/s and -4.4×10^{-2} cm/s for crystal rotation rates of 0, 10 and 20 rpm respectively. The radial fluid velocities near the bottom of the crucible are 3×10^{-4} cm/s, -7×10^{-2} cm/s and -3.8×10^{-2} cm/s for crystal rotation rates of 0, 10 and 20 rpm. The magnitude of the fluid velocity under the crystal is larger than the velocity near the crucible bottom for a given rotation rate, the crystal rotation being the dominant mechanism for the fluid motion.

The velocity tangential to the crystal surface at 0.5 of the radius of the crystal is shown if Figure 10.107(b). The fluid velocity tangential to the crystal interface increases with increasing crystal rotation. The velocities are 3×10^{-4} cm/s, 0.9×10^{-2} cm/s and 4.1×10^{-2} cm/s for crystal rotation rates of 0, 10 and 20 rpm.

10.2 Crucible Rotation

The thermal and fluid velocity fields were calculated with crucible rotation to determine the effect of the rotation rate on the shape of the solid/liquid interface and the magnitude of the fluid velocities. Crucible rotation rates of 0, 20, 40 and 60 rpm, with no crystal rotation, were examined. The axial fluid velocities along a radial line at 0.5 of the fluid height are shown in Figure 10.108. The axial velocity directly under the crystal is near constant increasing from -3.2×10^{-2}, -2.2×10^{-1}, and -3.3×10^{-1} cm/s for crucible rotation rates of 20, 40 and 60 rpm. The smallest change occurs between crucible rotation rates of 0 and 20 rpm. The axial velocity upward near the crucible wall increases with increasing crucible rotation being 4.4×10^{-2}, 1.2×10^{-1} and 1.4×10^{-1} cm/s for rotation rates of 20, 40 and 60 rpm. The largest increase in axial velocity at this location occurs

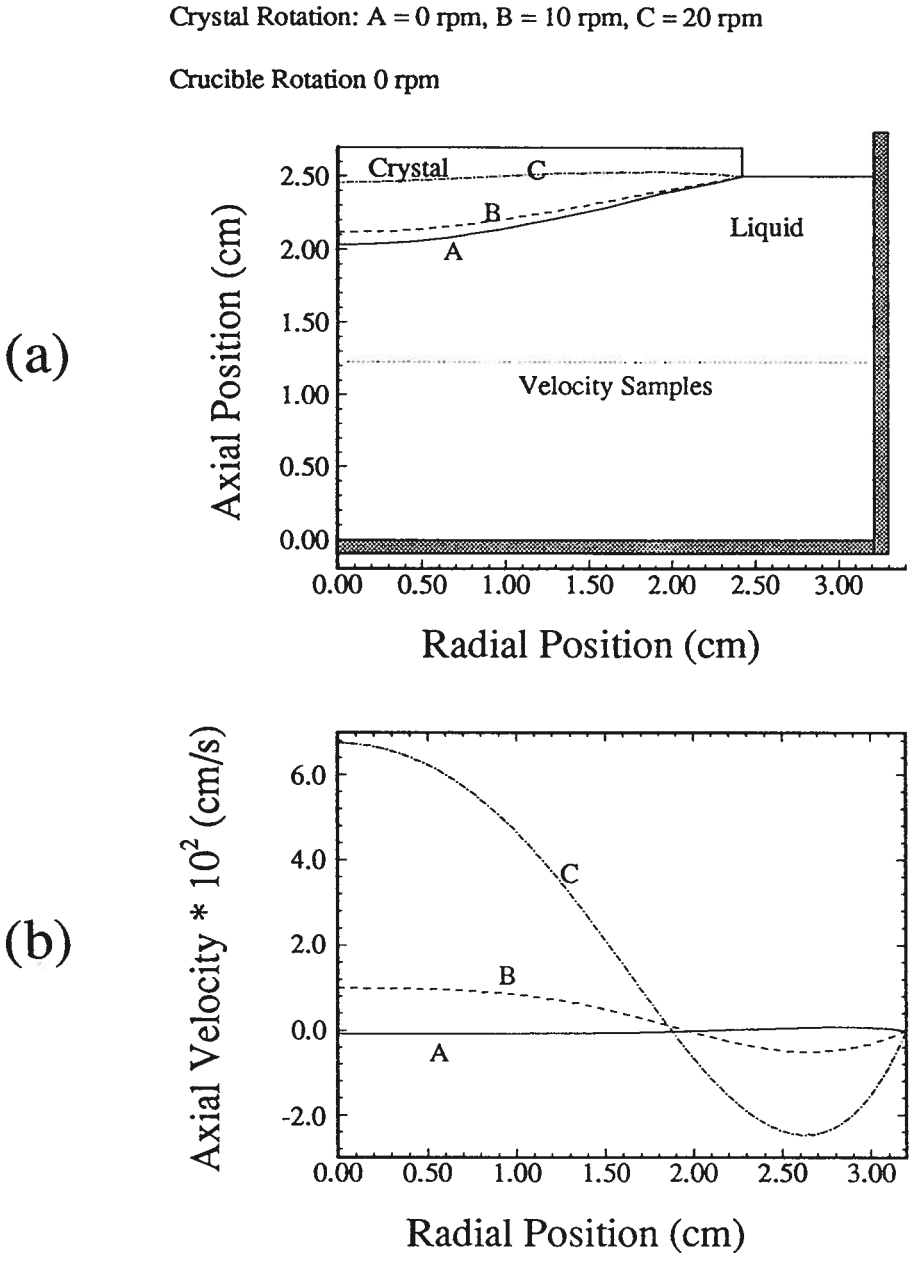

Figure 10.105: Axial velocities at 0.5 of the fluid height. 40.9 Wt% MoO_3 present in the fluid. Crystal rotated at 0, 10, and 20 rpm. Crucible is stationary. (a) Shape of the solid/liquid interface. (b) Axial Velocities.

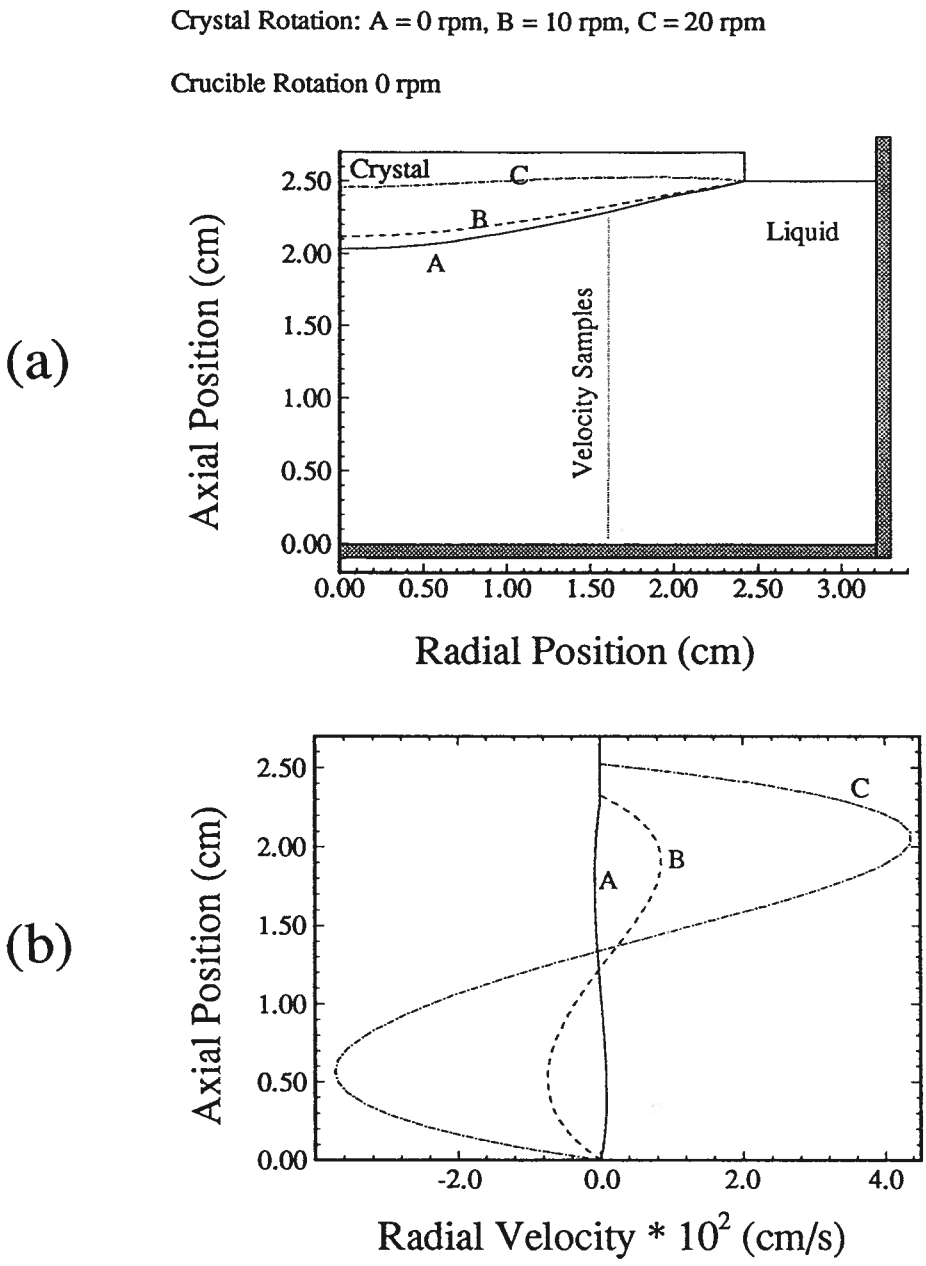

Figure 10.106: Radial velocities at 0.5 of the crucible radius. 40.9 Wt% MoO_3 present in the fluid. Crystal rotated at 0, 10 and 20 rpm. Crucible is stationary. (a) Shape of the solid/liquid interface. (b) Radial velocities.

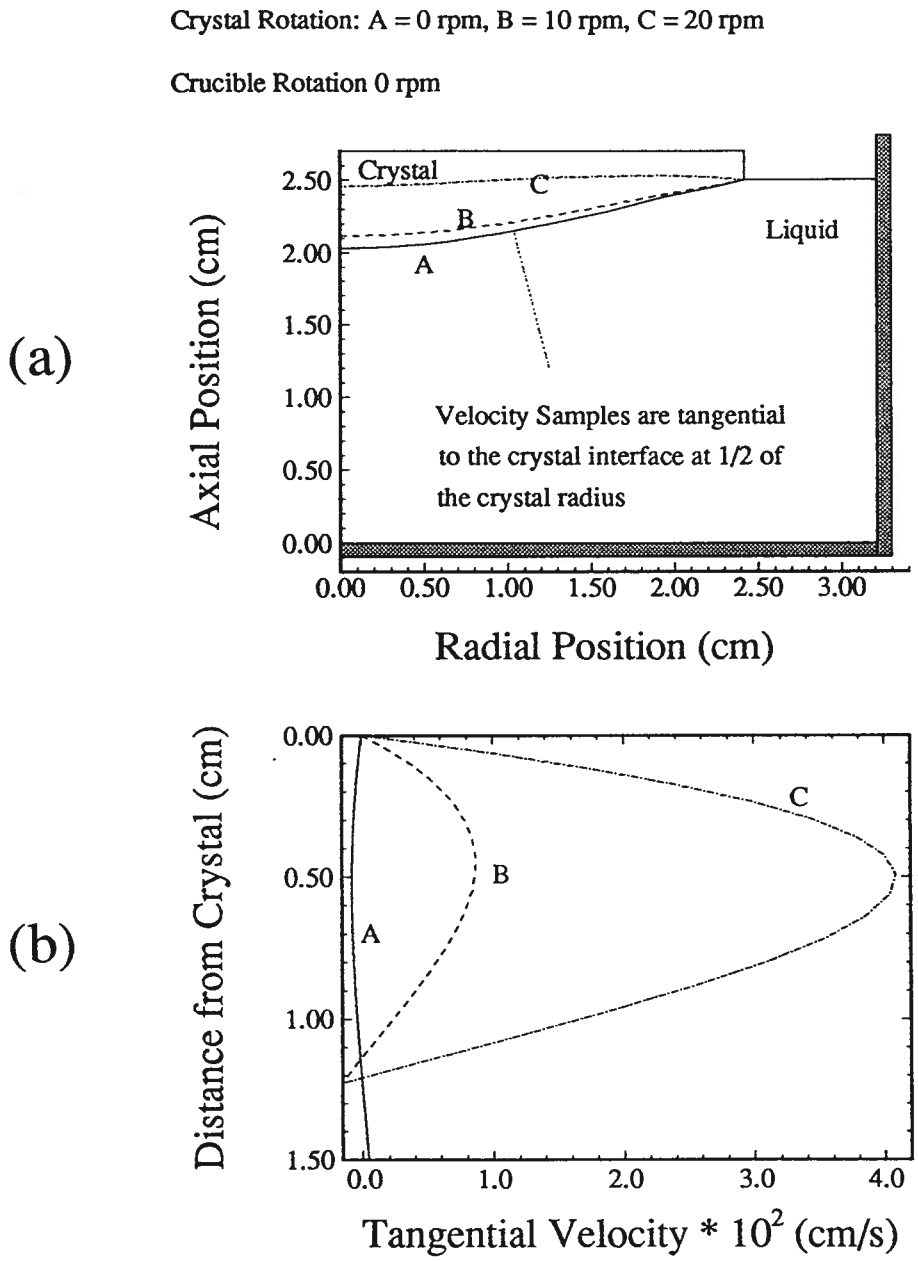

Figure 10.107: Velocities tangential to the crystal surface 0.5 of the crystal radius. 40.9 Wt% MoO_3 present in the fluid. Crystal rotated at 0, 10 and 20 rpm. Crucible is stationary. (a) Shape of the solid/liquid interface. (b) Tangential velocities.

between 40 and 60 rpm. The curvature of the crystal increases with increased crucible rotation, becoming more concave to the liquid. This is due to movement of hot fluid upward at the crucible wall and downward below the crystal. Increasing the crucible rotation rate causes the crystal to get smaller maintaining the same interface shape. The radius of the crystal is 2.4, 2.3, 1.6 and 1.1 cm for crucible rotation rates of 0, 20, 40 and 60 rpm respectively.

The radial velocities along a horizontal line at 0.5 of the crucible radius is shown in Figure 10.109. The radial fluid velocities near the bottom of the crucible are 0.6×10^{-1}, 1.7×10^{-1} and 2.3×10^{-1} cm/s for crucible rotation rates of 20, 40 and 60 rpm. The radial velocities near the surface are -0.5×10^{-1}, -1.5×10^{-1} and 2.2×10^{-1} cm/s for crucible rotations of 20, 40 and 60 rpm. The radial velocities near the crucible bottom are higher than the velocities near the surface since crucible rotation produces the fluid motion. The fluid velocity tangential to the crystal surface are shown in Figure 10.110(b). The tangential velocities are -0.5×10^{-1}, -1.6×10^{-1} and -2.1×10^{-1} for crucible rotation rates of 20 40 and 60 rpm.

10.3 Comparison of Crystal to Crucible Rotation

Fluid velocities are determined for a crystal rotating at 20 rpm with a stationary crucible. and a crucible rotating at 20 rpm with a stationary crystal. The magnitude of the axial velocities along a radial line at 0.5 of the fluid height are shown in Figure 10.111. The magnitude of the axial fluid velocity below the crystal is largest with crystal rotation decreasing from 6.8×10^{-2} cm/s at the centre line to zero at a radial position of 1.85 cm. The flow below the crystal due to crucible rotation is a maximum at 1.2 cm from the centre of the crucible, with a velocity of 4.8×10^{-2} cm/s. The axial flow velocity near the crucible wall is 2.4×10^{-2} and 4.4×10^{-2} cm/s for crucible and crystal rotation

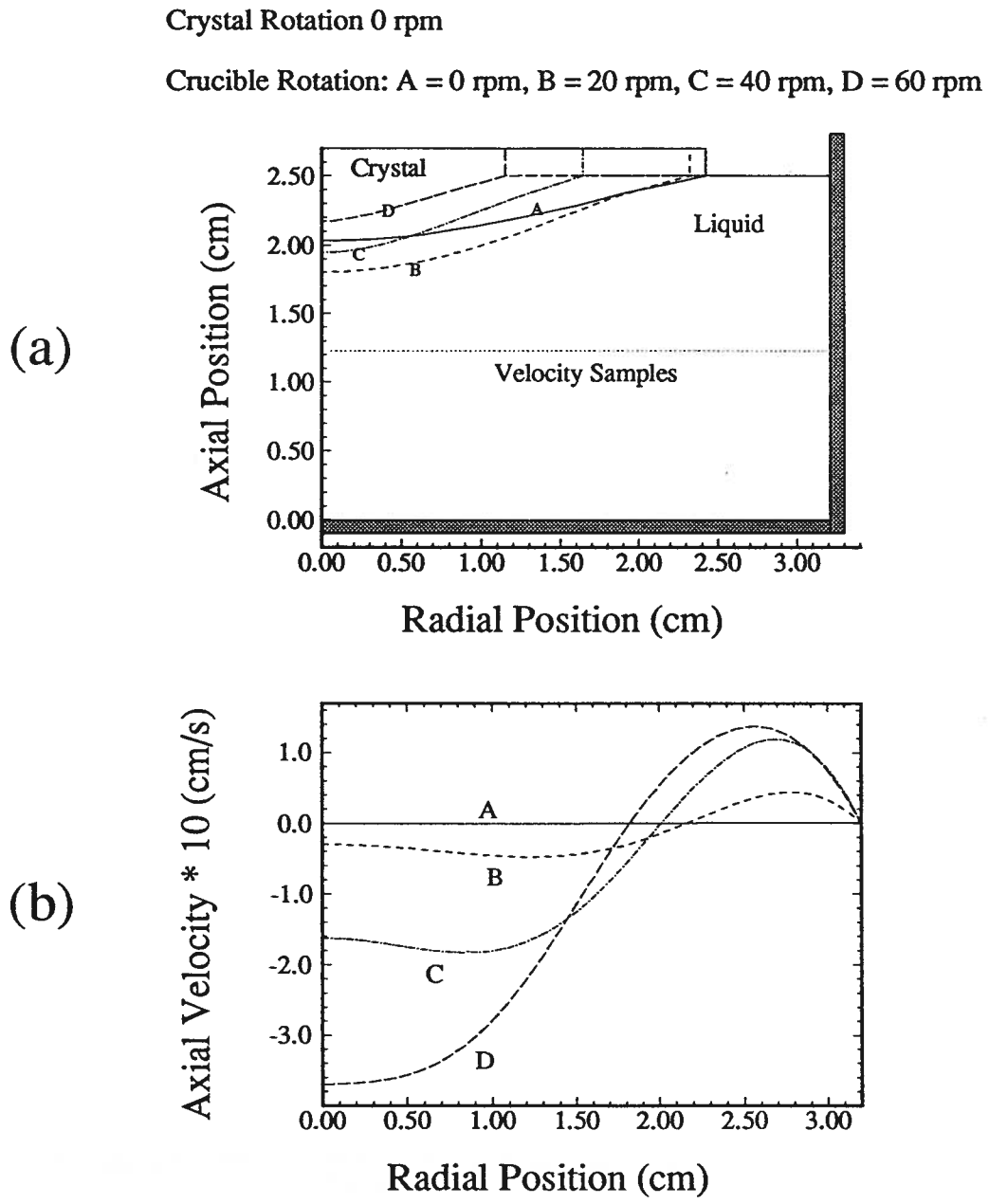

Figure 10.108: Axial velocities at 0.5 of the fluid height. 40.9 Wt% MoO_3 present in the fluid. Crucible rotated at 0, 20, 40, and 60 rpm. Crystal is stationary. (a) Shape of the solid/liquid interface. (b) Axial velocities.

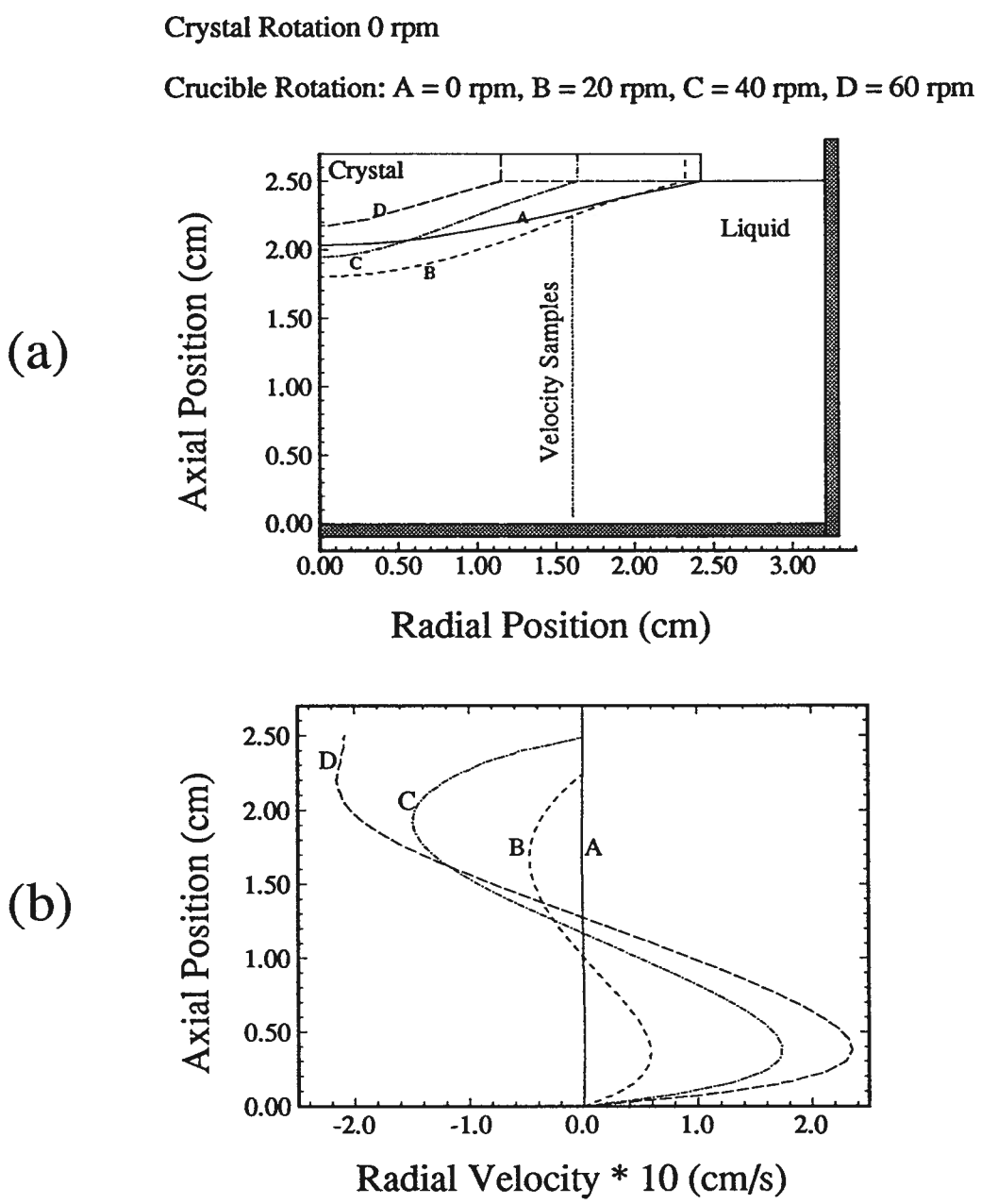

Figure 10.109: Radial velocities at 0.5 of the crucible radius. 40.9 Wt% MoO_3 present in the fluid. Crucible rotated at 0, 20, 40, and 60 rpm. Crystal is stationary. (a) Shape of the solid/liquid interface. (b) Radial velocities.

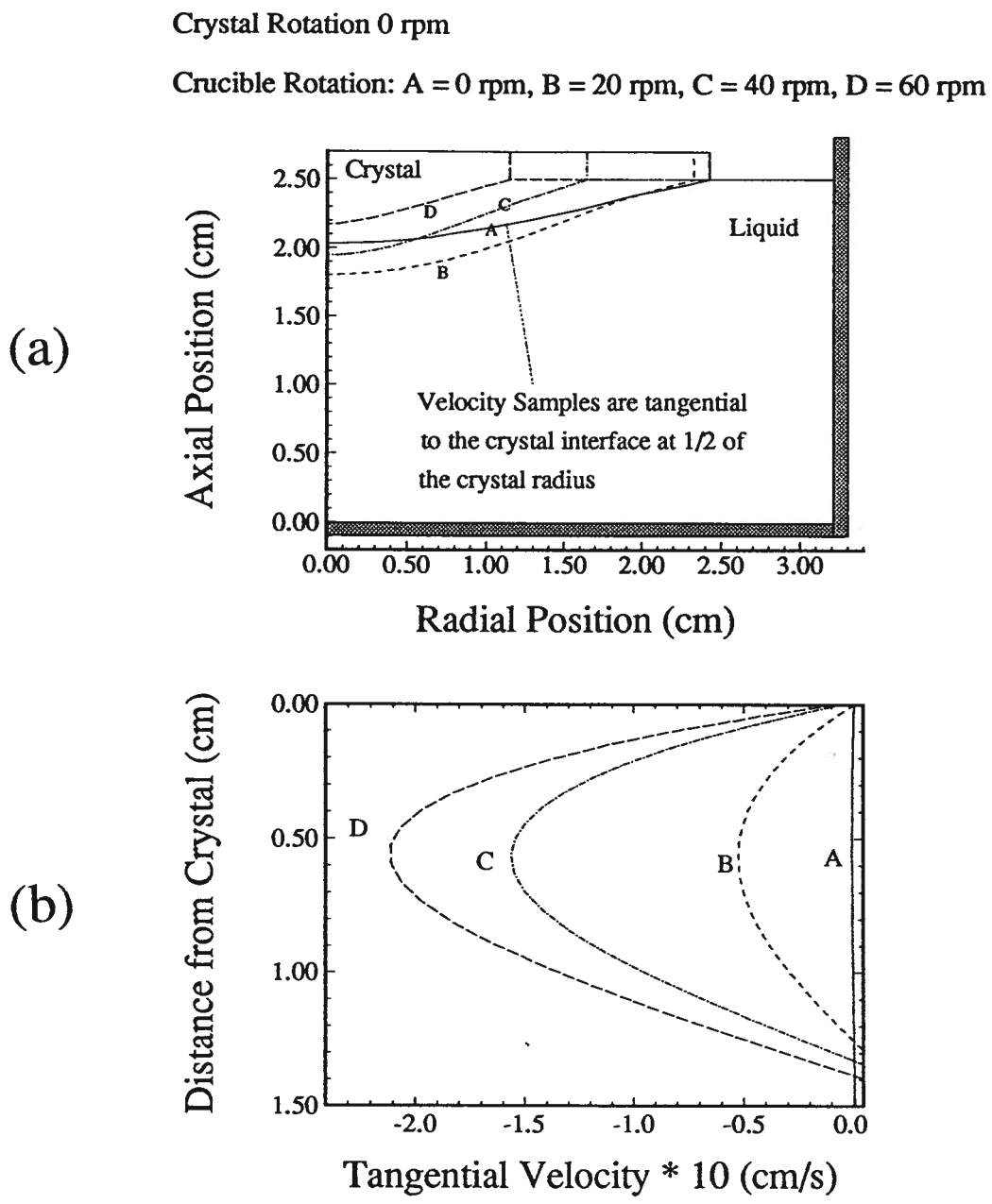

Figure 10.110: Velocities tangential to the crystal surface 0.5 of the crystal radius. 40.9 Wt% MoO_3 present Crucible rotated at 0, 20, 40, and 60 rpm. Crystal is stationary. (a) Shape of the solid/liquid interface. (b) Tangential velocities.

respectively.

The radial fluid velocities along a vertical line at 0.5 of the crucible radius are shown in Figure 10.112. The velocities near the crystal are approximately the same value for each rotation method. The radial velocities being 4.3×10^{-2} and 4.7×10^{-2} cm/s for crucible and crystal rotation respectively. The radial fluid velocity near the crucible bottom are 3.6×10^{-2} and 5.9×10^{-2} cm/s for crystal and crucible rotation respectively. The radial velocity due to crucible rotation is larger near the bottom of the crucible and near the surface. This is due to the larger diameter of the crucible as compared to the crystal diameter. The crucible being larger is able to rotate fluid at a higher theta velocity (swirl) thus giving it a larger centripetal acceleration.

The velocities tangential to the crystal surface at 0.5 of the crystal radius are shown in Figure 10.113. The velocities are 4.0×10^{-2} and 5.2×10^{-2} cm/s for crystal and crucible rotation respectively. As with the radial velocity the larger tangential velocity is due to crucible rotation.

The magnitude of the largest fluid velocity tangential to the crystal interface as a function of crystal or crucible rotation is shown in Figure 10.114. The tangential velocity due to crystal rotation with a stationary crucible goes from near zero at no crystal rotation to 4×10^{-2} at 20 rpm. Higher crystal rotation rates cannot be used due to melt back of the crystal. The tangential velocity with crucible rotation and a stationary crystal goes from near zero at no crucible rotation to approximately 20×10^{-2} cm/s at 60 rpm. For a given rotation rate crucible rotation produces a larger tangential velocity than crystal rotation. Much higher tangential velocities are thus attainable possible using crucible rotation.

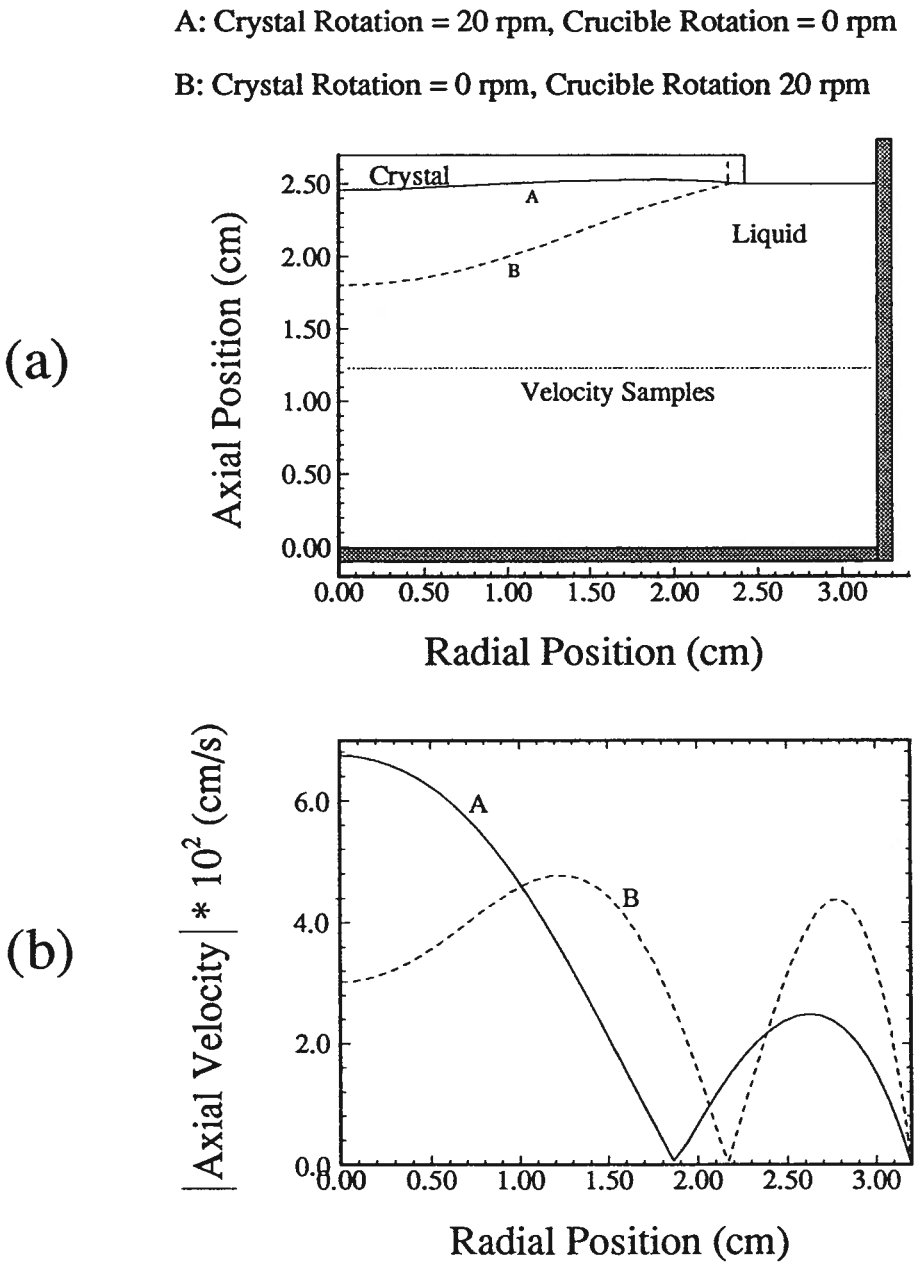

Figure 10.111: The magnitude of the axial velocities along a horizontal line at 0.5 of the fluid height. The two conditions examined are crucible rotated at 20 rpm with a stationary crystal and a stationary crystal with a crucible rotating at 20 rpm. (a) Shape of the solid/liquid interface. (b) Axial velocities.

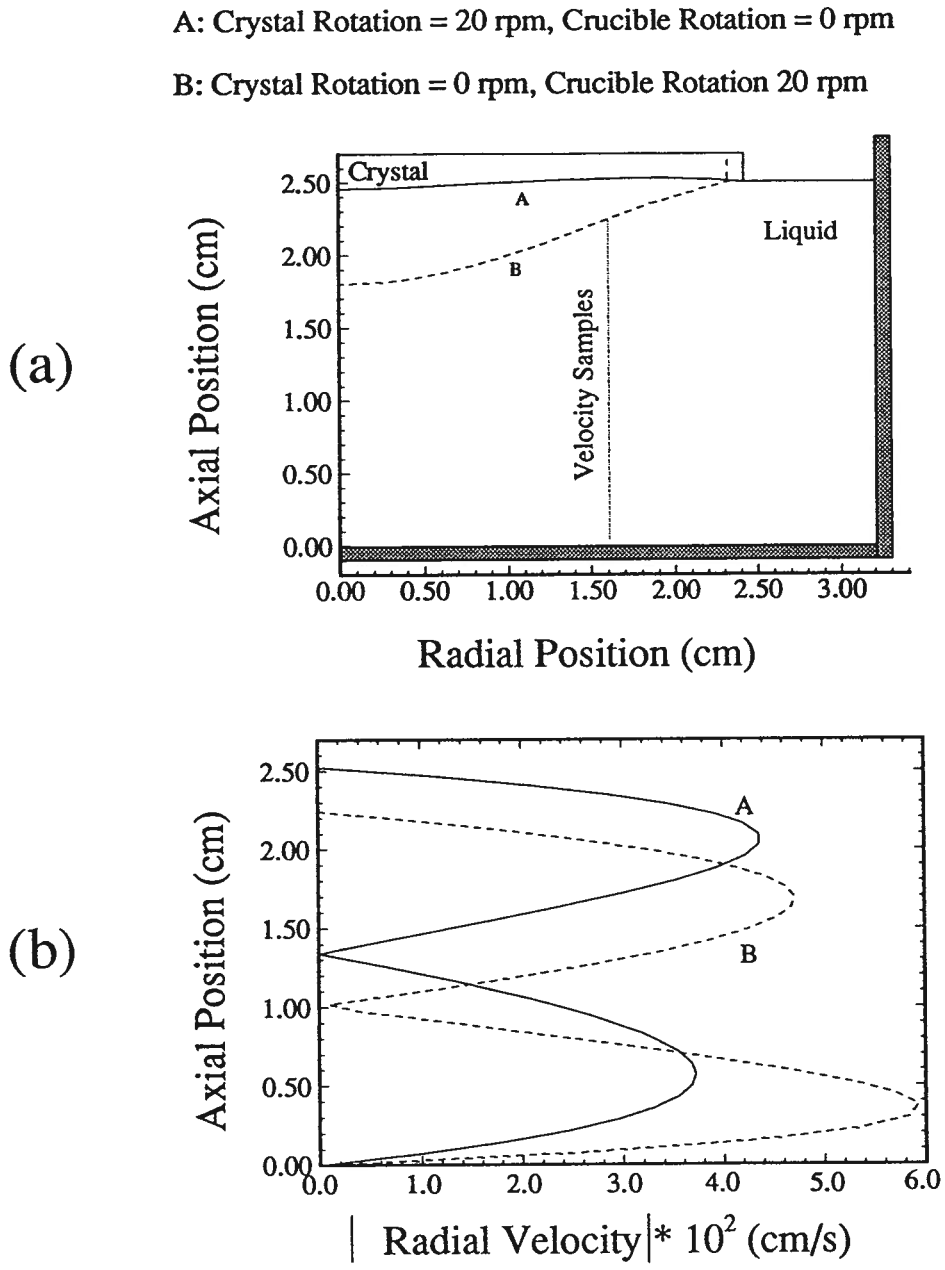

Figure 10.112: The magnitude of the radial velocities along a vertical line at 0.5 of the crucible radius. The two conditions examined are crucible rotated at 20 rpm with a stationary crystal and a stationary crystal with a crucible rotating at 20 rpm. (a) Shape of the solid/liquid interface. (b) Radial velocities.

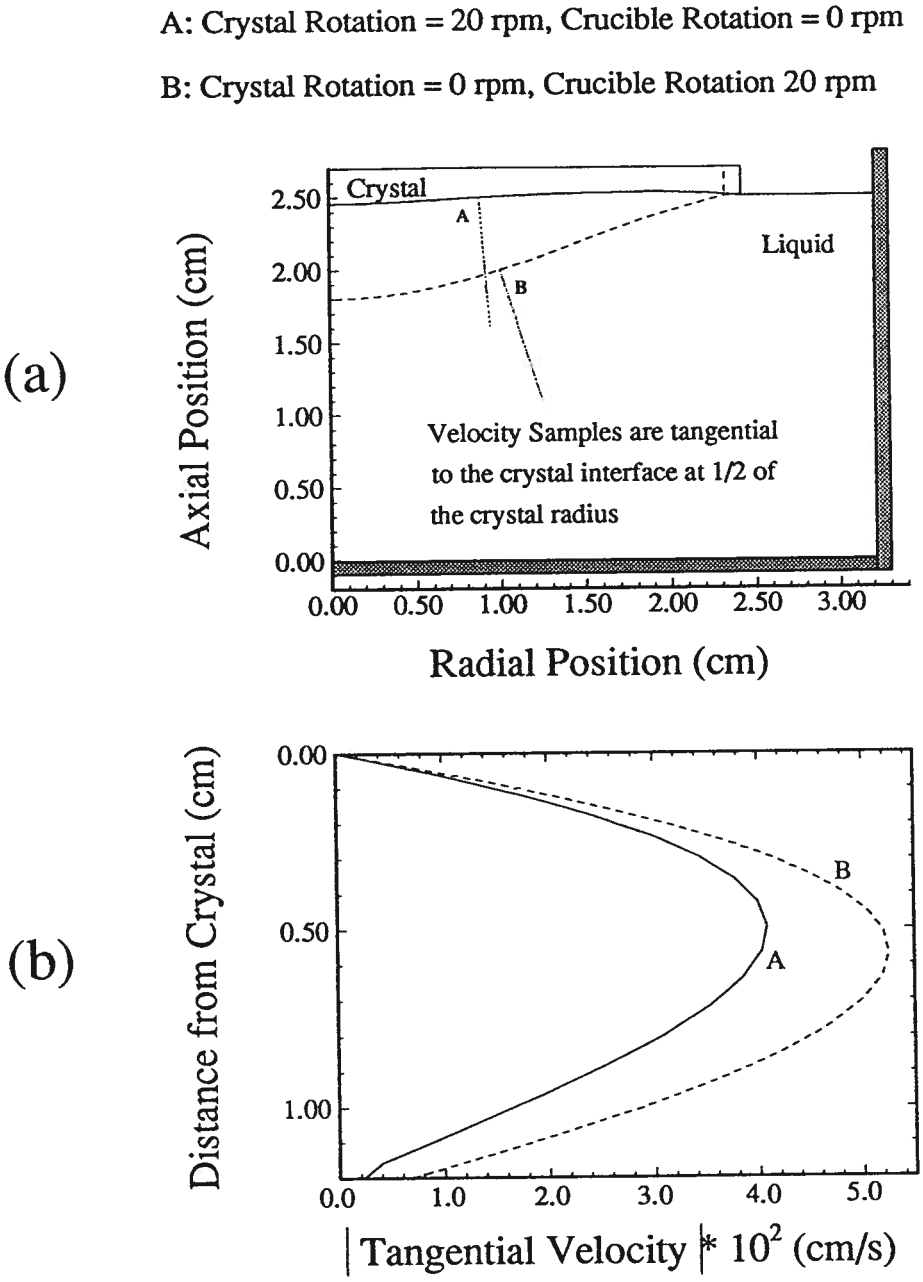

Figure 10.113: The magnitude of the velocities tangential to the crystal surface at 0.5 of the crystal radius. The two conditions examined are crucible rotated at 20 rpm with a stationary crystal and a stationary crystal with a crucible rotating at 20 rpm. (a) Shape of the solid/liquid interface. (b) Tangential velocities.

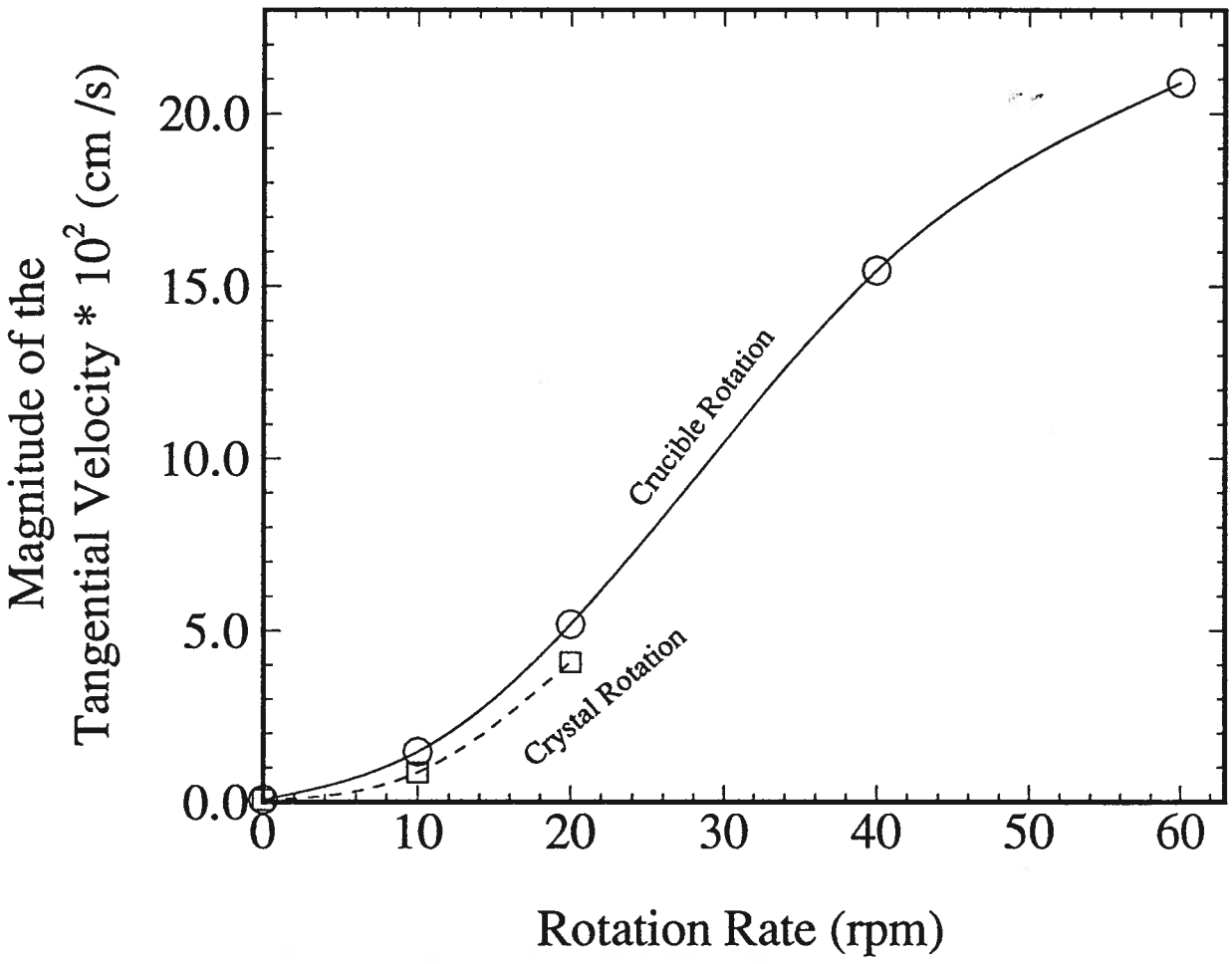

Figure 10.114: Magnitude of the tangential velocity 0.5 cm from the liquid/crystal interface for different crystal and crucible rotation rates. The calculations are for a rotating crucible with a stationary crystal and a stationary crucible and rotating crystal.

10.4 Comparison of the Flow Fields in Small and Large Crucibles

Fluid flow velocities in a small and large crucible rotated at 20 rpm, with no crystal rotation are compared. The axial fluid velocities along a radial line at 0.5 of the respective fluid heights are shown in Figure 10.115. The variation of the axial velocity with radius is similar for both crucibles. The large crucible has fluid velocities that are -5.3×10^{-1} cm/s downward under the crystal and 2.8×10^{-1} upward at the wall. These are approximately double the velocities in the small crucible, which are -3.6×10^{-1} cm/s downward below the crystal and 1.2×10^{-1} cm/s upward near the wall. The radial velocities along a vertical line at 0.5 of the crucible radius are shown in Figure 10.116. The radial velocities in the large crucible are 4.3×10^{-1} cm/s outward near the bottom of the crucible and -4.5×10^{-1} cm/s inward at the top of the melt. The radial velocities in the small crucible are approximately half of the large crucible velocities, being 2.4×10^{-1} cm/s outward near the bottom of the crucible and -2.1×10^{-1} cm/s inward at the top of the melt. The melt velocity tangential to the crystal interface at 0.5 of the crystal radius is shown in Figure 10.117. The tangential fluid velocity is 5.0×10^{-1} cm/s and 2.1×10^{-1} cm/s for the large and small crucible respectively. Fluid velocity is proportional to crucible size for crucible rotation driven flows. The larger the crucible that faster the theta fluid velocity near the outside of the melt. This in turn gives the fluid a larger centripetal acceleration which increases the overall flow velocity of the melt.

10.5 Iso and Counter rotation of the Crystal and Crucible

The axial, radial and tangential flow velocities are calculated for isorotation and counter rotation of the crystal and crucible. The rotation rates are ±10 and 20 for the crystal and crucible respectively. The tangential velocity is calculated 1 mm from the crystal interface for crucible rotation of 20 rpm and crystal rotation between -35 and 20 rpm.

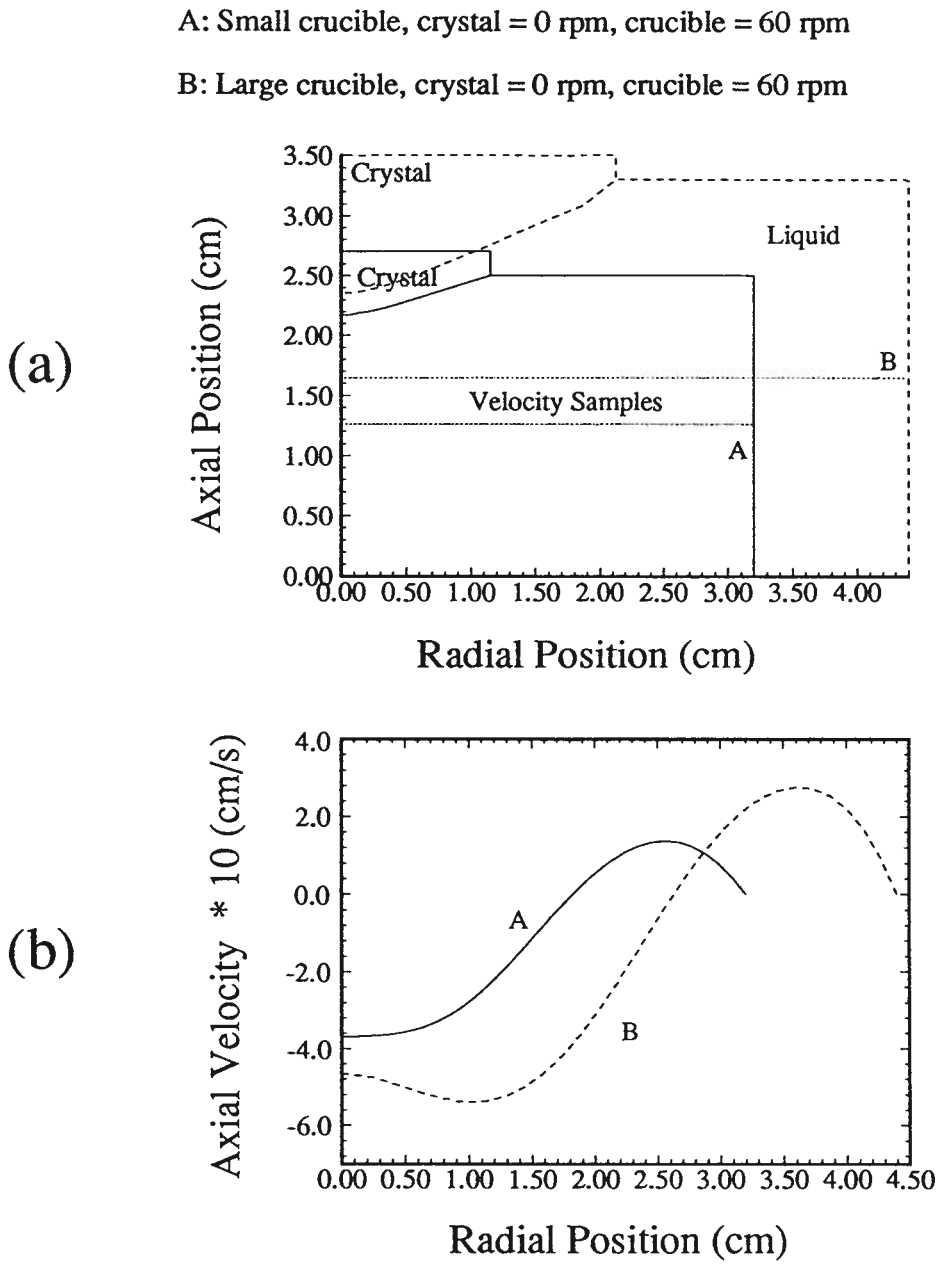

Figure 10.115: Axial velocities at 0.5 of the fluid height. Large and small crucible shown. 40.9 Wt% MoO_3 present in the fluid. Crucible rotated at 60 rpm. Crystal is stationary. (a) Shape of the solid/liquid interface. (b) Axial velocities.

A: Small crucible, crystal = 0 rpm, crucible = 60 rpm

B: Large crucible, crystal = 0 rpm, crucible = 60 rpm

(a)

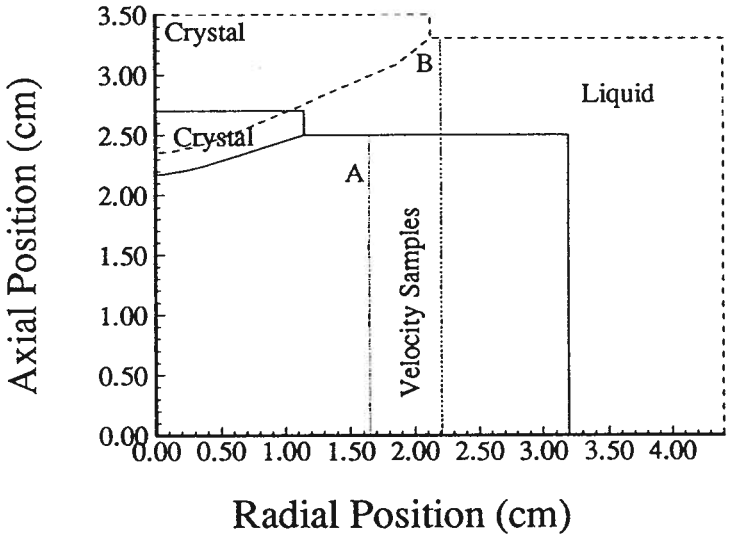

(b)

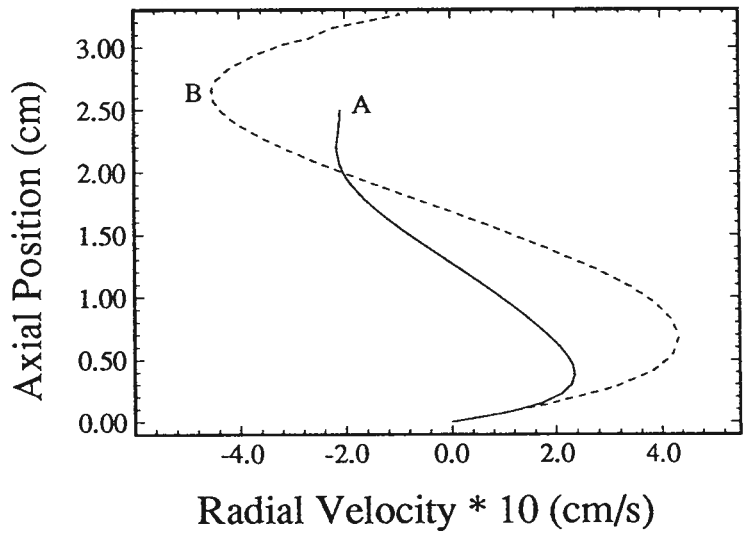

Figure 10.116: Radial velocities at 0.5 of the crucible radius. Large and small crucible shown. 40.9 Wt% MoO_3 present in the fluid. Crucible rotated at 60 rpm. Crystal is stationary. (a) Shape of the solid/liquid interface. (b) Radial velocities.

A: Small crucible, crystal = 0 rpm, crucible = 60 rpm

B: Large crucible, crystal = 0 rpm, crucible = 60 rpm

(a)

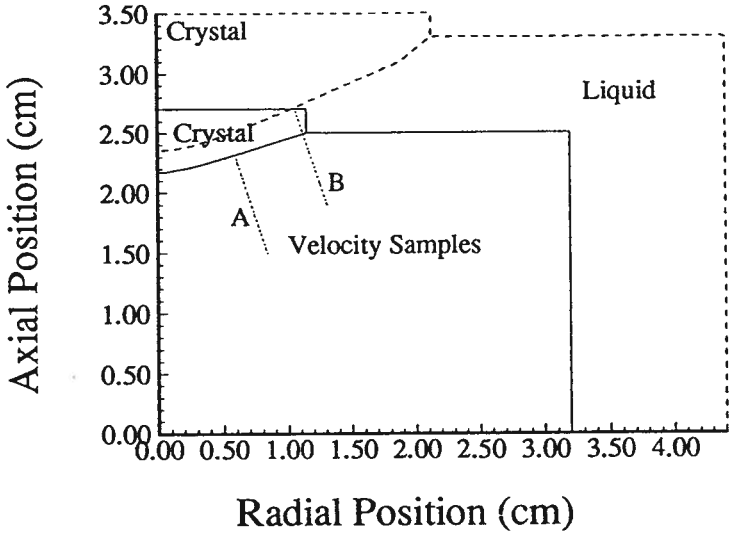

(b)

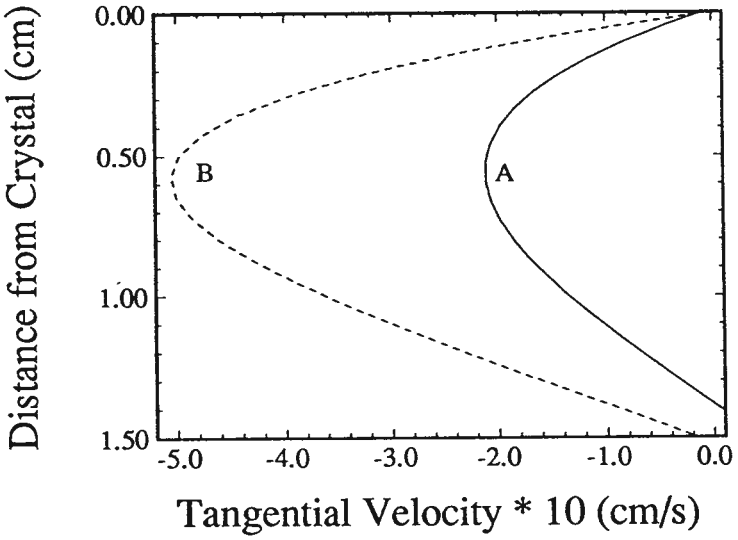

Figure 10.117: Velocities tangential to the crystal surface at 0.5 of the crystal radius. 40.9 Wt% MoO_3 present. Large and small crucible shown. Crucible rotated at 60 rpm. Crystal is stationary. (a) Shape of the solid/liquid interface. (b) Tangential velocities.

The axial fluid velocity along a vertical line at 0.5 of the fluid height is shown in Figure 10.118. The crystal and crucible rotation rates are ±10 and 20 rpm respectively. The curves in the Figures are marked I and CR for isorotation and counter rotation respectively. For both rotation cases the fluid velocity is downward under the crystal and upward near the crucible wall. This fluid motion occurs because the crucible rotation rate is higher and dominates the melt flow. For counter rotation (CR) larger fluid velocities are obtained than for isorotation (I). The axial velocities due to counter rotation (CR) are -5.2×10^{-2} cm/s downward under the crystal and 5.0×10^{-2} cm/s upward near the crucible wall. The axial velocities due to isorotation (I) are -3.2×10^{-2} cm/s downward under the crystal and 2.8×10^{-2} cm/s upward near the crucible wall. The solid liquid interface is different for the two different rotation modes. Counter rotation causes the crystal interface to be more convex to the melt and the radius smaller. This is due to the larger fluid velocities that occur with counter rotation.

The radial fluid velocities at a vertical line at 0.5 of the crucible radius are shown in Figure 10.119. The radial velocities are higher when the crystal and crucible are counter rotated. The radial velocities due to counter rotation are -5.2×10^{-2} cm/s inward under the crystal and 6.8×10^{-2} cm/s outward near the crucible bottom. The radial velocities due to isorotation are -3.2×10^{-2} cm/s inward under the crystal and 4.0×10^{-2} cm/s outward near the crucible bottom.

The melt velocity tangential to the crystal surface at 0.5 of the crystal radius are shown in Figure 10.120. The maximum tangential velocities for iso and counter rotation are -3.5×10^{-2} cm/s and -5.8×10^{-2} cm/s respectively. The tangential fluid velocity due to counter rotation is 60% higher than the isorotation case. The explanation of the difference in the fluid velocity due to iso and counter rotation requires the calculation of the flow patterns as a function of crystal rotation rate for a fixed crucible rotation. The fluid velocity at 0.5 of the crystal interface will be calculated for crystal rotation rates

A: Crystal Rotation = 10 rpm, Crucible Rotation = 20 rpm

B: Crystal Rotation = -10 rpm, Crucible Rotation = 20 rpm

(a)

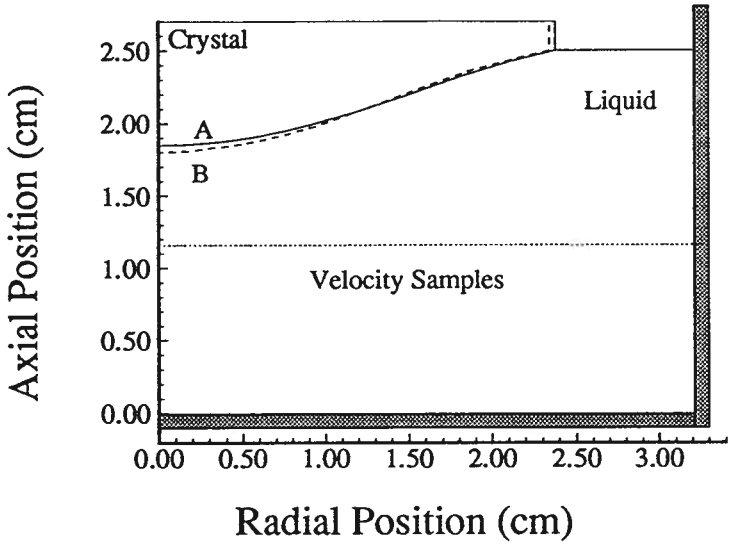

(b)

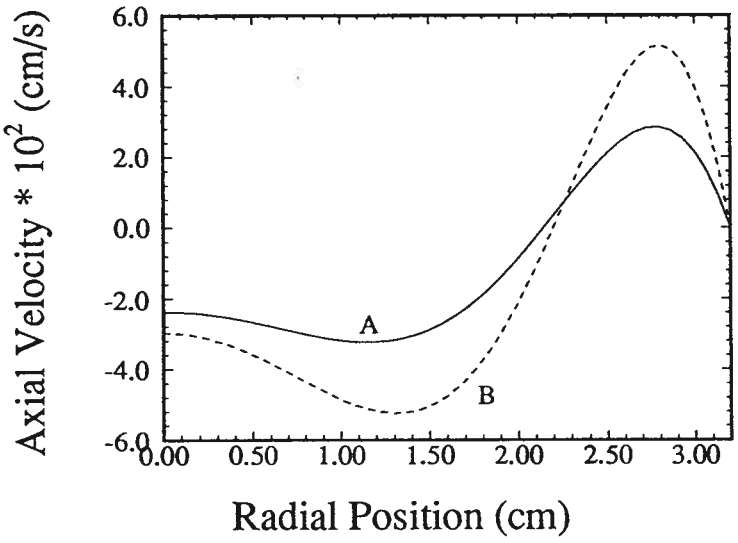

Figure 10.118: Axial velocities at 0.5 of the fluid height. 40.9 Wt% MoO_3 present in the fluid. Crystal rotated at $\pm$ 10 rpm and crucible rotated at 20 rpm. (a) Shape of the solid/liquid interface. (b) Axial velocities.

A: Crystal Rotation = 10 rpm, Crucible Rotation = 20 rpm

B: Crystal Rotation = -10 rpm, Crucible Rotation = 20 rpm

(a)

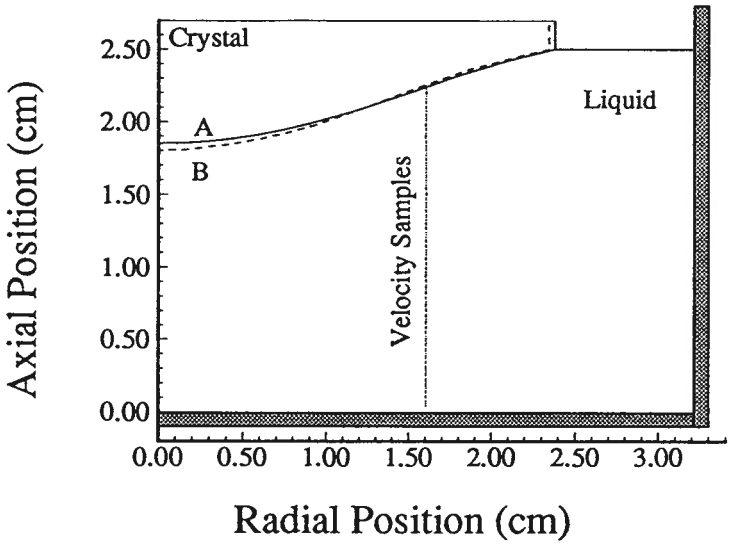

(b)

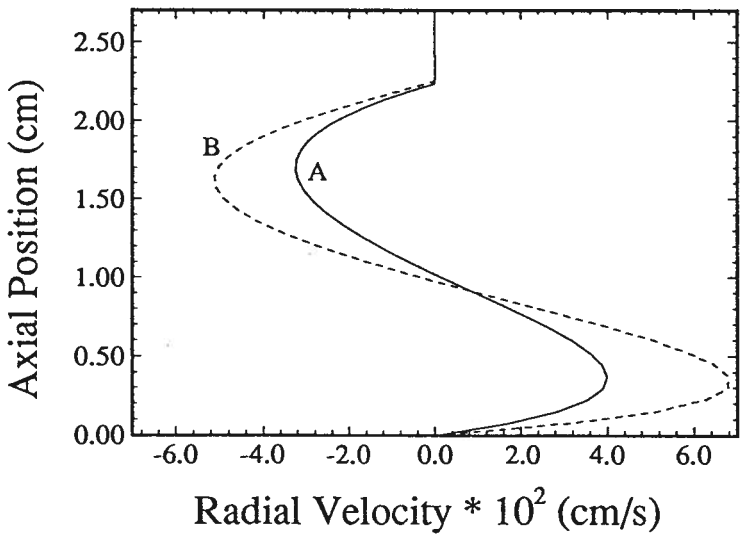

Figure 10.119: Radial velocities at 0.5 of the crucible radius. 40.9 Wt% MoO_3 present in the fluid. Crystal rotated at $\pm$ 10 rpm and crucible rotated at 20 rpm. (a) Shape of the solid/liquid interface. (b) Radial velocities.

between −35 and 20 rpm at a crucible rotation rate of 20 rpm. The tangential velocity at 1 mm from the crystal surface is used to examine the change in flow patterns and is shown in Figure 10.121. Four points, marked A to D, indicate positions where the flow pattern changes.

At point A both the crystal and crucible are rotating at 20 rpm. With both rotating at the same rate the fluid moves as a solid body in the theta (swirl) direction. This result in natural convection being the only force that moves the fluid in the radial and axial directions. The tangential fluid velocity is near zero and is similar to the natural convection fluid velocity calculations of Chapter 8. Decreasing the crystal rotation rates, moves the tangential velocity to point B, where crucible rotation dominates the flow. Fluid now moves up adjacent to the wall and down under the crystal. The maximum flow in this direction occurs with the crystal rotation at zero, point D. The tangential fluid velocity 1 mm from the crystal interface is -2.6×10^{-2} cm/s. A vector plot of the flow pattern is shown in Figure 10.122. The size of the reference vector in this plot and for vector plots at the different rotation conditions is the same, 0.1 cm/s. The flow with crucible rotation of 20 rpm and crystal rotation of 0 rpm goes up at the wall and down under the crystal.

The change in flow patterns between B and C is different than between A and B. Increasing the crystal counter rotation rate results in the fluid rotating in a direction opposite to that of the crucible. At point C the crystal is rotating at a sufficiently high rate, that the centripetal acceleration of the fluid under the crystal is large, causing the fluid to move outward. Thus, instead of the crystal matching the crucibles rotation rate to reduce the flow, point A, the crystal must be rotating at a sufficiently high rate to cause the fluid under the crystal to become stagnant. The vector plot of the flow patterns near point C is shown in Figure 10.123. Directly under the crystal, marked UC, the flow is stagnant. Moving from the crystal, the flow becomes significant, flowing up at the wall

and down under the crystal.

Increasing the crystal rotation rate, point C to D, causes the crystal to start to dominate the flow patterns. This will result in the flow changing from a stagnant state under the crystal, point C, to flowing upward under the crystal and downward at the edge of the crystal, point D. The tangential flow velocity 1 mm from the crystal interface is -3.0×10^{-2} cm/s at a crystal rotation of -35 rpm and a crucible rotation of 20 rpm, point D. The vector flow pattern at point D is shown in Figure 10.124. The flow has two cells. The flow directly under the crystal is upward at the centre of the crucible and outward. The flow flow near the crucible bottom is outward and upward at the crucible wall. Both flows join and move outward and upward at the crucible wall and inward and downward at a 45 degree to the crucible bottom.

A: Crystal Rotation = 10 rpm, Crucible Rotation = 20 rpm

B: Crystal Rotation = -10 rpm, Crucible Rotation = 20 rpm

(a)

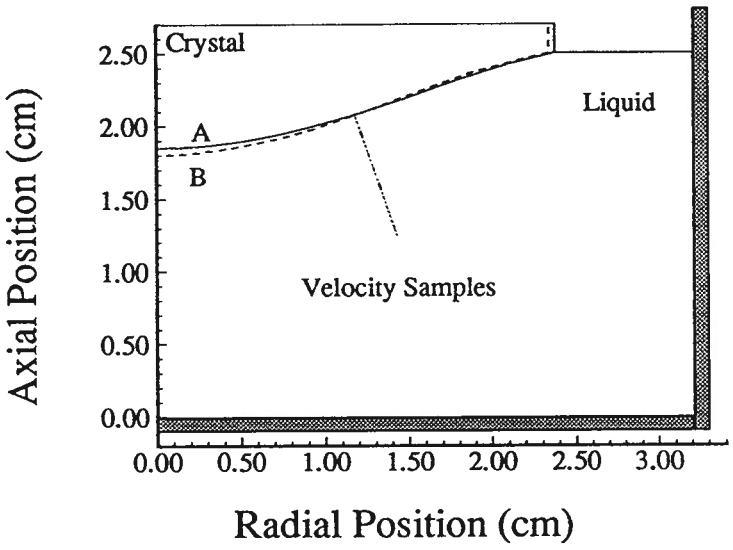

(b)

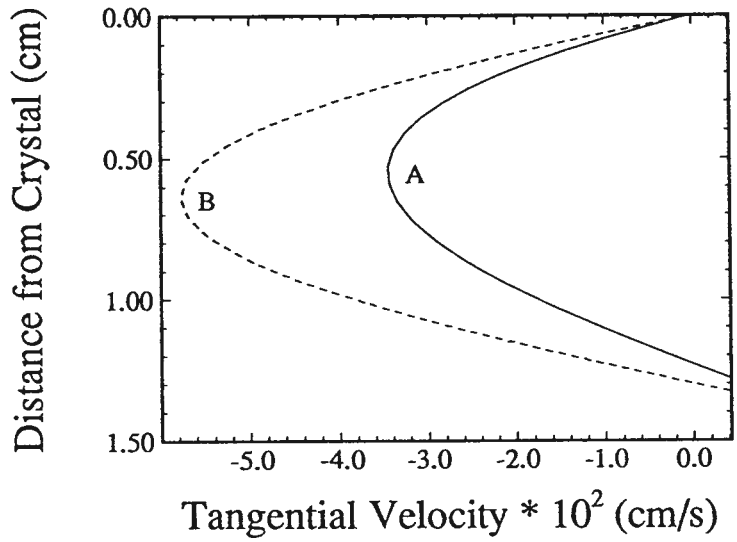

Figure 10.120: Velocities tangential to the crystal surface at 0.5 of the crystal radius. 40.9 Wt% MoO_3 present in the fluid. Crystal rotated at $\pm$ 10 rpm and crucible rotated at 20 rpm. (a) Shape of the solid/liquid interface. (b) Tangential velocities.

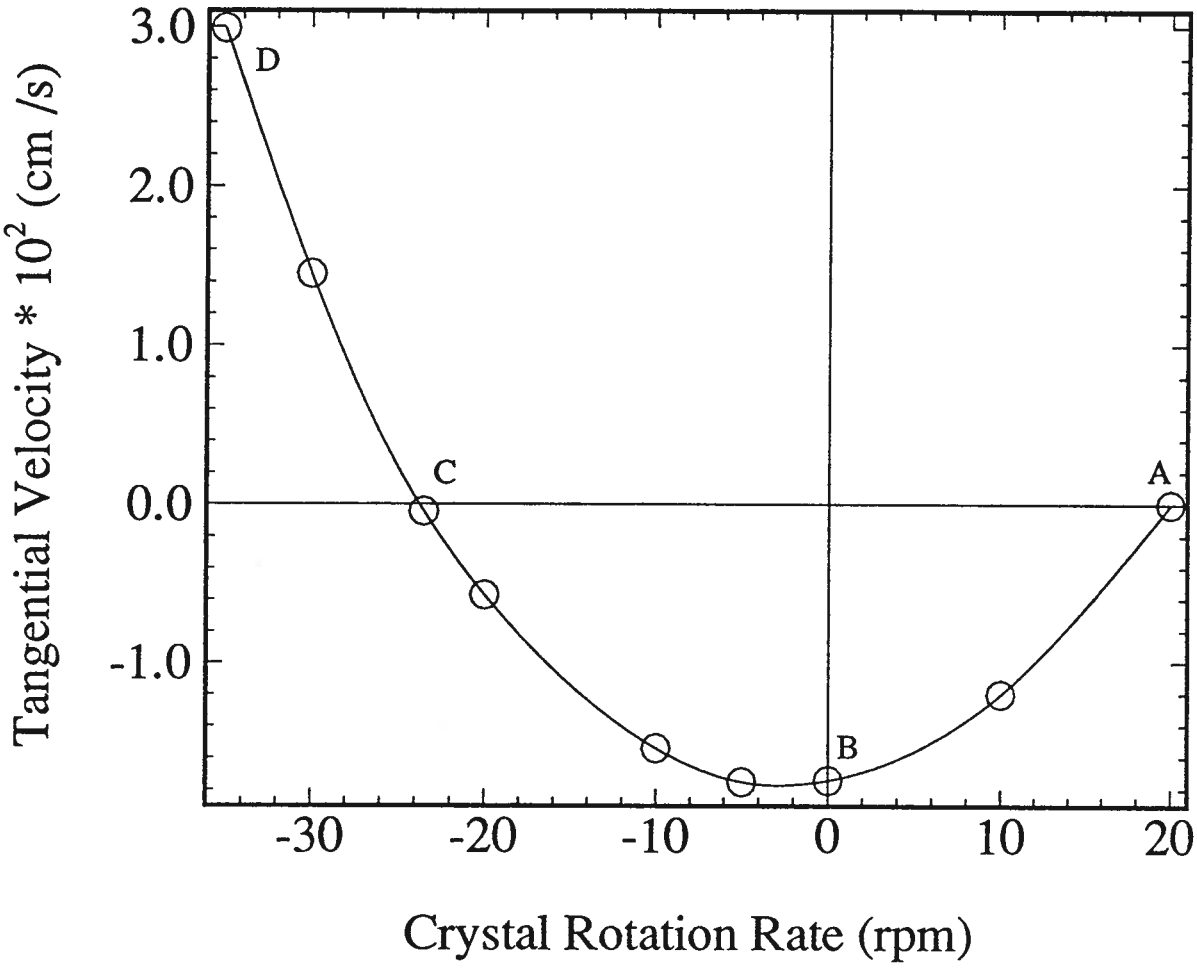

Figure 10.121: Fluid velocity tangential to the solid/liquid interface as a function of crystal rotation rate. The velocity is 1 mm from the crystal/melt interface and at 0.5 of the crystal radius. 40.9 Wt% MoO_3 present in the fluid. The crucible is rotated at 20 rpm.

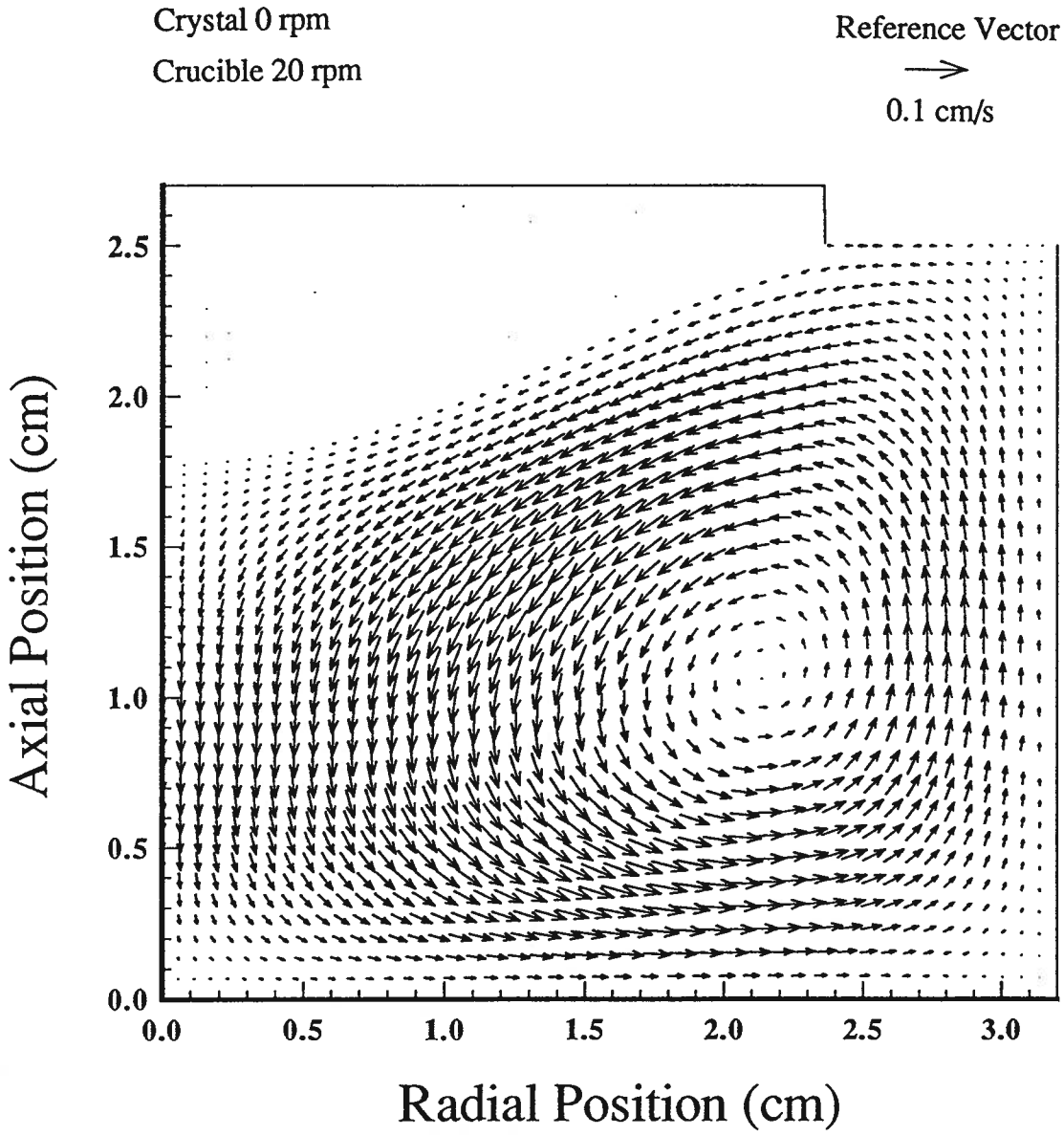

Figure 10.122: Vector plot of fluid velocity at a crucible rotation rate of 20 rpm and a crystal rotation rate of 0 rpm. Point B.

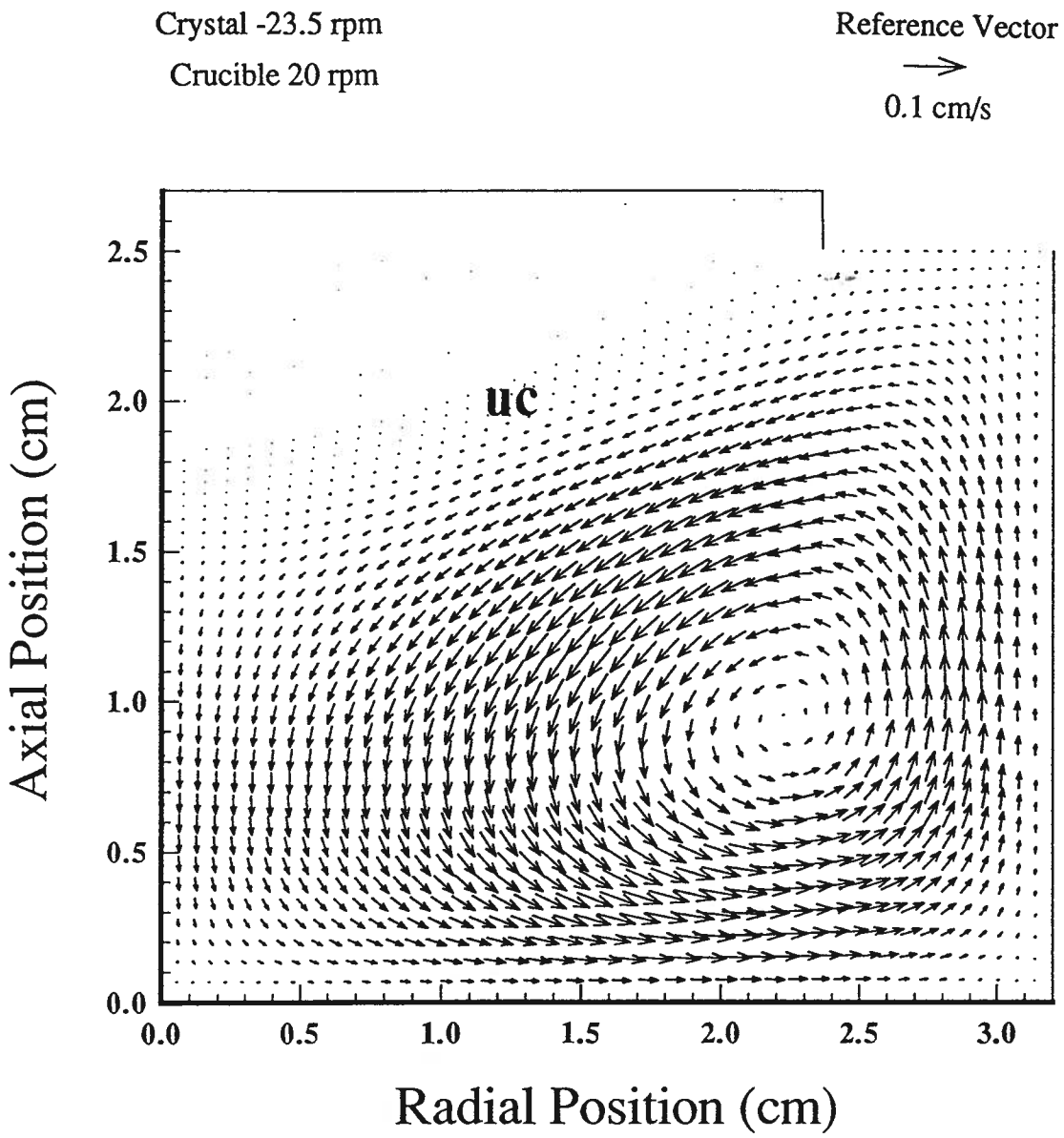

Figure 10.123: Vector plot of fluid velocity at a crucible rotation rate of 20 rpm and a crystal rotation rate of -23.5 rpm. Near point C.

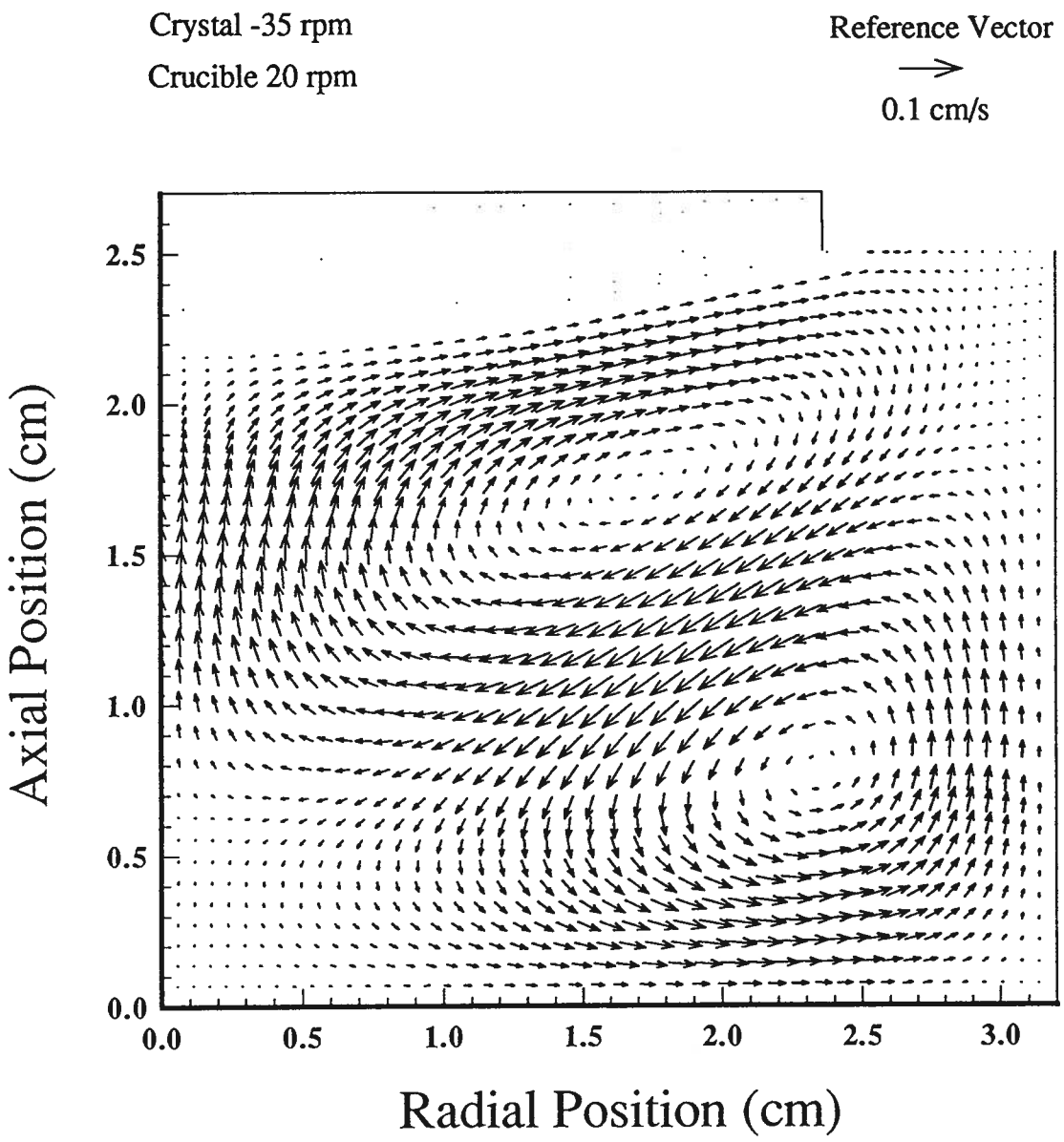

Figure 10.124: Vector plot of fluid velocity at a crucible rotation rate of 20 rpm and a crystal rotation rate of -35 rpm. Point D.

Chapter 11

Comparison of Temperature Measurements with Model Results

In this section, the calculated temperature fields in melts contained in 6.6 cm and 8.8 cm diameter crucibles determined from the model are compared to the corresponding measured melt temperatures. The model boundary conditions were determined from the melt temperatures with no crucible rotation. The values used are given in Figure 11.125 and Figure 11.126 for the small and large crucible respectively. The melt composition, material properties and crucible rotation rates used for the calculations are given in Table 11.17.

Melt temperatures were measured with two 3 mm outside diameter platinum sheathed thermocouples. The presence of the thermocouples in the rotating melt increases mixing and produces three dimensional flow. The axisymmetric model used in this analysis cannot properly calculate this type of fluid flow. However, the increased mixing in the melt can be approximated by setting the theta velocity boundary condition to zero where the thermocouples enter the melt. The standard theta velocity boundary condition for an axisymmetric melt are shown in Figure 11.127. The modified theta velocity boundary conditions are shown in Figure 11.128. Both boundary conditions are used in the calculations.

11.1 Small Crucible (6.6 cm diameter) Results

The measured and calculated axial temperature profiles in the melt for the small non-rotating crucible are shown in Figure 11.129. The axial temperature profiles at r=1.0,

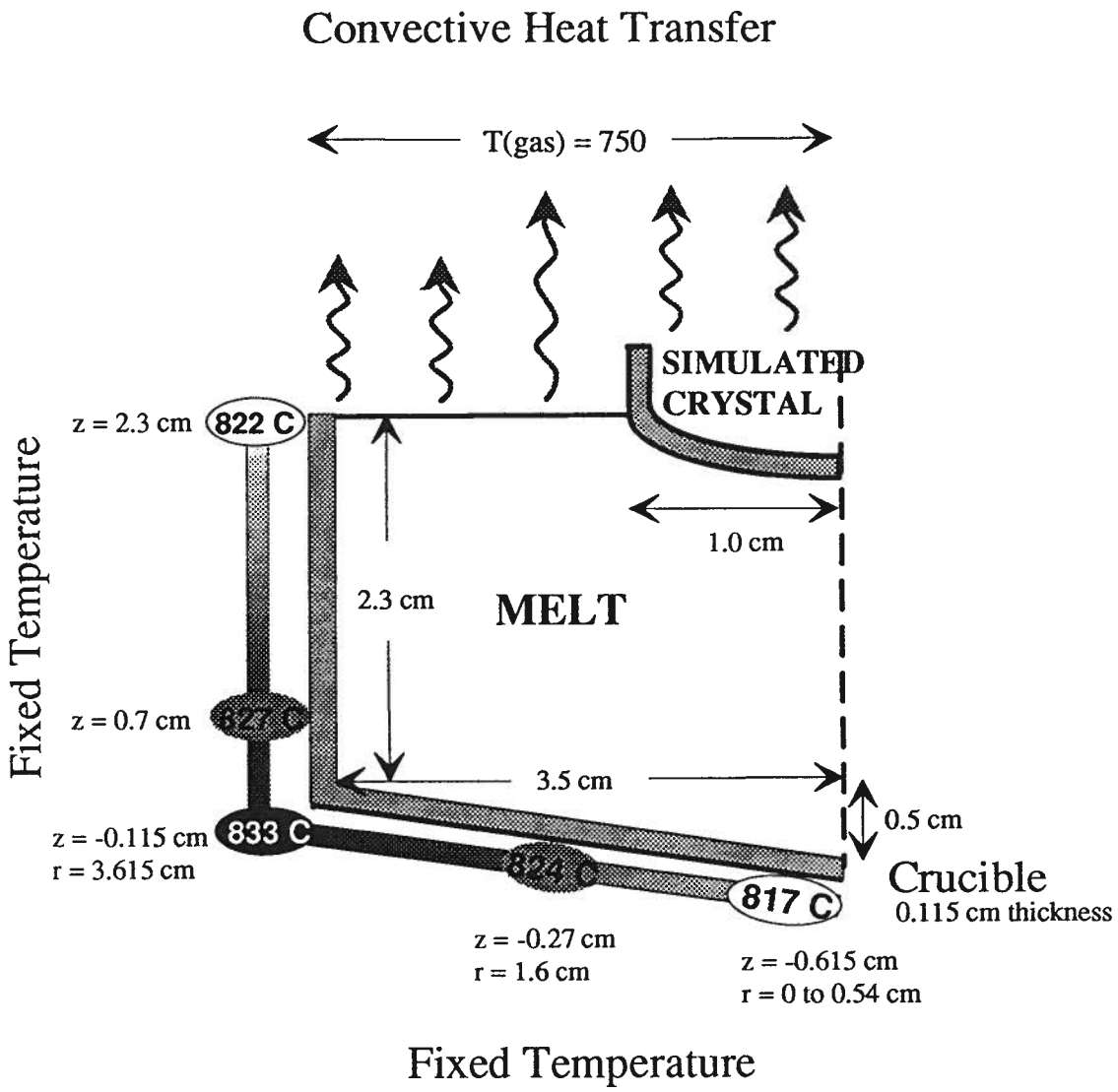

Figure 11.125: Temperature boundary conditions used for the small crucible model.

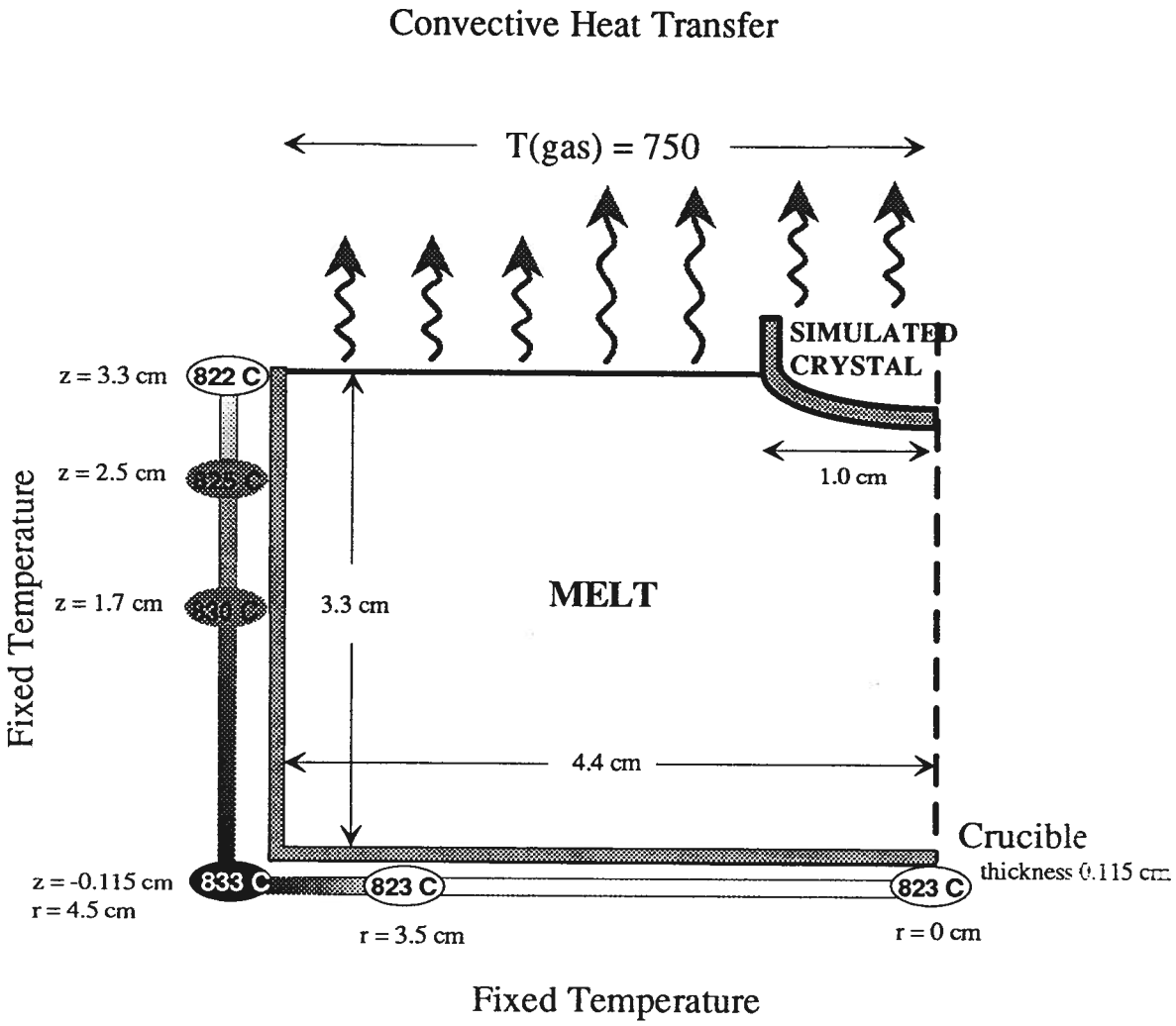

Figure 11.126: Temperature boundary conditions used for the large crucible model.

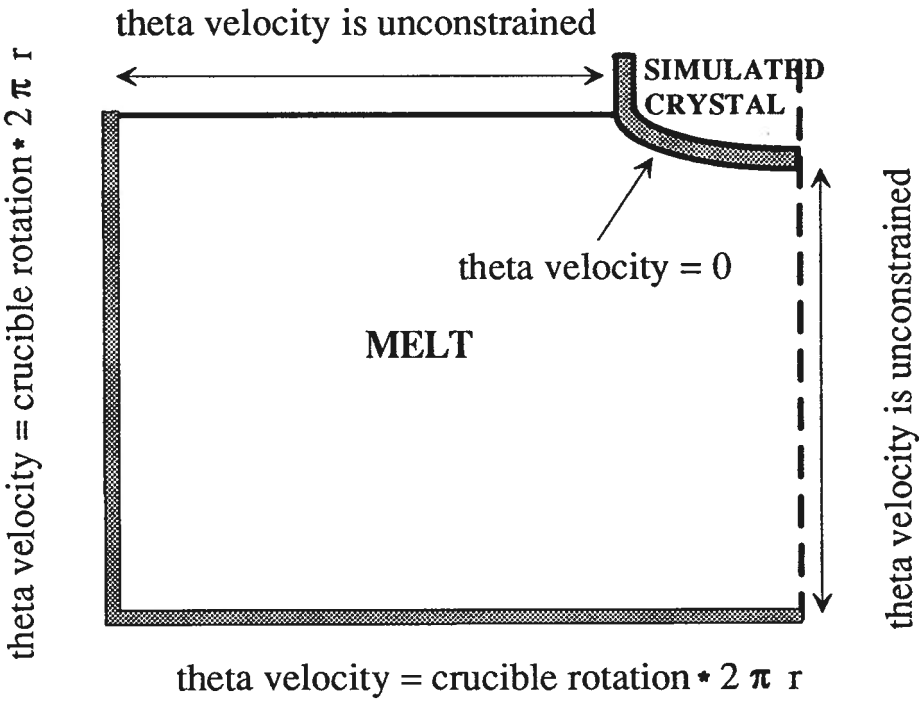

Figure 11.127: Theta velocity boundary conditions used in the model.

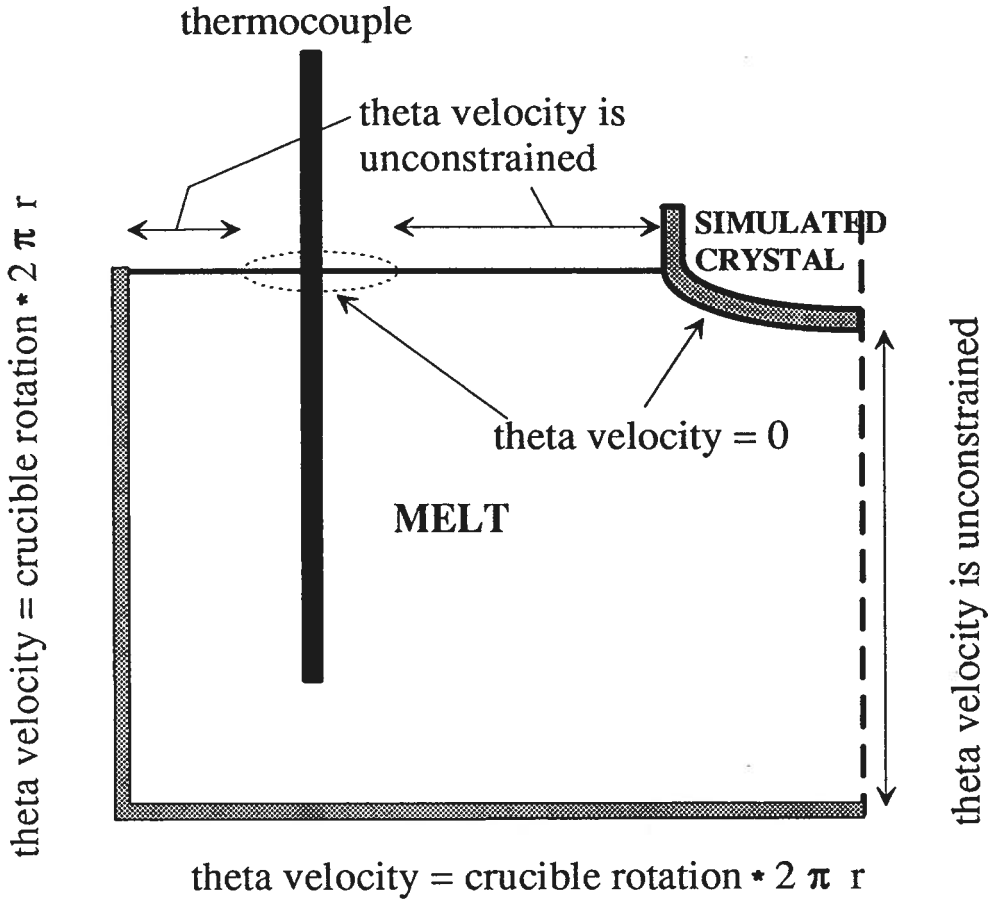

Figure 11.128: Theta velocity boundary conditions used in the model to account for the thermocouples in the melt.

Property	Unit	small crucible	large crucible
Amount MoO_3	Wt%	45.5	47.4
conductivity (k)	W/cm K	0.05	0.05
Specific Heat (Cp)	J/g K	0.621	0.625
density (ρ)	g/cm^3	3.14	3.19
viscosity (μ)	poise	3.27	2.82
Expansion Coefficient (β)	K^{-1}	6×10^{-6}	6×10^{-6}
crystal rotation	rpm	0	0
crucible rotation	rpm	0, 15, 20, 25, 30	0, 10, 20, 30

Table 11.17: Thermophysical properties and rotation values used in the model for comparison with experimental temperature measurements.

1.5, 2.6 and 3.1 are shown. The calculated temperatures are within 1°C of the measured temperatures at radial locations of 2.6 and 3.5 cm The calculated temperatures near the centre of the crucible (r = 1.0 and 1.5 cm) are within 2°C of the measured values. The good fit of the calculated and measured temperature is expected since the experimental values are used to determine the temperature boundary conditions in the model.

11.1.1 Results Assuming no Thermocouple/Melt Interaction (Small Crucible)

This section assume that there is no interaction between the melt and the thermocouple. The velocity boundary conditions are shown in Figure 11.127. The experimental and calculated temperatures for a crucible rotation rate of 15 rpm are shown in Figure 11.130. The measured axial temperature profiles near the centre of the melt (r = 1.0 and 1.5 cm) are constant near 820°C between z = 0.4 cm and 1.0 cm. Above 1.1 cm the temperature decreases with increasing height. The calculated temperature measurements at the same radial locations are within 2°C of the measured values.

The measured temperatures at r = 2.6 and 3.1 cm radius initially decrease with

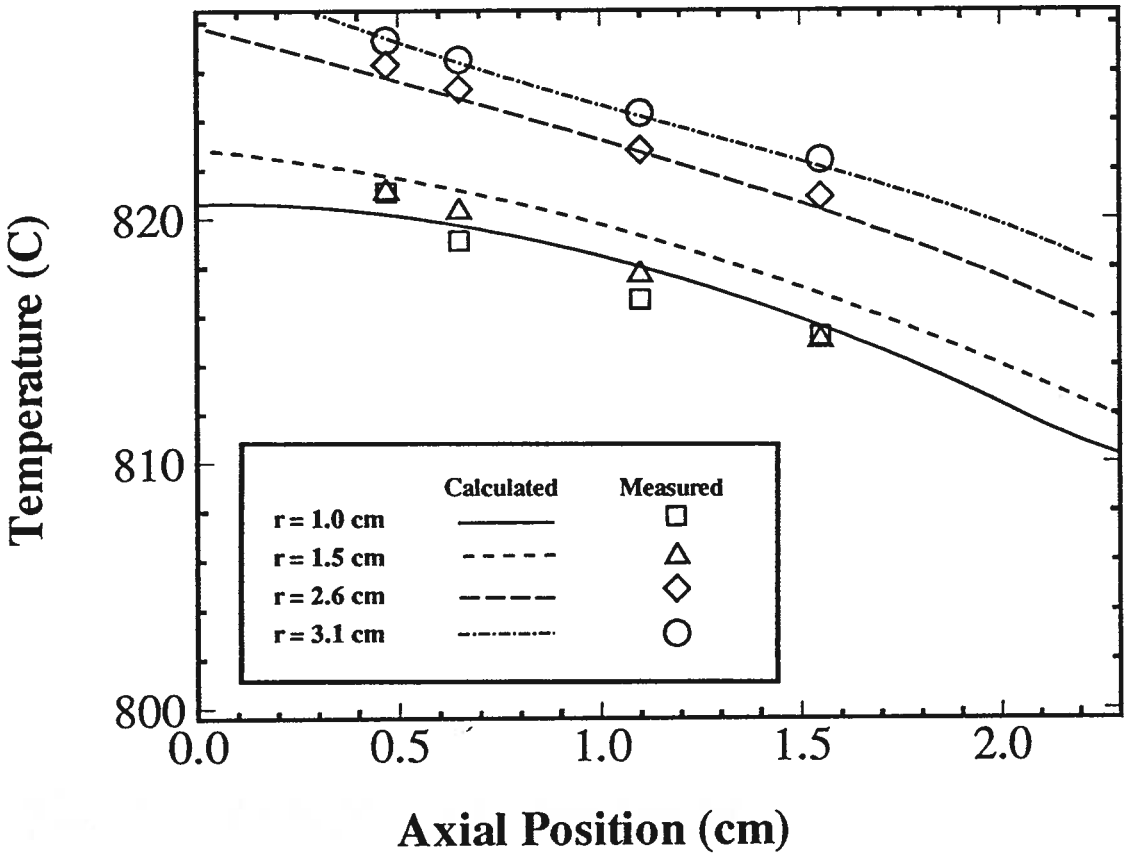

Figure 11.129: Experimental and calculated temperatures as a function of axial height. Small (6.6 cm diameter) crucible. Crucible rotation = 0 rpm.

increasing z to 1.0 cm then appear to be constant. The calculated results at r = 2.6 cm nearly coincides with three of the temperature measurements and are higher at 1.0 cm with a slight plateau. At r = 3.1 cm the calculated values are all higher than the measured value, with no plateau.

Figure 11.131 shows the measured and calculated axial temperature profiles at a higher crucible rotation rate of 20 rpm. Increasing the rotation rate to 20 rpm from 15 rpm does not significantly change the temperature distributions. The temperature profile at a crucible rotation rate of 25 rpm are shown in Figure 11.132. The measured axial temperature profiles at all locations become flatter and the temperature difference between the different axial profiles decreases. The calculated axial profiles near the centre of the melt (r=1.0 and 1.5 cm) become flatter and are within 2 to 3°C of the measured values. The calculated axial profiles near the crucible wall (r=2.6 and 3.1 cm) do not change significantly from the 20 rpm crucible rotation results.

The temperature profiles at a crucible rotation rate of 30 rpm are shown Figure 11.133. The experimental temperatures at the four radial positions are essentially constant at 823°C. The calculated temperature measurements at r = 1.0 and 1.5 cm becomes flat at 819°C and 820°C respectively. The calculated temperature at r = 2.6 and 3.1 cm do not change significantly from the 25 rpm case.

11.1.2 Results assuming Thermocouple/Melt Interaction (Small Crucible)

The model calculations in this section have the theta velocity boundary condition set to zero where the thermocouples enter the liquid (Figure 11.128). The experimental and calculated temperature profiles at 15 rpm are shown in Figure 11.134.

The calculated axial temperature profiles have a long plateau between z = 0.4 and 1.2 cm at all radial locations. At a rotation rate of 20 rpm, Figure 11.135, the calculated results fit the measured results at z values less than 1.0 cm. At values greater than this

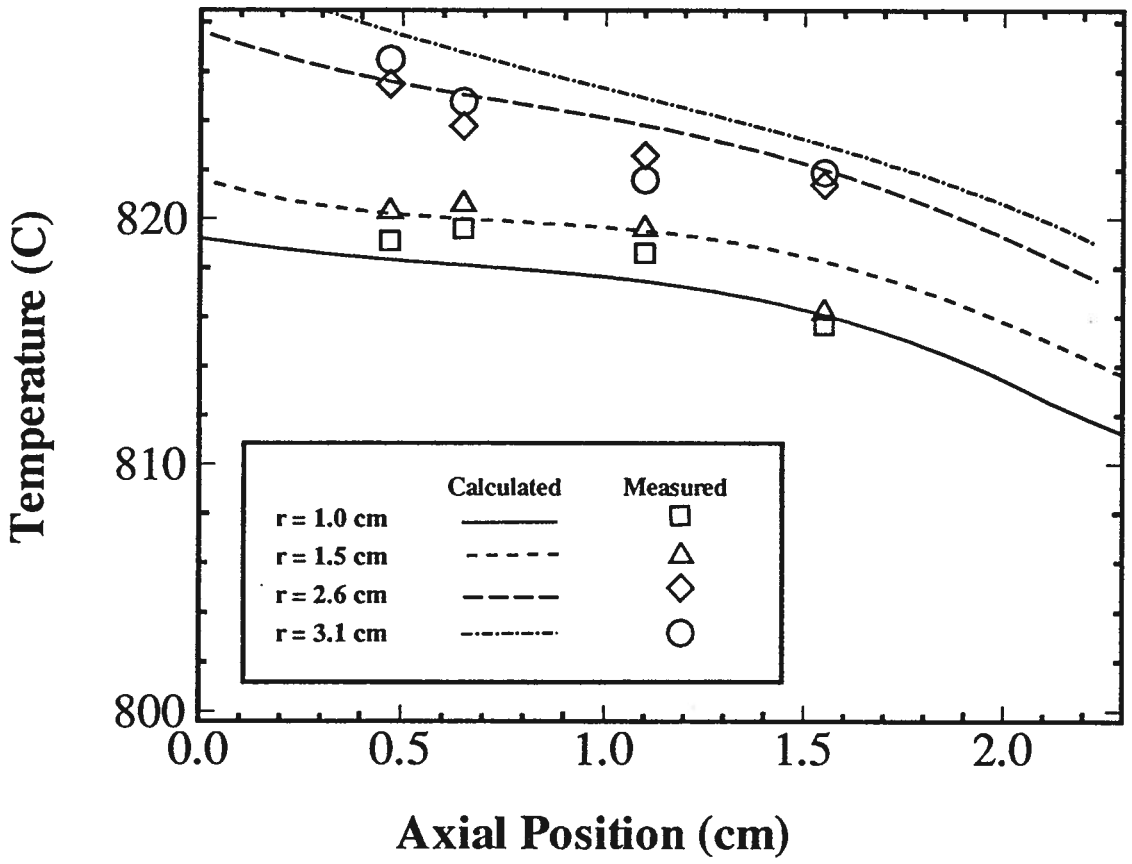

Figure 11.130: Experimental and calculated temperatures as a function of axial height at the radial locations indicated. Small (6.6 cm diameter) crucible. Crucible rotation = 15 rpm. Standard velocity boundary conditions are used (Figure 11.127).

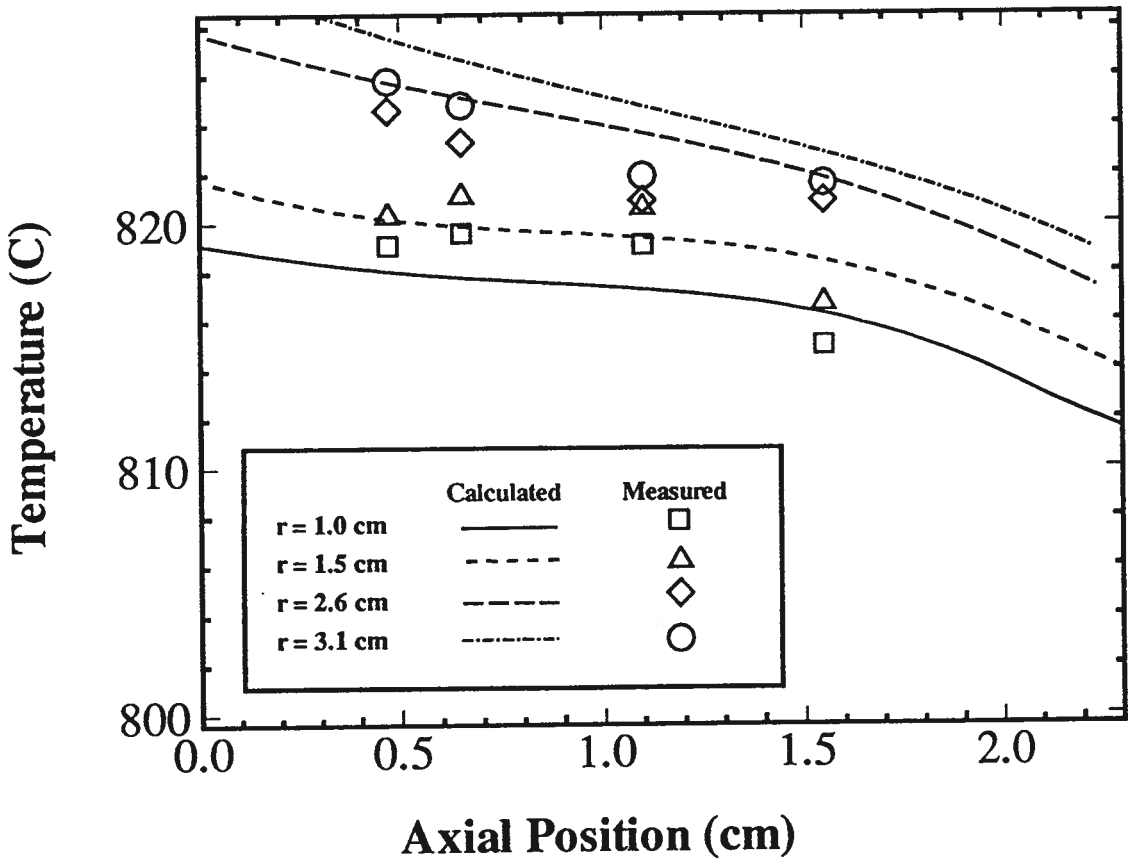

Figure 11.131: Experimental and calculated temperatures as a function of axial height at the radial locations indicated. diameter) crucible. Crucible rotation = 20 rpm. Standard velocity boundary conditions are used (Figure 11.127).

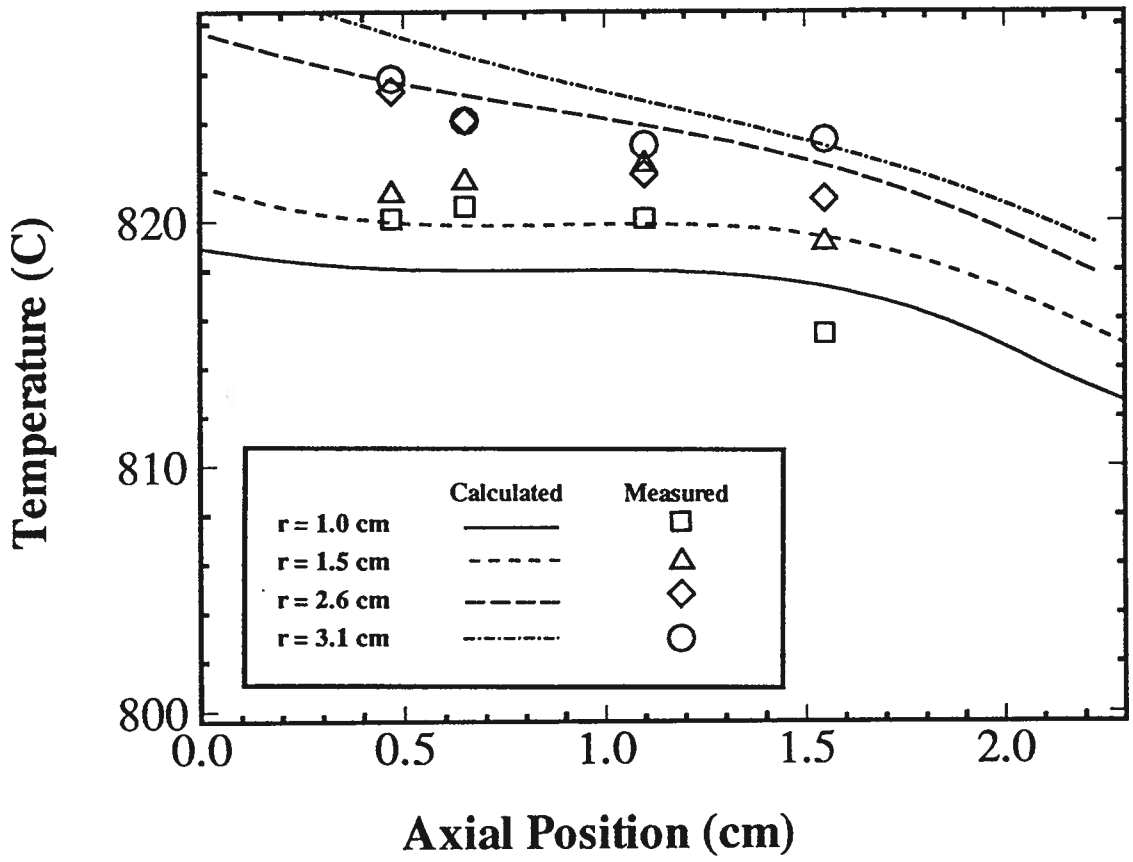

Figure 11.132: Experimental and calculated temperatures as a function of axial height at the radial locations indicated. Small (6.6 cm diameter) crucible. Crucible rotation = 25 rpm. Standard velocity boundary conditions are used (Figure 11.127).

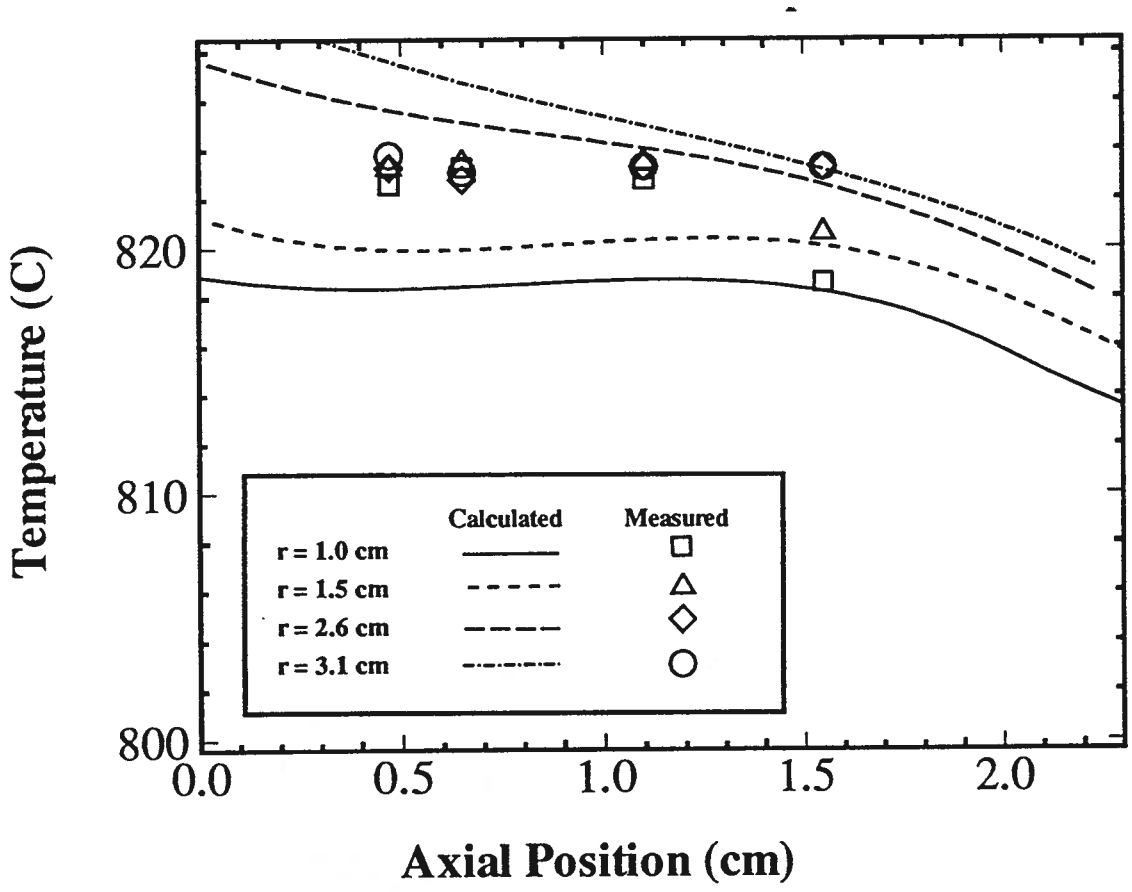

Figure 11.133: Experimental and calculated temperatures as a function of axial height at the radial locations indicated. Small (6.6 cm diameter) crucible. Crucible rotation = 30 rpm. Standard velocity boundary conditions are used (Figure 11.127).

the measured temperatures decreases faster than the model predictions. The calculated results at a crucible rotation rate of 25 rpm, Figure 11.136, are similar to the 20 rpm results. The calculated axial temperature profiles near the crucible wall (r = 2.6 and 3.1 cm) are in good agreement with the measured results. Figure 11.137 shows the measured and calculated axial temperature profiles for 30 rpm crucible rotation. The calculated results have a good general fit with the measured values. The fit is not good near the crucible wall (r =3.1 cm), and the centerline temperature values (r = 1.0 and 1.5 cm) near z = 1.5 cm. The calculated temperatures using the modified theta boundary condition, fit the measured temperatures reasonably well.

11.2 Large Crucible (8.8 cm diameter) Results

The measured and calculated temperatures for the large crucible (8.8 cm diameter) with no crucible rotation are shown in Figure 11.138. The calculated temperatures are in good agreement with the measured temperatures close to the crucible wall (r greater than 2.8 cm). The calculated results at r = 0.9 cm do not agree with the measured values.

11.2.1 Results Assuming no Thermocouple/Melt Interaction (Large Crucible)

Figure 11.139 shows the melt temperatures with the crucible rotating at 10 rpm. The calculated temperatures deviate markedly for the calculated values at all radial positions, with r = 4.2 cm showing the best fit. The calculated and measured results for crucible rotation rates of 20 and 30 rpm are shown in Figure 11.140 and 11.141 respectively. The calculated results are not in agreement with the measured values with the axial temperature profile at r = 4.2 cm being in closest agreement. The measured and calculated temperature profiles at r = 0.4 cm behave similarly with with increasing crucible rotation.

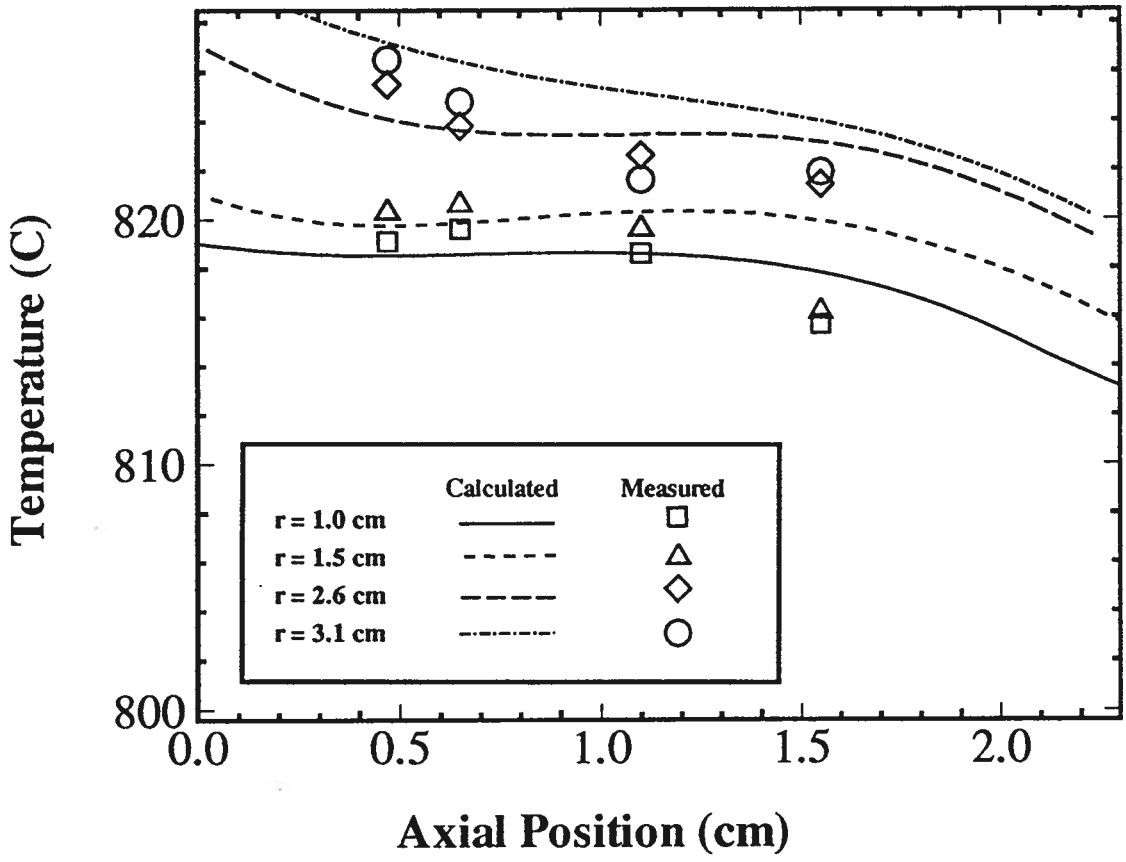

Figure 11.134: Experimental and calculated temperatures as a function of axial height at the radial locations indicated. Small (6.6 cm diameter) crucible. Crucible rotation = 15 rpm. Modified velocity boundary conditions are used. (Figure 11.128).

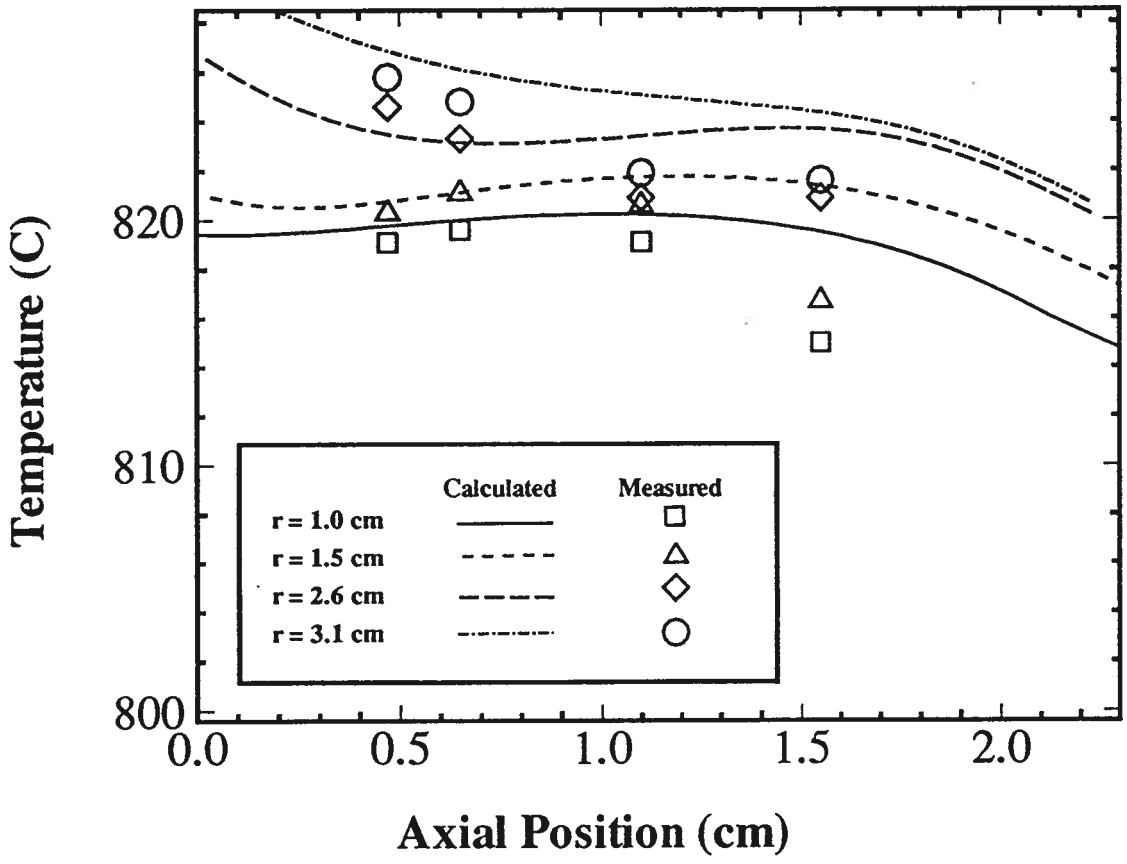

Figure 11.135: Experimental and calculated temperatures as a function of axial height at the radial locations indicated. Small (6.6 cm diameter) crucible. Crucible rotation = 20 rpm. Modified velocity boundary conditions are used. (Figure 11.128).

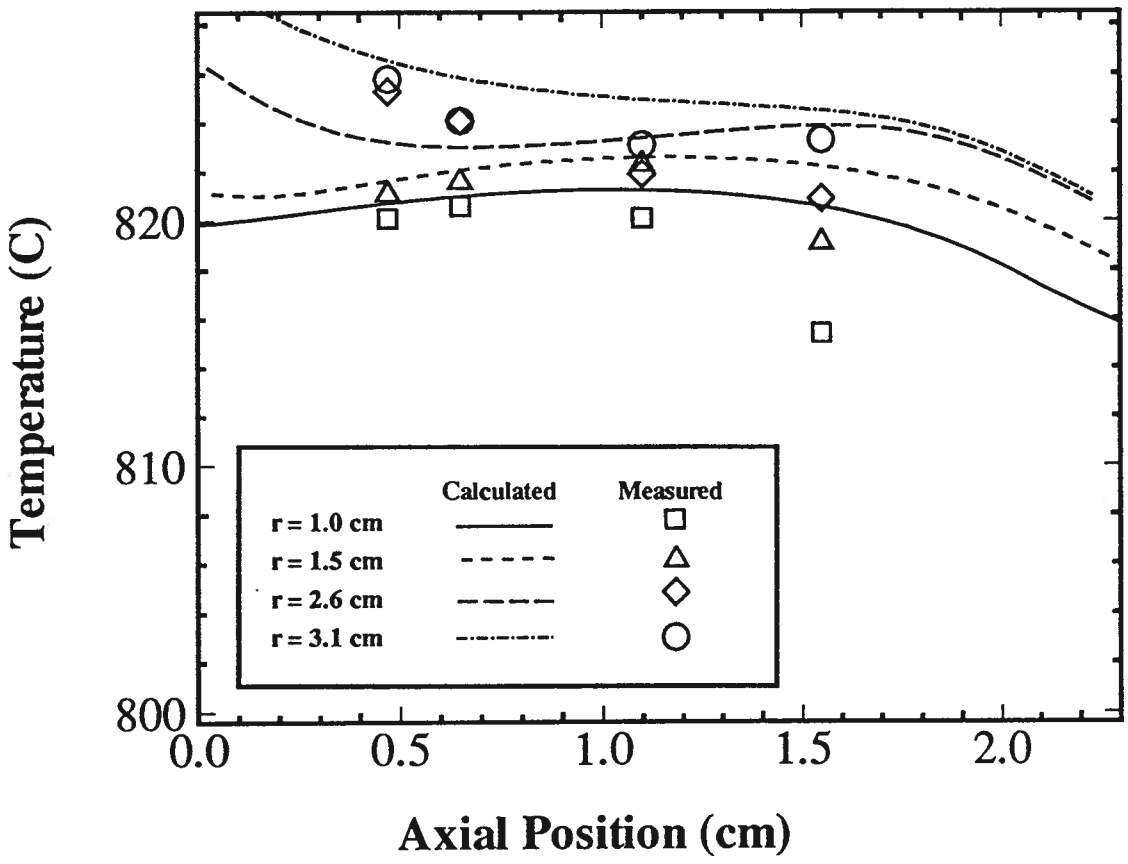

Figure 11.136: Experimental and calculated temperatures as a function of axial height at the radial locations indicated. Small (6.6 cm diameter) crucible. Crucible rotation = 25 rpm. Modified velocity boundary conditions are used. (Figure 11.128).

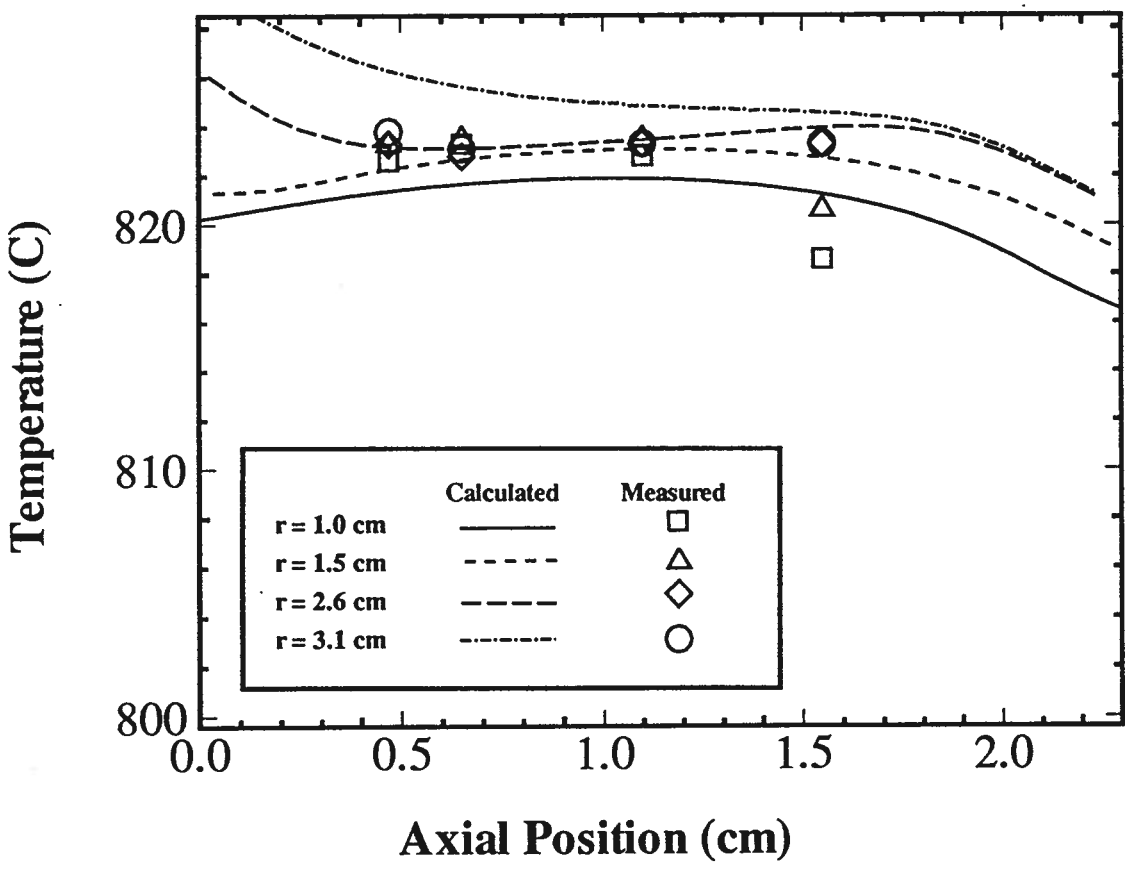

Figure 11.137: Experimental and calculated temperatures as a function of axial height at the radial locations indicated. Small (6.6 cm diameter) crucible. Crucible rotation = 30 rpm. Modified velocity boundary conditions are used. (Figure 11.128).

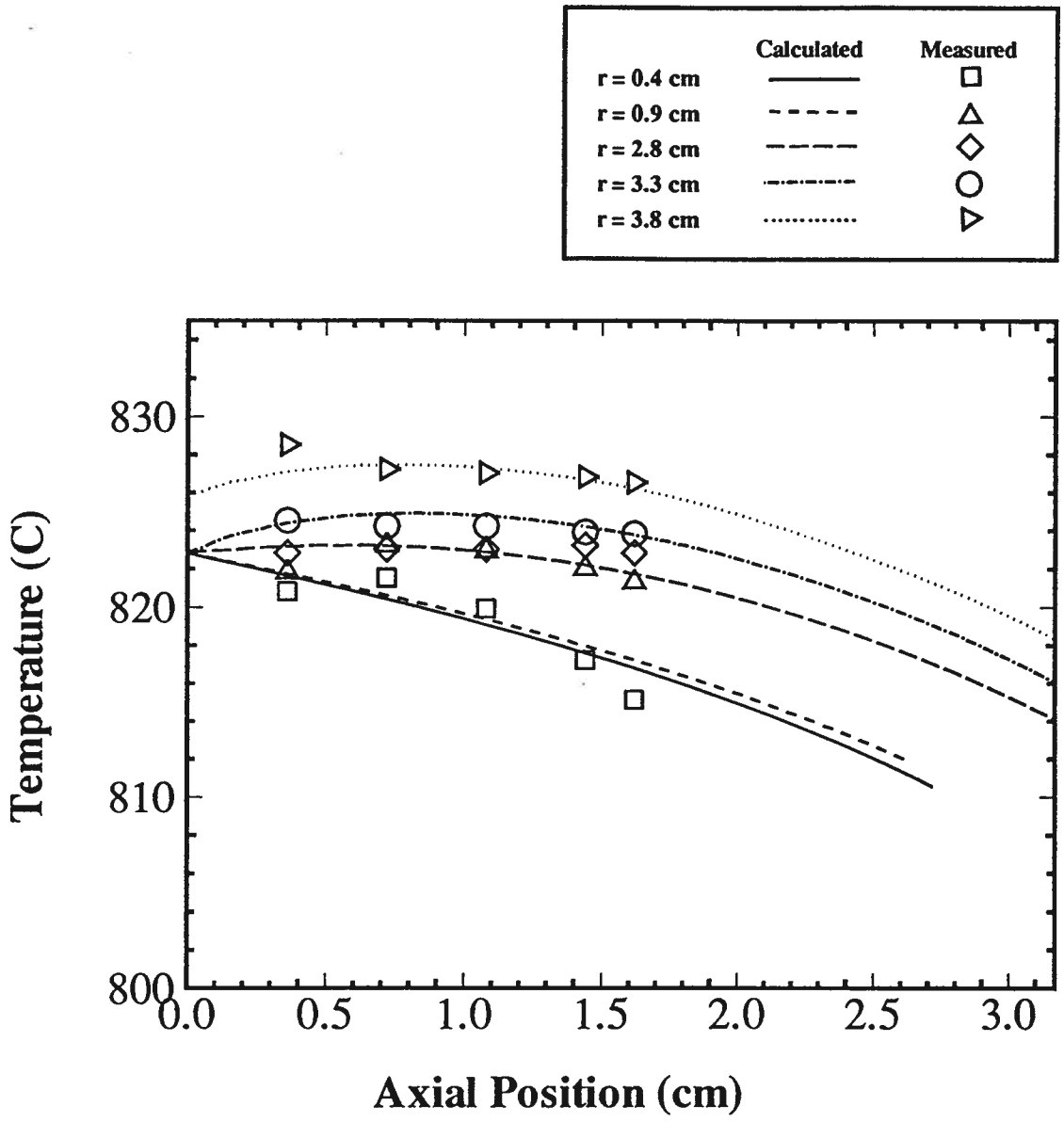

Figure 11.138: Experimental and calculated temperatures as a function of axial location along various vertical lines. Large (8.8 cm diameter) crucible. Zero crucible rotation.

Both the calculated and measured temperatures at z = 1.7 cm increase with increasing crucible rotation rate. The large difference between the calculated and measured results shows that there is more mixing in the melt than is predicted by the model. The results indicate that the thermocouples have a large effect on mixing in the melt.

11.2.2 Results assuming Thermocouple/Melt Interaction (Large Crucible)

The calculated and measured axial temperature profiles at a crucible rotation rate of 10 rpm are shown in Figure 11.142. The calculated axial temperature profiles at r = 2.8, 3.3 and 3.8 cm are approximately flat and the temperature difference between the different axial profiles is small. The measured temperature profiles at the same locations are similar to the calculated values except that measured temperatures are higher than the calculated values. The measured and calculated temperature profiles at r = 0.9 cm differ from the profiles above 2.8 cm. The calculated temperatures are constant at 820°C between z = 0.5 and 2.5 cm. The measured temperatures are approximately constant at 826°C between z = 0.3 and 1.0 cm. The measured temperature above z = 1.0 cm decreases progressively to 818°C at z = 1.6 cm.

The calculated and measured axial temperature profiles at a crucible rotation rate of 20 rpm are shown in Figure 11.143 The difference between the measured axial temperature profiles has decreased with increasing crucible rotation. The calculated axial temperature profiles are similar to that for 10 rpm. The measured axial temperature profiles are constant at 828°C for all radial positions except r = 0.4 cm. At r = 0.4 cm the measured temperature is constant at 828°C between z = 0.4 and 1.0 cm. Above z = 1.0 cm the temperature decreases progressively to 823°C at z = 1.6 cm. The calculated temperatures are constant, near 824°C, for the axial temperature profiles at r = 3.8, 3.3 and 2.8 cm. The calculated axial temperature profiles at r = 0.4 and 0.9 are constant near 822°C.

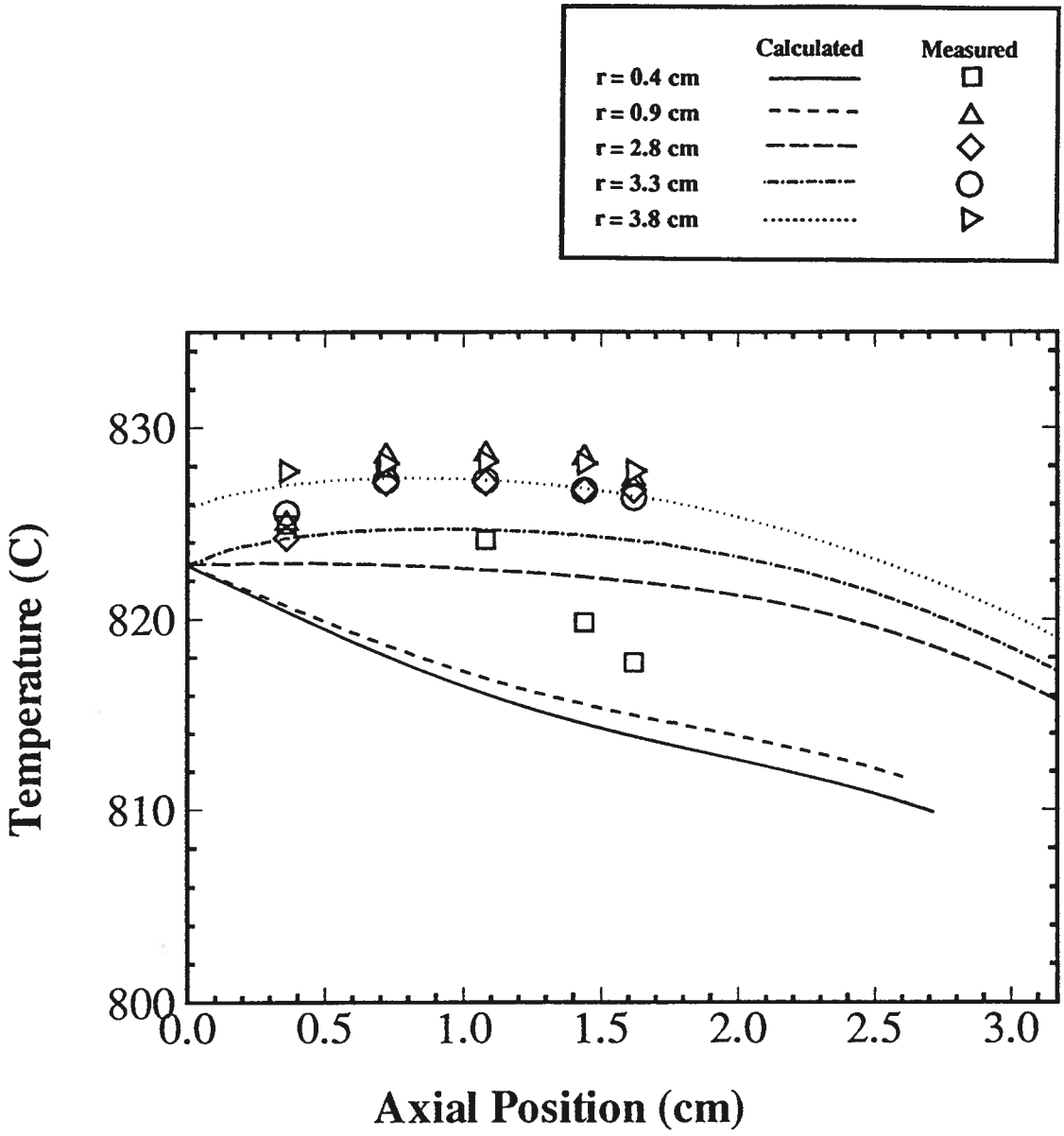

Figure 11.139: Experimental and calculated temperatures as a function of axial height at the radial locations indicated. Large (8.8 cm diameter) crucible. Crucible rotation = 10 rpm. Standard velocity boundary conditions are used (Figure 11.127).

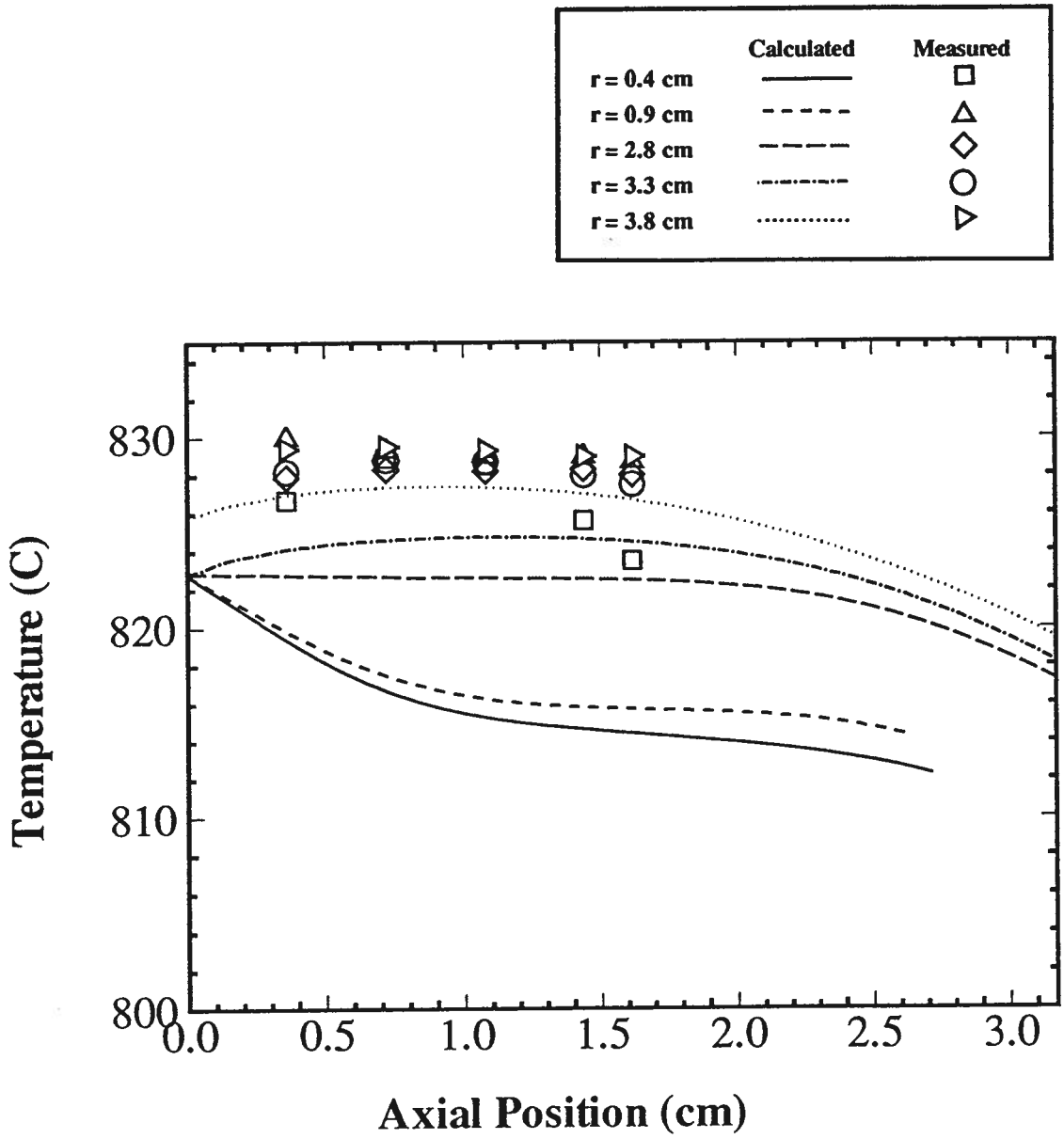

Figure 11.140: Experimental and calculated temperatures as a function of axial height at the radial locations indicated. Large (8.8 cm diameter) crucible. Crucible rotation = 20 rpm. Standard velocity boundary conditions are used (Figure 11.127).

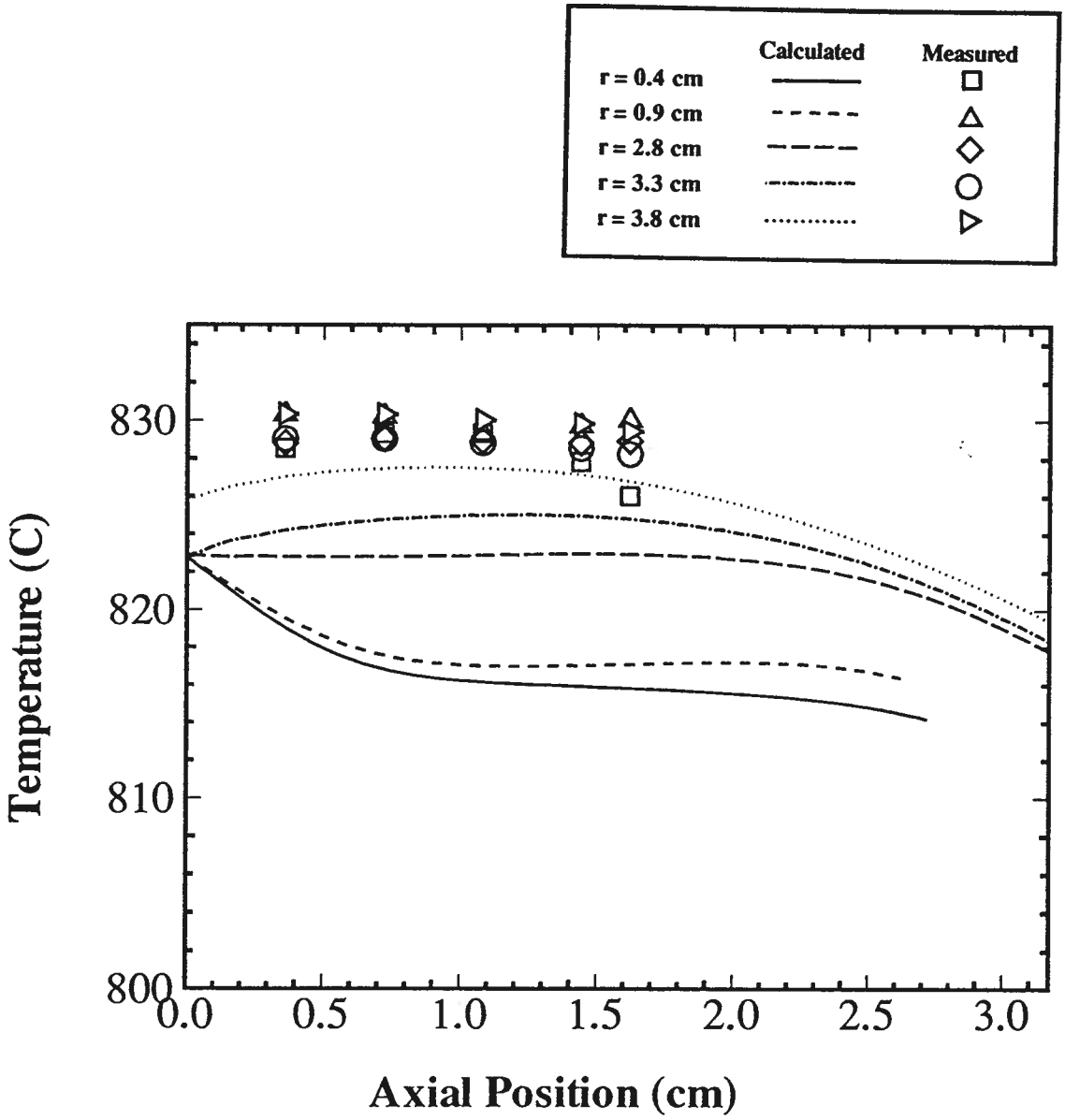

Figure 11.141: Experimental and calculated temperatures as a function of axial height at the radial locations indicated. Large (8.8 cm diameter) crucible. Crucible rotation = 30 rpm. Standard velocity boundary conditions are used (Figure 11.127).

Figure 11.144 shows the measured and calculated temperature profiles at a crucible rotation rate of 30 rpm. All of the measured temperature profiles are constant at 830°C. The calculated values are constant between 822°C and 824°C. The calculated change in temperature profile with crucible rotation rate is similar to the change in measured temperature with crucible rotation. The most notable similarity is the decrease in temperature difference between the axial profiles near the crucible wall (r = 2.8 to 3.8 cm) with increasing crucible rotation. Another similarity is the slow increase in temperature at the centre line of the crucible with increasing crucible rotation rate.

11.3 Summary of the Temperature Comparisons

The model can predict the temperatures within 2 to 4°C of the measured temperatures if the correct boundary conditions and thermophysical properties are used. The accuracy of the model predictions at higher crucible rotation rates indicates that the calculated melt velocity must be near the actual melt velocity. The insertion of the thermocouple in the melt increases mixing. This is not important when predicting the melt temperatures and melt velocity during crystal growth since no thermocouple is present.

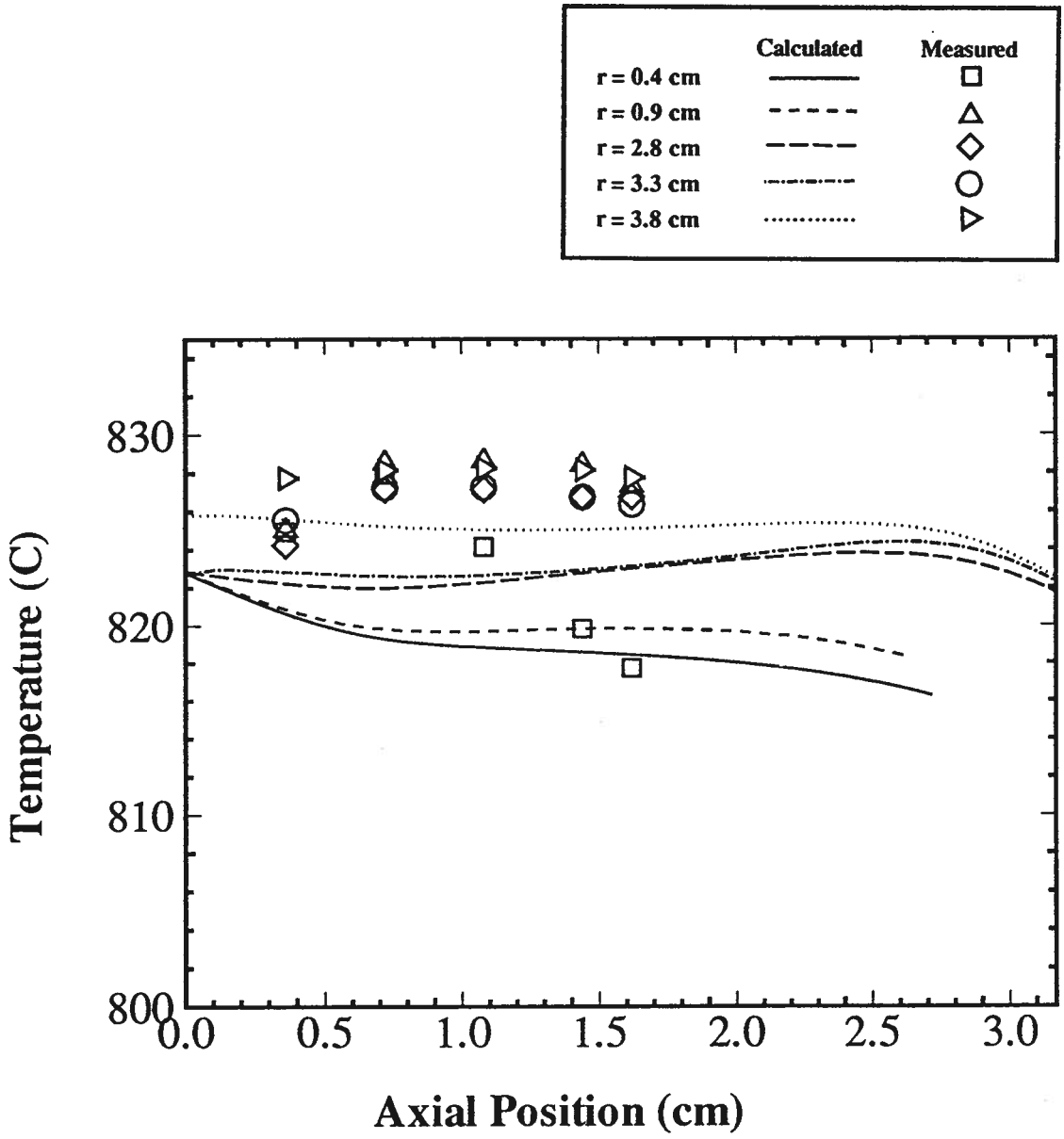

Figure 11.142: Experimental and calculated temperatures as a function of axial height at the radial locations indicated. Large (8.8 cm diameter) crucible. Crucible rotation = 10 rpm. Modified velocity boundary conditions are used. (Figure 11.128).

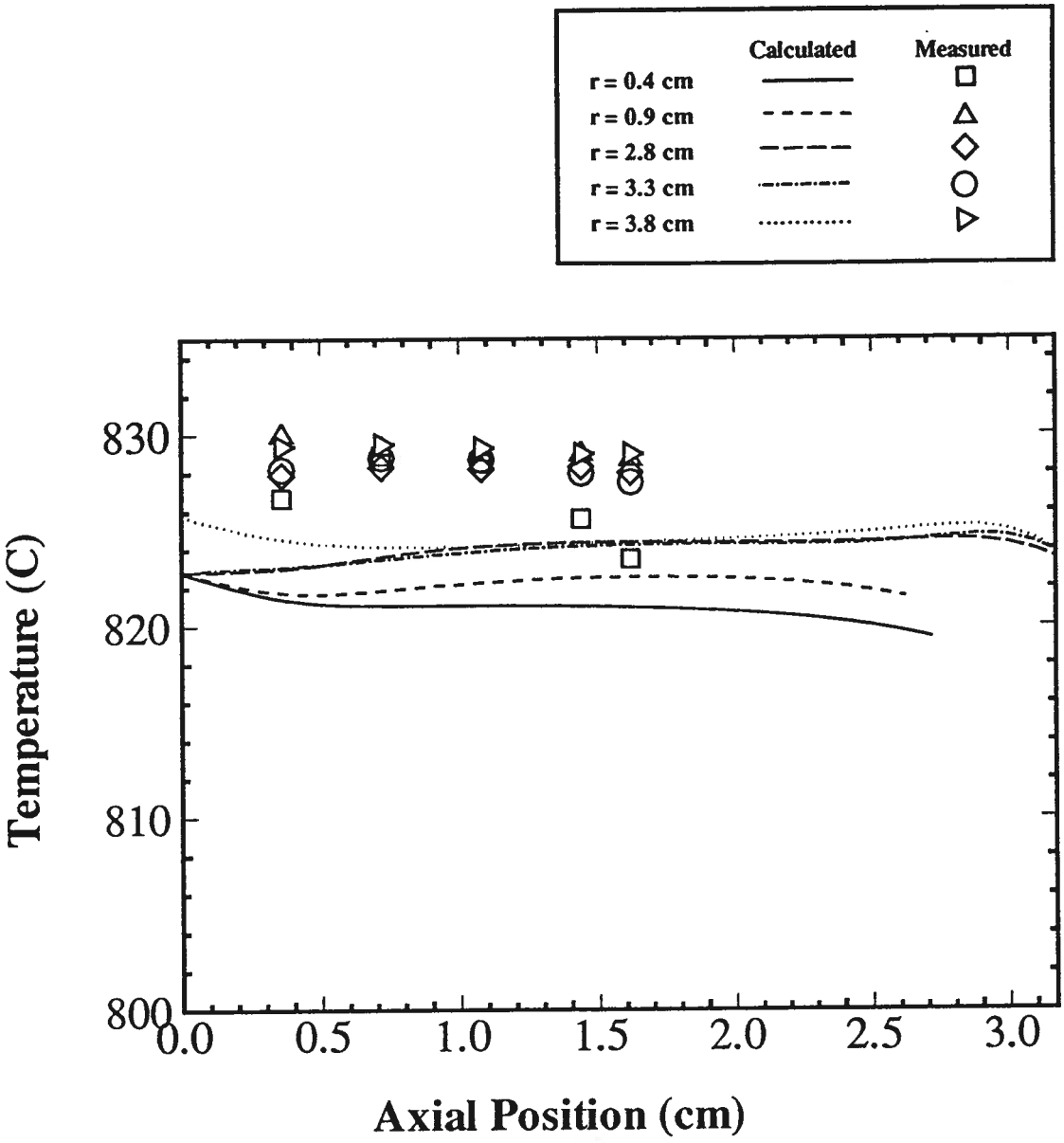

Figure 11.143: Experimental and calculated temperatures as a function of axial height at the radial locations indicated. Large (8.8 cm diameter) crucible. Crucible rotation = 20 rpm. Modified velocity boundary conditions are used. (Figure 11.128).

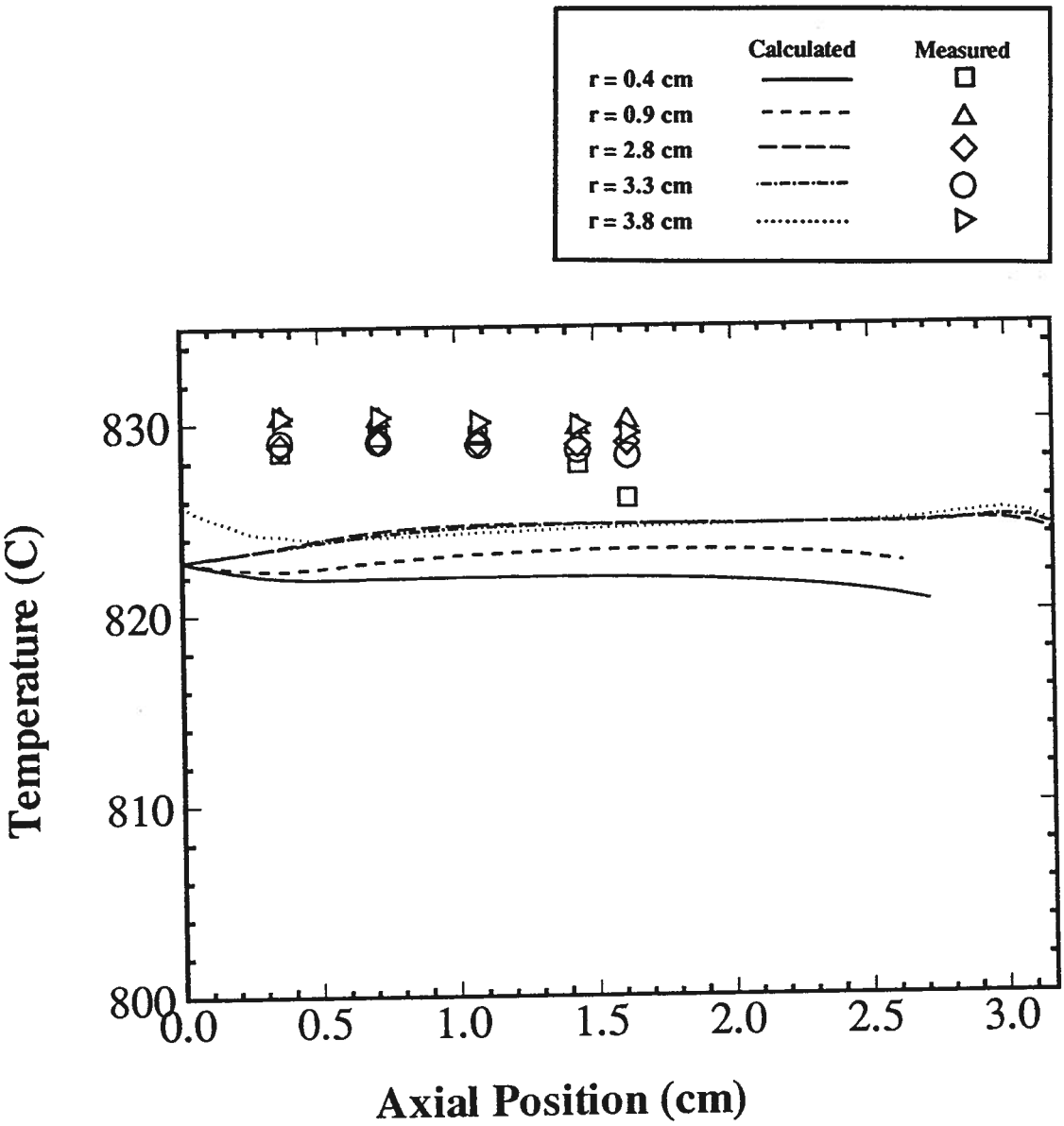

Figure 11.144: Experimental and calculated temperatures as a function of axial height at the radial locations indicated. Large (8.8 cm diameter) crucible. Crucible rotation = 30 rpm. Modified velocity boundary conditions are used. (Figure 11.128).

Chapter 12

Mass Transfer Calculations

The mass transfer calculations were conducted to elucidate the movement of MoO_3 away from the growing interface. This requires knowledge of the diffusion boundary layer thickness below the crystal, the growth velocity of the interface, the diffusion coefficient and the bulk concentration of MoO_3 in the melt. The boundary layer below a rotating disk in an infinite fluid has been determined analytically [45, 46]. The same solution has been extended to include a bottom rotating disk to account for crucible rotation [47, 48]. Unfortunately, the system examined in this research is very different. The bottom of the crystal is not shaped like a flat disk, the fluid is not infinite and the crystal preferentially grows in specific planes, and does not have a uniform radius. Despite these differences, the analytical solution was used in conjunction with the calculated fluid flow solution (Chapter 10)

The mathematical model was used to calculate the flow velocity under the crystal for a given crucible rotation rate. The crystal was assumed to be growing in the [001] direction in an 8.8 cm diameter crucible. An analytical solution was used to determine the crystal rotation rate that gives the same flow velocity under the crystal. The equivalent crystal rotation rate was used with analytical solution for mass transfer below a rotating crystal [45] to examine the change in interface concentration with growth time. Two crystal growth runs (Chapter 13) provided data for this analysis.

12.1 Procedure for Estimating the Equivalent Crystal Rotation Rate

The calculated tangential velocity at 0.5 of the crystal radius for an LBO crystal growing in an 8.8 cm diameter crucible rotating at 60 rpm were compared with the analytical solution to determine a rotation speed required for an infinite disc to produce the same flow velocities. Once this was determined the corresponding boundary layer thickness was calculated from Equation 12.11 and was assumed to apply to the growth of an LBO crystal. The radial velocity below a rotating infinite disk is given by.

$$V_r = r_a \times \omega \times F(z^*) \tag{12.9}$$

were V_r is the radial velocity, r_a is the radial location, ω is the angular velocity and $F(z^*)$ is a dimensionless variable and is given on Table 12.18. The axial location is given by

$$z = z^* \times \left(\frac{\mu}{\rho \times \omega}\right)$$

were z is the axial location, z^* is the dimensionless axial location, μ is the viscosity, ρ is the density and ω is the angular velocity. The radial location value (r_a) used in the analytical solution is equivalent to the surface length between the centre and 0.5 of the model crystal radius as shown in Figure 12.145.

The results of the comparison of the analytical solution to the calculated solution are given in Figure 12.146. The values of the thermophysical properties used for the analytical and calculated solutions are given in Table 12.19. The calculated fluid flow results are for a crucible rotation of 60 rpm and are seen to be identical to an infinite disk rotating at 40 rpm. Thus, the analytical solution with a infinite crystal rotating at 40 rpm ($\omega = 4.19$) can be used to determine the mass transfer that occurs with an 8.8 cm diameter crucible rotated at 60 rpm. It is assumed that this ratio of crucible to crystal rotation is independent of viscosity and density, as long as the same values are used in both calculations.

z^*	$F(z^*)$
0.0	0.0
0.1	0.0462
0.2	0.0836
0.3	0.1133
0.4	0.1364
0.5	0.1536
0.6	0.1660
0.7	0.1742
0.8	0.1789
0.9	0.1807
1.0	0.1801

Table 12.18: Numerical solutions for a rotating disk [46].

Property	Units	Values
density	g/cm^3	3.26
viscosity for 40.9 Wt% MoO_3	poise	21.31

Table 12.19: Thermophysical properties used in the Analytical solution for flow below a rotating disk.

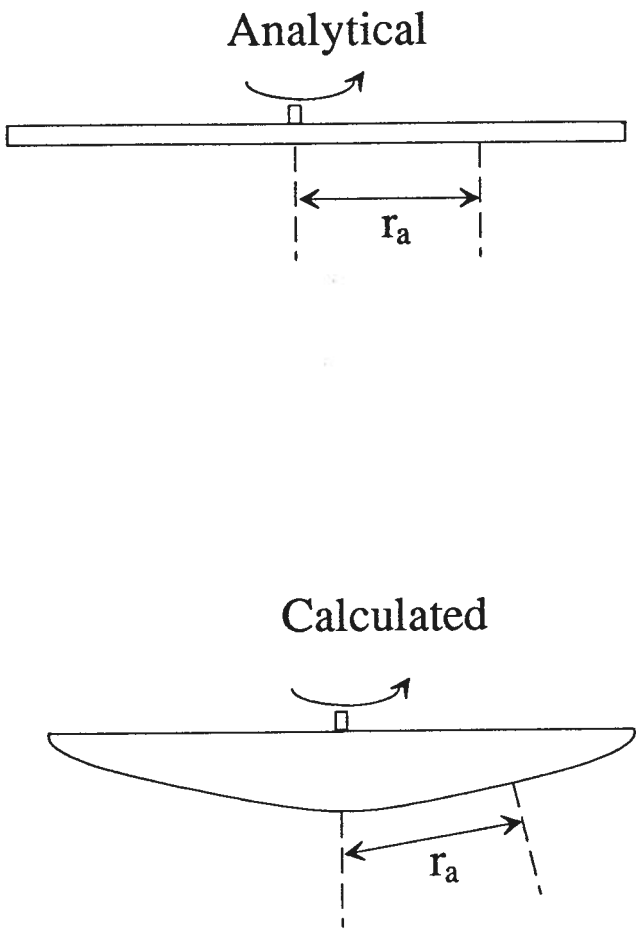

Figure 12.145: determination of the radius used in the analytical solution. The radius, r_a is equivalent for both the finite element analysis and the analytical analysis.

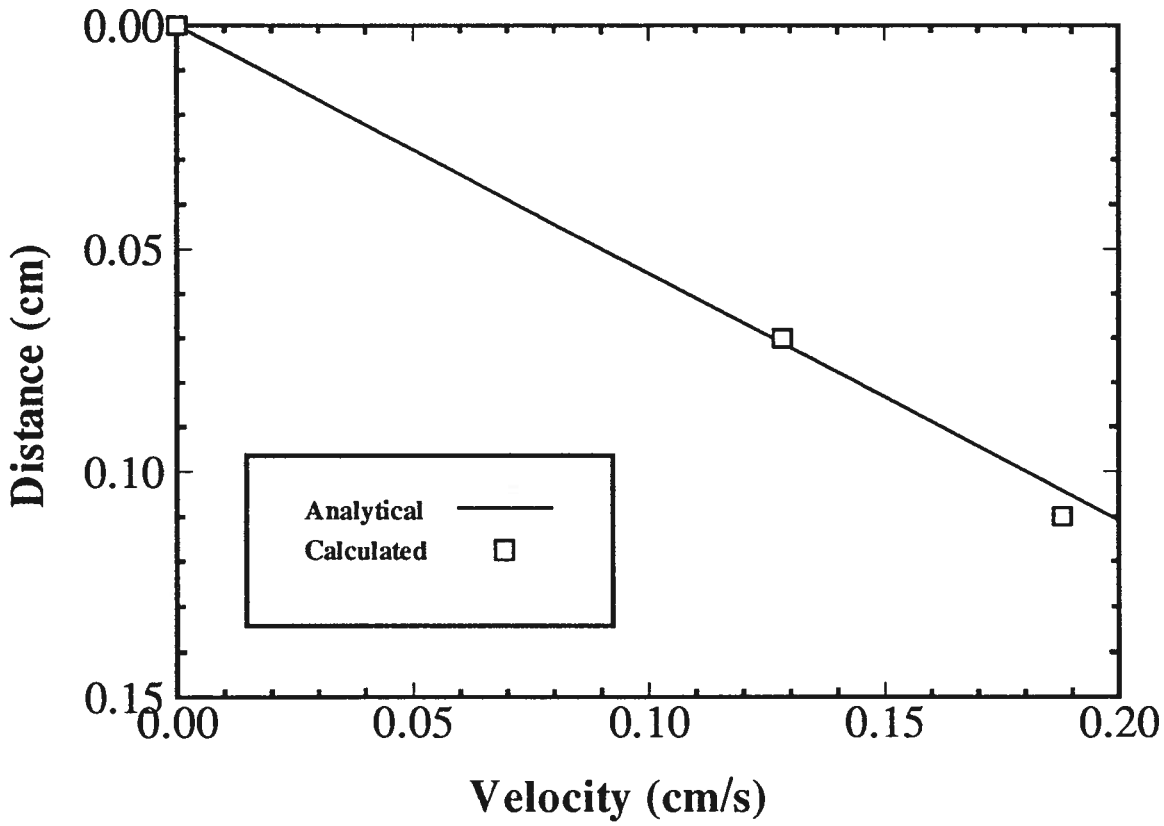

Figure 12.146: Calculated and analytical velocity values. The calculated tangential velocity values are at at 0.5 of the crystal radius. The analytical solution (flow past a rotating disk) for the radial velocity is at a radial location that is equivalent to the surface length of the calculated solution.

12.2 Mass Transfer Behavior of MoO_3 below the Crystal

The concentration of MoO_3 at the growing interface can be calculated [45]. The equation relating the bulk concentration of MoO_3 with the concentration at the interface is:

$$C_o = C_L \times exp\left(\frac{f \times \delta}{D}\right) \tag{12.10}$$

were C_o is the concentration of MoO_3 at the growing interface, C_L is the concentration of MoO_3 in the bulk, f is the growth velocity at the interface, δ is the thickness of the diffusion boundary layer and D is the diffusion coefficient. It is assumed that the movement of the interface (f) is the only flow within the diffusion boundary layer. It is also assumed that δ is constant between the centre and edge of the crystal. The diffusion boundary layer thickness (δ) for an infinite rotating disk is given as:

$$\delta = 1.6D^{1/3}\left(\frac{\mu}{\rho}\right)^{1/6}\omega^{-1/2} \tag{12.11}$$

were D is the diffusion coefficient of solute in the melt in cm^2/s, μ is the viscosity in poise (g/cm s), ρ is the density in g/cm^3 and ω is the rotation rate in rads/s. The growth velocity of the LBO crystal and the MoO_3/LBO diffusion coefficient is determined by combining Equation 12.11 and 12.10. The resulting equation is:

$$D = \left(\frac{f \times 1.6 \times \left(\frac{\mu}{\rho}\right)^{1/6}}{\omega^{1/2} \times ln\left(\frac{C_o}{C_L}\right)}\right)^{3/2} \tag{12.12}$$

All of the variables in the equation are readily available with the exception of the concentration of MoO_3 next to the interface (C_o). This value was determined by growing a crystal at a sufficiently high rate to cause eutectic formation. When this occurs the concentration of MoO_3 next to the interface is 61.5 Wt% MoO_3 (Figure 5.37).

A crystal growth experiment were conducted in which the crystal was slow cooled for a short time then pulled at a rate of 1.66 mm/day. Eutectic growth occurred upon

initiating the pulling sequence. Figures 13.155 and 13.156 show the interface breakdown that occurred when the crystal pulling started. The upper portion of the crystal is clear and free of MoO_3, the lower portion has a eutectic structure of MoO_3 rods in an LBO matrix. The growth rate is a combination of the cooling rate of the furnace and the pull rate of the crystal. The growth rate due to programmed cooling of 2.4°C/day was calculated to be 0.7 mm/day. This was determined by dividing the final height of the crystal by the total growth time for a crystal grown only by melt cooling. Thus the total growth rate (f) was 2.63 mm/day at eutectic formation. The rotation rate of the crucible was 60 rpm which corresponds to a disk rotation rate of 40 rpm. Table 12.20 gives the values of the variables used in determining the diffusion coefficient. The bulk concentration (C_L) is assumed to be the initial theoretical concentration of the melt (44.7 Wt% MoO_3). The viscosity was previously measured (Figure 5.39). The density was calculated using weight fractions of the LBO and MoO_3 with their respective density values.

The diffusion coefficient of MoO_3 in an LBO melt was estimated from Equation 12.12 as 2.42×10^{-8} cm^2/s. The same calculations were carried out assuming the pull rates within ±50% of 1.66 mm/day for comparison reasons. The diffusion coefficients are 3.73×10^{-8} and 1.24×10^{-8} cm^2/s for pull rates of 2.49 and 0.83 mm/day respectively. The variation in diffusion coefficient is minimal for the given changes in pull rate. Table 12.21 gives the values of diffusion coefficients in other liquid systems. The diffusion coefficients of liquid metals and liquid oxides are of the order of 10^{-5} and 10^{-7} respectively. The MoO_3/LBO diffusion coefficient is lower than the other oxide material diffusion coefficients. This may be due to the high temperatures of the oxides given in Table 12.21.

Property	Values
C_o	61.5 Wt% MoO_3
C_L	44.7 Wt% MoO_3
growth rate (f)	2.36 mm/day = 8.08×10^{-7} cm/s
viscosity for 44.7 Wt% MoO_3	12.5 poise
density	3.1 g/cm^3
rotation	40 rpm = 4.19 rads/sec

Table 12.20: Values of the variables used in the determination of the diffusion coefficient.

System	Temperature	Diffusion Coefficient (cm^2/s)
Pb in Lead (Self Diffusion)	343	2.5×10^{-5}
Cu in Cu_2S melt	1160	7.49×10^{-5}
Cu in 39% CaO, 21% Al_2O_3 40% SiO_2 slag	1400	6.7×10^{-7}
Si in 40% CaO, 20% Al_2O_3 40% SiO_2 slag	1430	1.0×10^{-7}

Table 12.21: Diffusion coefficient of some liquids [57].

12.3 Maximum Growth Rates and Growth Times for LBO

The MoO_3 concentration in the bulk of the melt and at the interface will change as the crystal grows. This is due to the rejection of MoO_3 by the solidifying crystal during growth which increases the melt concentration. Equation 12.10 has been used to calculate the concentrations at different times during the growth of the crystal. It was assumed that the system was at steady state at the slow growth rates used and that the diffusion boundary layer thickness does not change as the crystal grows. The crystal interface is assumed to be a cone growing into the melt and that the ratio of radius to crystal height is constant. The volume of the crystal is:

$$V_{xtal} = \frac{1}{3} h \times \pi r^2$$

were V_{xtal} is the volume of the LBO crystal, h is the height of the crystal and r is the radius of the crystal. The relation of the radius to height was determined from a crystal growth experiment where the interface was quenched during the initial stages of its growth (Figure 12.147). The relationship between the radius and height is:

$$\frac{r}{h} = 2.36$$

The increase in crystal height with time is assumed to be a function of the growth velocity:

$$h = f \times t$$

were t is the growth time, h is the crystal height and f is the crystal radius. The volume of the growing LBO crystal at any time during the growth is

$$V_{xtal} = \frac{1}{3} \left(f^3 \times t^3 \times \pi \left(2.36\right)^2 \right)$$

The corresponding weight of the LBO crystal is:

$$W_{xtal} = V_{xtal} \times \rho_{LBO}$$

were W_{xtal} is the weight of the LBO crystal and ρ_{LBO} is the density of LBO (2.474 g/cm^3). The bulk MoO_3 concentration of the fluid can be calculated knowing the amount of LBO that has been removed in growing the crystal.

$$C_L = \frac{Wt_{MoO_3}}{Wt_{MoO_3} + (Wt_{LBO} - Wt_{xtal})}$$

were C_L is the bulk concentration of MoO_3 in the melt, Wt_{MoO_3} is the initial charge weight of MoO_3 in the melt, Wt_{LBO} is the initial charge weight of LBO in the melt and Wt_{xtal} is the weight of LBO in the crystal. Equation 12.10 can be used to calculate the interface concentration. The viscosity and density are assumed to change with the bulk MoO_3 concentration. The melt is assumed to be at 720°C for all of the calculations and the variation in viscosity with MoO_3 concentration is taken from Figure 5.40.

$$\mu = exp(9.818 - Wt_{MoO_3} \times 0.169)$$

$$\rho = Wt\%_{LBO} \times 2.47 + Wt\%_{MoO_3} \times 4.69$$

The interface concentration was calculated for three separate cases. The normal growth rate of 0.70 mm/day (2.4°C/day), a growth rate 50% higher than the normal value (1.05 mm/day, 3.75°C/day) and a growth rate 50% lower than the normal value (0.35 mm/day, 1.2°C/day). The interface concentrations as a function of time are given in Figure 12.148. Table 12.22 gives the variation in interface concentration with time for the normal growth rate.

The interface concentration at the normal growth rate (0.7 mm/day) increases at a constant rate from 48.9 Wt% MoO_3 at day 0 to 49.39 Wt% MoO_3 on day 10. The interface concentration continues to increase until it reaches the eutectic concentration (61.5 Wt% MoO_3) on day 27. Increasing the growth rate by 50% (1.05 mm/day) causes the initial interface concentration to increase to 51.3% MoO_3. The rate of increase of the interface concentration is larger and the eutectic concentration is reached after 17.5

days. Decreasing the growth rate by 50% causes the initial interface concentration to be 46.7%. At the slow growth rates the eutectic is reached well after 30 days of growth. These calculations are very approximate due to the number of assumptions that were employed. However, the trend in the rate of change in interface concentration with growth time can be used to determine the growth time. Growth times should be limited to 27 days or less. This will avoid growing in the region where the increase in concentration with time is large.

There are two factors that have not been accounted for that will alter these predictions. Evaporation of MoO_3 occurs at the surface of the melt which reduces the bulk MoO_3 concentration and in turn the interface concentration. Under these conditions it is possible to grow the crystal for a longer time due to the decreasing bulk MoO_3 concentration. The surface of the crystal is assumed to be flat. Any faceting of the crystal interface, which is a real possibility, will create stagnant areas and increase the MoO_3 concentration at the interface.

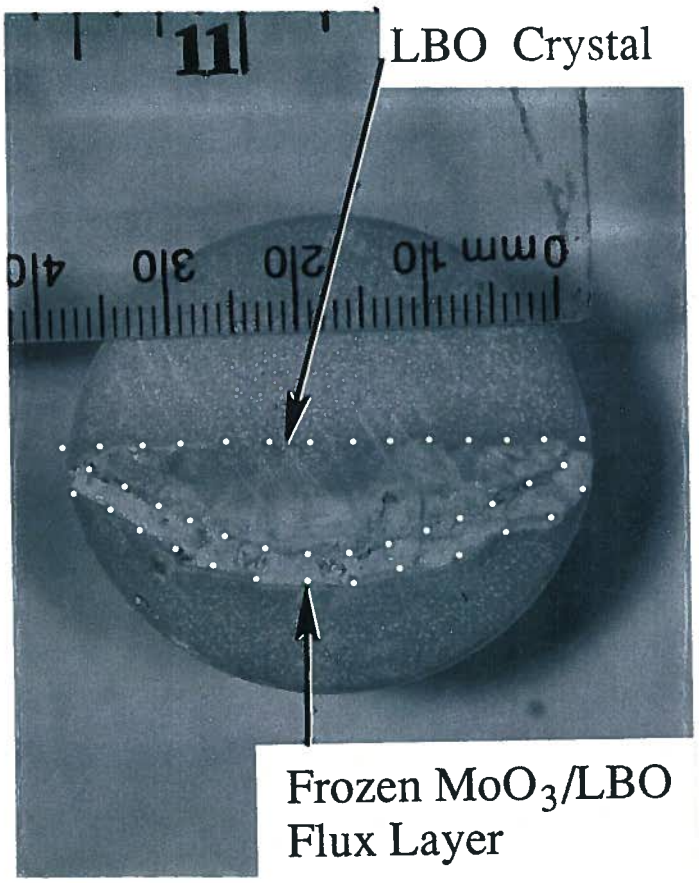

Figure 12.147: Cross section of crystal grown at a crucible rotation rate of 60 rpm. The radius of the crystal is approximately 2 cm and the height at the centre line is 0.85 cm.

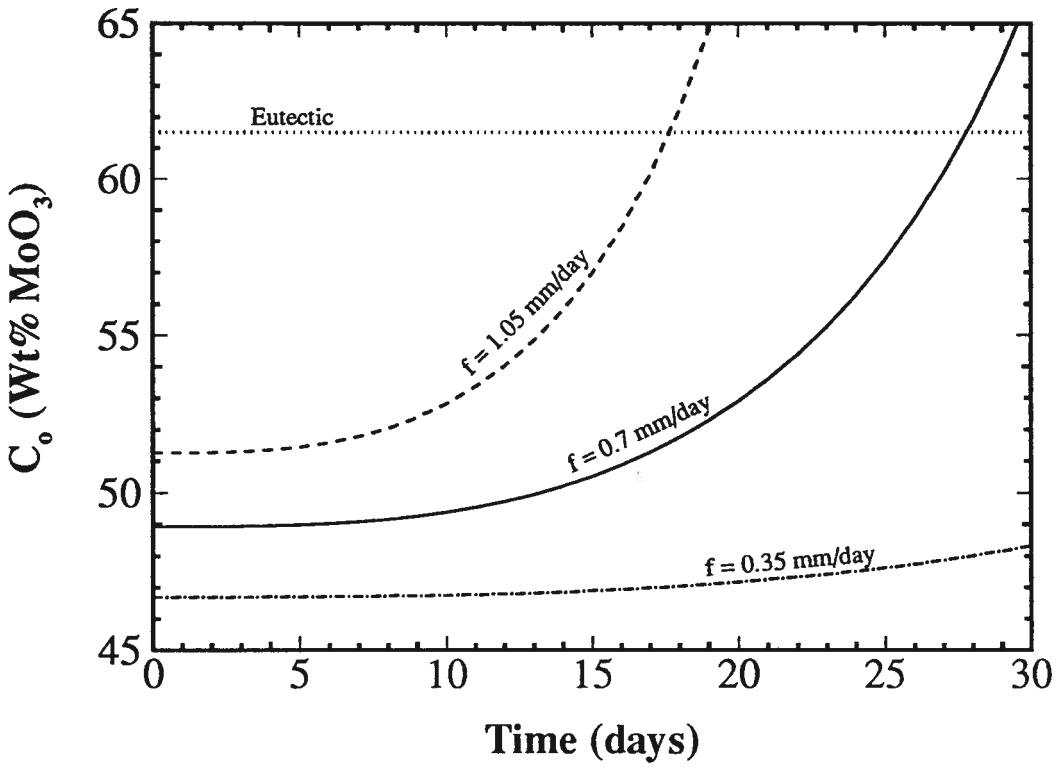

Figure 12.148: The concentration of MoO_3 next to the growing interface as a function of time for the growth rates (f) indicated for a crucible rotation of 60 rpm.

Time (days)	Weight of the LBO Crystal (grams)	Weight of LBO in the Melt (grams)	Weight of MoO_3 in the Melt (grams)	Viscosity (poise)	Density (g/bm^3)	δ (cm)	C_o
0	0.00	256.33	44.57	9.80	3.46	0.00257	48.93
1	0.00	256.33	44.57	9.80	3.46	0.00257	48.93
2	0.04	256.29	44.57	9.79	3.46	0.00257	48.93
3	0.13	256.20	44.58	9.78	3.46	0.00257	48.94
4	0.31	256.02	44.60	9.75	3.46	0.00257	48.96
5	0.61	255.72	44.62	9.70	3.46	0.00257	48.98
6	1.06	255.27	44.67	9.63	3.46	0.00256	49.03
7	1.68	254.65	44.73	9.53	3.47	0.00256	49.08
8	2.51	253.82	44.81	9.40	3.47	0.00255	49.16
9	3.58	252.75	44.91	9.24	3.47	0.00254	49.26
10	4.91	251.42	45.04	9.04	3.47	0.00253	49.39
11	6.53	249.80	45.20	8.80	3.48	0.00252	49.54
12	8.48	247.85	45.40	8.51	3.48	0.00251	49.73
13	10.78	245.55	45.63	8.19	3.49	0.00249	49.95
14	13.47	242.86	45.90	7.82	3.49	0.00247	50.22
15	16.56	239.77	46.22	7.41	3.50	0.00245	50.52
16	20.10	236.23	46.59	6.96	3.51	0.00242	50.88
17	24.11	232.22	47.02	6.47	3.52	0.00239	51.29
18	28.62	227.71	47.51	5.96	3.53	0.00236	51.76
19	33.66	222.67	48.06	5.42	3.54	0.00232	52.29
20	39.26	217.07	48.70	4.87	3.55	0.00228	52.90
21	45.44	210.89	49.42	4.31	3.57	0.00223	53.59
22	52.25	204.08	50.24	3.75	3.59	0.00218	54.38
23	59.70	196.63	51.17	3.21	3.61	0.00212	55.27
24	67.84	188.49	52.23	2.68	3.63	0.00205	56.28
25	76.67	179.66	53.42	2.19	3.66	0.00198	57.42
26	86.25	170.08	54.78	1.74	3.69	0.00191	58.71
27	96.59	159.74	56.33	1.34	3.72	0.00182	60.19
28	107.72	148.61	58.10	0.99	3.76	0.00173	61.87

Table 12.22: The concentration of MoO_3 next to the growing interface as a function of time. Diffusion coefficient is 2.38×10^{-8} cm^2/s. Growth rate (f) is 0.698 mm/day.

Chapter 13

Application of Process Engineering Principles to Crystal Growth

This section describes the Lithium Triborate crystal growth runs that were conducted with parameters based on results from the mathematical model, the physical model and experimental measurements of temperature and viscosity described in Chapters 10, 6, 5 and 7 respectively. The experimental measurements and mathematical model have shown that crucible/crystal rotation, crucible size and MoO_3 content in the melt are the parameters that have the greatest influence on fluid flow below the crystal.

In particular, the mathematical model established that crucible rotation produces the maximum fluid flow across the growing solid/liquid interface. Crystal rotation was not used in conjunction with crucible rotation since it would decrease the fluid flow at the growing crystal/liquid interface (Figure 10.121). The crucible rotation rates tested were 18.5, 30 and 60 rpm. The initial rotation rate (18.5 rpm) was similar to the crystal rotation used in the preliminary experiments (Section 5.3). An 8.8 cm diameter crucible was used for most of the crystal growth runs since melt velocity due to crucible rotation increases with crucible size. A 6.6 cm diameter crucible had to be used for the first two crystal growth runs since the 8.8 cm crucible was unavailable. A high MoO_3 melt content (44.5 Wt%) was used since the viscosity decreases with increasing MoO_3 content.

Parameters for the mass transfer model were estimated from the results of crystal growth runs LBO 19 and LBO 20 and were used to elucidate the change in interface concentration with growth time. The mass transfer analysis was conducted for crystals growing in the [001] direction. It was determined that the interface concentration initially

increases at a slow rate followed by an exponential increase. It was also found that the crystal growth velocity in the [001] direction had to be slower than the minimum pull speed of the crystal growth apparatus (1.66 mm/day) due to eutectic formation at this pull speed.

Certain aspects of crystal growth were not modeled or studied prior to the crystal growth runs. Two effects that are likely to influence crystal growth that were not considered are:

1. The influence of crystal orientation on the build up MoO_3 at the growing interface and inclusion/eutectic formation. Different crystal growth orientations could produce faceting which would result in higher inclusion formation/interface breakdown. The preferred growth direction used in this investigation was [001] given that devices had to be fabricated that were up to 1.5 cm in the [100] direction. The first two runs were carried out in the $[3\bar{1}2]$ direction until enough seed material was produced in the preferred direction.

2. The effect or growth atmosphere on crystal quality was not investigated. The furnace atmosphere was changed from air to dry nitrogen once it was determined that LBO decomposed in the presence of water vapour [6].

Nine crystal growth runs were conducted during this investigation (LBO 17 – LBO 25). The complete list of the parameters used in crystal growth runs are given in Tables 13.23 and 13.24. LBO 16 was completed before the initiation of this investigation (LBO 16) and is listed in Tables 13.23 and 13.24 as a reference for comparison.

13.1 LBO 17

The first crystal (LBO 17) was grown using the 6.6 cm diameter crucible in air. The crystal was grown in the $[3\bar{1}2]$ direction, the melt cooling rate for growth was 2.4°C/day:

which should yield a growth rate of 0.7 mm/day; the crucible rotation was 18.5 rpm and the crystal was stationary. The aim of this experiment was to determine if crucible rotation and a higher MoO_3 content would produce a better crystal. The previous run (LBO 16) was conducted with crystal rotation of 15 rpm, no crucible rotation and a 34.4 Wt% MoO_3.

During growth the growing crystal/liquid interface at the surface of the liquid was strongly faceted. The crystal was grown until its edges reached the outside of the crucible. After growth, the crystal was raised from the melt before cooling to room temperature at 10°C/hour. Unfortunately, the distance raised was insufficient, which resulted in it freezing into the melt.

Figure 13.149 confirms that LBO 17 froze into the melt. The upper surface of the crystal is a white translucent color. Large cracks, marked A, run along the diagonals of the crystal. The edge marked B is due to a piece of the crystal falling off while it was cooling to room temperature. Strong faceting is present at the edges of the crystal that correspond to the liquid/solid interface (C). The rounded edge of the crystal (marked D) is due to the crystal growing close to the side of the crucible. The uncracked pieces of LBO 17 are shown in Figure 13.150. All of the pieces of the crystals were inclusion free in the region that corresponded to the upper surface (marked E on some of the crystal pieces). The lower areas of the crystal shattered into a white powder when the solid/liquid interface froze (marked F on some of the crystal pieces).

Despite these problems there was a significant increase in crystal quality and yield size compared to preliminary growth experiments. Previously the average inclusion free region was approximately $3 \times 3 \times 3$ mm^3 (Figure 5.41). LBO 17 was predominantly inclusion free at the outer edges of the crystal, and average size of the individual pieces of LBO crystal were $15 \times 5 \times 5$ mm^3. The increased crystal quality can be attributed to the improved mixing in the melt due to crucible rotation, the higher MoO_3 content (44.5

versus 34.3 Wt% MoO_3) and the absence of interface breakdown.

13.2 LBO 18

LBO 18 was grown in the $[3\bar{1}2]$ direction as per the previous run. The melt cooling rate for growth was the same as in the previous run (2.4°C/day). Two of the growth parameters, crucible rotation and crystal pulling, were changed. The crucible rotation rate was increased to 30 rpm to improve mixing in the melt and the crystal was pulled at 1.66 mm/day to increase its thickness. The mathematical model predicts that the magnitude of the tangential velocity beneath the crystal should increase from 5×10^{-2} cm/s at 15 rpm to 10.5×10^{-2} cm/s at 30 rpm (Figure 10.114). The pull rate of the crystal was the minimum speed of the motor. The growth procedure consisted of slow cooling the furnace at 2.4°C/day until the crystal had grown to approximately 2 cm in diameter. The crystal was then pulled for 6 days at 1.66 mm/day to increase its axial thickness. After pulling, the furnace was slow cooled at 2.4°C/day for the remainder of growth. During growth the crystal had strong faceting at the solid/liquid interface.

Crystal LBO 18 is shown in Figure 13.151 and 13.152. The crystal has two distinct areas, the upper portion (A), due to a pull rate of 1.66 mm/day, and a lower portion (B) where only slow cooling was applied to the melt/crystal. The crystal grew along specific planes. Major cracks were present in the crystal, running from the outer points of the crystal inward to the centre. The bottom of the crystal was either clean (C) or covered with MoO_3 flux (D) that was white/green in color. The regions covered with flux were severely cracked. The surface of the clear regions were predominantly uncracked, however cracks from the flux covered region propagated into the clear regions. The crystal was free of MoO_3 inclusions with the exception of two locations, at the bottom surface of the crystal (D) and at the location where pulling was terminated (Between areas A and

B). This would indicate that growth along the $[3\bar{1}2]$ direction could be as high as 1.66 mm/day. Differences in growth rate and faceting with orientation are expected since the LBO crystal structure is orthorombic and the faceted shape has been previously shown (Figure 2.6). The crystal was moderately fragile and broke into pieces after a limited force was applied to it.

The individual pieces of flux free portions of the crystal (A in Figure 13.151) are shown in Figure 13.153. The uncracked and inclusion free piece is approximately $20 \times 15 \times 6$ mm^3. The decrease in inclusion density (increase in crystal quality) of LBO 17 and 18 can be attributed to three factors; using crucible rotation to increase the fluid velocity next to the growing interface, increasing the MoO_3 content to decrease the viscosity (which also increases the fluid velocity), and effects that are possibly due to the growth direction. Pulling the crystal at 1.66 mm/day did not result in interface breakdown which suggests that growth in the $[3\bar{1}2]$ direction can be large.

13.3 LBO 19

LBO 19 was grown in the [001] direction, which is the previous growth direction, in the large crucible (8.8 cm diameter). The crystal was slow cooled until its diameter was approximately 6 cm after which it was also pulled at a rate of 1.66 mm/day. The crystal is shown in Figure 13.154. The seed is marked A, the slow cooled portion of the crystal is marked B, the slow cooled/pulled at 1.66 mm/day area of the crystal is marked C and D. The area marked E is where a piece of the crystal had broken off. The crystal was very fragile and broke easily. The lower area of the crystal which grew while it was being slow pulled (C and D) was a white/green color indicative of interface breakdown. The growth rate was sufficiently fast that the diameter of the crystal decreased to a value of 1 cm (D).

The polished cross section of the crystal is shown in Figure 13.155. The crosses correspond to areas where X−Ray diffraction was conducted to determine the crystal orientation. The analysis was conducted at the seed, before the interface breakdown and at two points inside the white/green portion of the crystal. All of the X−Ray diffraction patterns were identical, and revealed that the crystal consisted of an LBO matrix. SEM photos were taken in the area were the interface break down occurred (Area C on Figure 13.155). Wavelength dispersive spectroscopy (WDX) was also carried out at the same locations to qualitatively determine if MoO_3 was present. Figure 13.156(a) is an SEM photo of the region where interface breakdown commenced. There are long rod like inclusions in the LBO matrix, and the growth direction is parallel to the rods. The corresponding molybdenum map of the same area, Figure 13.156(b), shows that the rods consist of molybdenum. A backscatter image and WDX image of an individual inclusion is shown in Figure 13.157. Unlike the previous run, LBO 19 formed eutectic material when the crystal was pulled at 1.66 mm/day. Two parameters were changed relative to growth of LBO 18; LBO 18 was grown along the $[3\bar{1}2]$ in a small crucible while LBO 19 was grown along the [001] direction in a large crucible. Increasing the crucible size has been demonstrated to increase the flow velocity below the crystal, thus the eutectic formation in LBO 19 cannot be attributed to the change in crucible size. The occurrence of the eutectic in LBO 19 must be due to the growth direction, indicating that that the [001] direction readily forms eutectic at a pull speed of 1.66 mm/day for crucible rotations of 30 rpm or slower.

13.4 LBO 20

LBO 20 was grown with a faster rotation rate (60 rpm) to improve the removal of MoO_3 from the interface. An increase in crucible rotation from 30 to 60 rpm increases the

magnitude of the tangential velocity beneath the crystal from 10.5×10^{-2} cm/s to 21×10^{-2} cm/s (10.114). The crystals were cycled through a slow cooling/pulling period for 1 day and a slow cooling period of 1 day to facilitate diffusion of MoO_3 ahead of the interface and to prevent the rapid reduction in crystal diameter. The crystal, Figure 13.158, is 5 cm in diameter. The crystal was very fragile and broke into several pieces, as shown in the figure, when it was handled. The top of the crystal was covered with a thin white powder. The cross section of the crystal is shown in Figure 13.159. The area marked A is part of the crystal that had broken off. The cross section of the crystal, was similar to LBO 19 in that the upper (slow cooled) portion was clear and the lower portion had the eutectic structure. The crystal diameter was reduced to approximately 4 cm with the pulling/cooling cycle. The pulling mechanism on the crystal growth station had a minimum pull rate of 1.66 mm/day with no diameter control mechanism. The previous two crystal growth runs, LBO 19 and 20, in conjunction with the mass transfer calculations, indicate that a pull rate of 1.66 mm/day will produce interface breakdown for [001] direction crystal growth for a 8.8 cm diameter crucible rotated at 60 rpm. Larger crucible rotation rates were not investigated since 60 rpm was close to the maximum rotation rate of the apparatus.

13.5 LBO 21

LBO 21 was grown using slow cooling without crystal pulling and with a dry N_2 atmosphere. The dry N_2 was used to prevent the upper surface of the LBO from decomposing at an elevated temperature in the presence of water vapour [6]. Unfortunately LBO 21 was slow cooled until a power outage froze the crystal into the melt. The crystal, Figure 13.160, was severely cracked due to it being frozen into the melt. The white/green colored material (A) is the LBO/flux that has been frozen onto the outside of the crystal

due to the fast quench. The crystal was removed in this area to show the surface of the growing interface. Two type of surfaces are present at the growing interface, rough and smooth depending on the orientation of the growing surface. The crystal surface (B) is clear due to the dry N_2 atmosphere. A portion of the surface of the crystal (C) is clear at the upper surface. The dry N_2 prevented the upper surface of the crystal from decomposing is in the previous runs.

13.6 LBO 22 and 23

The subsequent crystal growth run, LBO 22, was conducted under identical growth conditions as LBO 21. Unfortunately this run was unsuccessful due to failure of the motor and the crystal accidentally froze with the melt during the post growth cooling to room temperature. LBO 23 was grown using the identical conditions as LBO 21. Figure 13.161 and 13.162 shows the top and bottom of the crystal respectively. The bottom of the crystal has clear regions in addition to the portions that are covered with the MoO_3 flux. The upper surface is clear with the crystal changing to a white color close to the bottom of the crystal where the flux is present. The white color corresponded to areas where the crystal shattered due to differences in the thermal expansion coefficients of MoO_3 and LBO. The clear portion of crystal that grew as a flat surface was the 101 plane. The flux covered portions grew as a number of irregular planes in a shingle like configuration. A photo and schematic of the cross section of a plane that grew as a rough surface is shown in Figure 13.163. The region marked B is were the MoO_3 builds up. The rough surface creates stagnant areas were MoO_3 can accumulate. The areas of the crystal where the flux was attached to the bottom surface were fragile and broke apart with moderate to little force. The areas of the crystal that were free of flux, Figure 13.164, were crack resistant. The largest crystal size was approximately $20 \times 10 \times 8$ mm^3. The

previous three crystal growth runs(LBO 21, 22 and 23) demonstrated that the 101 plane grows as a flat surface while the other planes are faceted. The facets result in a build up of MoO_3 at the solid/liquid interface which sticks to the surface of the crystal after it has been separated from the melt. These crystal growth runs also confirm that LBO crystals can be grown under these conditions without interface breakdown which is in accordance with model predictions in Figure 12.148.

13.7 LBO 24

LBO 24 growth conditions were identical to LBO 21. The post growth cooling procedure was modified to reduce the thermal gradients in the crystal. Insulating bricks were placed over the top hole and separation of the crystal from the melt was carried out by lowering the crucible rather than raising the crystal. was lowered instead of the raising crystal to separate it from the melt. Measurements reported in Chapter 5 suggest that the axial and radial temperature gradients in the crystal can be reduced by moving the crystal to the centre of the furnace and insulating the top hole while the crystal is cooling to room temperature. This procedure also ensured that the crystal was as close as possible to the centre of the furnace elements thus reducing the thermal gradient in the crystal. Figure 13.165 and 13.166 shows the top and bottom of the crystal respectively. Figure 13.167 is a back light view of the crystal. As with the previous crystal growth runs the crystal had a flux build up on the rough surfaces of the growing interface (marked A in Figure 13.166). The 101 family of planes (marked B in Figure 13.166) were flat and the surface was free of flux. Areas adjacent to the flux covered surface were cracked to a fine white powder. The crystal, while still having macro cracks, did not break when a moderate force was applied to it. Thus reducing the thermal gradient in the crystal did result in improved strength. The largest crystal area that was uncracked between the

Growth Run	Date (mm/dd/yy)	Composition (Wt% MoO_3)	Seed Orientation	Crucible Diameter (cm)	Rotation Rate	
					Crucible (rpm)	Crystal (rpm)
LBO 16	5/21/92	30.0	non seeded	6.6	0	6
LBO 17	8/6/92	44.5	3 $\bar{1}$ 2	6.6	18.5	0
LBO 18	10/5/92	44.5	3 $\bar{1}$ 2	6.6	30.0	0
LBO 19	11/26/92	44.5	0 0 1	8.8	30.0	0
LBO 20	01/8/93	44.5	0 0 1	8.8	60.0	0
LBO 21	03/24/93	44.5	0 0 1	8.8	60.0	0
LBO 22	06/9/93	44.5	0 0 1	8.8	60.0	0
LBO 23	07/21/93	44.5	0 0 1	8.8	60.0	0
LBO 24	8/9/93	44.5	0 0 1	8.8	60.0	0
LBO 25	12/7/93	44.5	0 0 1	8.8	60.0	0

Table 13.23: Growth conditions used for the crystal growth experiments.

top and growing interface was $20 \times 10 \times 5$ mm^3. The increased strength of the crystal is a result of the lower thermal gradients during cooling to room temperature.

13.8 LBO 25

LBO 25 was grown to determine if the build up of flux at the interface was due to the length of the growth runs. Growth conditions identical to LBO 24 were used except that the crystal was grown for only 14 days. There was a MoO_3 build up at the rough interface. Figure 13.168 shows a portion of the crystal with the MoO_3 build up. The white regions correspond to flux attached to the crevices between the growing planes. As in the previous crystal growth runs, the 101 family of planes grew as a flat surface with no MoO_3 build up. The presence of the MoO_3 at this small crystal size indicates that flux build up occurs during all stages of crystal growth.

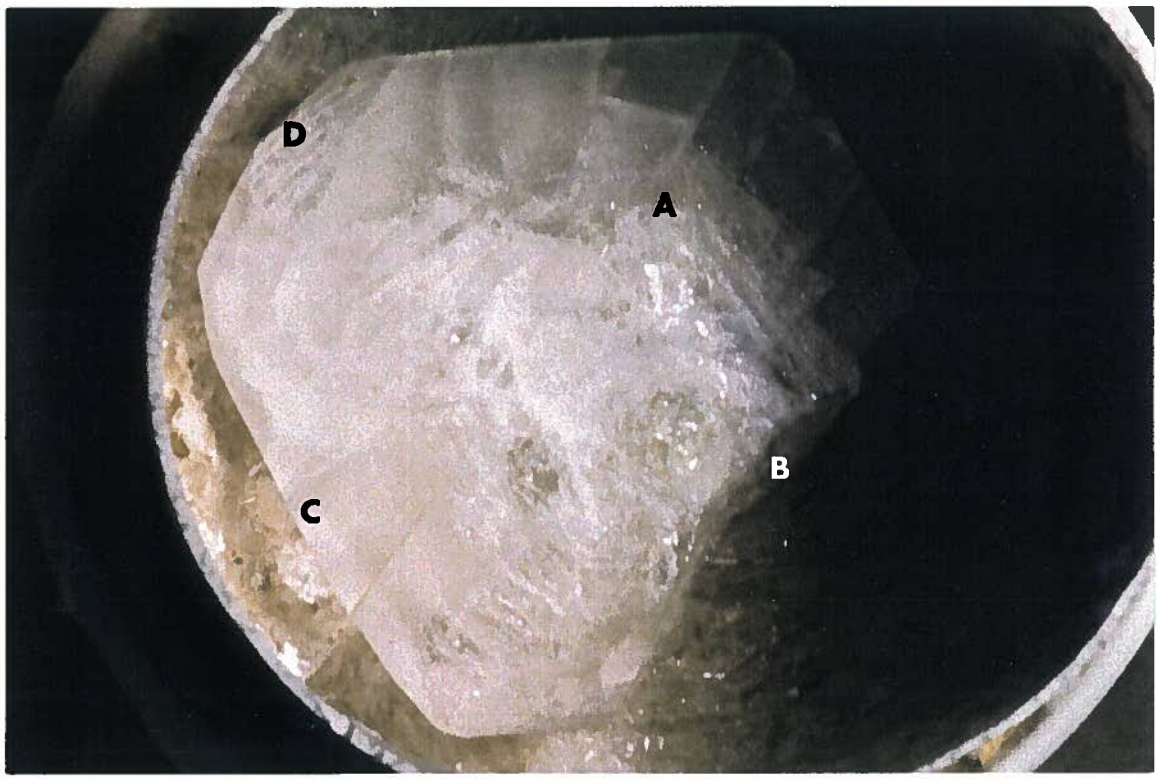

Figure 13.149: LBO 17 crystal frozen in the melt.

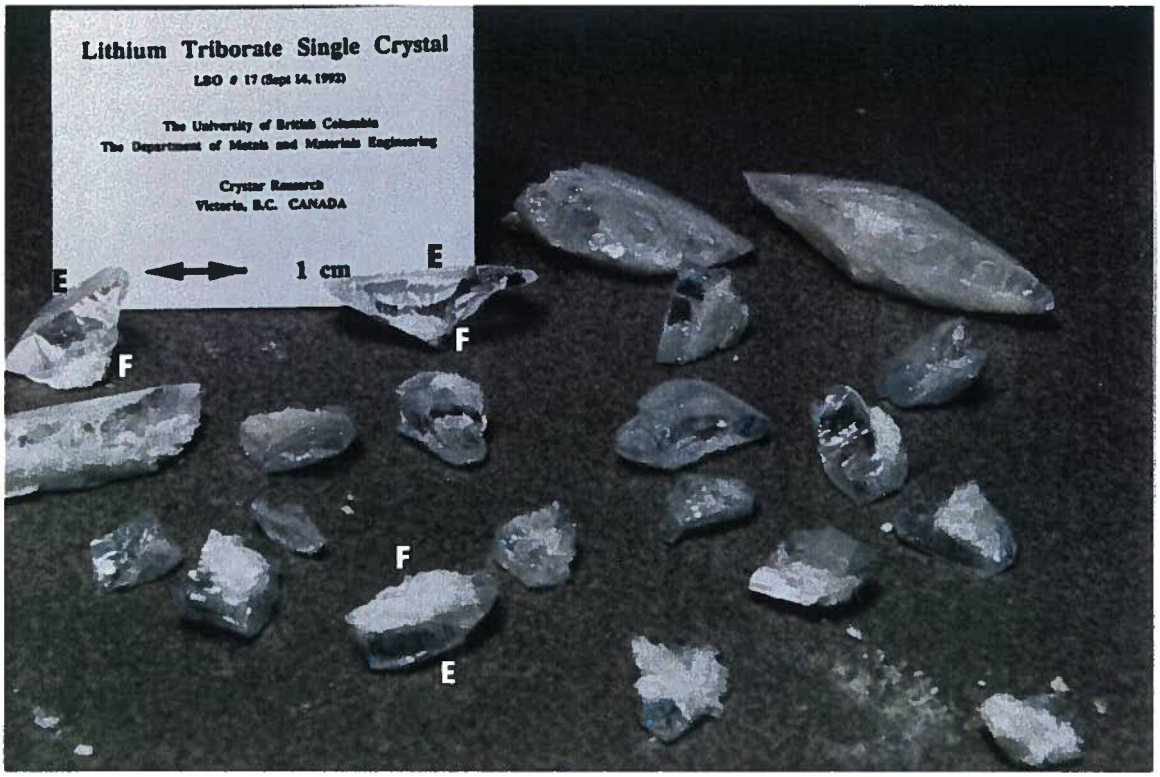

Figure 13.150: Uncracked portions of LBO 17 crystal.

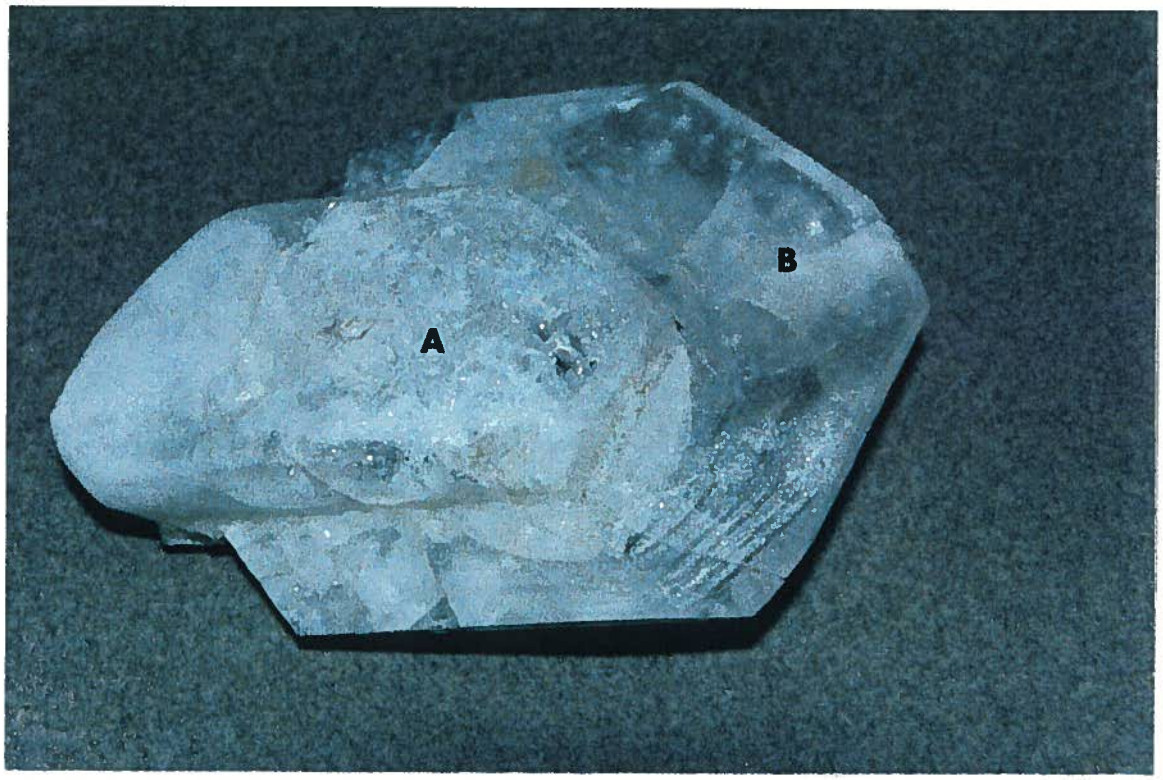

Figure 13.151: Top view of LBO 18 crystal.

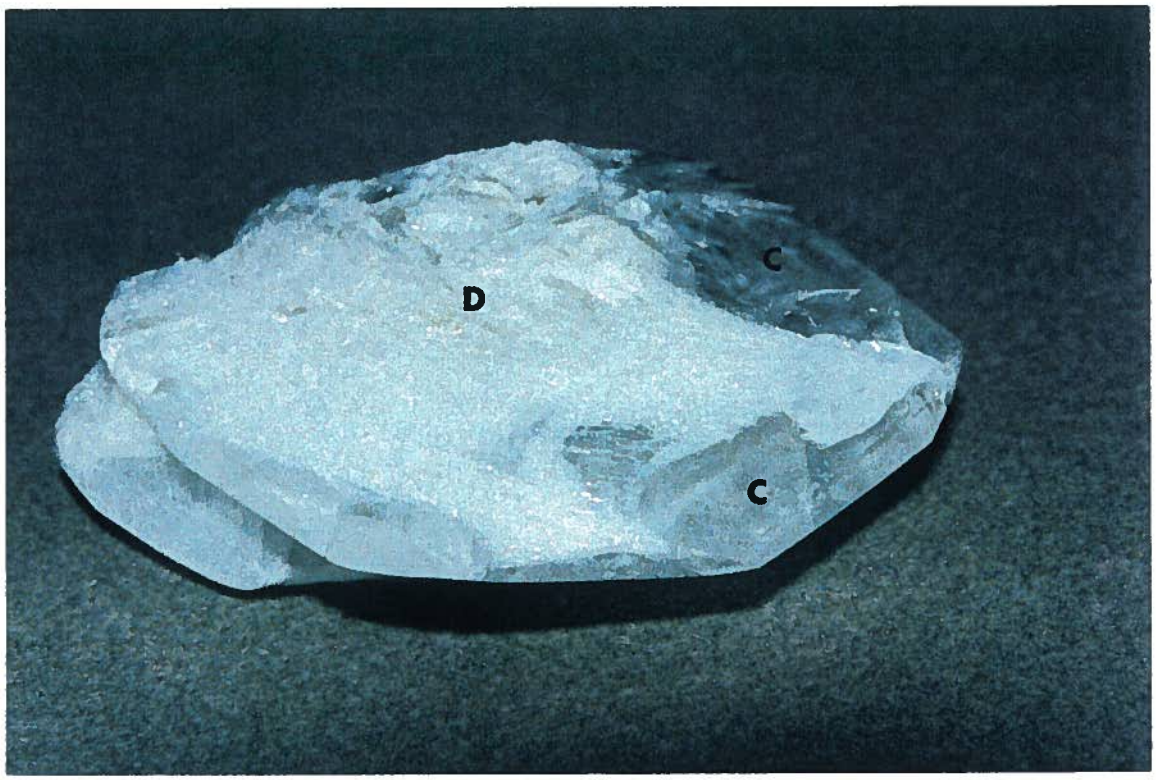

Figure 13.152: Bottom view of LBO 18 crystal.

Figure 13.153: Uncracked portions of LBO 18 crystal.

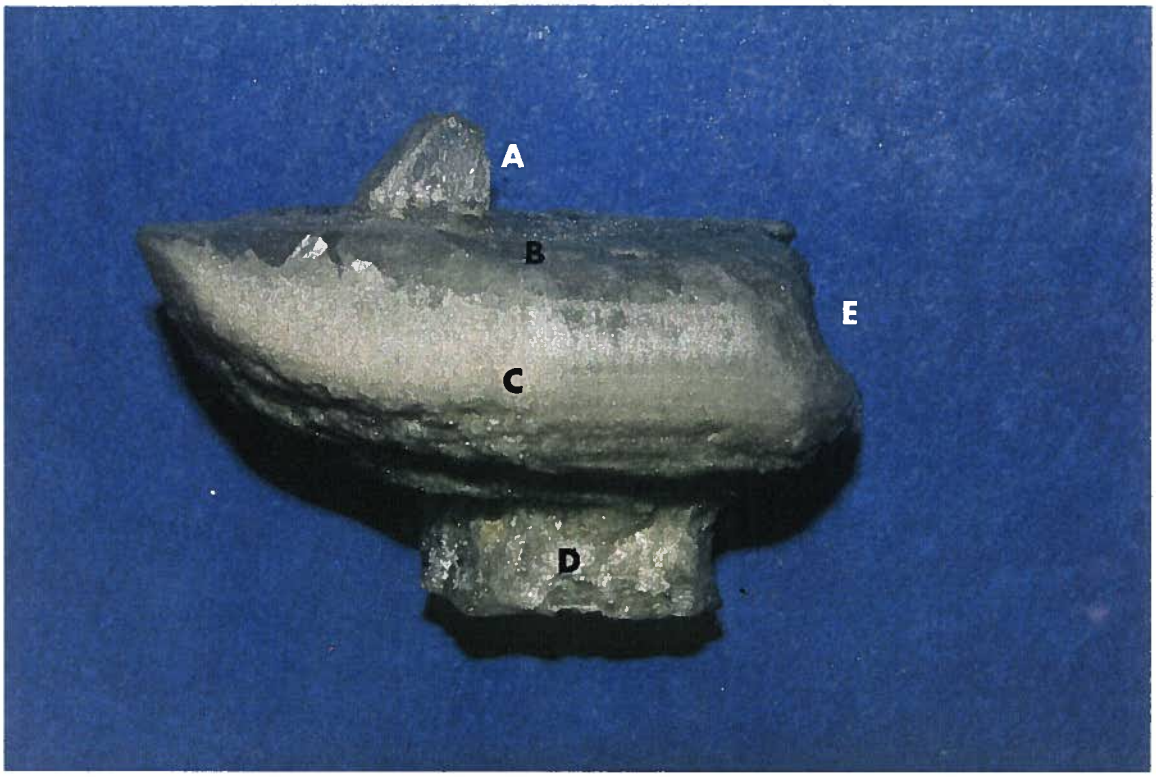

Figure 13.154: Side view of LBO 19 crystal

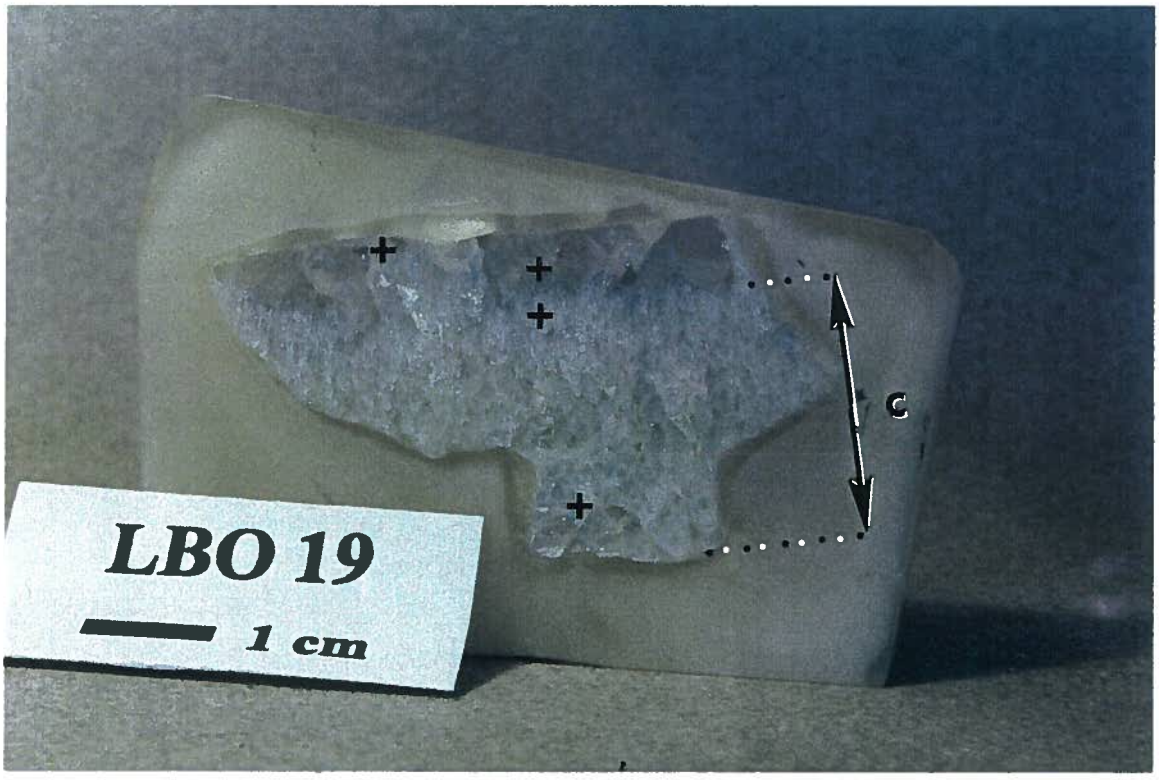

Figure 13.155: Cross section view of LBO 19 crystal. The crosses are regions were sample orientation was determined.

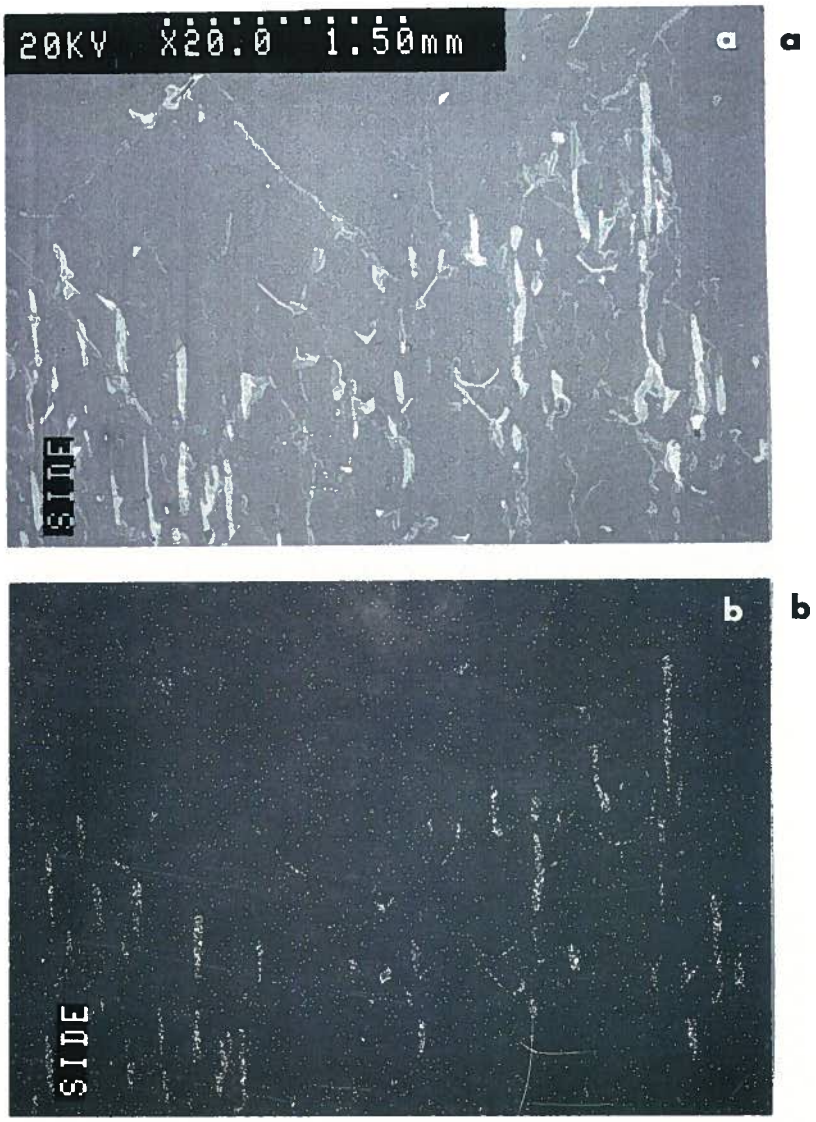

Figure 13.156: Area in LBO 19 were interface breakdown/eutectic growth started. Magnified 20 times. (a) SEM photo. (b) Map of molybdenum concentration. The bright regions correspond to a high molybdenum concentration.

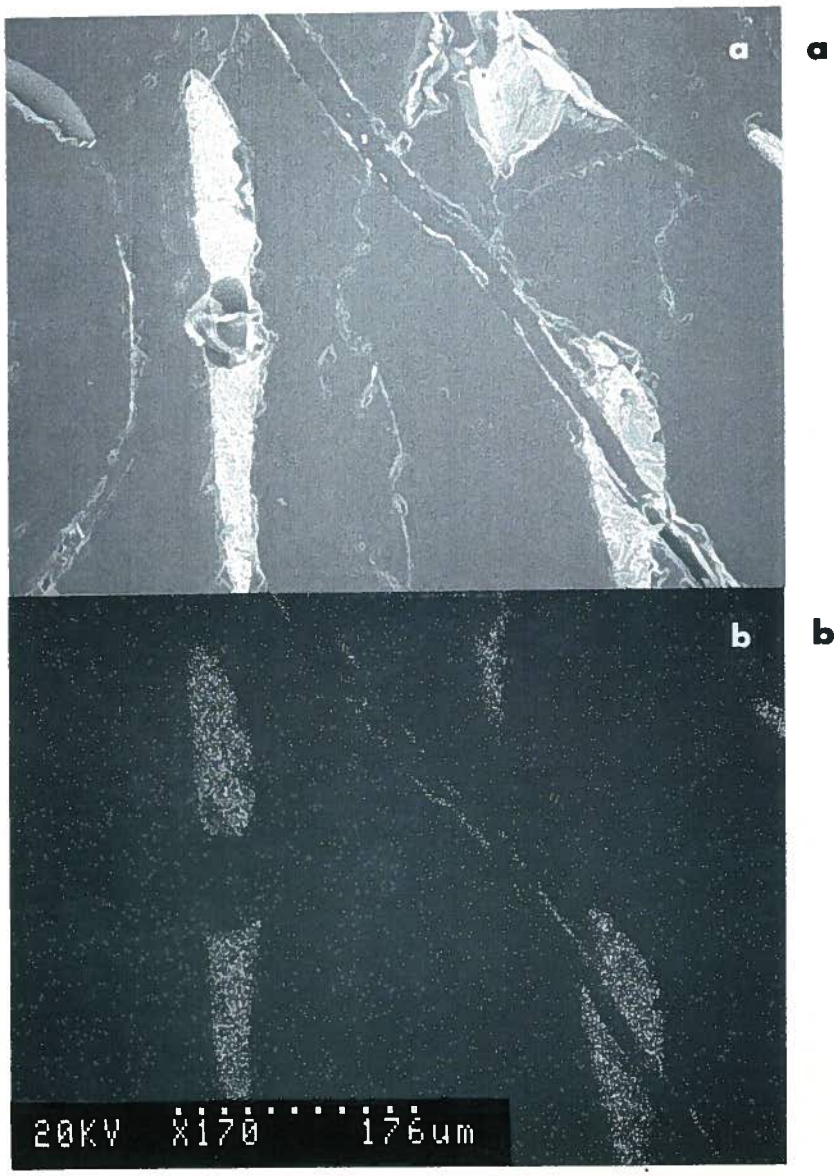

Figure 13.157: View of an molybdenum inclusion magnified 200 times. (a) SEM photo. (b) Map of molybdenum concentration. The bright regions correspond to a high molybdenum concentration.

Growth Run	Growth Rate		Growth Time		Atmosphere
	cooling (°C/day)	pulling (mm/day)	cooling (days)	pulling (days)	(days)
LBO 16	3.8	1.66	22	3	Air
LBO 17	2.4	0	27	0	Air
LBO 18	2.4	0	29	6	Air
LBO 19	2.4	1.66	16	12	Air
LBO 20	2.4	1.66	30	5.9	Air
LBO 21	2.4	0	17	0	N_2
LBO 22	2.4	0	21	0	N_2
LBO 23	2.4	0	27	0	N_2
LBO 24	2.4	0	32	0	N_2
LBO 25	2.4	0	9	0	N_2

Table 13.24: Growth conditions used for the crystal growth experiments, continued.

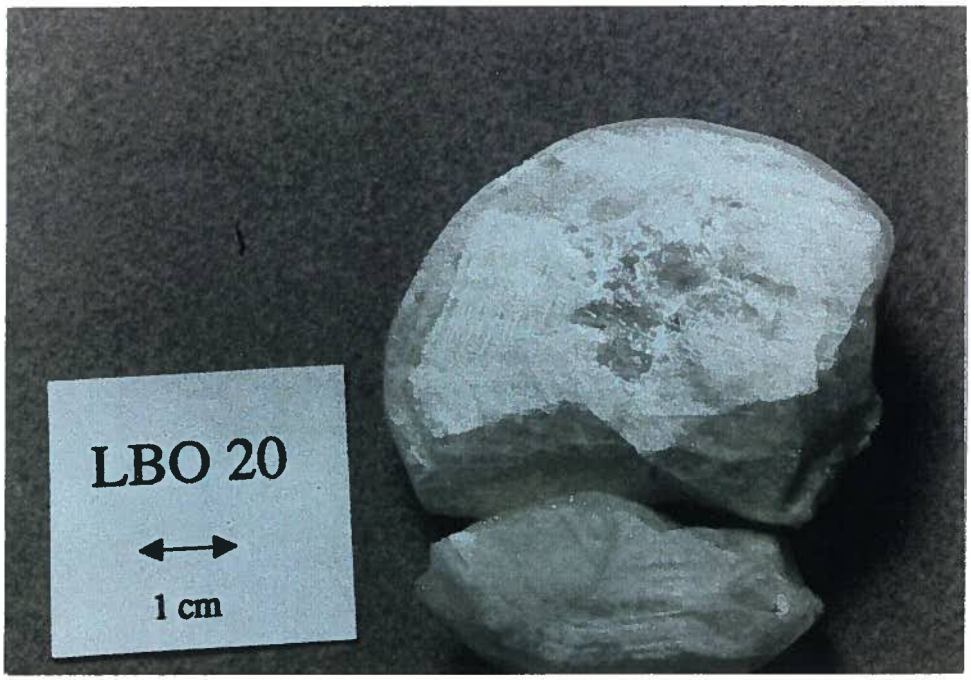

Figure 13.158: Top view of LBO 20 crystal

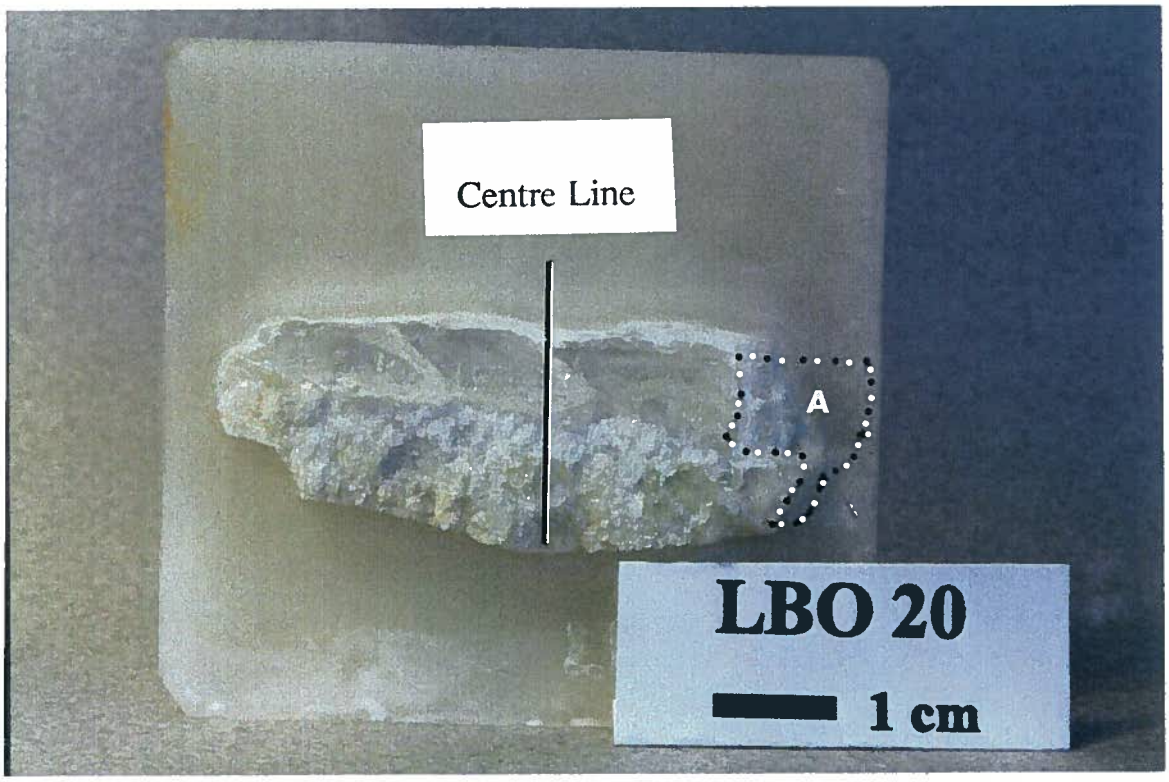

Figure 13.159: Cross section view of LBO 20 crystal.

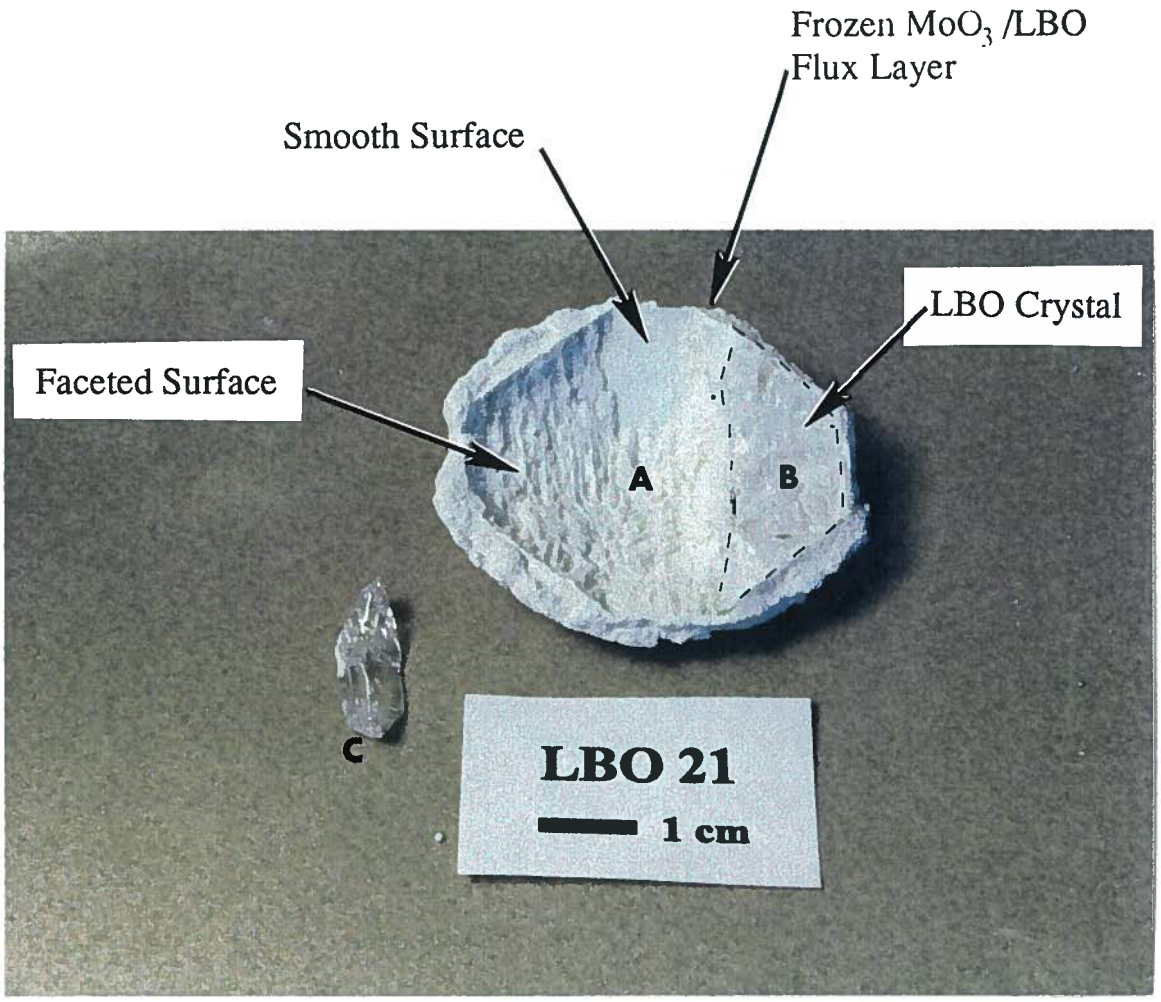

Figure 13.160: LBO 21 Crystal.

Figure 13.161: Top view of LBO 23 crystal.

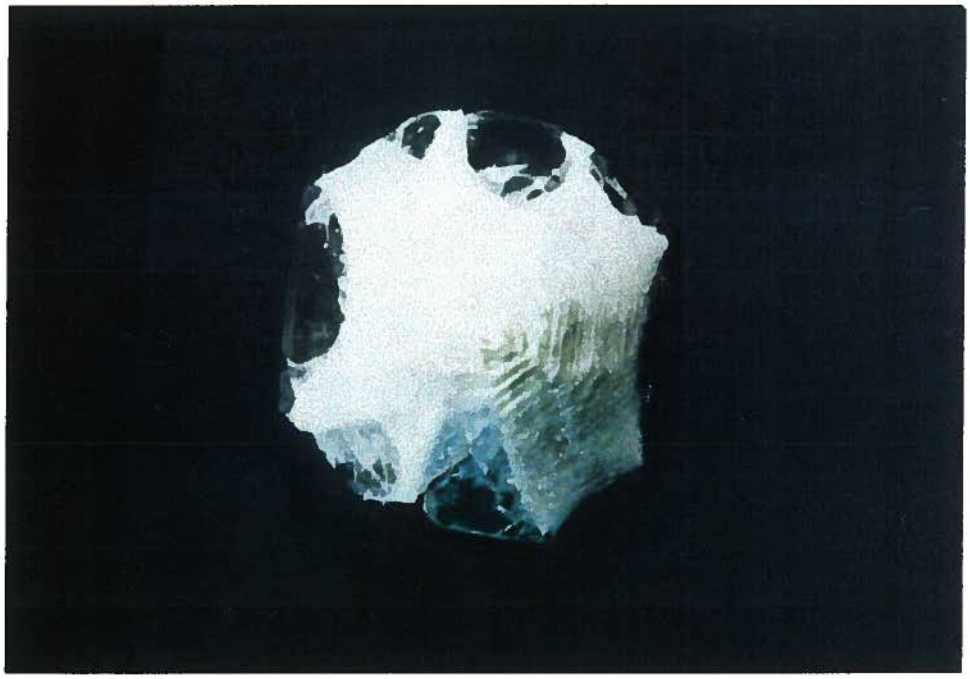

Figure 13.162: Bottom view of LBO 23 crystal.

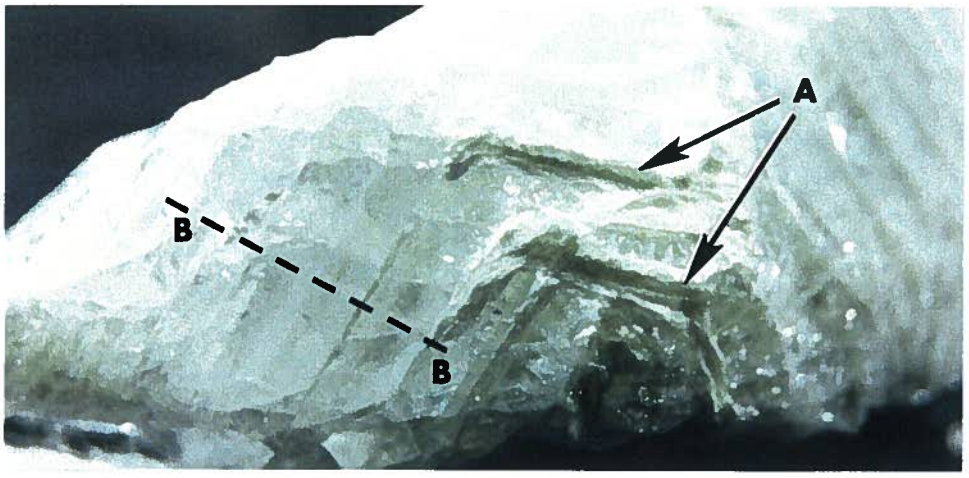

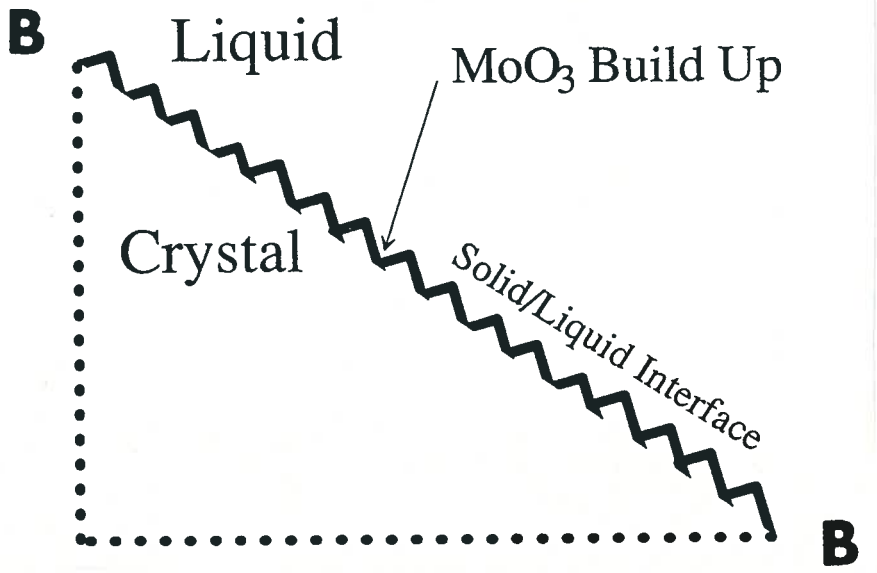

Figure 13.163: Interface appearance for planes were MoO_3 was stuck to the surface. (a) Photo of underside of crystal. The area A is a region of MoO_3 build up. (b) Schematic of surface along line B – B

Figure 13.164: Pieces of LBO 23 that were uncracked.

Figure 13.165: Top view of LBO 24 crystal.

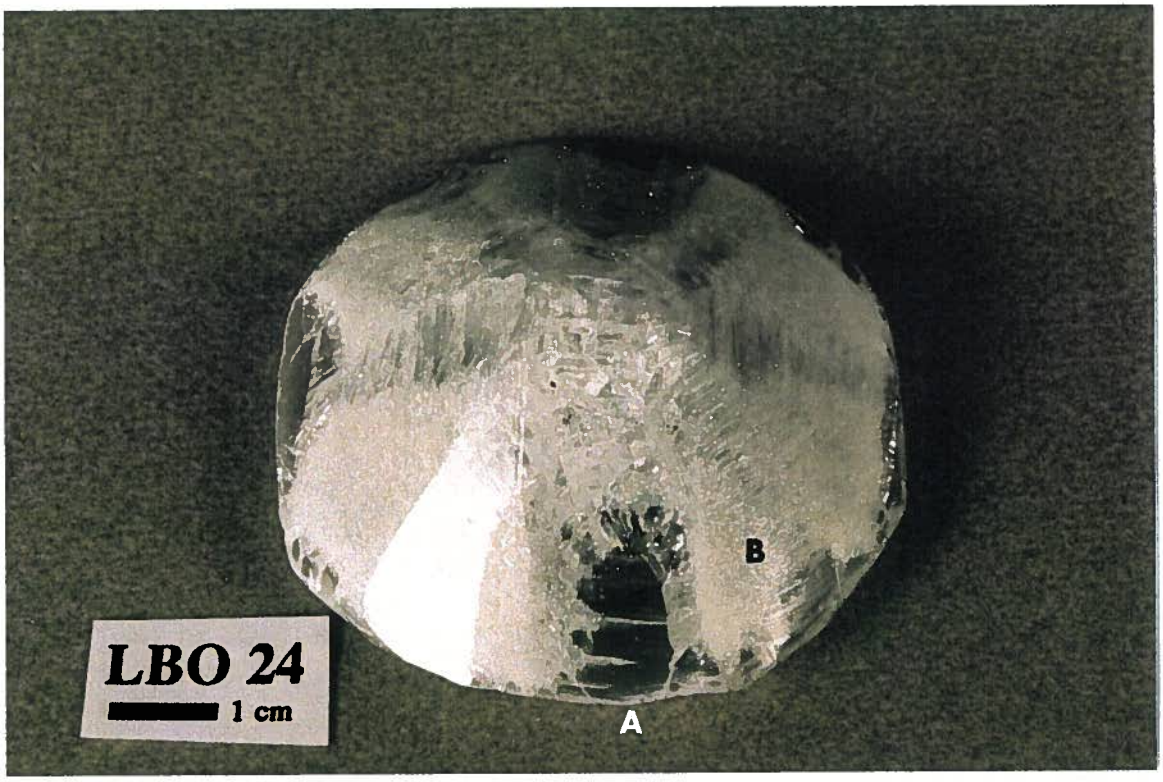

Figure 13.166: Bottom view of LBO 24 crystal.

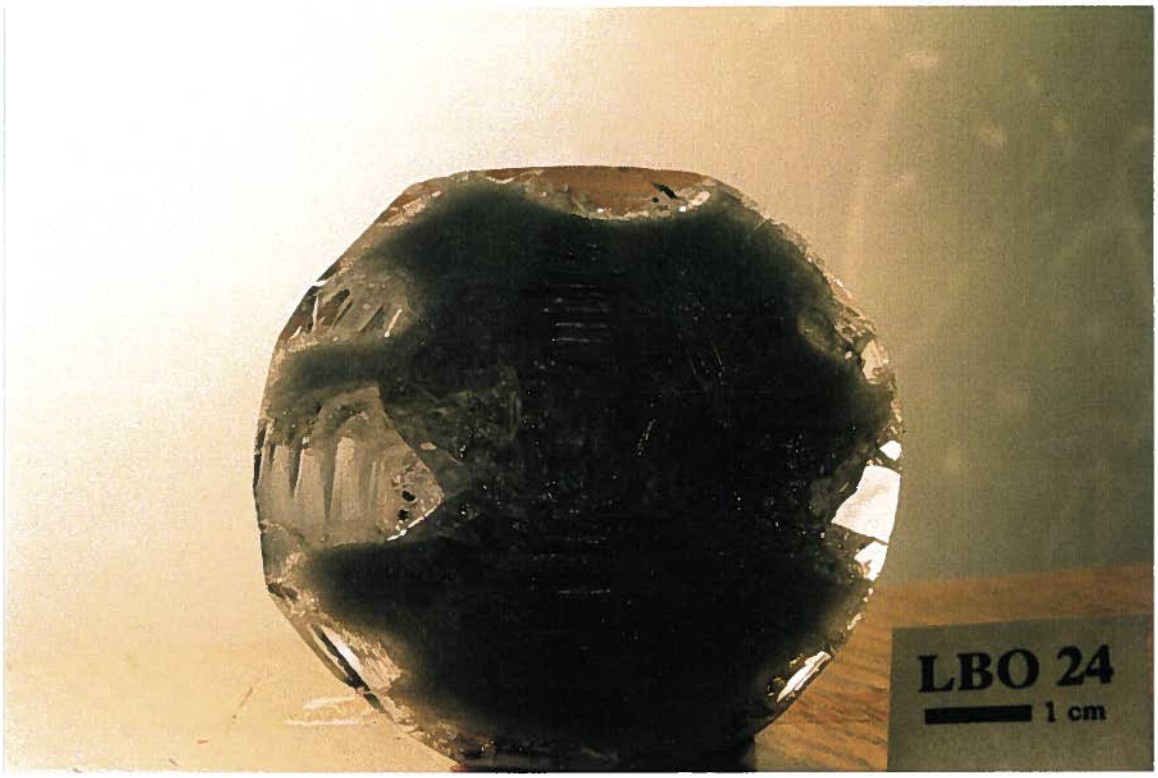

Figure 13.167: Back lit view of LBO 24 Crystal.

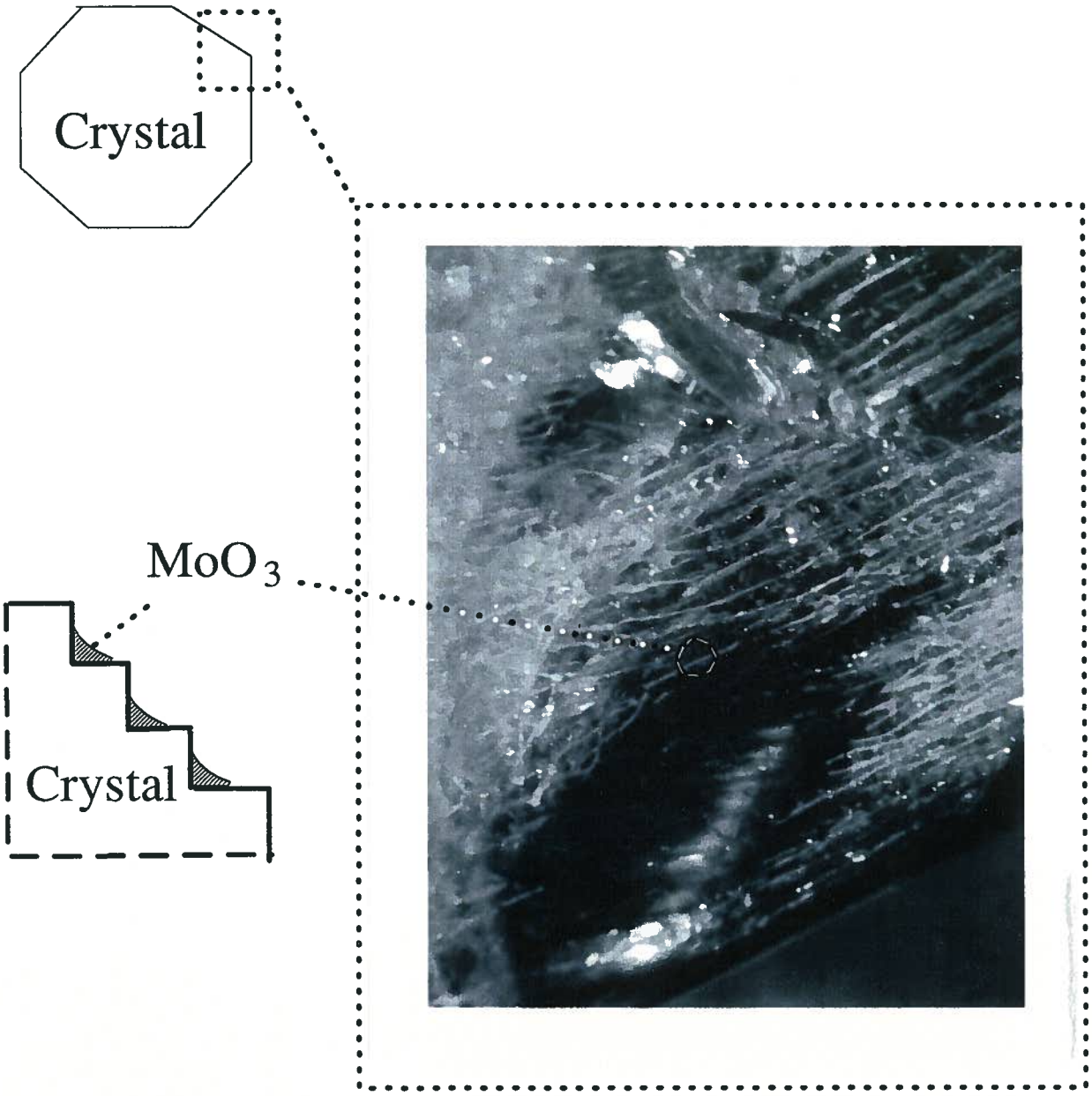

Figure 13.168: Schematic and photo of the MoO_3 on the LBO 25 crystal.

Chapter 14

Summary and Conclusions

A study was undertaken to grow Lithium Triborate crystals by the Top Seeded Solution Growth (Czochralski) method. Lithium Triborate cannot be grown directly since it forms as a result of a peritectic transformation at $834 \pm 4°C$. The addition of a MoO_3 flux modifies the phase diagram and allows LBO to be grown directly as a solid from the liquid. The flux addition increases the complexity of the system, since the MoO_3 that is rejected during growth builds up ahead of the growing interface which causes interface breakdown. Poor mixing in the melt, due to the high viscosity of B_2O_3, increases the possibility of interface breakdown.

The objective of this research was to establish reasons for interface breakdown and to optimize the growth process to produce large crystals of high optical quality. Mathematical and physical models have been employed to provide a quantitative understanding of heat transfer, fluid flow and mass transfer during the growth process. These analyses have been complemented by experimental measurements that were necessary to quantify thermophysical properties and boundary conditions. The primary reason for interface breakdown is eutectic formation at the growing interface. Although the initial composition of the melt is different from the eutectic, accumulation of MoO_3 due to poor mixing allows the eutectic composition to be reached during growth rates. A summary of the key findings are presented below:

1. The phase diagram for the LBO/MoO_3 system has been determined in the composition range of 44 and 74 weight percent MoO_3. The liquidus of the LBO phase

decreases from 682°C to 619°C between 44.8 and 60 weight percent MoO_3. The eutectic concentration has been estimated to be 61.5 weight percent MoO_3.

2. The viscosity of an LBO/MoO_3 melt is high, and was measured in accordance with ASTM standard C936-81 near 700°C. The viscosity of the melt containing 29.7 and 40.9 weight percent MoO_3 was found to be 234 and 21 poise respectively. The high viscosity retards mixing and inhibits mass transfer of the MoO_3 flux away from the growing interface. It has been found that interface breakdown occurs when the composition of the liquid at the solid/liquid interface reaches the eutectic. The viscosity decreases with the decreasing liquidus temperature as shown in Figure 5.40. Thus LBO crystal growth at higher MoO_3 concentration levels is more desirable, provided the overall concentration of the melt is below the MoO_3/LBO eutectic.

3. Temperature measurements have been conducted in a small (6.6 cm diameter) and large (8.8 cm diameter) crucible as a function of crucible rotation. A simulated crystal fabricated from platinum sheet was used create the type of mixing that occurred when an LBO crystal was present. At zero crucible rotation, axial and radial gradients were present in the melt. With crucible rotation the average temperature of the melt increased. At a crucible rotation of 25 rpm the melt temperature became more uniform in the axial and radial direction. In both crucibles, the difference in temperature of the melt with and without crucible rotation (30 rpm) was small being approximately 8°C to 10°C. However, the shape of the axial and radial temperature profiles changed significantly with crucible rotation.

4. The physical model examined the mixing due to crucible rotation in a high viscosity solution. A large (8.8 cm diameter) plexiglass crucible, plexiglass crystal 5.6 cm in diameter, glycerine solution and blue glycerine dye were used. The dye was used as a tracer to determine the flow patterns. It has been clearly demonstrated that

the flow and mixing is significant for crucible rotations 45 rpm and higher. Near the crystal the fluid moves in a semicircular arc toward the centre line of the melt. The axial component of the flow increases and eventually dominates as the fluid moves towards the centre of the crystal. This causes the fluid to move towards the bottom of the crucible. The fluid at the centre line moves toward the bottom of the crucible at which point it moves outward and then upward at the crucible wall. The fluid rotates in the theta direction while it moves in the axial and radial directions. The theta swirl is zero at the centre line of the melt and a maximum at the crucible walls. The fluid shears as it moves in the crucible. This causes the dye to mix into the bulk solution. The dye is completely dispersed in the melt after less than 5 minutes. Thus mixing of the melt due to crucible rotation is significant.

5. A mathematical model was used to determine the characteristics of fluid flow due to natural convection, crucible rotation, crystal rotation and crucible size. The model calculations without crystal and crucible rotation shown that the fluid velocity due to natural convection is very small, approximately 10^{-4} cm/s at 40.9 wt% MoO_3 ($\approx$ 12 poise at 730°C). Decreasing the MoO_3 content increases the viscosity of the solution which decreases the flow velocities in the melt. The flow due to natural convection with 29.7 wt% MoO_3 is approximately 10^{-6} cm/s ($\approx$ 86 poise at 730°C). Thus the melt is essentially stagnant at low concentrations of MoO_3. Inclusion formation and polycrystalline growth would be predominant under these conditions.

   Forced convection due to crystal and crucible rotation increases the amount of mixing in the melt. The average flow velocity is approximately 5×10^{-2} cm/s with 20 rpm crystal rotation and no crucible rotation. The flow velocity is the same order of magnitude for a crucible rotating at 20 rpm with a stationary crystal. However

the direction of flow is reversed. With crystal rotation the fluid flows upward under the crystal and down at the crucible walls. Crucible rotation causes the fluid to move up at the crucible walls and down under the crystal. Crucible rotation also produces higher tangential flow velocities at the crystal interface than crystal rotation. The fluid velocity tangential to the crystal/liquid interface is a maximum at the outer crystal diameter. The fluid velocity tangential to the crystal interface at 1/4 of the crystal radius is approximately one half of the tangential velocity at 3/4 of the crystal radius.

The model calculations show that the crystal interface will become concave to the liquid and eventually melt back at higher crystal rotation rates (greater than 20 rpm for the given thermal conditions). On the other hand, crucible rotation causes the crystal interface to become convex to the melt because the direction of the flow is reversed. Higher crucible rotation rates can be used to increase the flow velocity in the melt. The maximum calculated flow velocity at a crucible rotation of 60 rpm is approximately 2×10^{-1} cm/s. The maximum calculated fluid velocity at a crystal rotation rate of 20 rpm is 4×10^{-2} cm/s.

The flow velocity due to crucible rotation is dependent on the crucible size. The average tangential flow velocity at 0.5 of the crystal radius is -2×10^{-1} cm/s and -5×10^{-1} cm/s for the 6.6 cm and 8.8 cm diameter crucibles rotating at 60 rpm. Fluid velocity is proportional to crucible size for crucible rotation driven flows. The larger the crucible the higher is the rotational component of fluid velocity near the outside of the melt. This in turn gives the fluid a larger centripetal acceleration which increases the overall magnitude of the velocities of the melt.

The effect of counter and isorotation of the crystal and crucible on fluid flow have been shown. Crystal and crucible rotation cause the fluid to move in opposite

directions. Thus they compete with each other in determining the final fluid motion and velocity. A rotating crucible with a stationary crystal will result in a higher fluid velocity than a rotating crystal with a stationary crucible. Introducing crystal rotation at a given crucible rotation will result in decreasing the average flow rate. Increasing the crystal rotation to equal that of the crucible will result in the fluid becoming stagnant. If the crystal and crucible are rotating in the same direction at the same rate all of the fluid is stagnant. If the crystal and crucible are rotating in opposite directions at the same rate, then the area under the crystal is stagnant and there is some motion in the fluid due to the shearing motion. If the crystal rotation is larger than the crucible rotation then flow induced by crystal rotation will dominate.

6. The model calculations were compared to temperature measurements made in a rotating crucible with a stationary simulated crystal. Measurements in the small (6.6 cm diameter) and large (8.8 cm diameter) crucibles were employed for the comparison. The model predicts temperatures to within 2 to 4°C of the measured temperatures. The accuracy of the model predictions at higher crucible rotation rates indicates that the calculated melt velocity must be similar to the actual melt velocities.

7. Mass transfer calculations have been conducted for an LBO crystal, conical in shape, growing in the [001] direction to determine the growth time required to reach the eutectic concentration at the solid liquid interface. It was determined that at the normal growth rate (2.4°C/day $\approx$ 0.7 mm/day) the interface concentration reaches the LBO$-MoO_3$ eutectic after 27 days. The calculations indicate that the interface concentration increases slowly at the start of growth and accelerates at the end of growth. At a growth velocity of 0.35 mm/day results the eutectic

concentration is not reached within the 30 day time period examined. An interface growth velocity of 1.05 mm/day results in the interface concentration reaching the eutectic in 10 days.

8. The gradients in the crystal were measured to determine the influence of varying amounts of insulation. It was determined that independent of crucible size, the thermal gradients in the crystal are most sensitive to the addition of insulation over the seed hole in the furnace and the vertical position of the crystal. Moving the simulated crystal towards the centre of the furnace reduces the axial gradients and the insulated top reduces the radial gradients. Using a small crucible for crystal growth reduces both the axial and radial gradients provided that the crystal is surrounded by the walls of the crucible during the post growth cooling stage.

9. Crystals were grown with knowledge gained from the modeling and experimental measurements. Employing crucible rotation rates of 60 rpm resulted in an increase in single crystal yield from $3 \times 3 \times 3$ mm^3 to $20 \times 10 \times 8$ mm^3. Crystal growth rates in excess of 1.66 mm/day were possible for growth in the $[3\bar{1}2]$ direction. The same growth rates caused interface breakdown when the crystal was grown in the [001] direction. Growth in the [001] direction caused faceting to occur at all locations of the solid/liquid interface with exception of the 101 plane. The 101 plane grew as a flat surface and was free of MoO_3 flux. The crevices between the facets trap the MoO_3 flux which sticks to the surface of the crystal after it has been separated from the melt. The MoO_3 in these regions caused cracking of the crystal because of the mismatch in thermal expansion coefficients between MoO_3 and LBO.

In conclusion the results of the present investigation shows that good quality crystals of limited size can be grown from a melt of LBO containing MoO_3 as a flux. The major factor limiting the growth rate and crystal size is the concentration of MoO_3 at the

advancing interface. Since MoO_3 is not soluble in LBO, all of the MoO_3 rejected by the solid is accumulated ahead of the interface. The MoO_3 moves into the liquid by diffusion through a thin boundary layer adjacent to the interface and mixes in the bulk melt. When the concentration of MoO_3 at the interface reaches the eutectic concentration of 61.5 wt% starting with a melt concentration of 44.5 wt%, eutectic will form, which produces phase regions rich in MoO_3, effectively terminating growth of a good quality crystal. Accordingly, larger crystals can be grown if the thickness of the diffusion layer is decreased and the remaining MoO_3 is distributed uniformly in the liquid.

Higher flow rates in the melt below the interface, and thinner diffusion boundary layers are obtained with higher crucible rotation rates. Higher crystal rotation rates cannot be used since they are limited by remelting of the crystal. Buoyancy force flow is very small, due to the high viscosity of the melt. Reducing the concentration of MoO_3 in the melt would result in a decrease in the fluid flow in the melt due to an increase in the viscosity. This would also result in a higher MoO_3 concentration at the growing interface due to the lower fluid velocity. The size and quality of LBO crystals which can be grown from the melt by the top seeded solution growth (Modified Czochralski) process is limited by the nature of the materials and process. Growth must be slow and growth conditions selected to move the flux away from the interface as rapidly as possible primarily by crucible rotation. Some crystal orientations grow more readily than others due to faceting, which affects the local movement of the flux away from the interface. The grown crystals can crack readily under thermal stresses which requires the crystals to be cooled in a uniform thermal environment.

Chapter 15

Recommendations for Future Work

Several more sets of crystal growth runs should be carried out. In addition the mass transfer calculations should be improved to more accurately predict the process.

1. The size and quality of the LBO crystals is dependent on the orientation of the crystal. Crystals of [100], [010] and [101] directions should be grown to assess how significant the orientation is in obtaining higher quality crystals. In particular the extent of faceting of the interface, as a function of crystal orientation and the temperature gradient in the melt, should be determined. The relationship between faceting and the onset of the formation of MoO_3 inclusions should be established. On the basis of this information procedures should be developed to reduce faceting, if faceting is found to instigate the formation of MoO_3 inclusions.

2. After growth the crystal must be cooled slowly in a uniform thermal environment to prevent cracking. This must be done in the crystal growth furnace. Accordingly the furnace design should be modified to enable the crystal to cool at the center of the furnace where the thermal gradients are low. This would require modification of the lower portion of the furnace to allow the crucible to be lowered out of the area where the crystal will be cooled to room temperature.

3. The model should be extended to include important aspects of growth which were not considered. During growth MoO_3 evaporates from the top surface of the melt, changing the melt composition. The surface of the solid liquid interface in the

present model is assumed to be smooth. In fact it can be faceted which influences the model results and the onset of eutectic growth. The affect of faceting should be incorporated into future mathematical models.

4. The possibility of replacing the MoO_3 flux with another material which produces melts with much lower viscosities should be investigated. The flux would have to be insoluble in LBO.

Bibliography

[1] C. Chen, Y. Wu, A. Jiang, B. Wu, G. You, R. Li, and S. Lin, *J. Opt. Soc. Am. B*, Vol. 6, No. 4, 616 (1989).

[2] C. Chen, Y. Wu, A. Jiang, B. Wu, G. You, R. Li, and S. Lin, *United States Patent*, Patent No. 4826283, Date: May 2, 1989

[3] C. Chen, *Laser Focus World*, November 1989

[4] A. Napolotano, P.B. Macedo and E.G. Hawkins, *Journal of The American Ceramic Society*, Vol. 48, No. 12, 613 (1965)

[5] S. Zhao, C. Huang, H. Zhang, *Journal of Crystal Growth*, 99 (1990) 805-810

[6] E. Bruck, R.J. Raymakers, R.K. Route and R.S. Feigelson, *Journal of Crystal Growth*, 128 (1993) 933-937

[7] B. Sastry and F. Hummel, *Journal of the American Ceramic Society*, Vol. 41, No. 1, 7-17

[8] Von H. König and R. Hoppe, *Z. anorg. allg. Chem.*, 439 (1978) 71-79

[9] M. Ihara, M. Yuge and J. Krogh-Moe, *Yogyo-Kyokai-Shi*, 88(4) (1980) 179-184

[10] C. L. Tang, *Progress Report, Cornell University, Ithica, NY*

[11] C. Chen, Y. Wu, A. Jiang and G. You, *Scientia Sinica B*, Vol. 28, No. 3, 235-243

[12] A. Jiang, F. Cheng, Q. Lin, Z. Cheng and Y. Zheng, *Journal of Crystal Growth*, 79 (1986) 963-969

[13] R.S. Feigelson, R.J. Raymakers and R.K. Route, *Journal of Crystal Growth*, 97 (1989) 352-366

[14] I. Barin, O. Knacke, and O. Kubaschewski *Thermophysical Properties of Inorganic Substances*, Springer-Verlag, Berlin (1977).

[15] D.D. Wagman et al., *Selected Values of Thermodynamic Properties, National Bureau of Standards Series 270*, U.S. Department of Commerce, Washington, (1968-1971).

[16] Y.S. Touloukian, Series Editor, *Thermophysical Properties of Matter, the TPRC data series*, IFI/Plenum, New York, (1970-).

[17] Cleveland Crystals, Inc. *BBO and LBO Information Sheet*, 19306 Redwood Avenue, Cleveland, Ohio 44110

[18] Fujian Castech Crystals, Inc. *LBO Information Sheet*, Get this address York

[19] B.D. Cullity, *Elements of X-Ray Diffraction*, Addison-Wesley, Massachusetts, (1978)

[20] D. Elweel and H.J. Scheel, *Crystal Growth from High-Temperature Solutions*, Academic Press, London

[21] A. Horowitz, *Journal of Crystal Growth*, 78 (1986) 121-128

[22] A. Horowitz, *Journal of Crystal Growth*, 79 (1986) 296-302

[23] L. K. Cheng et al, *Journal of Crystal Growth*, 89 (1988) 553-559

[24] Feigelson, *SPIE* , 1104 (1989)

[25] S. Miyazawa, *Journal of Crystal Growth*, 49 (1980) 515-521

[26] B. Cockayne, *Journal of Crystal Growth*, 42 (1977) 413-426

[27] J. R. Carruthers *J. Electrochem. Soc.*, 114 (19) 959-962

[28] J. R. Carruthers and K. Nassau, *Journal of Applied Physics*, 39 (1968) 5205-5214

[29] W. E. Langlois and C.C. Shir, *Computer Methods in Applied Mechanics and Engineering*, 12 (1977) 145-152

[30] W. E. Langlois *Journal of Crystal Growth*, 42 (1977) 386-399

[31] N. Kobayashi and T. Arizumi, *Journal of Crystal Growth*, 49 (1980) 419-425

[32] N. Kobayashi, *Journal of Crystal Growth*, 52 (1981) 425-434

[33] N. Kobayashi, *Journal of Crystal Growth*, 55 (1981) 339-344

[34] R. Lamprecht, *Journal of Crystal Growth*, 65 (1983) 143-152

[35] M.J. Crochet and P.J. Wouters, *Journal of Crystal Growth*, 65 (1983) 153-165

[36] K. Takagi, T. Fukazawa and M. Ishi, *Journal of Crystal Growth*, 32 (1976) 89-94

[37] V. Nikolov, K. Iliev and P. Peshev, *Journal of Crystal Growth*, 89 (1988) 313-330

[38] A. Bottaro and A Zebib, *Journal of Crystal Growth*, 97 (1989) 50-58

[39] R. A. Brown, T.A. Kinney, P.A. Sackinger and D.E. Bornside, *Journal of Crystal Growth*, 97 (1989) 99-115

[40] M. Mihelcic, C. Schroeck-Pauli, K. Wingerath, H. Wenzel, W. Uelhoff and A. Van Der Hart, *Journal of Crystal Growth*, 53 (1981) 337-354

[41] M. Mihelcic, C. Schroeck-Pauli, K. Wingerath, H. Wenzel, W. Uelhoff and A. Van Der Hart, *Journal of Crystal Growth*, 57 (1982) 300-317

[42] H.J. Scheel *Journal of Crystal Growth* , 13/14 (1972) 560-565

[43] E.O. Schulz-Dubois *Journal of Crystal Growth* , 12 (1972) 81-87

[44] A. A. Wheeler, *Journal of Crystal Growth*, 97 (1989) 64-75

[45] J. C. Burton, R. C. Prim, and W.P. Slichter, *The Journal of Chemical Physics*, 21 (1953) 1987-1996

[46] F. W. White, *Viscous Fluid Flow*, McGraw Hill, New York

[47] L. O. Wilson, *Journal of Crystal Growth*, 44 (1978) 371-376

[48] J. J. Favier and L. O. Wilson, *Journal of Crystal Growth*, 58 (1982) 103-110

[49] Klaus J. Vetter, *Electrochemical Kinetics*, Academic Press, New York

[50] Hewlett Packard, *Practical Temperature Measurements* , Application Note 290

[51] Chris Parfeniuk, *M.A.Sc. Thesis* , The University of British Columbia (1990)

[52] *Fidap Users Manual* , Fluid Dynamics International, Evanston, Illinois 60201 (1991).

[53] J.C. Brice, *The Growth of Crystals from Liquids* , May 2, 1989

[54] F. Incropera, D. De Witt *Fundamentals of Heat and Mass Transfer,* John Wiley & Sons, New York

[55] B. Pamplin Editor *Crystal Growth,* Pergamon Press, Oxford

[56] F. Kreith and W. Black, *Basic Heat Transfer,* Harper and Row, New York

[57] J. Szekely and J. Themelis, *Rate phenomena in process metallurgy,* Wiley-Interscience, New York

Appendix A

Estimation of the Thermal Conductivity and the Gas Temperature

The accuracy of the mathematical model results depend on the how well the mathematical expressions describe the process being modeled, if the assumptions used to simplify the model are correct, whether the correct values of the thermophysical properties are used and if the correct boundary conditions are used. In the present case, the fluid flow calculations are more reliable since the liquid being considered has a high viscosity. The thermophysical properties of the system that are required for the mathematical model include, specific heat, density and the coefficient of thermal expansion. Values for these properties at high temperatures are available in the literature, as listed in Chapter 2. Viscosity values of the LBO/MoO_3 melts are required which are not available. These have been determined in the present investigation (Chapter 5). The low temperature thermal conductivity of LBO is available in the literature. High temperature values are not available, and in the present case are estimated as described below. The fixed temperature boundary conditions at the crucible wall have been estimated using temperature measurements in the melt, Chapter 7. The ambient gas temperature above the melt will be evaluated using the melt temperatures shown in Figure 7.52.

The thermophysical properties of the melt are assumed to be the sum of the weight percent average of the constituent properties.

$$\mathrm{Cp}_{melt}(J/gK) = \mathrm{Cp}_{LBO} \times \mathrm{Wt\%\ LBO} + \mathrm{Cp}_{MoO_3} \times \mathrm{Wt\%\ MoO_3}$$

The mathematical model is applied to a melt having a charge concentration of 50Wt% MoO_3. The value of the melt viscosity is obtained by extrapolating the viscosity−concentration

Property	Unit	Value
Cp	J/g K	0.63
ρ	g/cm^3	3.26
ν	poise	2.29
α	K^{-1}	6×10^{-6}

Table A.25: Thermophysical properties used in the model to determine the conductivity of the melt and the ambient gas temperature.

curves given in Figure 5.39. The average melt is taken to be 820°C. The viscosity as a function of concentration at 820°C extrapolated to 50 Wt.% is 2.29 poise. The melt properties used in the calculations are given in Table A.25.

A.1 High Temperature Thermal Conductivity Evaluation

The high temperature conductivity of the LBO/MoO_3 solution is approximated using the temperature measurements given in Figure 7.52 and the boundary conditions given in Figure 7.53. The liquid is modeled with fixed temperatures boundary conditions at the bottom, side and top of the melt, Figure A.169. Model calculations with different conductivities are compared with the experimental results at distances of 0.5 cm, 1.0 cm, 1.5 cm and 2.0 cm from the bottom of crucible at both 0 and 1.6 cm from the center of the crucible. The conductivity that gives model results with the best fit of the experimental data is assumed to be the correct value. The experimental results and model calculations are compared by the sum of the difference in the temperature values at the different locations.

$$\text{Difference} = \Sigma \left(T_{\text{experimental}} - T_{\text{model}} \right)$$

The model calculations using a conductivity of 0.1 W/cm K are examine. The fluid speed from natural convection, Figure A.170, is less than 0.02 cm/s due to the high viscosity

Conductivity (W/cm K)	Difference (Celsius)
1.0	19.8
0.1	13.6
0.075	10.3
0.05	4.7
0.025	-17.2
0.01	-95.4

Table A.26: Difference between the model and experimental temperature values as a function of the conductivity.

of the melt. Thus, conduction is the dominant mode of heat transfer in the melt. The approximation of the conductivity is easier due to no natural convection occurring in the melt.

Table A.26 and Figure A.171 gives the difference between the experimental results and model calculations for different conductivity values. An LBO/MoO_3 conductivity value of 0.05 W/cm K used in the model gives the best fit to the experimental temperature values. This is very close to the conductivity of LBO in the **c** direction, 0.039 W/cm K, as given in Table 2.2. It is assumed that the conductivity value of the LBO/MoO_3 melt is 0.05 W/cm K and it does not change with the stoichiometry of the melt.

A.2 Ambient Gas Temperature Approximation

The ambient gas temperatures at the top of the melt are approximated by determining which values give the best fit to the experimental data. Doing this allows the model to have the best possible fit for the thermal field in the melt. The thermophysical properties used are given in Table A.25. The value of the conductivity is 0.05 as determined in the previous section and the value of the convective heat transfer coefficient used is 0.006

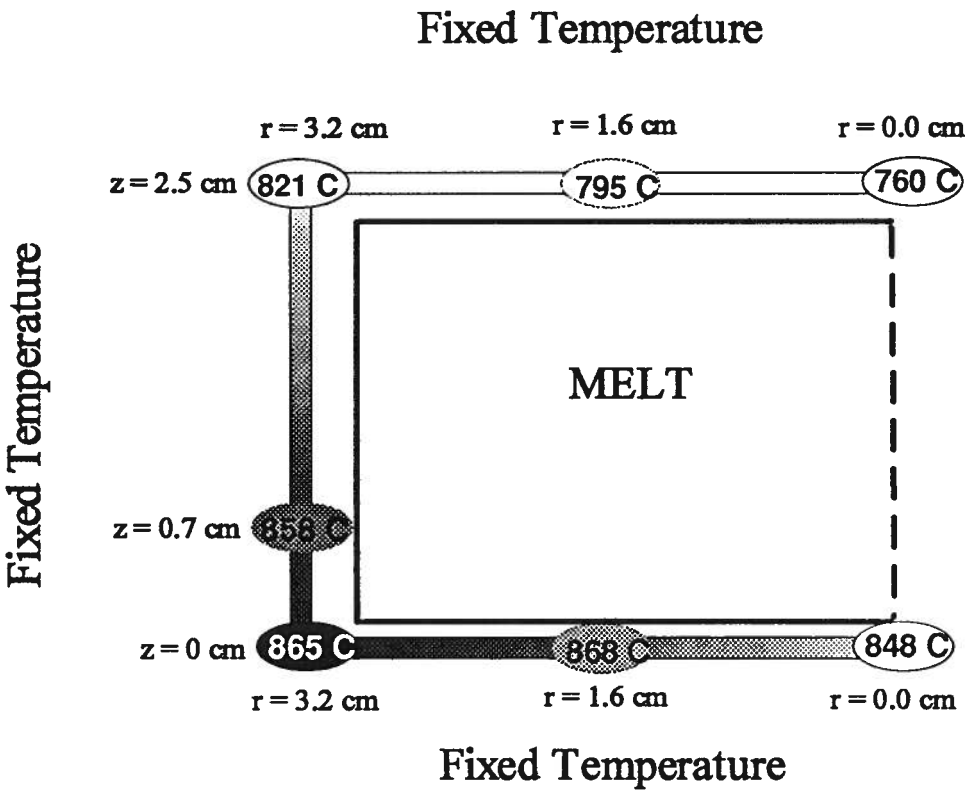

Figure A.169: Temperature boundary conditions used to approximate the conductivity of the LBO/MoO_3 melt.

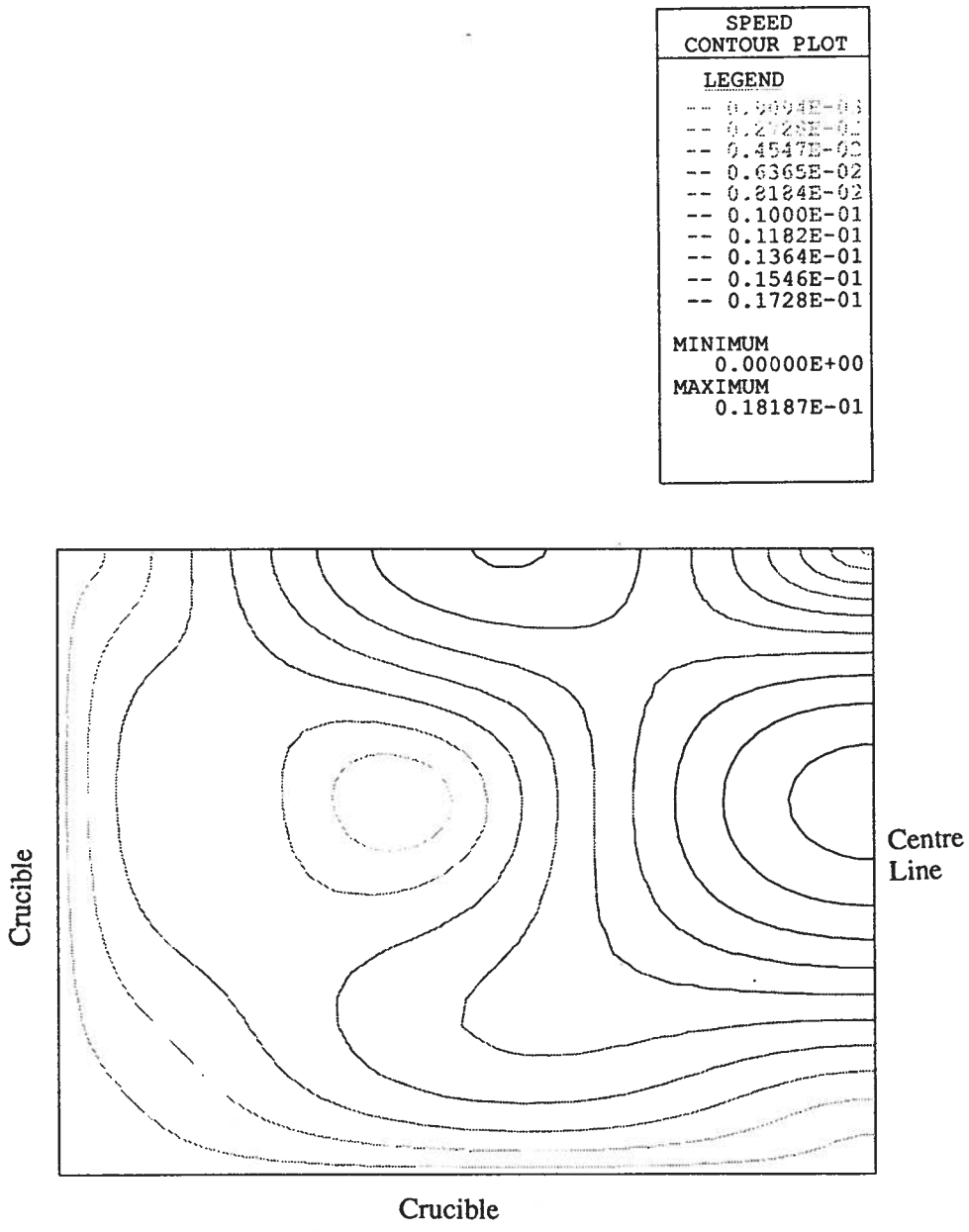

Figure A.170: Fluid speed $\left(U_r^2 + U_z^2\right)^2$ in the melt. The value of the conductivity used in the model is 0.1 W/cm K.

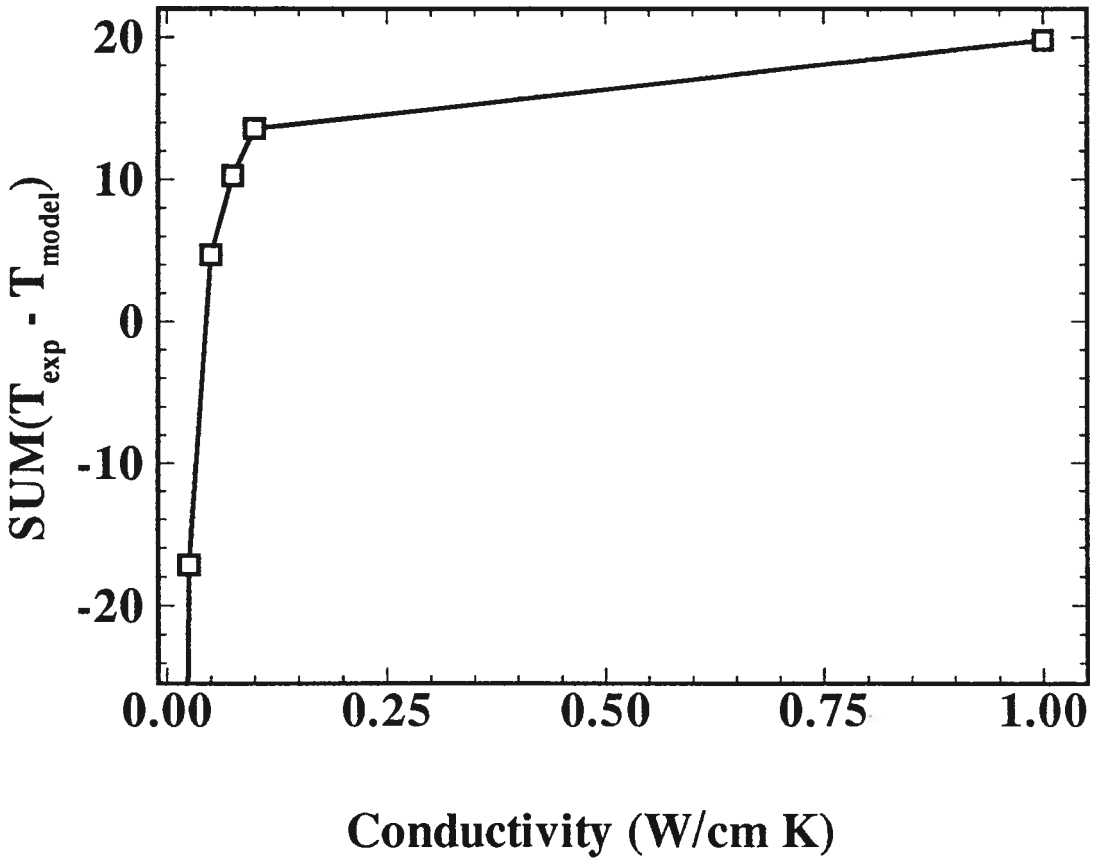

Figure A.171: Difference between the model and experimental temperature values as a function of the conductivity.

W/cm^2 K. The best fit for the ambient gas temperature was found to be:

$$T = 200 + 187.8 \times r - 23.7 \times r^2 \tag{A.13}$$

Where r is in centimeters and is the radial position that the convective boundary is in crucible and T is the ambient gas temperature in degrees celsius. Figure A.172 shows the measured temperature values and the model calculations using the best fit ambient gas temperature.

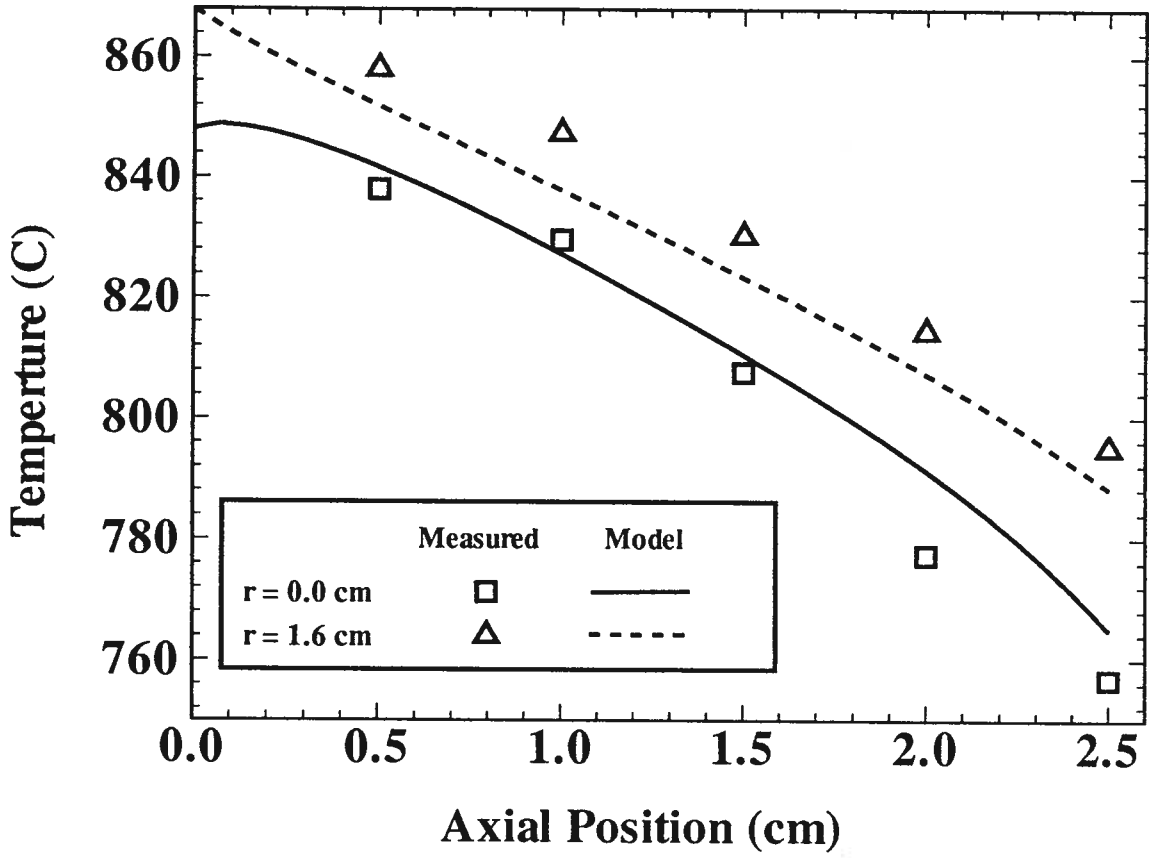

Figure A.172: Comparison with the experimental temperature data and the model results for the best ambient gas temperature values.